TECHNISCHE UNIVERSITÄT
MÜNCHEN
Physik-Department E12 - Dense and Strange Hadronic Matter

# Search for the kaonic bound state pp$K^-$

Exclusive analysis of the reaction p + p → p + $K^+$ + Λ at the FOPI experiment at GSI

Robert Helmut Münzer

TECHNISCHE UNIVERSITÄT
MÜNCHEN
Physik-Department E12 - Dense and strange hadronic matter

# Search for the kaonic bound state pp$K^-$

Exclusive analysis of the reaction p + p $\rightarrow$ p + $K^+$ + $\Lambda$ at the FOPI experiment at GSI

Robert Helmut Münzer

Vollständiger Abdruck der von der Fakultät für Physik der Technischen Universität München zur Erlangung des akademischen Grades eines

Doktors der Naturwissenschaften (Dr. rer. nat.)

genehmigten Dissertation.

| | | |
|---|---|---|
| Vorsitzender: | | Univ.-Prof. Dr. N. Kaiser |
| Prüfer der Dissertation: | 1. | Univ.-Prof. Dr. L. Fabbietti |
| | 2. | Univ.-Prof. Dr. P. Fierlinger |

Die Dissertation wurde am 19.03.2014 an der Technischen Universität München eingereicht und durch die Fakultät für Physik am 23.04.2014 angenommen.

# Zusammenfassung

Hadronen können bei niedrigen Energien im Rahmen der Quantenchromodynamik mit Hilfe von effektive Modellen, wie $\chi$PT, beschrieben werden. Eine besondere Herausforderung stellen dabei Hadronen mit Gehalt an seltsamen Quarks (Strangeness) dar. Beispiele dafür sind das Verhalten von Kaonen in der Gegenwart von Kernmaterie und die lange vorhergesagte Formation von gebundenen Zuständen zwischen Antikaonen und einem oder mehreren Nukleonen.
Im letzten Jahrzehnt verstärkte sich das Interesse an gebundenen kaonischen Zuständen durch experimentelle Ergebnisse zum $\Lambda(1405)$ und zu sog. kaonischen Clustern wie das pp$K^-$. Diese beiden Zustände sind eng verknüpft, da das $\Lambda(1405)$ heutzutage als molekularer Zustand beschrieben wird, der einen Beitrag aus dem gebunden Zustand $K^-$-p besitzt.
Die vorliegende Arbeit beschreibt die experimentelle Suche nach einem gebundenen pp$K^-$ Zustand in der Reaktion p+p$\rightarrow$p$K^+\Lambda$. Das Experiment wurde am FOPI Spektrometer an der GSI in Darmstadt mit einem Protonstrahl ($E_{\mathrm{Strahl}}$=3.1 GeV) und einem flüssig Wasserstoff Target durchgeführt. Zur Anreicherung der gewünschten Reaktion wurden die Strahldetektoren verbessert sowie ein neuer Trigger- und Spurdetektor für die $\Lambda$-Teilchen (Si$\Lambda$ViO) in das Spektrometer eingebaut. Mit Hilfe von rekonstruierten $\Lambda$-Teilchen konnte deren Anreicherung in den aufgenommen Daten um einen Wert von $14.1 \pm 7.9(stat)^{+4.3}_{-0.5}$ bestimmt werden.
Die Analyse der exklusiven Reaktion p+p$\rightarrow$p$K^+\Lambda$ wurde in unterschiedlichen Schritten durchgeführt. Für die Reduktion des Untergrunds wurde ein kinematischer Refit verwendet. Der verbleibende Untergrund konnte durch eine sog. Seitenband-Analyse Technik bestimmt werden. Insgesamt konnten 903 exklusive Reaktionen bei einem Restuntergrund von $\approx$61 Ereignissen extrahiert werden.
Die beobachteten Reaktionen wurden sowohl mit Phasenraum- als auch mit Transportmodell Simulation verglichen. In beiden konnte eine signifikante Abweichung zwischen experimentellen und simulierten Daten beobachtet werden. Eine hinreichende Beschreibung wurde mit Hilfe der Bonn Gatchina Partialwellen-Analyse (BG-PWA) erreicht, durch die eine kohärente Summe aus Übergangswellen an die experimentellen Daten gefittet wird.
Mit den Ergebnissen der BG-PWA konnte eine obere Grenze für die Produktion des pp$K^-$ bestimmt werden, indem die Wellen dieses Zustands in die BG-PWA Routine hinzugefügt wurden. Für eine Konfidenz Grenze von 95% wurde eine obere Grenze für den Produktions-Querschnitt zwischen 4.1$\mu$b und 16.9$\mu$b bestimmt, wobei für den Zustand eine Breite zwischen 20 MeV/c$^2$ und 80 MeV/c$^2$ und eine Masse zwischen 2.205 GeV/c$^2$ and 2.305 GeV/c$^2$ angenommen wurde. Diese Ergebnisse - besonders für kleine Breiten - liefern Randbedingung für zukünftige theoretische Berechnungen.
Darüber hinaus hat die Analyse gezeigt, dass die BG-PWA gute Ergebnisse für die Reaktion p+p$\rightarrow$p$K^+\Lambda$ liefert.

# Abstract

For low energies hadrons can be described in the framework of the Quantum Chromo Dynamics by effective models, like the $\chi$PT. One special challenge is the description of hadrons containing strange quarks. One example is the behaviour of kaons in the presence of nuclear matter and the predicted formation of bound states of anti kaons and one or more nucleons. In the last decade these kaonic bound state drew more and more attention triggered by experimental results on the $\Lambda(1405)$ and kaonic bound states, like the pp$K^-$. These states are strongly connected, since the $\Lambda(1405)$ is described nowadays usually as a molecular state with a certain contribution of a $K^-$-p bound state.
The presence work is focused on the experimental search of the pp$K^-$ in the exclusive reaction p+p$\rightarrow$p$K^+\Lambda$. The experiment was performed at the FOPI spectrometer at GSI in Darmstadt with a proton beam ($E_{\mathrm{beam}}$=3.1 GeV) and a liquid hydrogen target. This spectrometer was upgraded by a set of beam detectors and a dedicated trigger and tracking detector (Si$\Lambda$ViO) to enhance the event of interest. Exploiting reconstructed $\Lambda$ particle a value for enhancement of those particles in the recorded data of $14.1 \pm 7.9(stat)^{+4.3}_{-0.5}$ could be determined.
For the analysis of the exclusive reaction p+p$\rightarrow$p$K^+\Lambda$ different selection steps were performed. For the suppression of background reactions a kinematical refit frameworks was used. The determination of the remaining background could be performed using a so called sideband analysis technique. By these methods a final sample of 903 exclusive reaction events could be extracted with a remaining background of $\approx$61 events.
The observed reactions were compared with phase space and transport model simulations. Both have shown significant discrepancies between experimental and simulation data.
A sufficient description was obtained using the Bonn Gatchina Partial Wave Analysis framework which is able to fit a coherent sum of a set of transition waves to the experimental data. The results of a systematical analysis also fit to outcome of other experimental results.
For the determination of the upper limit the wave of the pp$K^-$ was included in the framework and a systematical scan for different properties of the pp$K^-$ was performed. For a confidence level of 95% upper limits of the production cross section between 4.1$\mu$b and 16.9$\mu$b were obtained assuming for the pp$K^-$ a width between 20 MeV/c$^2$ and 80 MeV/c$^2$ and a mass between 2.205 GeV/c$^2$ and 2.305 GeV/c$^2$. The resulting value - especially for low partial width - could provide constraint to further theoretical calculation. Furthermore, this analysis has shown the nice performance of the BG-PWA for the analysis of the reaction p+p$\rightarrow$p$K^+\Lambda$ .

# Contents

# List of Figures

# List of Tables

# Chapter I

# Introduction

## 1.1 Strong Interaction

### 1.1.1 The QCD Phase Diagram

The strong interaction between quarks and gluons is described by the theoretical framework of the Quantum Chromo Dynamics (QCD). The quarks as well as the gluons are carrying a color charge, which is used to define a local SU(3) symmetry. Since the gluons also carry charge, phenomena like gluon-gluon coupling appear, which leads to effects like asymptotic freedom and confinement.
Asymptotic freedom appears at high energies, which corresponds to small interaction distances. In this regime the coupling constant for the strong interaction $\alpha_s$ becomes low, which allows a pertubative calculation of the interaction. The asymptotic freedom was confirmed experimentally by measurements of multi jet production in high energy $e^+ - e^-$ annihilation experiments [Bet07].
In the low energy region the coupling constant gets bigger and the effect of confinement dominates. Due to this effect the interaction strength becomes so large that quarks and gluons can not be observed as free particles and produce colorless objects, called hadrons. These can be separated into mesons, consisting of a quark/anti-quark pair, and baryons, which are composed of three quarks. Due to the large coupling constant, pertubative calculations can not be applied anymore in this energy regime. The different phases of the nuclear matter can be illustrated by the phase diagram of the nuclear matter (Figure 1.1). At low energies and low baryonic density the quarks form hadrons. Due to the asymptotic freedom of the QCD, at higher energies and densities, the coupling constant reduces, which leads to a transition to a deconfined phase - the Quark Gluon Plasma (QGP) - with freely moving quarks and gluons. The transition to this QGP phase is predicted to happen at low baryonic densities in a smooth cross-over - which has been confirmed by Lattice QCD calculations [Dan01, FH11]. With increasing energies a critical point is predicted with a second order phase transition followed by an transition region (yellow band) in which first order phase transition appears. The production of this phase with a focus on the phase transition is currently explored at RHIC [JM12, d'E09, A$^+$05a, Esk95]. At LHC the properties of this QGP are explored, for example by the modification of the production of quarkonia states like $J/\Psi$ [Sco13].

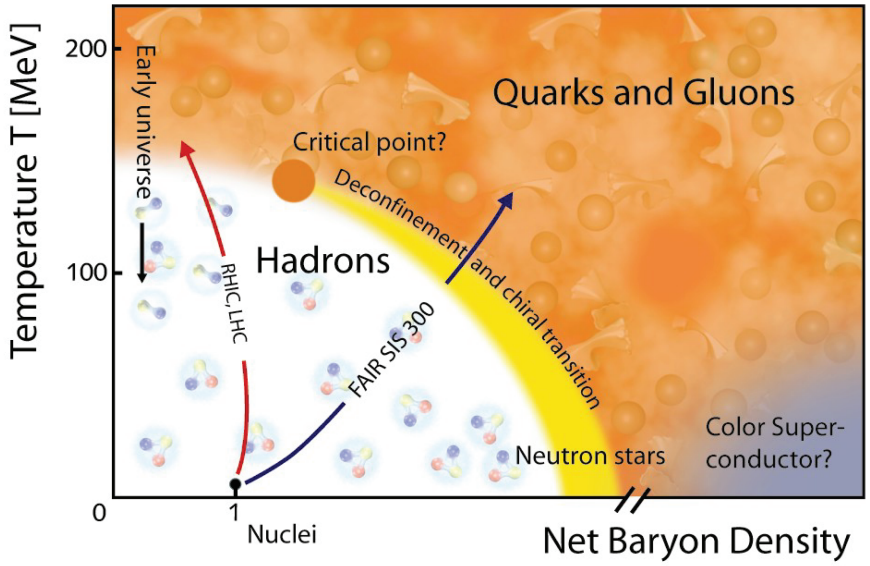


Figure 1.1: Phase Diagram of nuclear matter [Nor98]. At low energies and low baryonic densities the quarks form hadrons.The yellow band indicates the temperatures and densities at which a first order phase transition from the hadronic phase to the quark gluon plasma takes place. At the critical point the first order phase transition turns into a second order phase transition, while at low densities and higher energies a crossover between the two phase is predicted. The arrows indicate the regimes, which will be accessible by experiments at the LHC, RHIC (red) and future experiment at FAIR (black).

### 1.1.2 Equation of State

The behaviour of the hadronic matter depending on the temperature and the density is described by the equation of state (EoS). The equation of state is used to describe the energy density of hadronic matter as a function of density and temperature. While the properties of this matter are known for normal nuclear density ($\rho_0 = 0.16$ fm$^{-3}$), the behaviour especially at higher densities is not settled. One experimental approach to investigate the behaviour at higher densities are heavy ion reactions. The KaoS collaboration, for example, has measured $K^+$ yields in sub-threshold heavy-ion reactions ($C + C$ and $Au + Au$ at $0.8 - 1.5$ GeV per nucleon). Via comparison of their data to transport model predictions, they could conclude that the EoS of isopsin symmetric nuclear matter (approximately equal number of protons and neutrons) is rather soft in the tested density region [STC$^+$12] [Sie13].
Also further experiments like FOPI and HADES are investigating heavy ion reactions at densities of 1-3$\rho_0$ [A$^+$05c, A$^+$03, A$^+$11]. A promising observable is the measurement of the elliptic and direct flow of protons and pions [DLL02].
The determination of the EoS for hadronic matter is very important for the understanding of objects like neutron stars. Indeed, inside of such objects, high densities of nuclear matter can appear and depending on the EoS of hadronic matter different hypotheses about the components of the inner core of neutron star can be validated. In Figure 1.2 a diagram of neutron star mass versus the radius of the neutron star is shown. In this picture, the predicted mass-radius relation from different theoretical models, based on different EoS, are

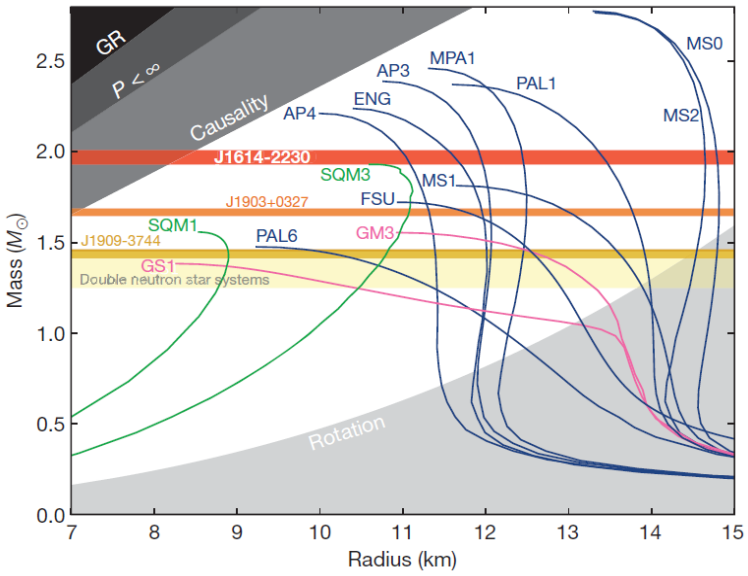


Figure 1.2: Neutron star mass versus the radius. The different lines represent different theoretical predictions [DPR+10], like nucleonic matter (blue lines), nucleonic plus exotic matter (pink lines) or strange quark matter (green lines) [LP01]. The horizontal bands are constraints from measurements of neutron stars [DPR+10, JHB+05, CRL+08].

presented. The lines represent calculation of pure nucleonic matter (blue), nucleonic plus strange matter (pink lines) or strange quark matter (green lines) [LP01]. The horizontal lines show the results of some of the measured neutron star masses [DPR+10, JHB+05, CRL+08]. These measurements provide some very strict constraints to theoretical predictions for the equation of state.
While these results seem to favour a stiff equation of state with pure nucleonic matter, it was shown by theoretical calculations, that from certain energy densities the production of strange hadrons, like $\Lambda$ and $K^-$, might be energetically favorable. Although those effects could lead to a softening of the equation of state, they are not completely ruled out by the constraint of neutron star mass measurements [SB08, WCSB12, RBW05].
This discrepancy between theoretical models, neutron star measurements and results form heavy ion reactions is still an open question. Especially the production of strange matter, like kaonic bound states, is a heavily discussed topic.

### 1.1.3 Chiral Symmetry and Hadron Masses

In the previous paragraph the behaviour of the hadronic matter under higher energy densities was discussed. At high nuclear densities the properties of hadrons, like their masses, might change due to chiral symmetry restoration.
To discuss this effect, first the origin of the hadron masses has to be explained.
One part of the hadron mass originates from the Higgs mechanism, which allows for example to explain the masses of the gauge bosons $W^+$, $W^-$ and $Z^0$ and also the masses of the free quarks [Daw94]. Only by summing up the free quark masses ($m_u \approx 2$ MeV/c$^2$, $m_d \approx 4$ MeV/c$^2$) the total mass of the hadrons can not be explained ($m_p \approx 930$ MeV/c$^2$). This observed mass

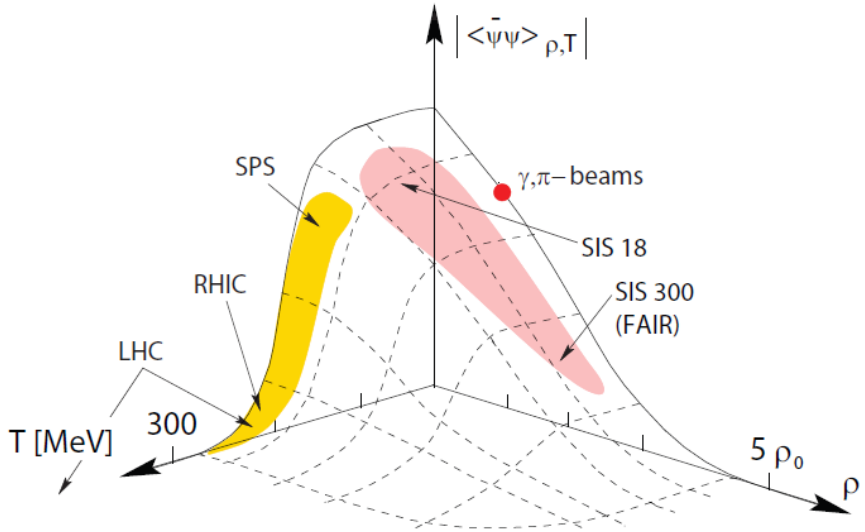


Figure 1.3: Chiral condensate as a function of the baryon density $\rho$ and the temperature T. [Dah08]. The red indicated the position of nuclear matter of density $\rho_0$. The red shaded area mark the region which is accessible by experiments at SIS18 and SIS300 at moderate temperatures and higher densities. The yellow area at low densities and high temperature is accessible by SPS, RHIC and LHC experiments.

difference is generated by the spontaneous breaking of the QCD chiral symmetry in vacuum. The QCD Lagrangian is characterized by a number of symmetries. The local $SU(3)_{color}$ symmetry and a global $U(1)$ symmetry being responsible for the baryon number conservation are exactly fulfilled [RW00] [Sie13]. Due to the finite quark masses the symmetry of the QCD Lagrangian is explicitly broken. In the chiral limit, with vanishing masses for the three light quarks, the symmetry of the QCD can be translated into a $SU(3)_L \times SU(3)_R$ symmetry, which is responsible for the conservation of the chirality[1]. By this Lagrangian a set of eight degenerated massless ground states - called Goldstone bosons[2] - is created.
Based on this chiral symmetry each particle should have a chiral partner, with the opposite parity and the same mass. Experimental results have shown that the isopsin multiplets with different parity are not degenerated (see also [S$^+$05]). For example, the chiral partner of the $\rho$ meson, the $a_1$ meson, is almost two times heavier.
This effect can be explained by a spontaneous breaking of the chiral symmetry. This spontaneous breaking of chiral symmetry results in different masses of chiral partners with opposite parity. The order parameter quantifying the spontaneous chiral symmetry breaking is the

[1] chirality: (greek: handedness)

[2] Goldstone Bosons: ($\pi^-$ ,$\pi^+$ ,$\pi^0$,$K^+$ ,$K^-$ ,$K^0$,$\eta$,$\eta'$). The non-zero masses of the Goldstone boson can be explained by the explicit symmetry breaking, which originates in the mass of the quark. The masses of the bosons are given by the Gell-Mann-Oakes-Renner relation [Koc95]. For example in case of the pion ($m_\pi \approx$140 MeV/c$^2$):

$$m_\pi^2 f_\pi^2 = -\frac{m_u + m_d}{2} \langle 0 | u\bar{u} + d\bar{d} | 0 \rangle$$

with the bare quark mass $m_u$,$m_d$ and the pion decay constant $f_\pi$

expectation value of the quark condensate $\langle q\bar{q}\rangle$. In Figure 1.3 the quark condensate $\langle q\bar{q}\rangle$ is plotted as a function of the baryon density $\rho$ and the temperature T. In the vacuum ($\rho$=0, T=0) it has a non-zero value. With increasing density and temperature the quark condensate decreases, which leads to a restoration of the chiral symmetry. As a consequence, this effect leads to a modification of the particle mass spectrum, embedded in the nuclear environment [BR91].

## 1.2 Kaons in the Nuclear Medium

This work is focused on the study of kaon properties. Since kaons are Goldstone bosons, their mass of $\approx 500$ MeV/c$^2$ originates from the explicit symmetry breaking of the QCD. In vacuum two types of kaons exist. These are on the one hand kaons with a strangeness content of $S = -1$ and on the other hand antikaons with a strangeness content of $S = +1$. Each specie appears in two different charged states with different isospins. In the case of the kaon these states are the $K^+$ and the $K^0$ and for the antikaon the $K^-$ and the $\bar{K}^0$.
In vacuum these particles are degenerated, since all of them are Goldstone bosons.
If these particles are located inside of the nuclear medium, this degeneration vanishes, which leads to a different behaviour of kaons and antikaons.
As already mentioned, the behaviour of hadrons cannot be described by perturbation theory because of the large coupling constant $\alpha_S$. For that reason kaons are described within chiral perturbation theory ($\chi$pT). In this theory the QCD Lagrangian is modified to an effective, non linear, chiral Lagrangian, with the the baryon octet and the pseudo scalar meson octet as effective degrees of freedom [HOL$^+$12,KN86,NK87].
By solving this effective Lagrangian [KL96, LJMR94, KSW95] one obtains the in-medium energy of the kaon:

$$E(\vec{k},\rho_N) = \left(m_K^2 + \vec{k}^2 - \frac{\Sigma_{KN}}{f_K^2}\rho_S\right)^{\frac{1}{2}} \pm \frac{3}{8}\frac{\rho_N}{f_K^2}, \tag{1.1}$$

with the three-momentum of the kaon $\vec{\mathrm{k}}$, the nuclear density $\rho_N = \langle\bar{N}\gamma^0 N\rangle$ and the scalar density $\rho_S = \langle\bar{N}N\rangle$. $f_K$ is the decay constant of the kaon. The third term in this equation corresponds to the attractive scalar interaction due to the explicit chiral symmetry breaking [HOL$^+$12]. This term depends on the kaon-nucleon sigma term $\Sigma_{KN}$ [3]. The last term originates from the repulsive vector interaction, while the upper/lower sign refers to the $K/\bar{K}$, respectively. This term - also called Weinberg-Tomozawa term - is responsible for the different behaviour of kaons and antikaons inside of the nuclear medium. While it is repulsive for kaons, which results in an increasing effective energy with increasing density, this term is attractive for antikaons, which results in a decreasing effective energy. In Figure 1.4 the effective energy of $K^+$ and $K^-$ is plotted versus the nuclear density. The yellow bands indicate the range predicted by theory.

Based on this calculation, especially the modification of the antikaon energy should have enormous consequence for the equation of state. Motivated by the predicted dropping of the antikaon mass within dense nuclear matter, it was predicted by [KN86,NK87] that kaon condensation should appear already at a density of $3\rho_0$. For higher densities the production of

[3] $\Sigma_{KN} = \frac{1}{2}(m_q + m_s\left[\frac{1}{2}\frac{\partial m_N}{\partial m_q} + \frac{\partial m_N}{\partial m_s}\right]$. The Sigma term depends on the strangeness content of the nucleon. For a strangeness content of 0.1-0.2 this value is 350 MeV $< \Sigma_{KN} <$ 405 MeV. Lattice calculations give a value of $\Sigma_{KN} \approx 450$ MeV [FKOU95, DL95].

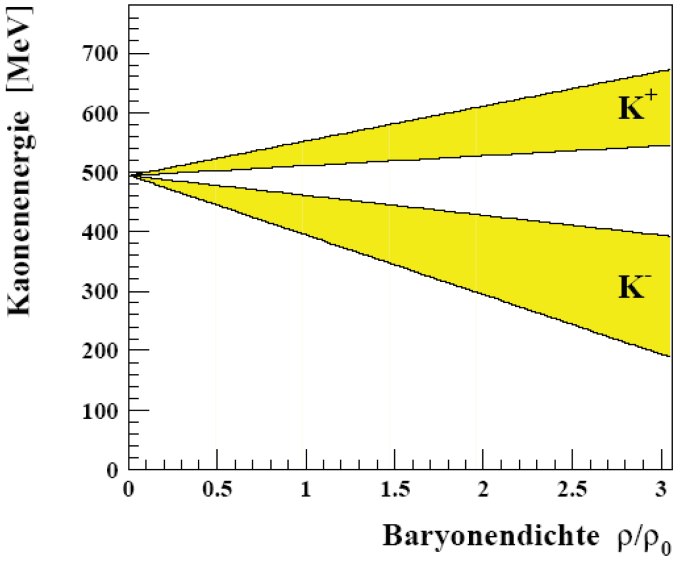


Figure 1.4: Effective energy of $K^+$ and $K^-$ with increasing nuclear density. The yellow bands refer to different theoretical predictions [Stu01].

kaons via the process $e^- \rightarrow K^- + \nu_e$ and $n \rightarrow p + K^-$ would become energetically favourable if the antikaon mass gets as small as the electron free energy and these processes should be able to reduce the Fermi pressure inside of neutron stars. Since this process would also soften the equation of state. it would contradict to some extend recent neutron star measurements, as it was stated in in Paragraph 1.1.2.
This considerations show, that the in-medium behaviour of the (anti)kaons is still of fundamental importance for itself but also to address the description of astronomic dense object.
Experimentally, the situation for the $K^+$ is rather settled. It has been confirmed that kaons feel a repulsive mean field potential of $20 - 40$ MeV at a normal nuclear density [B$^+$97, A$^+$10], which is in agreement with the predictions from Equation 1.1 [Sie13].
For antikaons the situation is not so clear,unless there is some experimental evidence that suggests an in-medium modification for antikaons too, e.g. from the KaoS and FOPI collaboration [Her96, L$^+$99, S$^+$06], but the situation is far from being clear. The reasons for the more difficult description of the $K^-$ are manifold. On the one hand the $K^-$ can be produced via different channels. While the production of the $K^+$ is dominated by the channel p+p$\rightarrow$p$K^+\Lambda$ , the $K^-$ is not produced via one dominant channel. Especially in heavy ion reactions at a collision energy below the NN production threshold the production via several inelastic exchange channels is possible [RBW05, Lut04, Fuc06]. Furthermore, the production via the decay of the $\Phi$ meson was found to be a non negligible contribution [A$^+$09].
On the other hand the production of baryonic resonances influences the interaction between $K^-$ and nucleons. Especially the existence of the resonances $\Lambda(1405)$ and $\Sigma(1385)$ has a strong influence on the $K^-$ , which are located close below the $\bar{K}N$ thresholds. This resonances allow the coupling between $\bar{K}$-N and $\Sigma/\Lambda$ -$\pi$ .

$$\Sigma + \pi \leftrightarrow \Lambda(1405) \leftrightarrow \bar{K} + N,$$
$$\Lambda + \pi \leftrightarrow \Sigma(1385) \leftrightarrow \bar{K} + N.$$

Due to the existence of these resonances the description of the $K^-$ cannot be achieved within the $\chi$PT. By the inclusion of self-consistent coupled channel calculations, the spectral function of the $K^-$ was determined by different groups [RBW05, Lut04, HOL$^+$12, RO00]. In

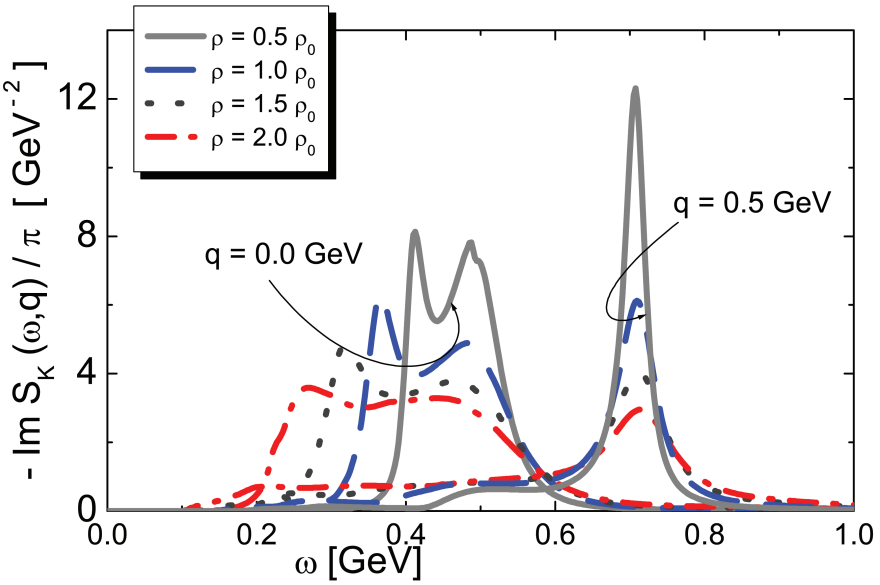


Figure 1.5: Antikaon spectral function obtained from a self-consistent coupled channel calculation [Lut04].

Figure 1.5 the antikaon spectral function calculated in [Lut04] is shown. In this spectrum the functions for different nuclear densities ($\rho = 0, 0.5, 1, 2\rho_0$) and different kaon momenta (q=0 GeV/c,q=0.5 GeV/c) are plotted. At low densities the kaon at rest show a interesting two peak structure, which washes out for higher densities. While the higher mass peak is explained by dressed kaons, which are propagating freely through the nuclear medium, the lower mass peak is associated to the formation of a $\Lambda(1405)$ from the $K^-$ and a nucleon.
If the $K^-$ moves inside of the nuclear medium (q=0.5 GeV/c) it can be seen again like a quasi particle, but still containing a large low mass tail.

## 1.3 The Role of the $\Lambda(1405)$ Resonance

As it was stated, resonances play an important role in the description of the $K^-$ inside of the nuclear medium.
Especially the $\Lambda(1405)$ is connected to the antikaon-nucleon interaction being at least partially considered as $K^-$-p bound system. This particle with a mass of 1405.1 MeV/c$^2$ and a width of 50 MeV/c$^2$ [B$^+$12] is located between the $\bar{K}$-N and the $\Sigma$-$\pi$ threshold[4]. Due to this close by thresholds the theoretical description of this state via chiral pertubative calculation fails [OM01].
Theoretically this state is described by non-pertubative coupled channels techniques [BNW05,

[4] $E_{thr,\Sigma\pi}$=1.33 GeV/c$^2$ $E_{thr,\bar{K}N}$=1.43 GeV/c$^2$

KSW95,OR98,HW08]. In this framework the scattering of a meson-baryon system is described by the self consistent Bethe-Salpeter-Equation:

$$T_{ij}(\sqrt{s}) = V_{ij}(\sqrt{s}) + V_{il}(\sqrt{s})G_l(\sqrt{s})T_{lj}(\sqrt{s}). \tag{1.2}$$

This equation describes the scattering matrix $T_{ij}$, which is connected to the differential cross section via Fermi's golden rule. In the first term the scattering from channel i to channel j is described, by the scattering potential $V_{ij}$. In the second term the loop integrals are described via the diagonal matrix $G_l$.

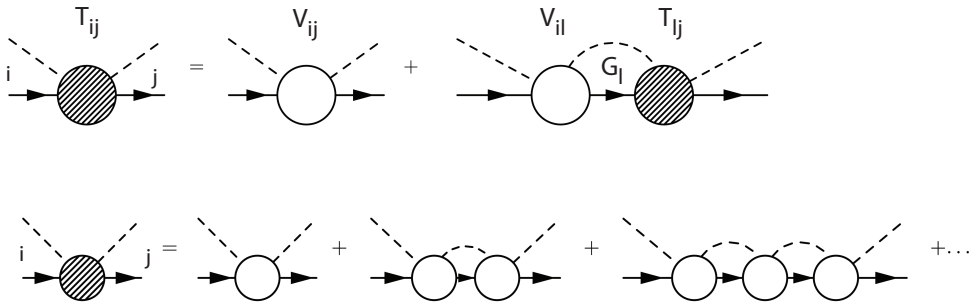


Figure 1.6: Schematic illustration of the Bethe-Salpeter Equation (Equation 1.2)(upper picture). The total scattering $T_{ij}$ from channel i to channel j consists of direct scattering $V_{ij}$ plus a scattering to an intermediate state l. The scattering from l to j is described again by $T_{lj}$, which leads to an infinite sum of loops (lower picture) [HW08].

The Bethe-Salpeter equation can be described schematically by the Feynman diagrams shown in Figure 1.6. In this illustration the scattering from an initial state i to a final the j via an infinite sum of intermediate states l is calculated. In the Isospin channel I=0 it turns out, that the dominant contribution is the coupling between the $\bar{K}$-N and $\Sigma$-$\pi$ channels. These two states appear as two poles in the complex energy plane - shown in Figure 1.7. The real part in this frame correspond to the energy of a pole, while the imaginary part is correlated to the width. In this picture the pole around $Re(z)$ ≈1420 MeV is associated with a narrow $\bar{K}$-N bound state, while the second pole $z_1$ is seen as a broad resonance of $\pi$ $\Sigma$. The different positions of the poles indicated by the red and blue crosses correspond to the single channel ($\pi$ $\Sigma$/$\bar{K}$N only), double channel (2) and full channel (4) calculation. From these spectrum the influence of channel coupling to the pole positions is visualized.
Due to this the $\Lambda(1405)$ is on the hand strongly correlated to the $\bar{K}N$ interaction but on the other hand it is difficult to drawn direct conclusions on the strength of the $\bar{K}$-N interaction due to the coupling of the two channels. Furthermore, the $\Lambda(1405)$ is only decaying into $\Sigma\pi$ pairs. Thus, the strength of the $\bar{K}N$ interaction can not be deduced directly from the $\Lambda(1405)$ spectral function.
Furthermore, different experimental results indicates that the line shape of the $\Lambda(1405)$ appears differently in $\pi$ ,$\gamma$ and kaon induced reactions [MS10, TEFK73, BGH$^+$77, EFK$^+$65]. Recent results on the $\Lambda(1405)$ published by the HADES collaboration [ABB$^+$13] have shown that the $\Lambda(1405)$ spectral function reconstructed by $\Sigma\pi$ invariant mass exhibits a maximum at 1385 MeV/c$^2$, hence shifted with respect to the nominal peak position.

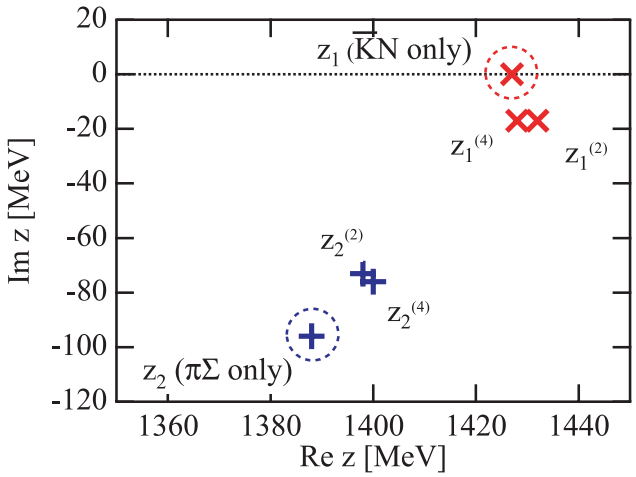


Figure 1.7: Position of the poles of the two channels of the $\Lambda(1405)$. The pole $z_1$ is seen as a broad resonance of $\pi$ $\Sigma$, while $z_2$ is associated with a narrow $\bar{K}$-N bound state. The different positions for each pole indicate different calculations, which are single channel ($\pi$ $\Sigma/\bar{K}$N only), two channel (N$\bar{K}$ and $\pi$ $\Sigma$) (2) and full channel (all states in I=0 and I=1) (4) calculations [HW08].

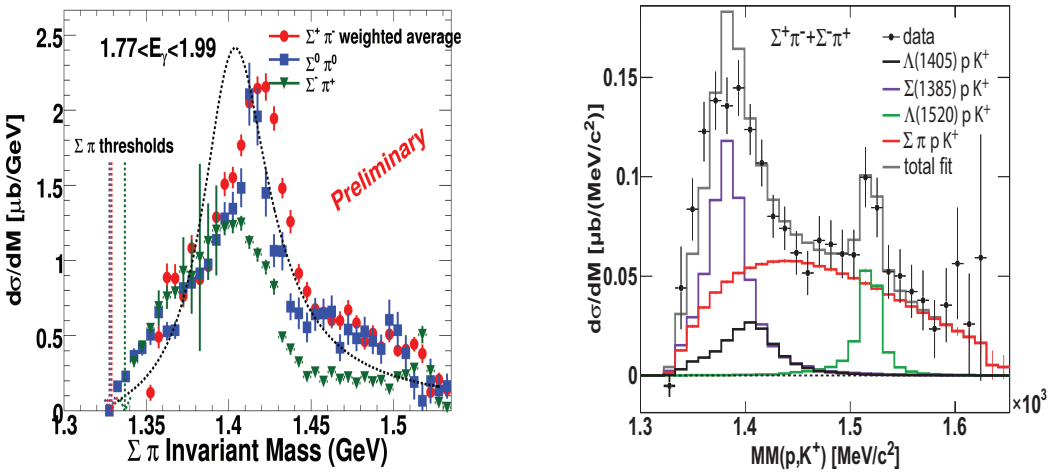


(a) (b)

Figure 1.8: Spectral functions of the $\Lambda(1405)$ measured in $\gamma$ induced reactions (left) [MS10] and p induced reactions (right) [ABB$^+$13]. In the left panel the spectral function for the three decay channels are shown separately. In the right panel the sum of the two charged decay channels is shown.

In Figure 1.8 the results obtained by the CLAS collaboration (a) and the HADES collaboration (b) are shown. The CLAS results show the $\Lambda(1405)$ spectrum in the three possible decay channels ($\Sigma^+\pi^-$,$\Sigma^0\pi^0$,$\Sigma^-\pi^+$) by different colored dots. The HADES results show the sum of the two possible charged decay channels. In these spectra a clear difference of the peak position form the $\gamma$ induced reactions (CLAS) and the p induced reactions (HADES) is visible. These results could be seen as an indication that in different reactions different coupling to

the two $\Lambda(1405)$ poles appears and therefore the position of the $\Lambda(1405)$ depends itself on the initial reaction. Another interpretation of this shifted peak position of the $\Lambda(1405)$ takes into account the inference of the two poles of the $\Lambda(1405)$ with the background channels [SF13]. Furthermore, a difference in the three different decay channels in the CLAS data is visible, which originates in the different Isospin compositions of the decay channels [NOTR99].
These results show, that an extraction of the $\bar{K}$-N interaction from the spectral function of the $\Lambda(1405)$ requires a well understood description of the coupling of the channels.

## 1.4 Kaonic bound states

During the last decade another possibility for the determination of the $\bar{K}$-N potential was focused in the works of Akaishi and Yamazaki. Already in the last century the existence of kaonic clusters was predicted by some works [Nog63, Wyc86]. Triggered by the successful observation of a bound state of $\pi^-$ mesons inside of $^{207}$Pb [YHI$^+$96, IOH$^+$00, GGK$^+$00] and $^{205}$Pb [GGG$^+$02], which were extended also to searches for bound states of $\omega$ and $\eta$ in light nuclei, Akaishi and Yamazaki considered also the existence of nuclear bound states of $\bar{K}$ mesons, with binding energies in the order of $\approx$ 100 MeV and with a small width of $20 - 40$ MeV [AY02].
The lightest of the predicted bound states is the so called pp$K^-$ state. Based on the assumption that the $\Lambda(1405)$ consists partially of $\bar{K}$-N bound state, also a state with an additional proton was predicted to be bound. In this picture the $\Lambda(1405)$ is predicted to serve as a doorway for the production of the pp$K^-$ . A binding energy of B=48 MeV and a width of

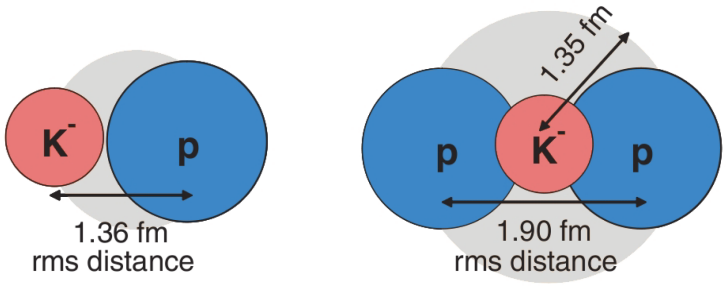


Figure 1.9: Structure and dimensions of the $\Lambda(1405)$ (left) and of the $ppK^-$ state (right), predicted in [AY02].

$\Gamma$=61 MeV was evaluated for this state within the first phenomenological calculation [AY02]. A schematic representation of the structure of the $K^-$ -p and pp$K^-$ states is shown in Figure 1.9. In this picture also the calculated r.m.s. (root mean square) radii of the $K^-$ is shown, as well as the mean distance between the two protons. This radius was predicted to reduce significantly to 1.90 fm in comparison to the p-n system in the deuteron (d=3.90 fm). Due to this small radius the kaon the estimated density reached by the kaonic bound systems is very high (up to $\approx$ 5 $\rho_0$) and if this hypothesis would hold, this would have strong consequences of the EoS at high densities [AY02].
The results of Akaishi and Yamazaki, normally referred as AY-Ansatz, were criticised by other groups. In [SGMR07] the authors claimed, that the pp$K^-$ has to be treated as $\bar{K}$NN state,

| Calculation | Reference | $B_{ppK^-}$ (MeV) | $\Gamma$ (MeV) |
|---|---|---|---|
| Three-body Faddeev | [SGM07, SGMR07] | ≈50-70 | ≈100 |
| AMD | [DW07] | <53 | |
| Optical Potential | [Wyc86] | 100 | 20 |
| Phenomenological Potential | [YA02] | 48 | 61 |
| Three-body Calculation | [BGL12] | 16 | 40 |
| Variational Calculation | [DHW08] | 19±3 | 40-70 |
| Variational Calculation | [DHW09] | 20±3 | 40-70 |
| Coupled-channel Faddeev | [IS07] | 44-67 | 43-50 |
| Variational Calculation | [WG09] | 40-80 | ≈ 75 |

Table 1.1: List of different theoretical predictions for the binding energy and the width $\Gamma$ of the pp$K^-$ .

with a total isospin of I=1 in the N-N system[5]. In their calculation the authors of [SGMR07] obtained a coupling of the $\bar{K}$NN state with the $\pi\Sigma$N system - similar like in the calculations of the $\Lambda(1405)$. Nevertheless, they obtained a binding energy for the $\bar{K}$NN of $B_{ppK^-} \approx 50 - 70$ MeV and a width of $\Gamma \approx 100$ MeV.
Another criticism to the AY-Ansatz resides in the fact that their approach is a purely phenomenological approach, which interprets the $\Lambda(1405)$ as an almost pure $K^-p$ bound state with a negligible contribution of the $\pi\Sigma$ resonance [HW08]. In the AY-Ansatz the binding energy of the $\bar{K}$-N is determined to be 27 MeV, while in the chiral SU(3)-Ansatz in [HW08] this value is calculated to be 12 MeV.
In [DW07] a calculation based on this chiral SU(3) $\bar{K}$-N interaction and a realistic N-N interaction was performed using the Antisymmetrized Molecular Dynamics (AMD) method. In this calculation a maximal binding energy of the pp$K^-$ system of $B_{ppK^-}$ =53 MeV was obtained.
In Table 1.1 further results of theoretical predictions are listed additionally to already mentioned calculations. This list shows that the situation is not clear at all, being the expected width and binding energy is distributed within a rather broad range. Nevertheless the existence of the pp$K^-$ state is predicted within all these methods.
Like the theoretical predictions, the results obtained from different experiments through the last decades also do not show a clear picture.
Experimentally the pp$K^-$ can be accessed via its decay into proton-$\Lambda$. Since the main decay channel of the $\Lambda$ goes into p and $\pi^-$ , no measurement of neutral particles is required [IKMW05].
In 2005 the Finuda collaboration published results obtained from $K^-$ absorption data, measured at the DA$\Phi$NE $e^+e^-$ collider. At this collider $\Phi$ particles are produced, which decay into $K^+$ -$K^-$ pairs. The produced $K^-$ interact with different targets like $^6$Li, $^7$Li and $^{12}C$ and are absorbed. In the final state the $\Lambda$ and p particles were selected, which are emitted with a relative angle of ≈180°. In Figure 1.10 the invariant mass spectrum of p and $\Lambda$ after background subtraction is plotted. In the small inlet picture the acceptance corrected spectrum is shown.

[5]This state of $\bar{K}$NN state is not a pure pp$K^-$. It could also be a state of pn$\bar{K}^0$, which has the same quantum numbers. However, this state is also often called pp$K^-$ in literature

From this spectrum they extracted a binding energy of $B = 115^{+6}_{-5}(stat)^{+3}_{-4}(syst)$ and a width of $\Gamma = 67^{+14}_{-11}(stat)^{+2}_{-3}(syst)$ [A$^+$05b].

While this structure was interpreted in [A$^+$05b] to give a clear evidence for the pp$K^-$,

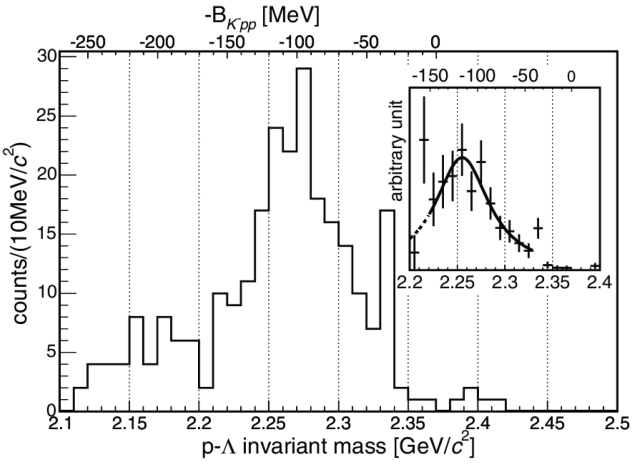


Figure 1.10: Invariant mass (p,Λ) spectrum measured by the FINUDA collaboration in $K^-$ induced reaction [A$^+$05b].

a different interpretation was given by [MORT06]. In their calculation they explained the observed structure as originating from the reaction $K^-$ p N $\rightarrow$ $\Lambda$ N followed by a further interaction of the $\Lambda$ and N in the nucleus. The authors of this article also pointed out, that the presence of the absorbing nucleus may complicate the interpretation. For this reason, the authors of [MORT06] claimed the need for the investigation of p+p $\rightarrow$p $K^+$ $\Lambda$ reactions.
Experimental results from proton proton reactions were published by the DISTO collaboration. In this experiment proton proton reactions at a beam energy of $E_{beam}$ = 2.85 GeV with the final state p $K^+$ $\Lambda$ was measured. In this exclusive measurement the experimental results were compared to phase-space simulations of the underlying reaction pp$\rightarrow$p$K^+\Lambda$ . This comparison shows a significant discrepancy in the invariant mass and missing mass distributions between simulations and experimental data. This discrepancy appears in events containing a proton, which is emitted under large polar angles. In Figure 1.11 the deviation spectrum of invariant mass spectrum of $\Lambda$ and p is shown for these events. This deviation spectrum show the division of the experimental data by p$K^+\Lambda$ phase space simulations. In this spectrum a clear Gaussian shaped structure can be seen, which was interpreted as the signal of a pp$K^-$ with the binding energy of B=105$\pm$2 MeV and a width $\Gamma$=118$\pm$8 GeV [Y$^+$08]. This peak structure was just visible in the so called large angle proton region. For protons emitted under small polar angles no evident signal is visible.
This different signatures were interpreted as a dominant production of the pp$K^-$ in reactions with a large momentum transfer [Y$^+$08].
This dominant production of the kaonic bound states was already postulated in [YA07]. In this work the formation of a pp$K^-$ in p+p reactions was investigated theoretically and compared to the production via a transfer reaction, e.g. $K^-$ absorption reactions. In this calculation the $\Lambda$(1405) - stated as $\Lambda$* - played a major role in the production of the pp$K^-$.
In contrast to transfer reactions, in formation reactions the proton and the $\Lambda$* are created in

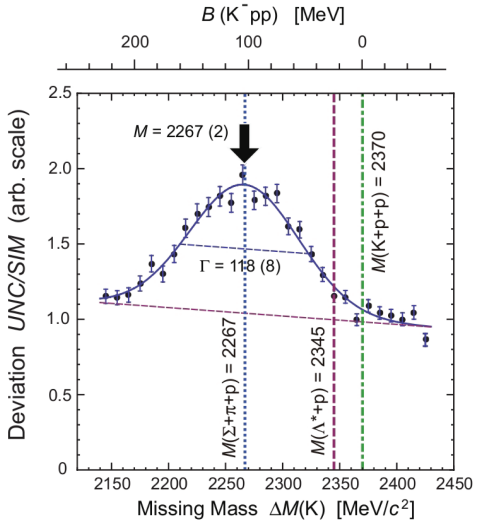


Figure 1.11: Invariant mass (p,$\Lambda$) measured by the DISTO collaboration in the reaction p+p $\rightarrow$p $K^+$ $\Lambda$. The spectrum is presented for events containing a proton, which is emitted under large polar angles [Y$^+$08].

reactions with large momentum transfer. Due to this the phase space of the $\Lambda$* and the proton overlaps, which would increase the probability for them to build the pp$K^-$ . In Figure 1.12 the results for the calculation from [YA07] are shown. On the left side the Feynman diagram of the production is shown. In the right spectrum the differential cross section as a function of the mass is plotted. From the calculation a clear dominance of the production of the bound state compared to the quasi free production is predicted. This distribution depends on the radius of the pp$K^-$ (indicated by different coloured curves). A denser system is correlated with a higher production probability.
The interpretation of the DISTO data has been criticized on the hand by theoretical groups, due to the lack of a theoretical prediction, which could reproduce a binding energy of B=105 MeV. In an early calculation of [Wyc86] such binding energies are not ruled out, but it was also predicted, that for such binding energies the width should be significantly lower, due to the energetically closed decay channel pp$K^-$ $\rightarrow\pi\Sigma$p.
On the other hand also the experimental analysis method is questionable. For the description of the background in the analysis a pure phase space distribution was used. In this model no final state interaction between the particles was implemented and also no intermediate resonances were considered in the production process. Since it was already shown by the COSY-TOF collaboration [AB$^+$10, AES$^+$10] that both could have major impact on the final state distribution, the question arises, if the shape of the assumed background is correct.
Recent results obtained by the LEPS experiment, show a quite different result on the pp$K^-$. In this experiment the $\gamma$ induced reaction $\gamma$+d $\rightarrow K^+ + \pi^- +$ X was investigated at an energy range $E_{gamma}$ =1.5-2.4 GeV. In this experiment, the LEPS collaboration did not investigate the pp$K^-$ via its decay into $\Lambda$ and p, but they looked to the missing mass spectrum of the $K^+$ and $\pi^-$.

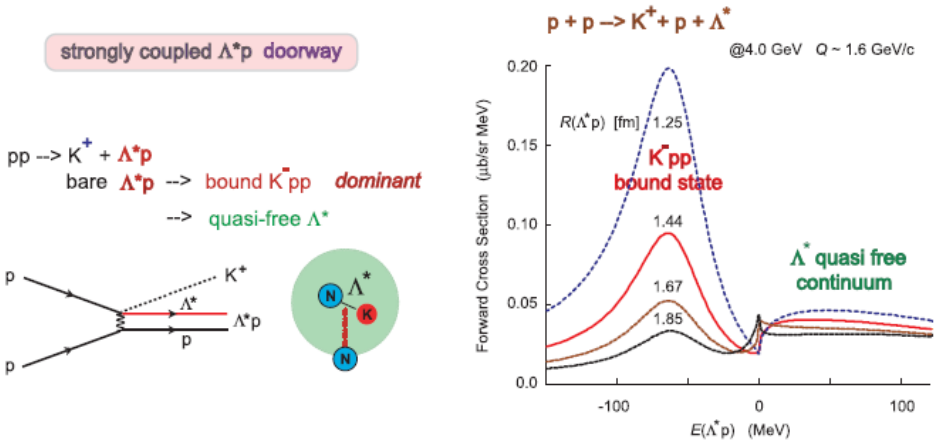


Figure 1.12: Production of the pp$K^-$ in formation reactions. The $\Lambda^*$ serves as doorway to the production of the pp$K^-$ (left). Due to the high momentum transfer, the production of the pp$K^-$ bound state is dominant against the quasi free production of $\Lambda^*$ p, especially for small radii of the pp$K^-$ [YA07].

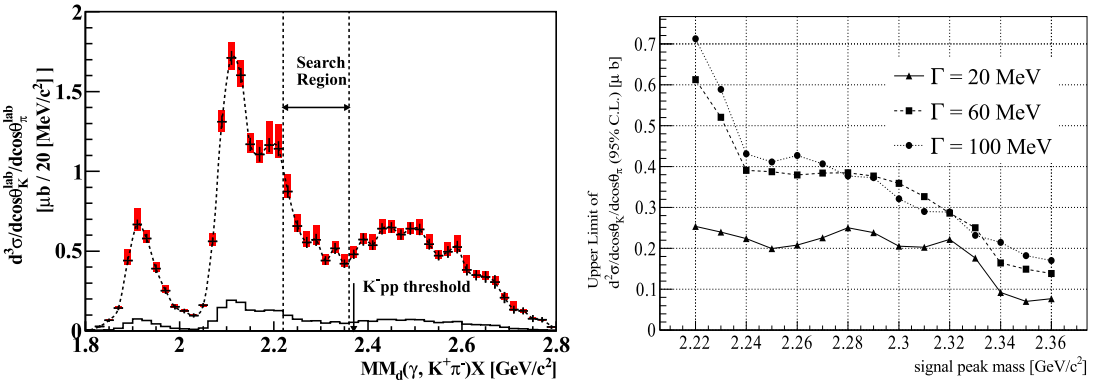


Figure 1.13: The missing mass ($K^-$ ,$\pi^-$ ) spectrum measured at the LEPS experiment. The region in which the pp$K^-$ signal is expected is marked (left). The right panel shows the upper limit at a CL of 95% for different values of the pp$K^-$ width [T+14].

In Figure 1.13 (left) the resulting missing mass spectrum is shown. In the expected region no peak structure is visible. The dotted line correspond to the background from the reaction $\gamma n \rightarrow \Lambda\ K^-\ \pi^-$ , $\gamma p \rightarrow \Sigma^+ K^+\ \pi^-$, $\gamma n \rightarrow \Lambda\ K^+\ \pi^-\ \pi^0$ and $\gamma p \rightarrow \Sigma(1385)^+ K^+\ \pi^-$. Since no signal is visible, an upper limit was determined for possible binding energies from 10 MeV to 150 MeV and widths of 20 MeV, 60 MeV and 100 MeV, respectively. The pp$K^-$ signal was added to the background cocktail via a Breit-Wigner distribution. The upper limit of the production cross section within the detector acceptance at a confidence level of 95% versus the peak mass of the assumed pp$K^-$ is shown in Figure 1.13 (right panel). The upper limits

for the width Γ=20, 60, 100 MeVare (0.07-0.2),(0.1-0.6) and (0.2-0.7) μb,respectively.
Most recently the HADES experiment analysed the exclusive reaction p+p→p $K^+$ Λ. In their analysis also no direct indication for the existence of the pp$K^-$ could be found, but the experimental data could be reproduced with known sources, like the direct p$K^+\Lambda$ production and the production via intermediate $N^*$ resonances. In contrast to the LEPS experiment they used a Partial Wave Analysis framework for the analysis. In this analysis a coherent sum of all sources is build, which takes also interference effects into account. In this experiment also an upper limit for the production of the pp$K^-$ of $\approx 4$ $\mu$b has been extracted [Epp14].
From all these result no clear picture about the existence of pp$K^-$ can be drawn.
The pp$K^-$ was predicted by several theoretical calculations, but with different width and binding energies. Also the existences of such a state cannot be completely ruled out from experimental results. For that reason, this work shall contribute to this open question with an exclusive measurement realized at the FOPI spectrometer located at GSI. In this experiment the reaction p+p→p$K^+\Lambda$ is investigated.
In the experiment at the FOPI spectrometer a beam energy of 3.1 GeV was chosen to cover the energy range between DISTO (2.85 GeV) and the HADES results (3.5 GeV).

## 1.5 p$K^+\Lambda$

The study of the pp$K^-$ in proton proton reactions is performed by the analysis of the final state p$K^+\Lambda$. In order to observe a possible signal, the mechanism of the reaction p+p→p$K^+\Lambda$ has to be understood properly.
The production mechanism can be described by the one boson exchange model (OBE). In this model it is assumed, that the initial protons exchange a virtual meson like a K or a $\pi$. In Figure 1.14 the different Feynman diagrams are shown, representing the so-called t-channel exchange [FS67].

In the case of the final state p$K^+\Lambda$ four reactions might contribute to the production

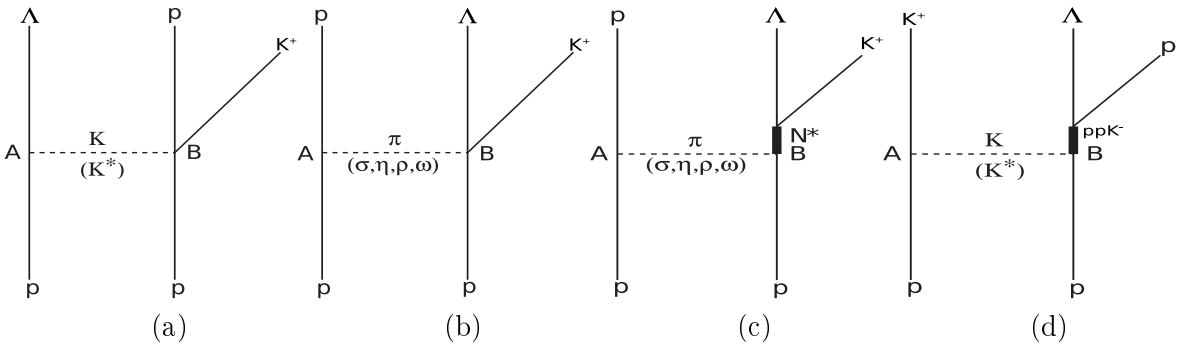


Figure 1.14: Feynman diagrams of the production of p$K^+\Lambda$ according the one boson exchange model [Sie13].

mechanism. In panel (a) and (b) the direct production is shown, which can be realized by the exchange of a strange or a non-strange boson. In diagram (c) and (d) the production of an intermediate resonance is presented. In (c) the production of a $N^*$, which decays into a Λ and a proton. In the OBE the pp$K^-$ can be produced via the exchange of a strange virtual boson (Figure 1.14 (d)). Within this picture the contribution by $N^*$ plays an important role since for the vertex B $\pi$p→$K^+$ Λ the cross section for the production of an intermediate $N^*$

is rather high [AB$^+$10,SPM01].

From experimental results by the COSY-TOF collaboration this significant contribution

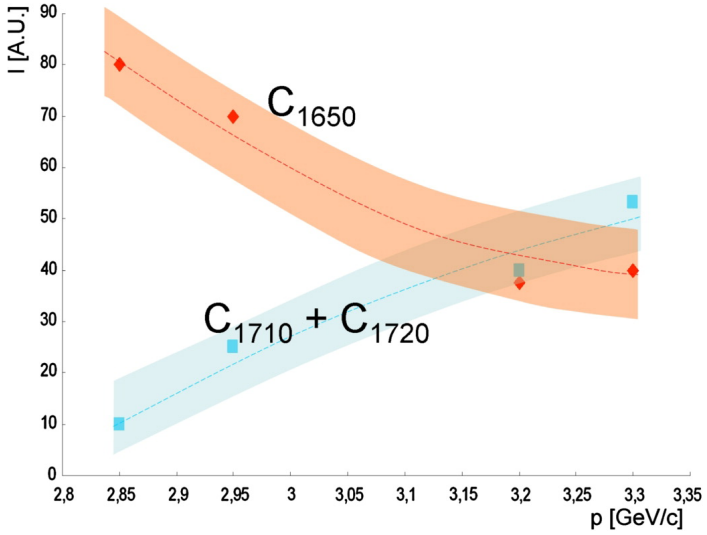


Figure 1.15: Contribution of $N^*(1650)$ and $N^*(1710)/N^*(1720)$ to the production of p$K^+\Lambda$.

of intermediate $N^*$ has been verified. The exclusive reaction p+p→p$K^+\Lambda$ was investigated for different beam energies between 1.5 GeV and 2.8 GeV and the relative contribution of the different resonances could be extracted. By comparing the different resonance strengths at various beam energies, an energy dependence of the single $N^*$ contribution strengths can be deduced. This dependence is shown in Figure 1.15. The red diamonds represent the $N^*$ (1650) strengths, the combined strengths of $N^*(1710)$ and $N^*(1720)$ are shown by the blue squares. The dashed curves indicate the fits to the data points and the colored bands visualize the three error bands of the fits to the contribution strengths [AES$^+$10]. In this plot the decreasing contribution of the $N^*(1650)$ is clearly visible [AES$^+$10]. Extrapolating these results to beam energies of the FOPI experiment one would expected a stronger contribution of $N^*(1710)/N^*(1720)$. Also a contribution of $N^*$ resonances like $N^*(1900)$ would be expected, due to the higher available energy. Also in the HADES experiment a significant contribution of higher mass $N^*$ resonance was found [Epp14].

# Chapter II

# The FOPI-Detector and the SiΛViO Upgrade

The FOPI detector was build at the end of the 1980's at the "Helmholzzentrum für Schwerionenforschung" with the goal to measure the properties of compressed matter in heavy ion reaction. This fixed target spectrometer is very well suited for heavy ion reaction experiments, since the SIS18 accelerator is capable to accelerate proton up to 4 GeVand heavy ion particle up to 2AGeV(see Section 2.1) the design of the spectrometer was realized in a way to cover a solid angle of almost $4\pi$ (as indicated by the name **F**Our **Pi**).

The FOPI detector - shown in Figure 2.1 - can be divided in two different subsystem, which are the forward and the backward system[1]. The two hemispheres are covered by different sub detectors, which will be explained in the following chapter. The backward hemisphere is covered by the Central Drift Chamber CDC (2.4), which is surrounded by two time-of-flight detectors, the Plastic Barrel (2.8) and the resistive Plate chamber (2.9). The forward hemisphere consists of the drift chamber Helitron (2.5) and a scintillator wall (2.6). Additionally to the standard FOPI detector setting a further detector was build, which should improve the tracker and trigger capabilities of the spectrometer (2.10).

The whole system besides the Plastic Wall is surrounded by a super conducting magnet, which creates a solenoid magnetic field of 0.3 T.

The FOPI spectrometer is show in Figure 2.1. In the upstream direction of the FOPI spectrometer two additional beam detectors were located. These detectors - not shown in Figure 2.1 - were build for start time determination and trigger creation (2.3)

## 2.1 The Proton Beam

For the proton-proton experiment a proton beam with an energy of at least 3.0 GeVwith high intensities is needed. The accelerator system at the GSI, consisting of the linear accelerator LINAC and the SIS18, is very well suited for these requirements.

The protons are extracted by an ion source and accelerated up to an energy of 11.4 MeVby the linear accelerator UNILAC [Gro13a]. This particle beam with intensities of $10^7$ protons per bunch is injected to the SIS18 synchrotron, with an injection time of 130µs, where the particle bunches are further accelerated up to an energy of 3.1 GeV. The particle bunches

[1] The forward/backward hemisphere measured mainly particle, which are emitted in the forward/backward direction in the center of mass frame of the fixed target reaction.

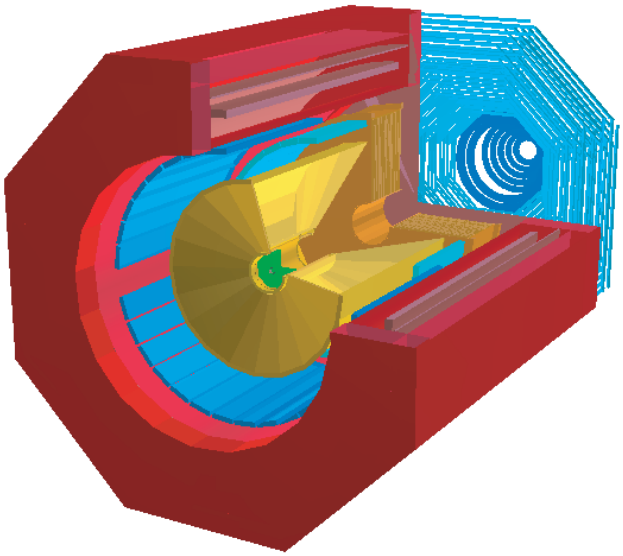

Figure 2.1: Schematic View of the FOPI Spectrometer. The backward hemisphere consisting of the Central Drift Chamber CDC (yellow), which is surrounded by two different time-of-flight detectors, the Plastic Barrel (blue) and the resistive Plate chamber (turquoise).The forward hemisphere consists of the drift chamber Helitron (dark yellow) and a scintillator wall (blue). The whole system is surrounded by a super conducting magnetic (red)

are extracted from the synchrotron to a beam line, which guides the beam to the FOPI spectrometer. Along the beam line a fraction of the particles gets lost. The final beam intensity at the target is around $10^6$ - $10^7$ particle per bunch. The total time ($\approx$10 s) of injection, acceleration and extraction is called spill.

## 2.2 The Proton Target

For this experiment a liquid hydrogen target was used. A cell made of Kapton, located at the end of the beam pipe (see Figure 2.2), was connected by pipes with a reservoir of liquid Hydrogen - liquefied by a cryogenic cooler.
The target cell had a cylindrical shape with a radius of 2 cm and a length of 1.5 cm, stabilized by two small aluminum rings at the front of the cell. Due to the higher pressure inside the cell, the actual length of the target cell was around 2 cm.
The resulting interaction probability of the beam protons with an energy of 3.1 GeV with the target structure was 0.004 % for the Kapton foil and 0.372 % for the liquid hydrogen.

## 2.3 Beam detectors

### 2.3.1 Start Detector

The start detector provides the reference time for the multi wire chamber(see Paragraph 2.4.1) and the start time for the time of flight detectors (Section 2.6). Additionally, the signal is used for the trigger creation (Section 2.11).
This detector - used in the proton beam experiment - was located 2 m upstream of the target. To cope with beam intensities up to $10^7$ protons/s, focused on a beam spot of about 6 mm diameter, the readout was realized on both sides with booster photo multipliers[2], which are working at rates up to several MHz. Since the magnetic field inside FOPI at the position of the start detector is still in the order of 60 mT the photo multipliers were shielded with iron tubes. The intrinsic time resolution of this detector was about 130 ps at a hit rate of 2 $10^6$Hz [BHS+09] [MBF+14].

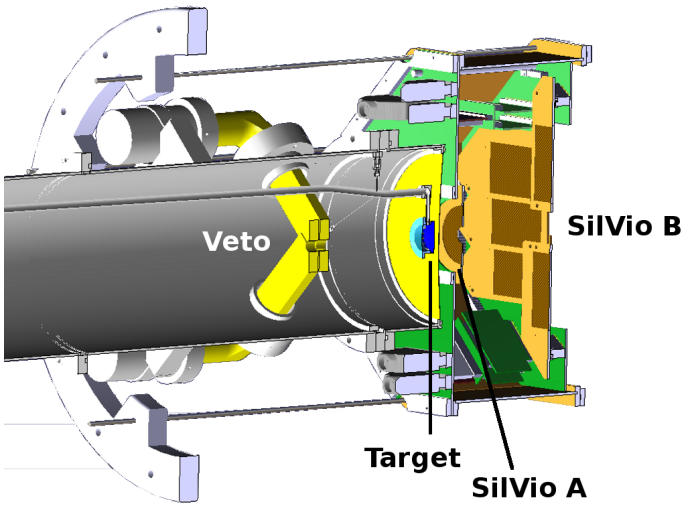


Figure 2.2: Cross section of the beam pipe containing the veto detector and the hydrogen target. After the beam pipe the trigger and tracking detector SiΛViO (2.10) is located. [Ber09]

### 2.3.2 Halo and Veto Detector

In the measurement of particle reactions it is necessary to discard reactions, which took place before the target. To suppress such events two detectors - HALO and VETO detector - were installed before the target. Their signal was used as a trigger veto.
The HALO detector consists of two scintillator paddles positioned 1.5 m in front of the target around the beam pipe.
The Veto detector is positioned 5 cm in front of the target inside the beam pipe. Figure 2.2 show the cross section of the beam pipe containing the veto detector. This detector consists of two 5 mm thick scintillators which were read out on one side only by fine-mesh PMTs

[2]Hamamatsu H6524-01MOD with modified booster lines.

[3]. The two scintillators are rotated by 90° with respect to each other and were split into two segments each, to facilitate the installation. Both detectors have an inner hole of 1 cm diameter to enable the passage of the beam and were positioned around 10 cm before the target edge. The efficiency of this detector was evaluated to be above 98% [BHS+09] [MBF+14].

## 2.4 The Central Drift chamber (CDC)

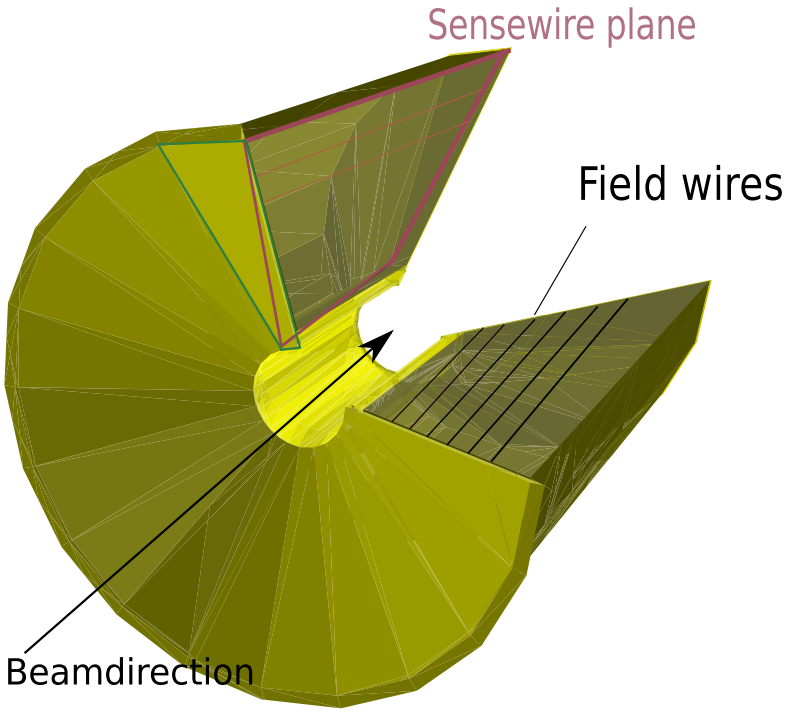


Figure 2.3: Schematic View of the Central Drift Chamber. The field wires - indicated by the black lines - are spanned in parallel to the beam direction in the middle of the sectors (green lines). The sense wires (red) are spanned in parallel to the beam axis but are tilted against the field wires.

The particle tracking in the backward region of FOPI is done by the the Central Drift Chamber (CDC). It is a conical shaped Multi Wire Drift Chamber divided into 16 sectors. The inner diameter and length are 30 cm and 80 cm, respectively. The outer diameter and length are 174 cm and 1.8 m, respectively. (see Figure 2.4 (left)).
The sectors of the CDC, which divide the chamber in the x-y-plane (see Figure 2.4 (right)), are separated by 252 cathode wires. Each sectors contains 61 field wires (diameter 125 µm) and 60 sense wires (diameter 20 µm). All wires are parallel to the beam axis. The sense wire planes of each sector are tilted by 8° against the sector boarders to avoid left-right ambiguities. The used drift gas is a mixture of 88 % Argon, 10 % Isobutane and 2 % Methane, which leads to a nearly homogeneous, drift-field independent drift velocity of 4 cm/ns.
A voltage of −15 kV is applied to the cathode wires, which generates a drift field of around

[3]Hamamatsu H6152-01B with modified booster lines

800 V/cm. In order to provide an electric field with a 1/r dependence at the position of the sense wires, a voltage of -1275 V is applied to the field wires.
The sense wires of the CDC are read out by Flash ADCs, which are able to provide an energy and a timing signal.

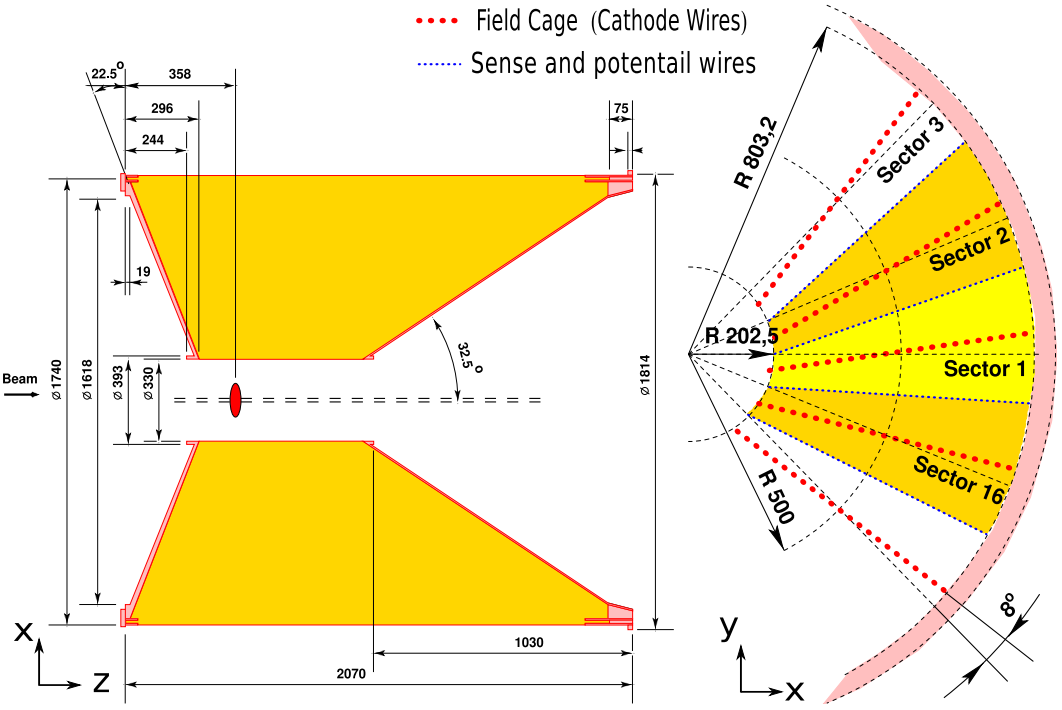


Figure 2.4: Cross section of the Central Drift Chamber in the x-z-planes, together with the position of the target (red dot) positioned on the beam axis (left schema). The right schema shows the cross section in the x-y-plane together with the field, sense and potential wires [Ben07].

### 2.4.1 Track Reconstruction in the Central Drift Chambers

The first step of the track identification in the CDC is the reconstruction of hit points. Particles, which are traversing the drift gas, are loosing energy and are producing electrons by gas ionization. These electrons are drifting along the electric field to the sense wires. Close to the sense wire the increasing electric field causes an avalanche effect of the primary electrons increasing the total charge arriving at the sense wires.
The distance from the primary ionization position depends on the drift time $t_{Drift}$, the drift velocity $v_D$ (see Equation 2.1) and the Lorentz angle $\alpha_L$. Since the drift volume of the Central Drift Chamber is positioned completely inside the homogeneous solenoid magnetic field, the drifting electrons are also effected by the Lorentz force. Due to this, the drift path does not follow the electric field lines, but is tilted by the Lorentz angle $\alpha_L$, according to Equation 2.2:

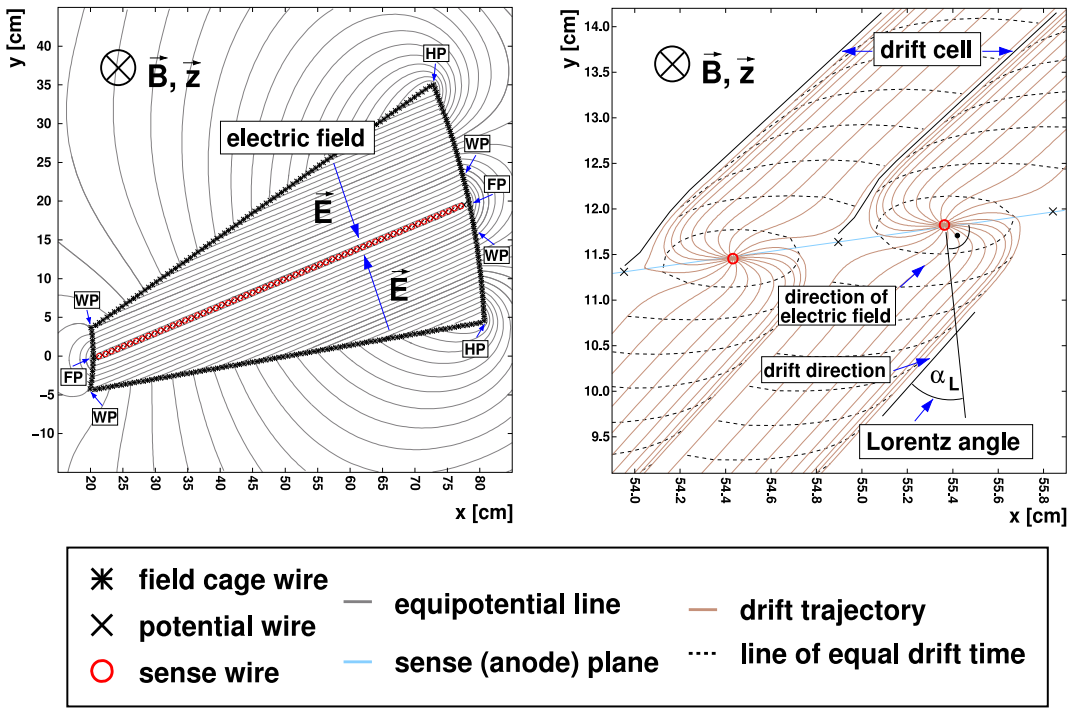


Figure 2.5: Illustration of the field configuration along the field wires of the CDC [Mer04].

$$v_D = \left(\frac{eE\tau}{2m_e}\right)\left(\sqrt{1+\frac{eB\tau}{m_e}}\right)^{-1}, \tag{2.1}$$

$$\alpha_L = \arctan\left(\frac{eB\tau}{m_e}\right), \tag{2.2}$$

where:

$m_e$ : Electron mass
$e$ : Electron charge
$\tau$ : Mean time between two collisions
$B$ : Magnetic field strength
$E$ : Electric field strength

The hit position in the x,y-plane can be determined by Equation 2.3:

$$\begin{pmatrix} x_{hit} \\ y_{hit} \end{pmatrix} = \begin{pmatrix} x_{wire} \\ y_{wire} \end{pmatrix} \pm \begin{pmatrix} \cos(\alpha_L) \\ \sin(\alpha_L) \end{pmatrix} \cdot v_D(t - t_{wire} - t_0), \tag{2.3}$$

where $(x_{Wire}, y_{Wire})$ is the position of the sense wire in the x-y plane at which the charge was collected, t is the drift time of the electrons to the sense wire, $t_{Wire}$ is the wire dependent

time offset[4] and $t_0$ is the absolute time offset, which is provided by the start detector (see Paragraph 2.3.1).
To determine the calibration parameter $(t_0, \alpha_L, v_D)$ a self-consistent procedure is applied using high momentum tracks, which are crossing a sector border of the CDC. Figure 2.6 shows a reconstructed hit in the CDC with a wrong (a) and a correct (b) drift velocity calibration. With the wrong calibration one can see a mismatch between the two track segments in the separate sector. [Ben07]
Additionally to the hit position in the x-y-plane the z component of the hit point is measured.

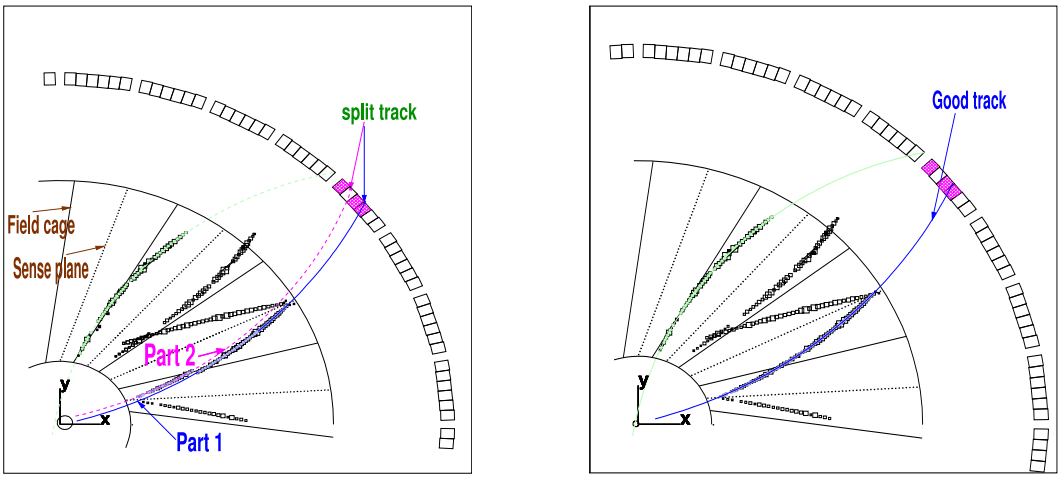


(a) (b)

Figure 2.6: (a) Event with wrong Lorentz angle. The lower track is broken in two parts in the sector border. (b) The same event with the proper Lorentz angle.

The z position is obtained by a charge division method [Pin95, FHR73]. The ratio of the charges collected on the left (upstream) and right (downstream) end of a wire is proportional to the ratio of the relative distances where the avalanche occurred and is given by the formula:

$$\frac{Q_L}{Q_R} = \frac{z}{L - z}, \tag{2.4}$$

where $Q_L$ and $Q_R$ are the collected charges on the left-hand and right-hand side. z is the position along the sense wire with the length L. The total charge is related to the numbers $A_L$ and $A_R$, measured by the Flash ADC modules, multiplied by the gain factors $g_L$ and $g_R$ as follows:

$$A_{L/R} = g_{L/R} Q_{L/R}. \tag{2.5}$$

The z position of the hit is determined by the following formula:

$$z_{\text{hit}} = z_0 + \frac{l_{eff}}{2} \frac{Q_R - Q_L}{Q_R + Q_L}, \tag{2.6}$$

with the geometrical position in the z-direction of the wire $z_0$ and the effective length of the sense wire $l_{\text{eff}}$. The effective length of the sense wire is defined by the resistance of the

[4] The wire dependent offset is correction for the different readout time of wires with a different length

preamplifier $R_0$ and the sense wire resistance $R_W$:

$$l_{\text{eff}} = l_0 \left(1 + \frac{2R_0}{R_W}\right). \tag{2.7}$$

### 2.4.2 Momentum Measurement with the CDC

The Central Drift Chamber is located inside of a solenoid magnetic field. The trajectories of charge particles traveling through the chambers are helices.
To determine the momentum, the curvature of the particle trajectory has to be measured. This is done by reconstructing the position of the hits in the x-y-plane belonging to a track. The transverse and the absolute momentum is calculated with the following equations:

$$p_t\,[\text{GeV/c}] = 0,3 \cdot |Z[e]| \cdot B[T] \cdot R[m], \tag{2.8}$$

$$p\,[\text{GeV/c}] = \frac{p_t}{\sin\Theta}, \tag{2.9}$$

where

$B$ : Magnetic field in Tesla
$Z$ : Charge of particle in units of e
$R$ : Radius of the Particle Track
$\Theta$ : Polar angle of the Particle

Additional to the hit point of the particle, the energy loss of the particle is measured. Since the energy loss of a particle is independent from its mass, it can be used together with the measured momentum to identify different particles. Figure 2.4.3 shows the energy loss of a particle versus its momentum. The blue lines show the nominal lines corresponding to the Bethe-Bloch, calculated for given particles.

$$\frac{dE}{dx} = -\frac{4\pi n z^2}{m_e c^2 \beta^2} \cdot \left(\frac{e^2}{4\pi\epsilon_0}\right)^2 \cdot \left[\ln\left(\frac{2m_e c^2 \beta^2}{I \cdot (1-\beta^2)}\right) - \beta^2\right]. \tag{2.10}$$

$z$ : Charge of Particle
$n$ : Electron density of the Medium
$m_e$ : Mass of Electron
$I$ : Excitation Energy of the the Material

### 2.4.3 Energy-Loss Calibration

The total energy loss of the particle traversing the active volume of the CDC is proportional of the collected charge in each drift cell. The total energy loss for a hit is given by

$$\Delta E = f\left(A_R + \frac{g_R}{g_L} A_L\right), \tag{2.11}$$

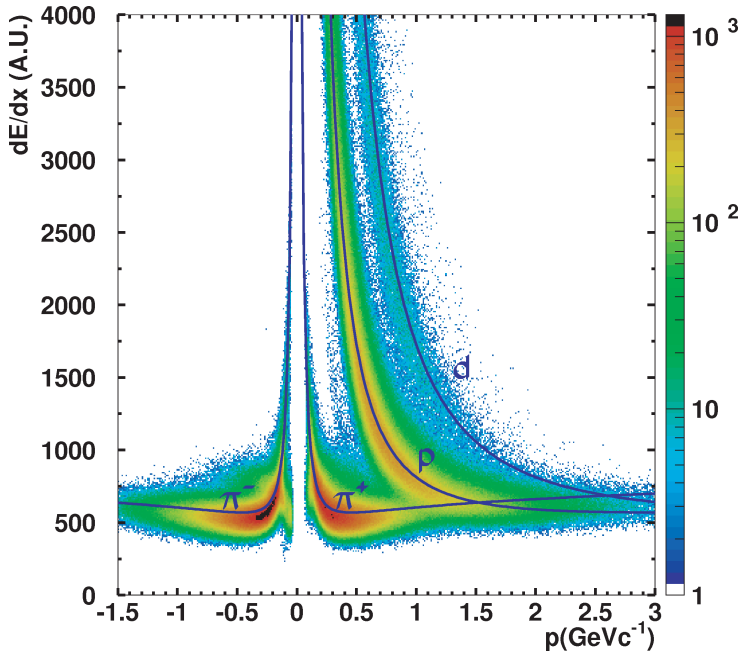


Figure 2.7: Energy loss versus momentum measured in the CDC. The blue lines correspond to the nominal energy loss calculated by the Bethe-Bloch formula.

where $f$ is a factor which takes into account the gas gain and the amplification factors of the preamplifiers at both ends of each wire.
The energy loss per unit path length for each track is calculated by

$$\frac{dE}{dx} = f\left(A_R + \frac{g_R}{g_L}A_L\right)\frac{\sin(\Theta)}{\Delta r_{xy}}, \tag{2.12}$$

where $\Delta r_{xy}$ is the length of the track in the (x,y)-plane and $\Theta$ is the polar angle of the track.

## 2.5 The forward drift chamber (Helitron)

The Helitron is the drift chamber, which covers the forward hemisphere of the FOPI spectrometer. It consists of 24 sectors covering the polar angles from 4.5° up to 27° [Mue08] in the full $2\pi$ azimuthal angle. Each sector of the Helitron has 53 sense wires (diameter 50 µm) and 53 potential wires (diameter 125 µm), that are positioned orthogonal to the beam axis.
The gas mixtures consists of Ar, Isobutane and Methane in the ratio 88:2:10. The drift potential is at $-12.3$ kV. The resulting electric field is around 750 V/cm [Har03].

### 2.5.1 Track Measurement with the Helitron

#### Hit point measurement

Particles which are passing the Helitron are creating electrons, which are drifting to the sense wires. In the electric field the electrons are producing avalanches and the charges are collected by the sense wires. Due to the presence of the magnetic field the trajectories of the electrons

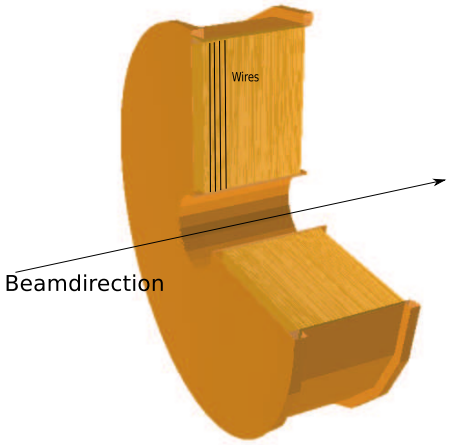


Figure 2.8: Schematic view of Helitron. The wires of the Helitron are spanned in orthogonal direction to the beam axis (indicated by the black lines).

are tilted against the electric field lines by the Lorentz angle $\alpha_L$. Figure 2.9 shows a schematic view of a sector. The hit position in the sector coordinate system is determined y Equation 2.13.

$$x = x_{DZ}, \qquad y = y_{DZ} + y_{LT}, \qquad z = z_{Wire} \tag{2.13}$$

$x_{DZ}$ and $y_{DZ}$ are obtained by the drift time measurement of the electrons.

$$x_{DZ} = t v_{Drift} \cos(\alpha_L), \tag{2.14}$$
$$x_{DZ} = t v_{Drift} \sin(\alpha_L), \tag{2.15}$$

where $y_{LT}$ is determined by the charge division along the sense wire (Equation 2.16).

$$y_{LT} = \left( \frac{1 - \frac{q_i}{q_o}}{1 + \frac{q_i}{q_o}} \right) l_{eff}. \tag{2.16}$$

The effective length can be calculated by the impedance of the preamplifier $R_V$, the length of the wire $l$ and the wire resistance $R$.

$$l_{\text{eff}} = \frac{l}{2} \left( 1 + \frac{2R_V}{R} \right) \tag{2.17}$$

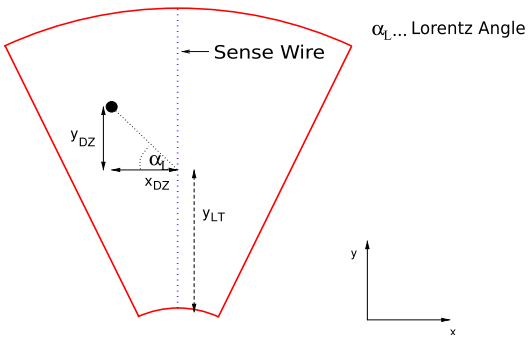


Figure 2.9: Schematic View of a Helitron sector. The hit point is measured by the drift time component $x_{DZ}, y_{DZ}$ and the charge sharing component $y_{LT}$ [Ple99].

The z-position of the hit is obtained by the z-position of the corresponding sense wire. For the pattern recognition in the Helitron a global Hough-transformation algorithm is used. The

angular difference of a hit in the middle of the Helitron to the remaining hits is plotted in a histogram. Hits, which belong to the same track, are represented by cluster points.

#### Track Identification

After the corresponding hits have been selected, the position with respect to the sense wire plane has to be determined. From the measurement of the drift time only the distance to the sense wire can be determined. This effect leads to mirror tracks as it is illustrated in Figure 2.10.
To identify the correct track one uses the *staggering*. The sense wires are displaced by 200 µm from the center of the sector alternating left and right. The value for the displacement is calculated for each event. At first, a polynomial function is fitted through the drift time coordinates of one track. From the difference of the fitted to the measured drift time one obtains the displacement of the wire. The sign of that difference is related to the side of the wire plane [Ple99].

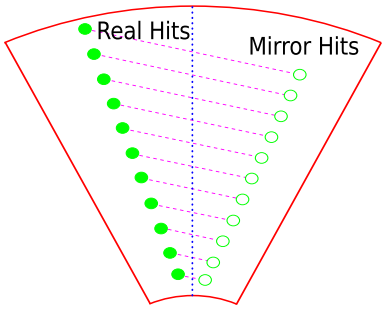


Figure 2.10: Creation of mirror hits in a Helitron sector [Ple99]. Due to the magnetic field the mirror axis of each point is tilted be the Lorentz angle $\alpha_L$.

### 2.5.2 Momentum Measurement

Particles, which are traveling through the Helitron are moving - constrained by the Lorentz force - on circular trajectories in the x-y plane. The transverse momentum over the charge is given by the formula:

$$\frac{p_T}{q} = rB_z, \tag{2.18}$$

with the longitudinal magnetic field $B_z$ and the radius r. With a dedicated algorithm using normalized cubic B-spline one can calculated from the z-dependence of the x and y coordinates and their first and second derivative the $\frac{p}{q}$ ratio for a given particle track. The procedure is described in Appendix B.

## 2.6 The Plastic Wall

The Plastic Wall is a time of flight wall, which covers polar angles from 4.5° till 28° with a full $2\pi$ azimuthal acceptance. It consists of 512 scintillator strips, which are arranged in 48 radial sectors [Goe95]. These are 1.8 cm thick and 2.4 cm wide. The length ranges from 45 cm to 165 cm. The strips are read out from both sides by photo multipliers. Hence every plastic scintillator provides a time signals $t_{L,R}$ and two amplitudes, which correspond to the energy loss $E_{L,R}$.
From those quantities the time-of-flight can be determined with Equation 2.19.

$$t_{tof} = \frac{1}{2}\left(t_l + t_r\right)) + t_{const.}, \tag{2.19}$$

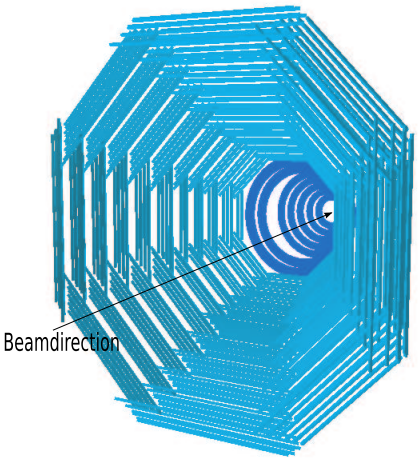


Figure 2.11: Schematic view of Plastic Wall (light blue) with Zero Degree counter (dark blue).

where $t_{const}$ is the reference time, which is provided by the start detector (see Paragraph 2.3.1). The position of the hit along the bar is calculated on the one hand by the time information Equation 2.20 using the speed of light in the scintillator material $c_{\mathrm{pad}}$, the energy information Equation 2.21 and the wave length $\lambda$:

$$x_t = \frac{c_{pad}}{2}\left(t_L - t_R\right), \tag{2.20}$$

$$x_e = \frac{\lambda}{2}\ln\left(\frac{E_L}{E_R}\right)c_{pad}. \tag{2.21}$$

The time of flight resolution of the start detector-PLAWA System was about 400 ps [Lei11]. The position resolution is about 1.2 cm to 2.0 cm [Rit95].

## 2.7 The Zero Degree Detector

At low polar angles the Plastic Wall is completed by the Zero Degree Detector. It consists of 252 pie like plastic scintillators, which are arranged in seven concentric circles (Figure 2.11). The polar acceptance ranges from 0.1° to 4.5°. The scintillator modules are read out at one side. In the proton experiment the signal of the zero degree detectors is used only for trigger purposes (see Section 2.11).

## 2.8 The Scintillator Barrel

At polar angles from 50° up to 117° the Central Drift Chamber (see Section 2.4) is surrounded by the plastic barrel with an azimuthal coverage of around 85%.
The barrel consists of 180 plastic scintillator strips, each with a rectangular cross section of 4x3 $\mathrm{cm}^2$ and a length of 150 cm. The light produced in a strip is collected by PMTs on each side [Ben07]. Combined with the signal from the start detector (see Paragraph 2.3.1) the

barrel delivers the flight time of the particle. Additionally the plastic scintillators, whose z component is defined by the time difference between the two photo multipliers, record the hit position [Ryu09]. The position resolution is about 7 cm [Ben07].
In the proton-proton experiment the time resolution of the Plastic Barrel was around 400 ps [Her12].

## 2.9 The Resistive Plate Chamber (RPC) Barrel

The polar region of the Central Drift Chamber, which is not covered by the plastic barrel - from 27° to 50° - is covered by the Restive Plate Chamber Barrel. This consists of 32 so called super modules, each equipped with 5 Multi-strip Multi-gap Resistive Plate Chambers (MMRPC). The detectors are positioned with an overlap such to maximize the coverage [KCD+11].

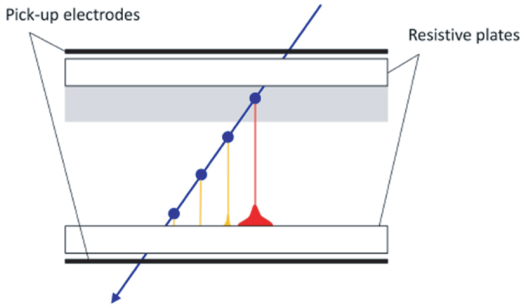


Figure 2.12: Schematic view of a single gap RPC. Only the ionization which occurs in the gray area produces enough avalanche charge to produce a readable signal (red)

The RPC detectors consist of a gas volume enclosed within two layers of high-ohmic material (e.g. glass), coated with copper on the outside (see Figure 2.12 (a)). Due to the high bias voltage - applied to the chamber - produced electrons travel through the chamber to the anode, where an avalanche formation takes place. Only primary ionisation, which happens next to the cathode, is creating an avalanche, which is high enough to generate a detectable signal on the anode. Due to this small region of ionization and the very high drift velocity, the RPCs are able to generate timing signals with very good resolution.

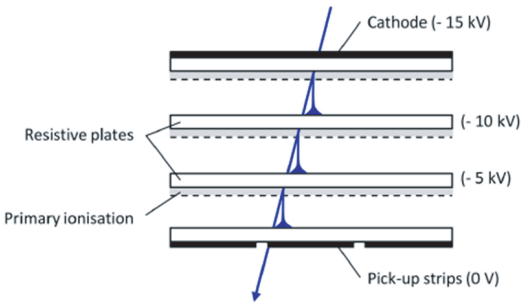


Figure 2.13: Schematic view of a multi-gap RPC. The size of the primary ionization zone is decreased in each gap.

The resistive plate chambers used in the FOPI spectrometer are advancements of those single gap RPCs (see Figure 2.13). These have a segmented anode (multi strip), which allows an increased azimuthal resolution. The gas volume is divided into three sub volumes (multi-gap), which reduces the volume of the detectable primary ionization, followed by an increased time resolution. The intrinsic time resolution of the MMRPC detectors is around 65 ps [KCD+11]. At the proton-proton experiment this lead to a total time of flight resolution of around 180ps [Her12]. The FOPI MMRPCs are filled with a gas mixture of R134a, $SF_6$ and Isobutane with the ratio 80:15:5. A voltage difference of 9.6 kV - applied to the two electrodes - produces an electric field of around 110 kV/cm. The strips on the MMRPC are read out on both ends, which allow to determine the z position of the particle hit.

## 2.10 The Lambda Trigger and Tracker (SiΛViO)

For the proton-proton experiment an additional detector was build, the Λ-Trigger SiΛViO (**Si**licon for Λ -**V**ertexing and **I**dentification **O**nline). This detector serves for two different purposes. On the one hand in order to generate a trigger signal for events, which contain a Λ particle. On the other hand this detector should provide an additional hit point to improve the tracking capability in the forward hemisphere.

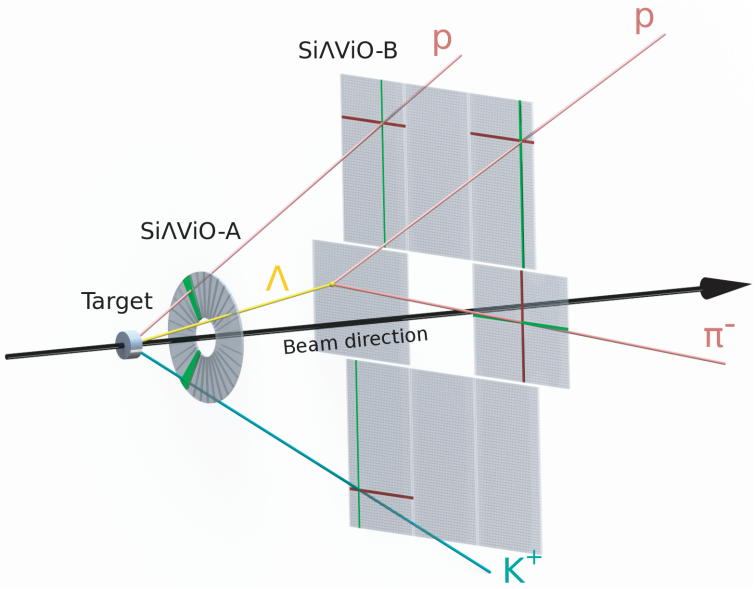


Figure 2.14: Schematic View of the SiΛViO Detector with a typical p$K^+\Lambda$ Event [MBF$^+$14].

### 2.10.1 Detector setup

The detector consists of one single sided segmented silicon detector with an annular shape (SiΛViO A) and a patchwork of eight double sided segmented rectangular silicon detectors (SiΛViO B). Figure 2.14 shows a schematic view of the arrangement of the silicon detectors of SiΛViO.
The two layers are positioned directly after the target (see Figure 2.2). The distance to the target of SiΛViO A is 4 cm and of SiΛViO B is 16 cm [MBF$^+$14, Mue08, Ber09].
The read out of the SiΛViO A and one side of the SiΛViO B layer is realized by fast a readout chain (shaping time ≈150 ns [MBF$^+$14]) of Mesytec preamplifiers[5], which are able to create a trigger-signal depending on the multiplicity of strips measuring a signal above a certain threshold. The second side of the SiΛViO B layer is readout by APV25 chips [Lea05, JFM$^+$99, RCF$^+$00]. These have 128 input channels. Each signal is amplified, shaped (shaping time of 50 ns) and sampled. This sampled signal of all channels is finally multiplexed and stored in a ring buffer. Additionally, the chip has an input, that triggers the chips to send the stored data from one sampling bin to the DAQ[6]-system. Due to the fast trigger processing

[5] The read out by Mesytec was realized by the preamplifier MPR16 and the Shaper STM16+ [KG13]
[6] DAQ = Data Acquisition

in the FOPI DAQ System, the time relation between the shaped event and the corresponding trigger signal is constant within the width of one sampling bin, which is necessary. This time relation has to be measured and are set in the APV25 chip [MBF+14].

### 2.10.2 Raw-Signal and Calibration

The raw signal distributions for the two different readout electronics are shown in Figure 2.15. The amplitude distributions for one channel of the analog Mesytec (a) and of the APV25

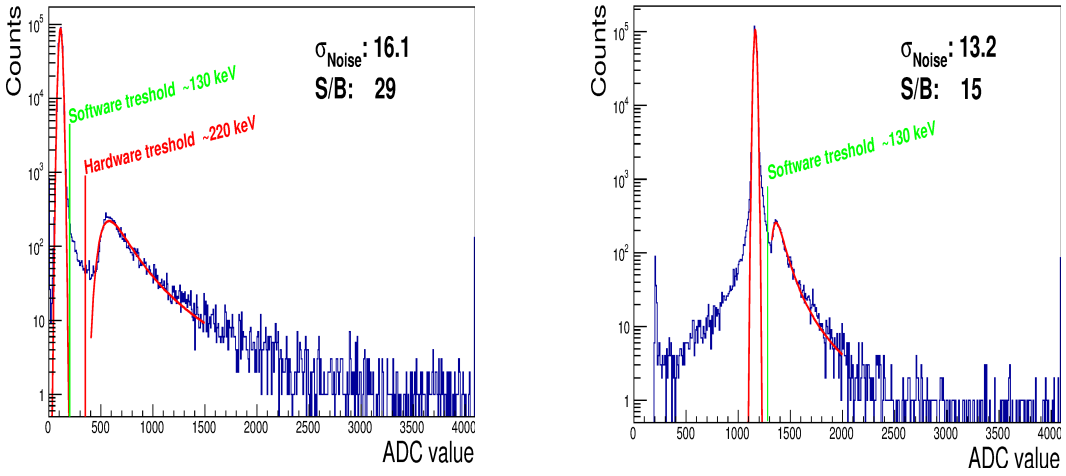


(a) (b)

Figure 2.15: Raw Spectra of one channel for the Mesytec (a) and for the APV25 (b) read-out. The left peak in each spectrum, which are fitted by an Gaussian function, is the noise distribution, the right peak is associated with the MIP signal. The position of the hardware/software threshold is marked with the red/green line (see text).

read-out (b) are plotted in Figure 2.15. One can clearly see the MIP[7] peak (right peak) well separated from the noise peak (left peak) for both cases. A signal to noise ratio (SNR) of 29 and of 15 was obtained for the Mesytec and for the APV25 read-out, respectively. The events below the noise peak in the APV25 spectrum are caused by the drop of the baseline.
The hardware threshold was set for each channel separately directly above the noise level. In the offline analysis a threshold corresponding to 3.5 times the noise width was chosen.
The hardware and the software threshold are shown in Figure 2.15 (green line and red line respectively). The energy values were deduced from the calibration with the known energy loss of one MIP in 1 mm silicon. The energy value of the hardware threshold is deduced from the threshold value in the module, which is correlated to the energy [MBF+14].

### 2.10.3 Clustering and Track Point Creation

From the measured particle signals in the detector, the particle hit points are created. The x and y position are deduced from the measured signal in the two sides of the rectangular shaped detectors of the SiΛViO B layer. The z position is fixed for every detector by the mounting structure. Since the detector can measure two coordinates, this can lead to ambiguities if two

[7] MIP = Minimal ionizing particle: particles with the lowest possible energy loss per length - according to Bethe-Bloch formula.

hits are reconstructed. Those ambiguities can only be solved in the matching procedure with further detectors (see Paragraph 3.1.1).

### 2.10.4 Trigger capability

Charged particles, which are passing a silicon layer, are loosing energy to the material, which leads to the production of electron-hole pairs in the semiconductor material. Due to the doping of the material and an applied bias voltage, these electron-hole pairs are pulled to opposite readout sides of the detector, where they create a signal. The energy loss of neutral particles is quite small compared to the one of charged particle, thus they do not create a readable signal.
Λ particles emitted from the primary vertex are decaying with a high probability ($\approx 70\ \%$)[8] before the SiΛViO B layer after have been flying through the SiΛViO A layer. The decay particles of the main decay channel of Λ [1] are generating each a signal in the second layer. Thus the number of signals in the SiΛViO B is greater than in SiΛViO A.
The read-out of both layers is done by fast electronic, which are able to create a multiplicity dependent trigger signal for each of the two layers.

## 2.11 Trigger Creation in the p-p Experiment

One central element of the data acquisition of every experiment is the trigger, which applies already a pre-selection of the events. In the p-p experiment we are interested in events containing a Λ particle and a kaon candidate in the Resistive Plate Chamber.

### 2.11.1 First Level Trigger (LVL1)

The first Level Trigger requires the following conditions:

**Proton Beam** The Proton Beam Trigger consists of the trigger signal of the start detector (2.3.1) in anti-coincidence with the signal of the halo and veto (2.3.2) detectors.
An additional protection ($\approx 20\mu s$) was used to ensure that two different events are separated in time, to avoid pile up.

**Reaction Trigger** The Reaction Trigger ensures, that a reaction has occurred. A positive trigger signal requires a hit multiplicity greater than one in the plastic wall and at least one hit in the Barrel time of flight detectors, e.g. RPC or Plastic Barrel

**Anti reaction Trigger** To neglect elastics reactions, in which one proton is emitted in a very small polar angles and passing the zero degree detector, a coincidence with a maximum multiplicity trigger is added to the trigger signal: $Mult_{ZDD} < 2$

This trigger was applied to enhance events with a kaon candidate in the Resistive Plate Chamber. First Level Trigger Events were written out with a downscale-factor[9] of 10.

[8] $c\tau_\Lambda = 7.8$ cm [B$^+$12].
[1] The Λ hyperon is partially decaying into a p and a $\pi^-$ (Branching Ratio: 62,8%) [B$^+$12].
[9] Downscale: Only a fraction of events ($\frac{1}{2^{n_{ds}}}$) is written out

### 2.11.2 Silvio Trigger Condition

The SiΛViO trigger requires at least one hit in the SiΛViO A and at least two hits in the SiΛViO B layer. Those events were written out with a downscale of 7. This trigger condition should enhance the amount of events containing a Λ candidate.

### 2.11.3 Second Level Trigger (LVL2)

The second level trigger condition requires a positive LVL1 and SiΛViO trigger. Those trigger events were not downscaled. This trigger condition should enhance events containing a Λ candidate and a $K^+$ candidate in the RPC.

### 2.11.4 Event Reduction and Background Suppression

The previously described trigger settings are meant to increase the Λ content of the recorded events. Obviously they introduce a bias for the accepted events. This effect must be taken into accounted if one wants to extract final cross-sections and can be estimated with the help of simulations by comparing reconstructed data to Monte Carlo tracks. For this purpose the p$K^+\Lambda$ signal was generated with the PLUTO (see Section 4.2) event generator including the angular distribution extracted from [AB$^+$10] for the Λ hyperon. The errors of this angular distribution are treated separately (indicated by (ang)). The background events were generated with the UrQMD transport code (see Section 4.2) without strangeness production [Gro13b, SGH$^+$98].

In Table 2.1 the acceptance for the signal and background events are listed for different trig-

| | LVL1- Acceptance | LVL2 - Acceptance |
|---|---|---|
| Signal (pKΛ) | $0.52 \pm 0.003(stat) \pm 0.16(ang)$ | $0.29 \pm 0.002(stat) \pm 0.09(ang)$ |
| Background | $0.183 \pm 0.003$ | $2.51 \pm 0.02 \cdot 10^{-2}$ |
| pKΛ Bkg. Supp. | $2.86 \pm 0.05(stat) \pm 0.91(ang)$ | $11.93 \pm 0.12(stat) \pm 3.7(ang)$ |

Table 2.1: Acceptance for signal and background events for different trigger conditions. For the signal acceptance an angular distribution taken from [AB$^+$10] was taken into account. The resulting error values for the angular correction (ang) are shown separated from the statistical errors (stat).

ger conditions as well as the resulting background reduction for the LVL1 and LVL2 condition. The error values for the background suppression are dominated by the errors originating from the errors of the angular distribution (ang).

Rather low acceptance for the signal events is mainly caused by the fact that a charged particle hit is required in the region covered by the RPC or Barrel detector. Indeed a good kaon identification is mandatory to select the reaction $p + p \rightarrow p + K^+ + \Lambda$, which is only possible in the RPCs. This explains the numbers shown in Table 2.1.

For the LVL1 the background reduction is $2.86 \pm 0.05(stat) \pm 0.91(ang)$ and for the the LVL2 trigger condition $11.93 \pm 0.12(stat) \pm 3.7(ang)$. This leads to an enhancement of the signal to background ratio from LVL1 to LVL2 by a factor of $4.09 \pm 0.08(stat) \pm 1.8(ang)$ within the geometrical acceptance. Moreover the LVL2 settings enable an efficient suppression of the off-target events, as discussed in Section 5.1.

# Chapter III

# The Data Analysis

In the following chapter the different steps of the data analysis are described. Starting from the reconstruction of tracks in the different subsystems of the FOPI spectrometer - explained in the previous chapter - a new framework was developed for the analysis of the proton-proton data.
In the first step the two different hemispheres - the forward and backward - were treated separately. For the forward hemisphere the track information of the Helitron is combined with the hit information of SiΛViO and the Plastic Wall. In Section 3.1 the procedure of matching, momentum determination and the particle identification is explained.
In the backward hemisphere the track information from the CDC were used for particle identification. For the matching of the track information with the reconstructed hits in the RPC, routines already developed for this purpose were used (3.2).
After the separate extraction of the track information in the two hemispheres, the tracks were combined in the general data format, which can be accessed by the different physical analysis routines.
For the physics analysis three different types of reactions were reconstructed for different purposes.
One reaction is the elastic scattering of protons. Due to the fixed kinematical constraint, this reaction is used to calibrate the detector response. The identification is explained in Section 3.3.
For this beam time the detector SiΛViO was built to serve as an trigger to enhance the amount of events containing a $\Lambda$ particle. In order to quantify the performance of the system an inclusive reconstruction of $\Lambda$ particles is necessary - as described in Section 3.4.
The main part of the analysis is dedicated to the p$K^+\Lambda$ final state, for which the pp$K^-$ particle might be a possible production channel. The different steps which are necessary to extract an exclusive sample from the whole recorded data sample is explained in Section 3.5

## 3.1 Forward Track Identification

The tracks in the forward direction are created from the tracking information of the Helitron, the Plastic Wall and the SiΛViO Detector. The track reconstruction of the Helitron is described in Section 2.5.
The merging of Helitron tracks and reconstructed hits in the Plastic Wall detector - which is a part of the standard FOPI code - is done by geometrical matching. A successfully merged

combination can be refitted using the momentum fitting routine of the Helitron. This routine allows to add additional hit points from other detectors (see Section B).
To reject fake tracks in the Helitron chamber, only tracks matched with a Plastic Wall hit are used for the further analysis. Those tracks are named Helitron tracks in the following.
Those Helitron tracks have to be combined with the information of the SiΛViO detector, which is explained in Paragraph 3.1.1. To improve the particle momentum resolution the tracks are refitted (3.1.2). The identification, which tracks correspond to which particle, is explained in Paragraph 3.1.3.

### 3.1.1 Track Matching with SiΛViO Hit Points

The hit point of the SiΛViO-B layer is combined with the track information of the Helitron drift chamber of FOPI via geometrical matching. The reconstructed Helitron tracks are extrapolated through the magnetic field of FOPI to the z-position of the SiΛViO B layer. The difference between the extrapolated track points and the SiΛViO hit points in x and y direction is plotted in Figure 3.1. The combination with a distance in the x- and y- direction within $3.5\sigma$ is accepted. In case of more than one accepted SiΛViO-B hit the one with the smaller distance was chosen. The inaccuracy resulting of this procedure is negligible, since the number of tracks with more than one possible hit points is negligible.
The ratio of Helitron tracks matched with SiΛViO to all Helitron tracks in the SiΛViO acceptance is shown in Figure 3.2 as function of different track parameters. One can see a homogeneous distribution of an average matching efficiency of 91.2 ± 0.6 % is achieved [MBF$^+$14].

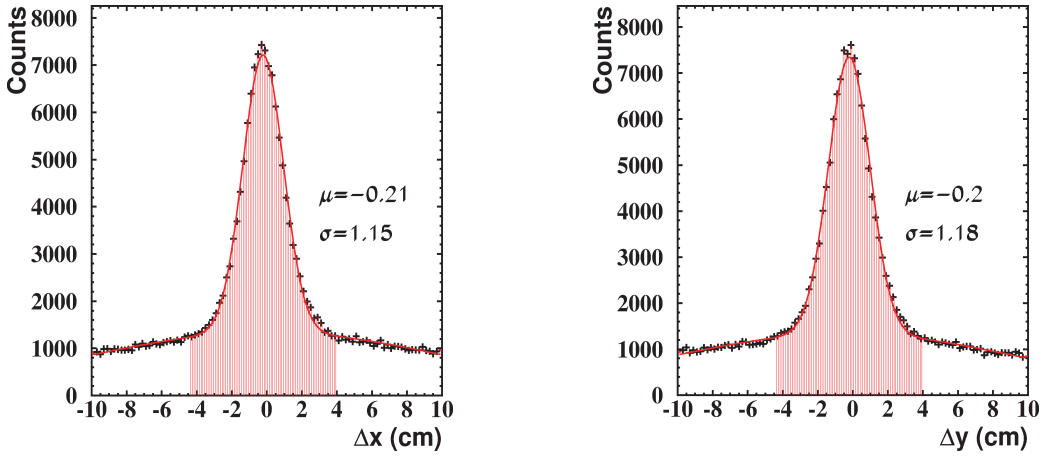


(a) (b)

Figure 3.1: Distance of the SiΛViO B hit point to the extrapolated point of the Helitron track on the x-y plane at the SiΛViO-B z-Position (x (a) respectively y (b)) [MBF$^+$14].

### 3.1.2 Track Refitting of Forward tracks

By adding the hit points of SiΛViO to the track reconstruction one can improve the momentum resolution in forward direction. Therefore the hit-point of SiΛViO is included in the refitting of the associated Helitron track. This procedure is necessary, since the radial resolution of the

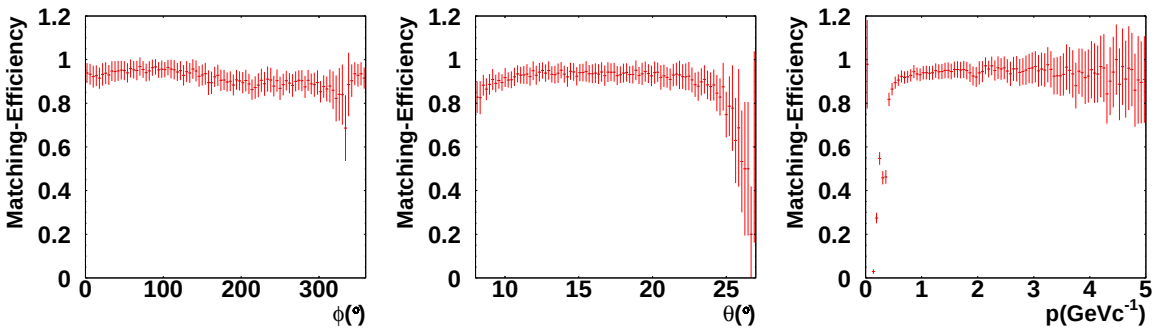


(a) (b) (c)

Figure 3.2: Ratio of Helitron tracks matched with SiΛViO hit point divided of all Helitron tracks in SiΛViO acceptance. Upper left picture shows the ratio versus $\theta$ of the track. In the upper right the ratio versus $\phi$ of the track is shown. The lower picture shows the ratio versus the track momentum [MBF+14].

Helitron is very poor. In the first step the polar angle of the particle is recalculated. Since FOPI is using a solenoid magnetic field, the particle trajectories are straight in the rz-plane[1].

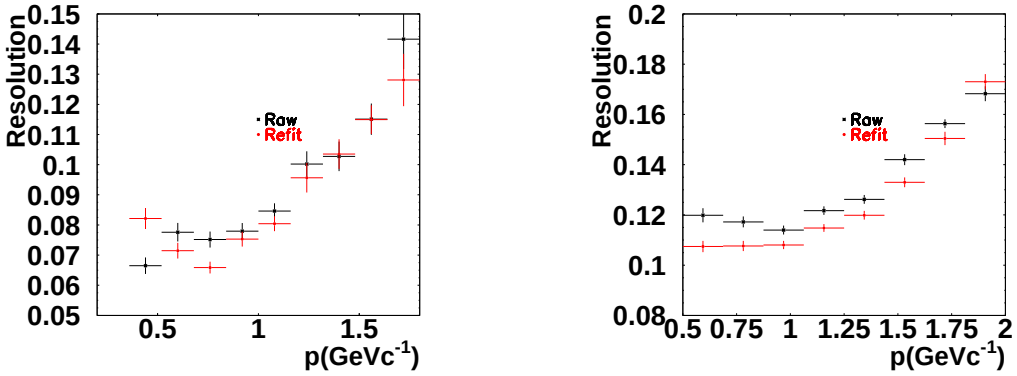


(a) (b)

Figure 3.3: The left row shows the momentum resolution for pions (panel (a)) and protons (panel (b)), for Helitron alone (black) and after refitting with the SiΛViO point (red).

Without SiΛViO the polar angle of the particle is calculated using the hit point information of the plastic wall under the assumption, that the particle originated from the vertex[2]. With the the SiΛViO hit point the vertex-assumption can be discarded and the $\theta$ can be calculated. The second step is to fit a track to the hit points and to calculate the momentum of the particle [Win78]. The resolution improvement of this procedure was checked in simulations. Figure 3.3

[1] r=$\sqrt{x^2+y^2}$: Distance to the beam axis
[2] As vertex the origin with the coordinate (0,0,0) is used

shows the resolution, which is defined as the width of the distribution of Equation 3.1:

$$\text{Resolution} = \frac{p_{reco} - p_{sim}}{p_{sim}} = \frac{\Delta p}{p}. \tag{3.1}$$

The resolution for pions and protons with and without the refit is shown in Figure 3.3 ((a) and (b)). One can see that for the pions an average improvement of 4% while for the protons more than 5% improvement is possible. Due to the used tracking routine of the Helitron the improvement of the momentum resolution is not very large. This tracking routine uses - in case of no available hit point in SiΛViO - the target as a starting point. Due to the long lever arm from the Helitron points to SiΛViO or the target, the difference is quite low for the momentum. Since the SiΛViO detector was built to improve the reconstruction of a secondary vertex, the small effect on the momentum resolution was expected.

### 3.1.3 Particle Identification

The particles in the forward hemisphere are identified via their momentum and velocity information. Figure 3.4 shows the particle momentum versus the velocity for positive (a) and negative charged particles (b). From these pictures a clear separation of protons and pions can be seen. The black lines follow the relativistic momentum function for the nominal particle masses (see Equation 3.2):

$$p = m_0 \beta \gamma c. \tag{3.2}$$

The particles are selected by two dimensional cuts on those spectra - indicated by the red lines. Since the particles of interest for this analysis are protons and negative pions the cut for positive pions is not plotted.

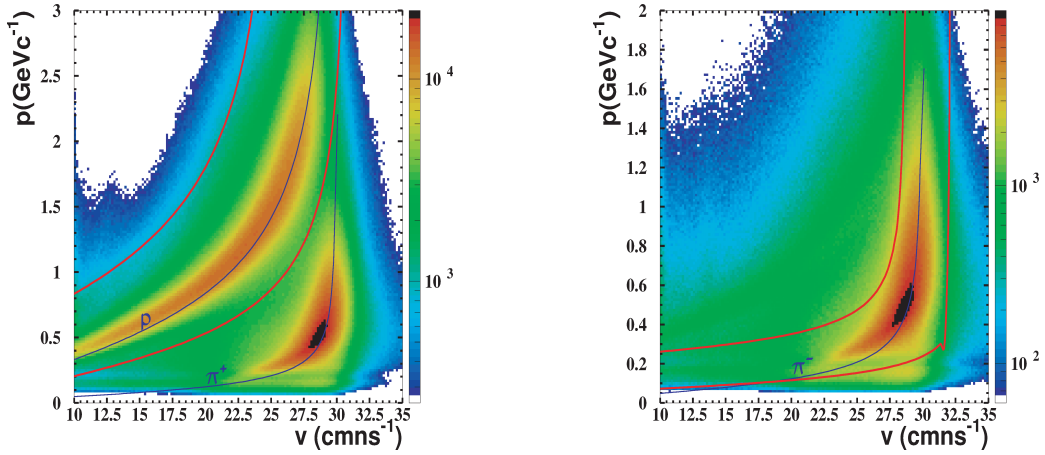


(a) (b)

Figure 3.4: Momentum versus velocity particle flight through the forward hemisphere (Silvio, Helitron, PLAWA). Figure (a) show particles with positive charge and (b) with negative charge. The black lines follow the relativistic momentum function $p = m_0 \beta \gamma c$ for the nominal particle masses. The cuts selection cuts for proton and negative pions are indicated by red lines.

## 3.2 Particle Identification in the Backward Hemisphere

The second track reconstruction system of FOPI is the system of the Central Drift Chamber CDC (2.4), the plastic barrel (2.8), and the resistive plate chambers (2.9). These three detectors cover the so called backward hemisphere of FOPI.

### 3.2.1 Energy-loss Identification

The main part of the track reconstruction is done by the CDC (2.4.1). The tracking procedure of the CDC also allows the reconstruction of the particle momentum (2.4.2) and the energy loss (2.4.3). According to the Bethe-Bloch formula (Equation 3.3) the combined measurement of momentum and energy-loss of a particle allows its identification. Due to its complexity one cannot obtain a analytical formula for the mass. For this reason the particle identification can only be done by a two dimensional selection function applied to the energy-loss versus momentum spectrum.

$$\frac{dE}{dx} = -\frac{4\pi n z^2}{m_e c^2 \beta^2} \cdot \left(\frac{e^2}{4\pi\epsilon_0}\right)^2 \cdot \left[\ln\left(\frac{2m_e c^2 \beta^2}{I \cdot (1-\beta^2)}\right) - \beta^2\right]. \tag{3.3}$$

To allow a separation of positive and negative particles in Figure 3.5 the energy-loss versus momentum times charge spectra are shown for positive (a) and for negative particles (b), respectively.

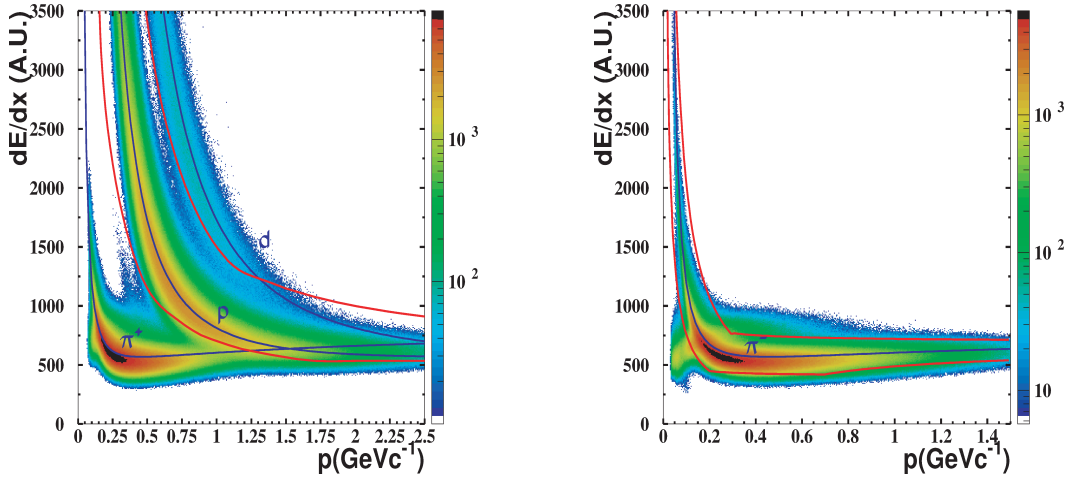


(a) (b)

Figure 3.5: CDC energy loss versus momentum

In this spectrum the nominal particle lines according to the Bethe-Bloch distributions are shown by the blue curves. The regions in which the particles are selected are shown by the red lines.
Like in the previous section the selection cut for positive pions is not shown.

### 3.2.2 Time of Flight Identification

For the exclusive reconstruction of the reaction pp $\rightarrow$ p$K^+\Lambda$ a $K^+$ has to be identified. Since this is not possible for the energy-loss versus momentum spectra due to insufficient resolution, in addition the flight time of the particle, measured by the RPC barrel detector, is required.
The reconstructed CDC track - described in Section 2.9 - is extrapolated to the geometrical

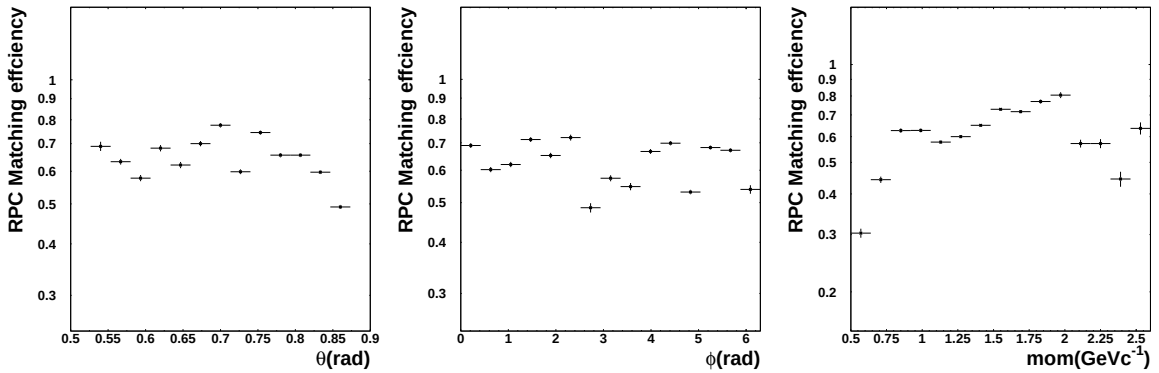


(a) (b) (c)

Figure 3.6: Differential CDC - RPC Matching $\epsilon$ versus the polar angle (a) the azimuthal angle (b) and the particle momentum (c).

position of the RPC-Barrel. If a reconstructed particle-hit in the RPC-Barrel is within a geometrical overlap region of this extrapolated track, this combination is stored. Due to detector inefficiencies not all particles are measured in both detectors. The differential matching efficiency $\epsilon$ is plotted in Figure 3.6 versus the polar angle (a), the azimuthal angle (b) and the particle momentum (c). The averaged matching efficiency is $62 \pm 0.5\%$.
From the time of flight information of the RPC-Barrel the particle velocity is deduced. The resulting momentum versus velocity plot is shown in Figure 3.7. The black lines show the distribution for the nominal particle masses. The chosen cuts [Her12] allow for a good $K^+$ -$\pi^+$ separation up to 0.7 GeV/c and 25 cm/ns. From this selection a two dimensional cut region - indicated by the red line - is obtained for the $K^+$ selection. To allow a sufficient background determination the selection band for the $K^+$ can be broadened.

## 3.3 Reconstruction of Elastic Proton Proton Collisions

The study of elastic reactions is a very frequently used tool, to study detectors response. Due to the two body scattering process, which follows discrete kinematics it is possible to selected a pure event sample, with a negligible amount of misidentified or fake tracks. The reconstructed elastic pairs are used for an efficiency correction of the simulation package (see Section 4.3.3).

### 3.3.1 Elastic Kinematics

The kinematics of two body collisions is fixed in the center of mass frame. Due to momentum conservation the scattered protons are emitted back to back in the center of mass frame

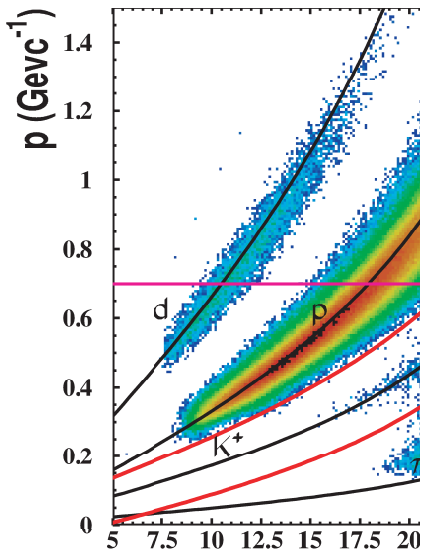


Figure 3.7: Momentum versus velocity of CDC-RPC tracks. Black lines show the distribution for the nominal particle masses. Pink lines show the border of clear $K^+$ -$\pi^+$ separation. The selection of $K^+$ is done by a two dimensional cut band. [Mue13].

(Figure 3.8 (a)).

Since we are studying such reaction in a fixed target experiment, the center of mass kinematics have to be transformed into the laboratory frame (Figure 3.8 (b)). This transformation leads to the following correlation of the polar angles:

$$|\theta_{1,Lab} \cdot \theta_{2,Lab}| = \frac{1}{\gamma^2_{CMS}} = 0.299 \ , \tag{3.4}$$

with the Lorentz factor $\gamma_{\mathrm{CMS}}$ calculated from the kinetic beam energy ($\mathrm{E_{kin}}$=3.10 GeV) and the proton mass ($\mathrm{m_p}$=0.938 GeV/$\mathrm{c^2}$):

$$\gamma_{CMS} = \frac{E_{kin} + 2 \cdot m_p}{\sqrt{2 \cdot m_p^2 + 2 \cdot E_{Kin} m_p}} = 1.83 \ . \tag{3.5}$$

Since the center of mass is moving along the z-axis the azimuthal angle of the particles are not affected by the Lorentz transformation which leads to the following correlation:

$$|\phi_{1,Lab} - \phi_{2,Lab}| = 180^\circ. \tag{3.6}$$

### 3.3.2 Identification of Elastics Events

In the first step events, which contain exactly two reconstructed and identified protons, are selected. Since this selection still contains background events, due to misidentification and efficiency losses, further cuts are necessary to select elastic events. Based on the strict kinematic constraints of the elastic reaction, described in the previous paragraph, the following cut parameters are applied.

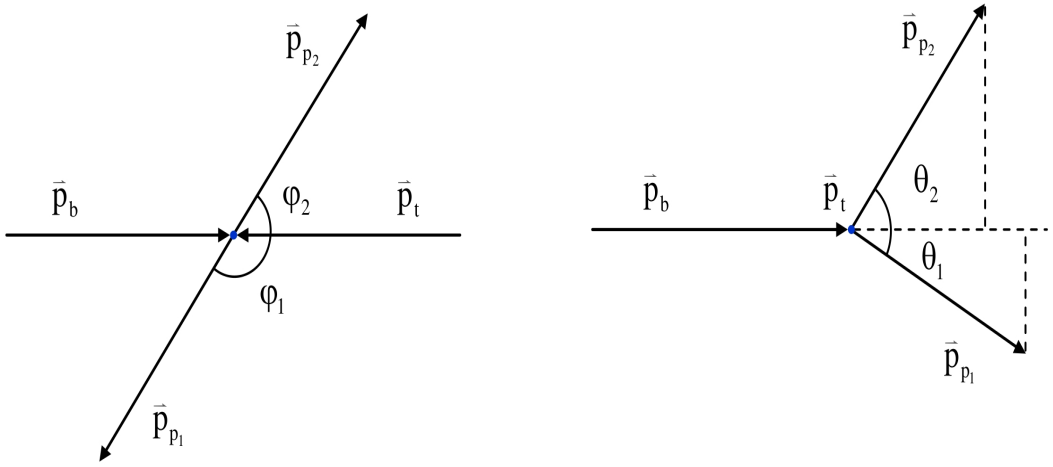


(a) (b)

Figure 3.8: Reaction Kinematics in elastics proton proton reaction in the center of mass frame (a) and in the laboratory frame (b) [Ple12].

**Azimuthal Difference - $\Delta\phi$:** The difference of the azimuthal angle of the two protons $\Delta\phi$ has the nominal value - according to Equation 3.6 of 180°. Figure 3.9 (a) shows the distribution of $\Delta\phi$ with a clear peak around 180°. The red shaded area indicates the selected region ( $176° \leq \Delta\phi \leq 186°$).

**Polar Difference - $\Delta\theta$:** Based on the Lorentz corrected correlation of the protons (see Equation 3.4) the difference of the polar angles can be deduced - shown on Equation 3.7:

$$\Delta\theta = \theta_{p_2} - \text{atan}\left(\frac{1}{\gamma^2 \text{tan}\theta_1}\right) \tag{3.7}$$

The distribution of Figure 3.9 (b) shows a clear peak around the nominal value of 0°. The red shaded area indicates the selected region ($-8° \leq \Delta\theta \leq 5°$).

**Total invariant mass - $M(p_1, p_2)$** In case of elastics scattering the total energy is carried by the two protons, which leads to a nominal value for the invariant mass of 3.06 GeV/$c^2$. Events between 2.550 GeV/$c^2$ and 3.50 GeV/$c^2$ were selected.

**Confidence Level - pvalue** The kinematical refit procedure (see Appendix C) - mainly developed for the exclusive particle analysis - was modified to be applied to elastic reactions [Ple12]. This allows to use the confidence level extracted from the refit (see Appendix C.b.ii.) as an additional cut for the background reduction. The constraints for the elastic reaction were energy- and momentum conservation.
The confidence level distribution is shown in Figure 3.9 (c). Remaining background events are located - by definition - in the peak around zero. A cut on a p-value higher than 0.05 allow to reject remaining background events.

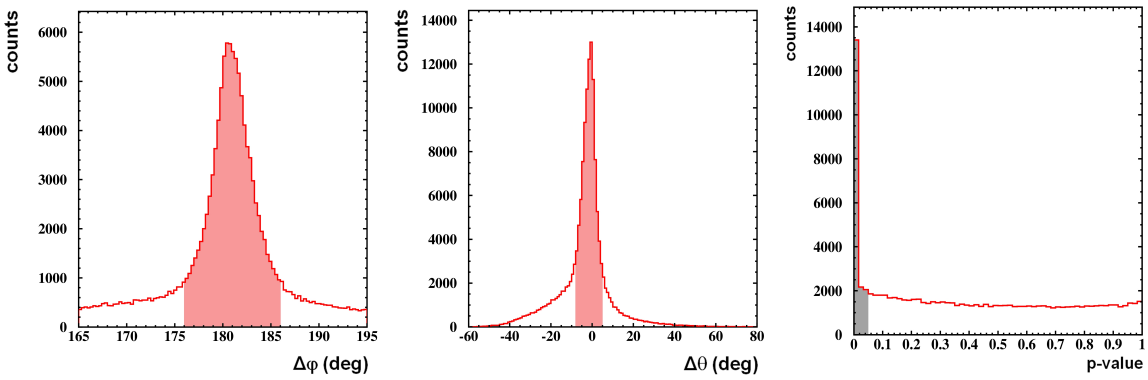


(a) (b) (c)

Figure 3.9: $\Delta\phi$ (a) and $\Delta\theta$ (b) distribution of the two protons and the confidence level (c) [Ple12].

## 3.4 Inclusive Λ Reconstruction

To determine the enhancement of Λ particles due to SiΛViO, their inclusive production has to be analyzed. The underlying production process is shown in reaction 3.8. The Λ particles are identified via the decay in a pair of p and $\pi^-$ :

$$p + p \xrightarrow{3.1GeV} \Lambda + ... \qquad (3.8)$$
$$p + \pi^- \quad 63.9\%$$
$$n + \pi^0 \quad 35.8\%.$$

### 3.4.1 Event Selection

In the first step events, which contain at least one negative pion and one proton, have to be selected. The identification of the different particles is done by the selection cuts described in Paragraph 3.2.1 and Paragraph 3.1.3. From the measured particle momenta the four momenta of the p and $\pi^-$ is calculated. Since the mass determination of the particle depends on the momentum measurement, the nominal particle masses [B+12] are taken to avoid an additional error.
In Figure 3.10 the invariant mass distribution of proton-pion pairs is shown.

### 3.4.2 Primary Vertex Reconstruction

For the background reduction (3.4.4) the position of the primary vertex is required. In the first case the primary vertex is calculated using all reconstructed particle tracks. In the first step the intersection point of track pairs is calculated. In the second step the vertex is determined by the center of mass of all intersection points. Since the Λ particle does not decay at the primary vertex, if the secondary particles - stemming from the Λ decay - are used in the calculation, the resulting primary vertex position is not correct (see Figure 3.13).
To improve the determination of the primary vertex an advanced procedure is applied to

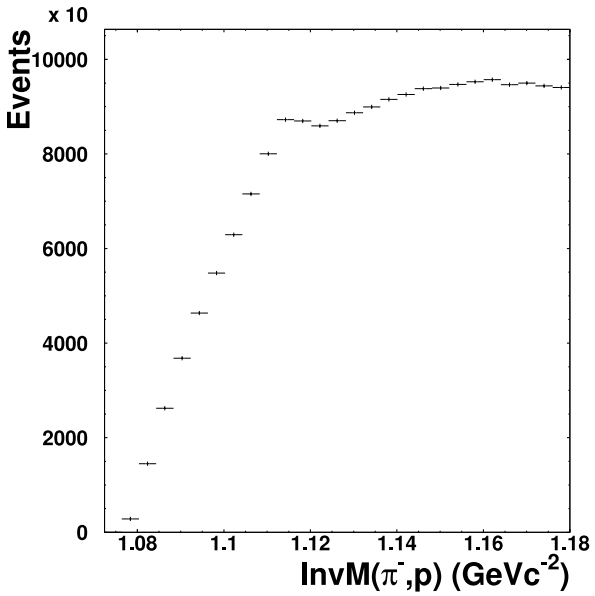


Figure 3.10: Invariant mass of the p-$\pi^-$ pairs from experimental data.

recalculate its coordinates under the assumption, that the proton and pion are stemming from a $\Lambda$ hyperon, which originates at the vertex position. The momentum vector of the $\Lambda$ is calculated from the momenta of the daughter particles, which defines the direction of the $\Lambda$ particle. This particle track is used to recalculate the vertex position in the previous described method with the other primary particles.
In the case the proton and pion are the only reconstructed particles, the primary vertex is determined by the point of closest approach of the $\Lambda$ vector to the beam axis. Figure 3.11 shows the reconstructed vertex position before (black crosses) and after the recalculation (red crosses). The resolution values are listed in Table 3.1. From those values it can be seen, that the vertex resolution can be improved by about an factor 10.

| | Before Refit [cm] | After Refit [cm] |
|---|---|---|
| $\sigma_x$ | 3.84 | 0.09 |
| $\sigma_y$ | 2.98 | 0.04 |
| $\sigma_z$ | 5.50 | 0.31 |

Table 3.1: Primary vertex resolution before and after the recalculation.The black dots show the position before (black dots) and after the recalculation (red dots). The solid curve represent the according fitting function, which is the sum of two Gaussian function. The width is obtained from the small Gaussian function.

### 3.4.3 Background Determination

The signal and the amount of background in the $\Lambda$ spectrum is extracted by fitting the signal distribution by a Gaussian and the background distribution by an polynomial function. In heavy ion reactions the background distribution is usually determined by mixed-event

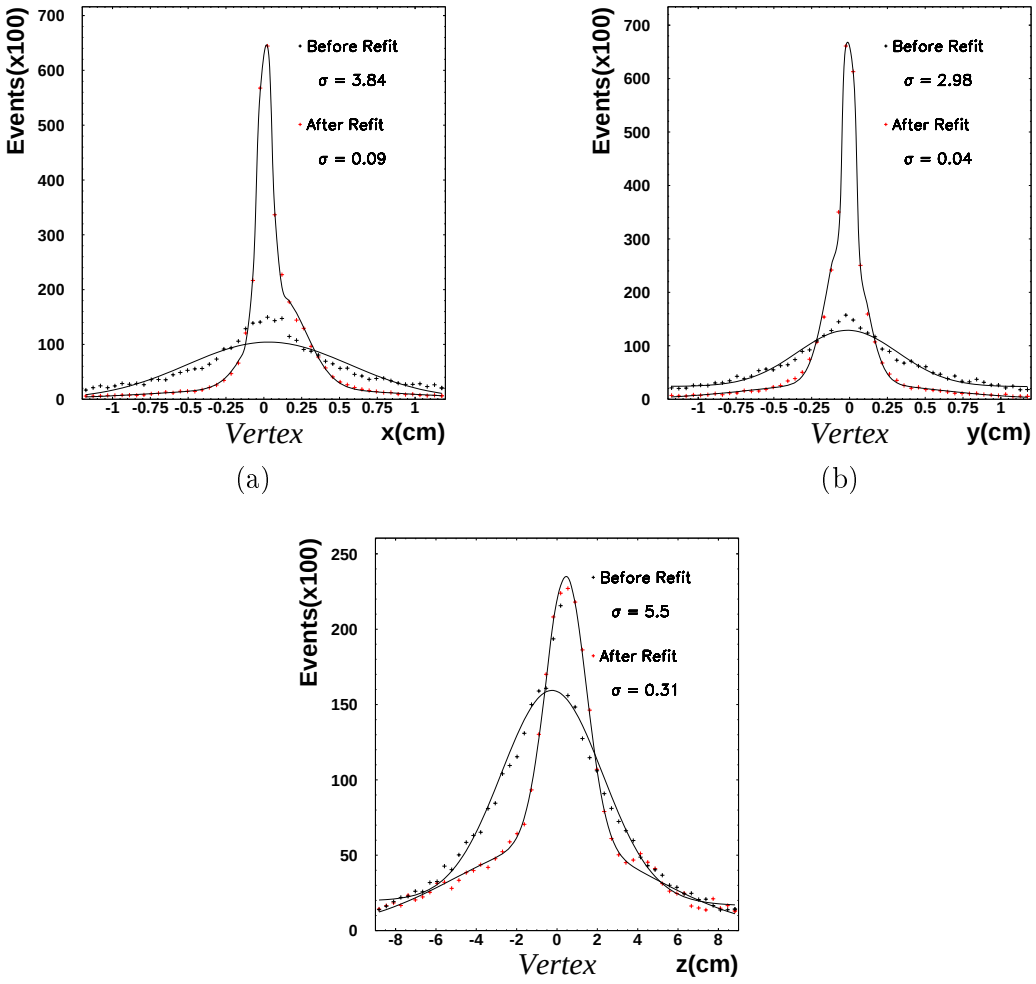


Figure 3.11: Primary vertex reconstruction in inclusive Λ analysis.

technique[3] [Mer04]. This method can be applied to such kind of reactions, since the number of produced particles is quite high. Thus, the main background contribution beneath the Λ signal is created by uncorrelated proton-pion pairs, which can be described by the event-mixing method. For proton-proton reactions the assumption of uncorrelated proton-pion pairs is not fulfilled, since the number of produced particles is low, which leads to a final state interaction, which cannot be described by the event mixing technique.
The best description of the total distribution of signal and background is obtained in two steps: in a first step, a polynomial function is fitted to the mass distribution without the mass region around the Λ mass. An example of this fitting is shown in Figure 3.12 (a). This fitting allows to obtain correct starting value for the combined fit, which is been done in a second step. In this step the whole mass distribution is fitted by the sum of the polynomial function extracted in the first step and the Gaussian function, with a peak position in the region of the Λ mass.

[3]Event mixing: The mixed event background is created by building proton-pion pairs of particles from different events

The result is shown in Figure 3.12 (b). The red curve corresponds to the sum function of the polynomial and the Gaussian function. The green curve is the resulting polynomial function describing the background. The data points in the lower part of Figure 3.12 (b) shows the resulting function after subtracting the background distribution from the total mass distribution.
This method is used for the background determination of all proton-pion invariant mass spectra.

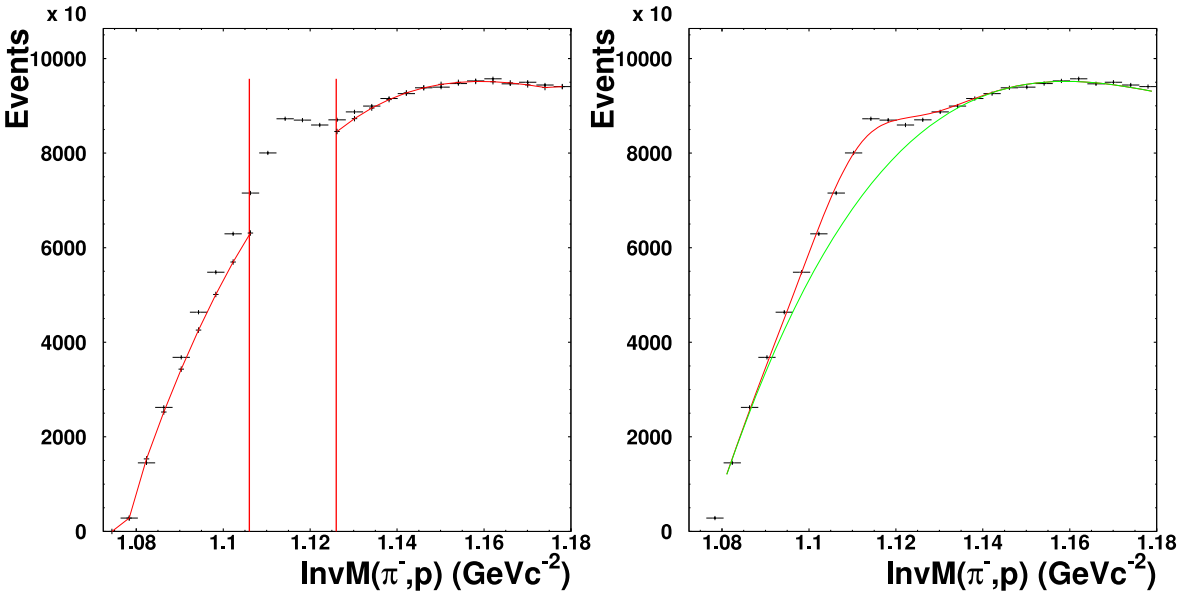


(a) (b)

Figure 3.12: Background determination for Λ spectrum. In the first step the spectrum - except the Λ region - is fitted by an polynomial function (a). In the second step the whole spectrum is fitted by and polynomial plus an Gaussian function (red curve). The polynomial contribution is plotted in red.

### 3.4.4 Background Reduction

To reduce the amount of pairs, which are not originating from a Λ particle, additional cuts on the decay vertex have to be applied. The existence of SiΛViO allows to calculate a vertex position in case a particle is flying through the Helitron, which is not possible without the additional track point, due to the vertex assumption of the tracking procedure (3.1.2). Since the Λ hyperon has a decay length of around 7.86 cm on average the vertex of its decay position can be separated from the primary vertex. Other uncorrelated proton-pion pairs are stemming from the primary vertex.
To reduce the amount of background geometrical cuts on the track topology have to be investigated. Figure 3.13 shows the event kinematic of inclusive produced Λ particles. The Λ particle decays into a p (red) and a $\pi^-$ (green). The thick lines are the actual particle tracks. The thin lines are the extrapolated particle tracks, which are needed to calculate the distance of closest approach of the tracks to the primary vertex. The Λ tracks (magenta) is reconstructed from the momenta of the two daughter particles.

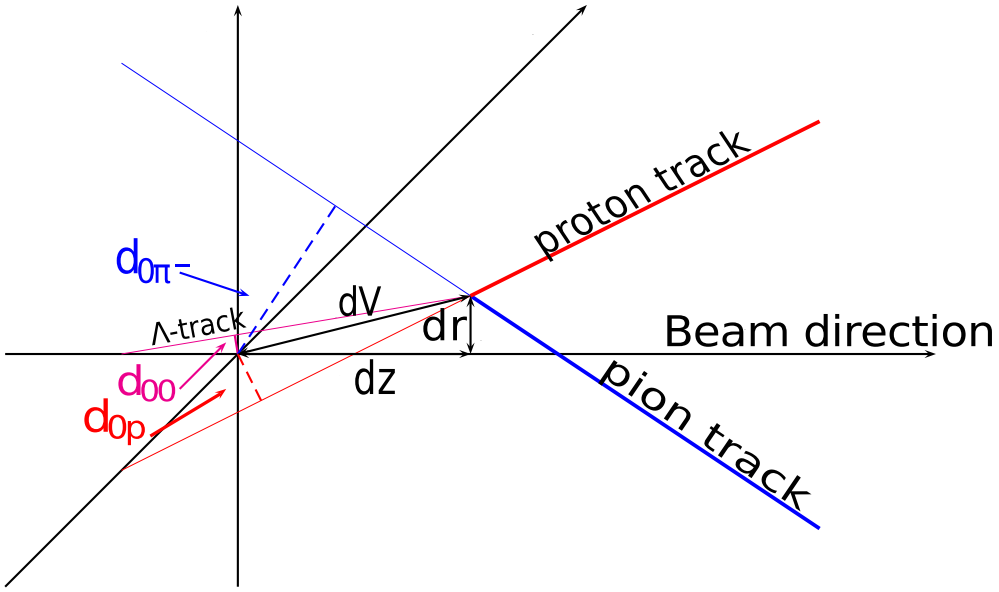


Figure 3.13: Event topology of a $\Lambda$ particle produced in the vertex. The particle travels until it decay into a p (red) and a $\pi^-$ (green). The thick lines are the actual particle tracks. The thin lines are the extrapolated particle tracks. The $\Lambda$ tracks (magenta) is reconstructed from the momenta of the two daughter particles. The dashed lines are the minimal distances of the particles to the vertex. The different parameters for the events selection are plotted (explanation see text).

The following geometrical cut parameters are extracted:

$\vec{V}_{prim}$ : Recalculated primary position
$d_0$ : Minimal distance pf $\pi^-$ and p track
$d_{00}$ : Distance of closest approach of extrapolated $\Lambda$ track to the primary vertex.
$d_{0\pi^-}$ : Distance of closest approach of the $\pi^-$ track to the primary vertex.
$d_{0p}$ : Distance of closest approach of the proton track to the primary vertex.
$dV$ : Distance of the secondary and primary vertex in three spacial dimensions.
$dr$ : Distance of the secondary vertex from the beam axis.
$dz$ : Distance of the secondary vertex from target x-y plane.

The best set of parameters is determined by a systematical scan of different parameters settings. For each parameter set the $\Lambda$ signal and the signal to background value are obtained by the method described in Section 3.4.4. The set is chosen by maximizing the observable $Signal \times \frac{Signal}{Background}$. The best set is listed in Table 3.2. The dimension of the primary vertex correspond to the actual target size in the x and y direction. In the z direction the target had a length of 2 cm.
The corresponding $\Lambda$ spectrum is shown in Figure 3.14.

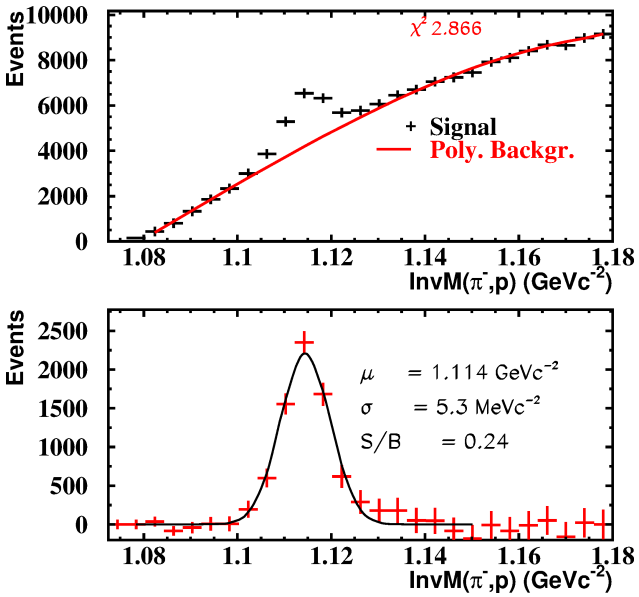


Figure 3.14: Invariant mass of the p-$\pi^-$ pairs from experimental data. The red line in the upper panel shows the polynomial fit to the combinatorial background. The lower panel shows the background subtracted spectrum. The black line corresponds to a Gaussian fit to the signal.

| value | minimal value [cm] | maximal value [cm] |
|---|---|---|
| $primvertex_x$ | -1.0 | 1.0 |
| $primvertex_y$ | -1.0 | 1.0 |
| $primvertex_z$ | -2.0 | 2.0 |
| dr | 3.0 | $\infty$ |

Table 3.2: Cut value used for the extraction of the $\Lambda$ signal shown in Figure 3.14.

The upper panel shows the invariant mass of all p-$\pi^-$ pairs after applying the vertex cuts mentioned above.

## 3.5 Exclusive p$K^+\Lambda$ Event Reconstruction

The main goal of the experiment was to identify the final state p $K^+$ and $\Lambda$. The full reaction is shown in reaction 3.9. The selection of an exclusive event is done in several different steps, which are explained in the following section.
In the first step events with a correct amount of tracks are selected (3.5.1), followed by the selection of $K^+$ in the RPC region. In the analysis two different types of $K^+$ cuts are used in the following steps.
The reconstruction of $\Lambda$ particles is described in Section 3.5.3. The important step of the background reduction is explained in Section 3.5.4, which makes use of the kinematical refit. The remaining background after the refit is further reduced by a momentum dependent cut on the Kaon mass spectrum (3.5.5). Exploiting the method of sideband analysis, explained

in Section 3.5.6, a very good description of misidentification background is obtained.

$$p + p \xrightarrow{3.1GeV} \Lambda + p + K^+ \tag{3.9}$$
$$p + \pi^-$$
$$n + \pi^0$$
$$\xrightarrow{3.1GeV} \Sigma^0 + p + K^+ \tag{3.10}$$
$$\Lambda + \gamma$$
$$p + \pi^-$$
$$n + \pi^0$$
$$\tag{3.11}$$

Due to the very similar reaction mechanism of the $\Sigma^0$ (Reaction 3.10), which differs just in the production of an additions $\gamma$, a certain amount of this channel is still existing after all previous cuts. The amount of this contribution is described in Paragraph 3.5.7.
The resulting p$K^+\Lambda$ sample is presented in Section 3.5.8 .

### 3.5.1 Event selection

In the first step of the exclusive analysis events are selected, which only contain four reconstructed tracks. The reaction, that we want to reconstruct consists of four charge particles in the final state (Reaction 3.9). To maximize the statistics first just a rough particle selection is applied, which means, that events are accepted, with three particles of positive and one particle of negative charge.

### 3.5.2 Kaon Selection

From the data set containing four particles, those have to be extracted, which contain a $K^+$. The identification of those particles and the separation of such particles from the signal of protons and positive pions is rather challenging, due to resolution issue. In the case of FOPI the identification of $K^+$ is only possible, if this particle is detected in the region of the CDC and the RPC detectors, since only such detector combination allows a measurement of the momentum and the velocity with a sufficient resolution. As shown in Section 3.2.2 with certain cuts, kaons can be separated quite efficiently from protons and positive pions.
Based on this particle identification, particle cuts can be obtained, which can be used for the kaon selection. Like in the case of the event selection, the selection cuts are kept to a minimum to obtain a maximal signal.
Additional to the kaon selection region extracted in Section 3.2.2 a broader cut region were analysed separately. This cut also includes a part of the proton and pion signal, that allows a better determination of the remaining background signal of the selected kaon candidates. The two different selected regions, which will be referred to in the following as narrow and wide cut, are shown in Figure 3.15 in left and right panels respectively.

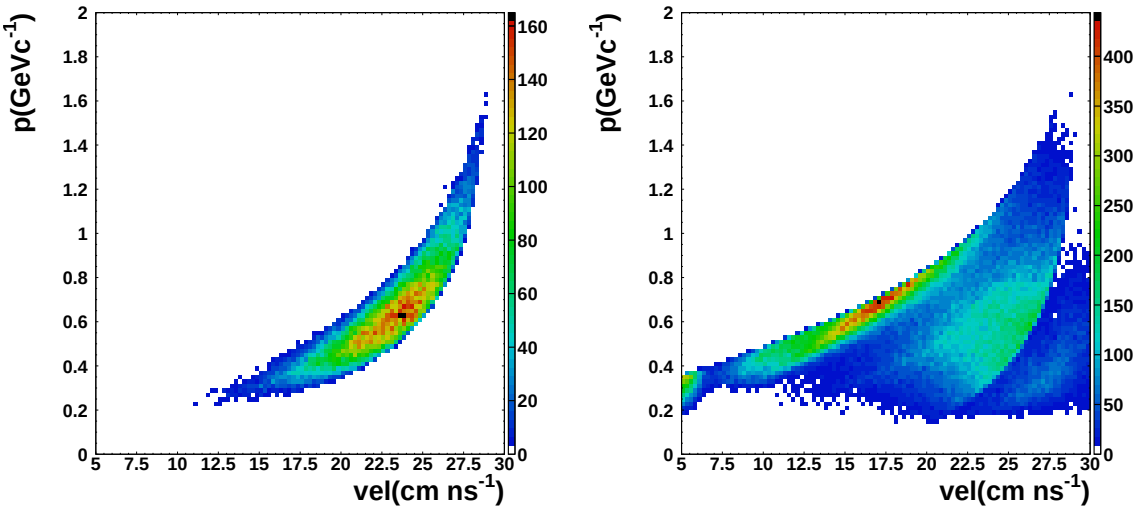


(a) (b)

Figure 3.15: Selected Kaon in the Momentum versus velocity frame. Left Narrow cut. Right wide cut

### 3.5.3 Λ Identification

After a sample with $K^+$ candidates is chosen, those event have to selected, which contain a Λ candidate. These are selected by their decay into proton-pion pairs (see reaction 3.9).
In Figure 3.16 the invariant mass distribution of all proton-pion pairs is shown for narrow kaon selection (a) and the wide kaon selection (b), respectively.
It can be seen that in both cases the resolution is quite broad ($\sigma_{Narrow} = 13.9$, $\sigma_{wide} = 14.8$ MeV/c$^2$). For this reason a precise determination of the background is not possible.

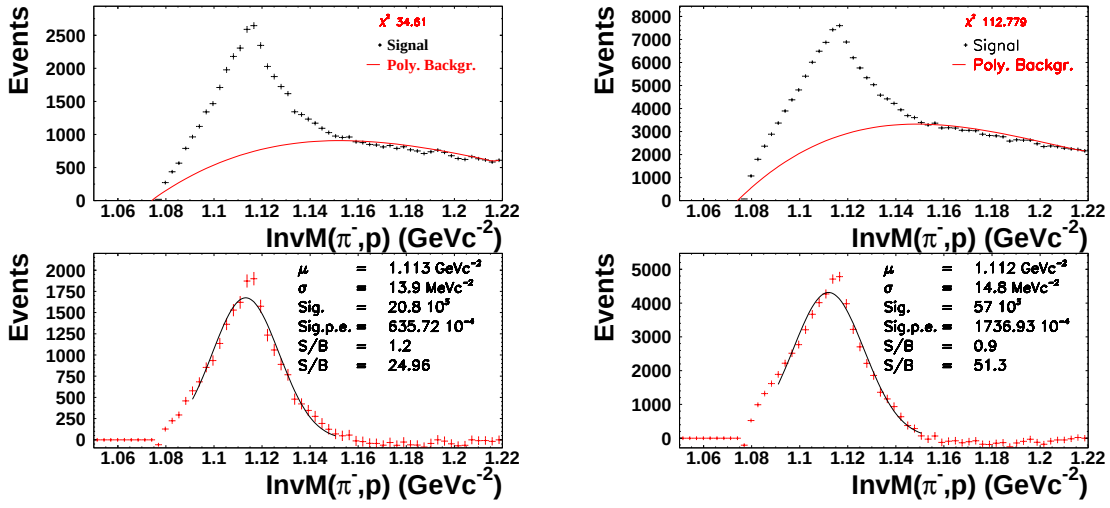


(a) (b)

Figure 3.16: Invariant mass $\pi^-$ and proton after the primary kaon selection for the narrow kaon selection (left) and the wide selection (right).

### 3.5.4 Kinematical Refit

For the selection of the exclusive events, the kinematical refit - described in Appendix C -is applied.
In this case the kinematical refit is applied to the four selected charged particle candidates: kaon, pion and two protons. For the $\Lambda$ identification the two protons are clearly identified as the primary and secondary proton.
The following constraints are required for the refit with four particles in the final state:

**Selection constraint:** For the selection of the exclusive reaction events, the constraints of energy- and momentum conservation have to be fulfilled.

**Analysis constraint:** After the selection of the exclusive event an additional constraint can be applied to the kinematical refit, which requires, that the invariant mass of the secondary proton and the pion is equal to the nominal mass of the $\Lambda$ .

To crosscheck the refit the invariant mass distribution of protons and pions is used. For that reason the analysis constraint cannot be applied, since this constraint would force that invariant mass to be exactly the nominal $\Lambda$ mass. This constraint will be used after the selection procedure for the analysis of the final state p$K^+\Lambda$ . The application of this constraint allow to improve the resolution, since the width of the $\Lambda$ mass can be neglected.

#### Error Determination

To ensure that the kinematical refit is working properly the error determination plays an important role. To optimize the selection capability of the kinematical refit for exclusive events the systematical and the statistical errors of the different parameters have to determined. For this procedure the pull values of the kinematical refit are used (see Appendix C.b.i.).
While the statistical error can be set directly in the refit procedure the systematical error has been corrected by a systematical shift of the corresponding parameter.
Due to the fact that certain dependencies exist between the errors of the different parameters the full set of error parameters has to be determined by a scanning routine, which determines the best possible combination of error values. This routine is explained in Appendix D.
After the best set of errors is determined, the pull distributions do not fully follow the shapes, which they should have in the ideal case. The reason for this are further more complex systematical errors, which cannot be corrected by a systematical shift.

#### Cut Determination

After the determination of the optimal error parameters the kinematical refit is used to suppress the background from not exclusive reactions. This is done by cutting on the pvalue of the kinematical refit. As explained in Appendix C.b.i. for signal events this value is distributed between 0 and 1. The pvalues for background events are very small. To determine the optimal cut position of the pvalue a scanning procedure was applied. For each pvalue cut position the $\Lambda$ signal was extracted. The final cut was set such to maximize the $\Lambda$ signal.
Since particles are measured in different detectors different cuts have to be applied. For this reason the FOPI spectrometer was separated in three different detector regions:

**Helitron and SiΛViO :** The particle is reconstructed in the Helitron and in SiΛViO

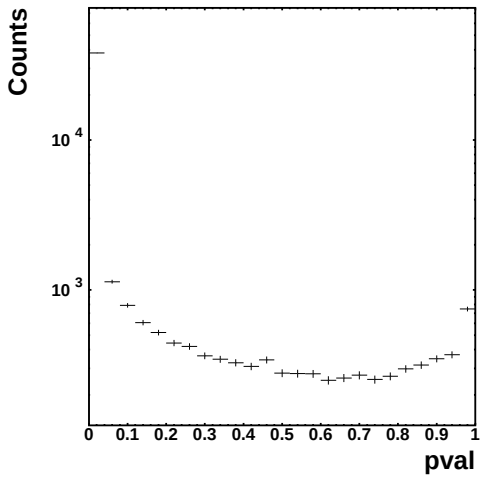


Figure 3.17: Pvalue Distribution for the topology (0-00).

**Helitron only:** The particle is reconstructed only in the Helitron.

**CDC:** The particle is reconstructed in the CDC. A matching with RPC is not required.

Since the primary proton, the secondary proton and the pion can be detected in all three different regions, 27 selections have to be carried out. The list of all different topologies are shown in Table 3.3 with the corresponding minimal cut value of the pvalue.
In Figure 3.17 an example for the pvalue distribution of the topology 0-00 is shown. The spike at the first bin is created by background events. After the cut on the pvalue is applied, the background contribution below the $\Lambda$ signal in the invariant mass spectrum - plotted in Figure 3.18 - has reduced significantly.

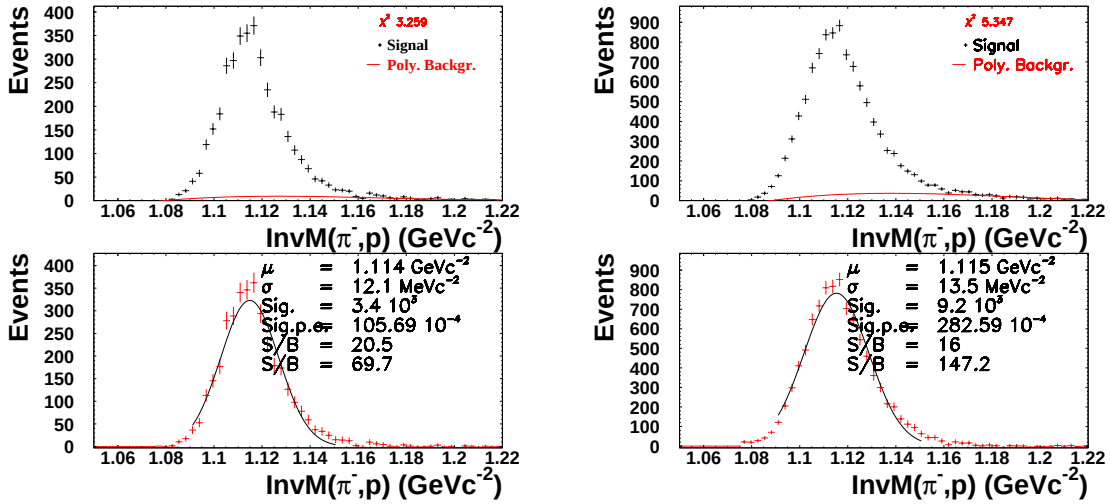


(a) (b)

Figure 3.18: Invariant mass $\pi^-$ and proton after refit selection for the narrow $K^+$ selection (left) and the wide selection (right)

| Topology | prim. proton | sec. proton | pion | min. pvalue cut |
|---|---|---|---|---|
| 0-00 | Hel. and SiΛViO | Hel. and SiΛViO | Hel. and SiΛViO | 0.0069 |
| 0-01 | Hel. and SiΛViO | Hel. and SiΛViO | Hel. only | 0.04 |
| 0-02 | Hel. and SiΛViO | Hel. and SiΛViO | CDC | 0.008 |
| 0-10 | Hel. and SiΛViO | Hel. only | Hel. and SiΛViO | 0.04 |
| 0-11 | Hel. and SiΛViO | Hel. only | Hel. only | 0.4 |
| 0-12 | Hel. and SiΛViO | Hel. only | CDC | 0.4 |
| 0-20 | Hel. and SiΛViO | CDC | Hel. and SiΛViO | 1.0 |
| 0-21 | Hel. and SiΛViO | CDC | Hel. only | 1.0 |
| 0-22 | Hel. and SiΛViO | CDC | CDC | 0.664 |
| 1-00 | Hel. only | Hel. and SiΛViO | Hel. and SiΛViO | 0.59 |
| 1-01 | Hel. only | Hel. and SiΛViO | Hel. only | 0.24 |
| 1-02 | Hel. only | Hel. and SiΛViO | CDC | 0.0000001 |
| 1-10 | Hel. only | Hel. only | Hel. and SiΛViO | 0.4 |
| 1-11 | Hel. only | Hel. only | Hel. only | 0.4 |
| 1-12 | Hel. only | Hel. only | CDC | 0.4 |
| 1-20 | Hel. only | CDC | Hel. and SiΛViO | 0.176 |
| 1-21 | Hel. only | CDC | Hel. only | 1.0 |
| 1-22 | Hel. only | CDC | CDC | 1.0 |
| 2-00 | CDC | Hel. and SiΛViO | Hel. and SiΛViO | 1.0 |
| 2-01 | CDC | Hel. and SiΛViO | Hel. only | 1.0 |
| 2-02 | CDC | Hel. and SiΛViO | CDC | 1.0 |
| 2-10 | CDC | Hel. only | Hel. and SiΛViO | 0.4 |
| 2-11 | CDC | Hel. only | Hel. only | 0.0001 |
| 2-12 | CDC | Hel. only | CDC | 1.0 |
| 2-20 | CDC | CDC | Hel. and SiΛViO | 1.0 |
| 2-21 | CDC | CDC | Hel. only | 1.0 |
| 2-22 | CDC | CDC | CDC | 1.0 |

Table 3.3: Minimal cuts on the pvalue for the different topologies

### 3.5.5 Second kaon selection

After the selection of events that have passed the kinematical refit selection, background events are still present, which can be seen from the kaon mass distribution. Figure 3.19 shows the mass distribution for the narrow (a) and the wide (b) kaon pre-selection. From spectrum of the wide selection it is clear, that a contribution of misidentified protons as well as $\pi^+$s is still visible in the kaon spectrum. Although the kaon spectrum for the narrow selection seems to have no remaining background contribution, the presence of a background contribution is visible in the lower plot of Figure 3.19(a). The assumed signal of $K^+$ is not Gaussian shaped and can just be fitted by the sum of two Gaussian function, which are indicated by the green and the blue curves. The stated value for $\mu$ and $\sigma$ are the mean values of both gaussian functions. The background subtracted spectrum for the wide kaon selection cut ( Figure 3.19(b) lower panel) can be described quite nicely by a Gaussian distribution. For that reason it is necessary to proceed with the event sample of the wide kaon selection, since in this case, a sufficient background description is possible.

While the contribution of protons can be excluded, the contribution from the $\pi^+$ strongly overlaps with the $K^+$ signal. The remaining background distribution can be subtracted from the data using a sideband technique - described in Section 3.5.6.

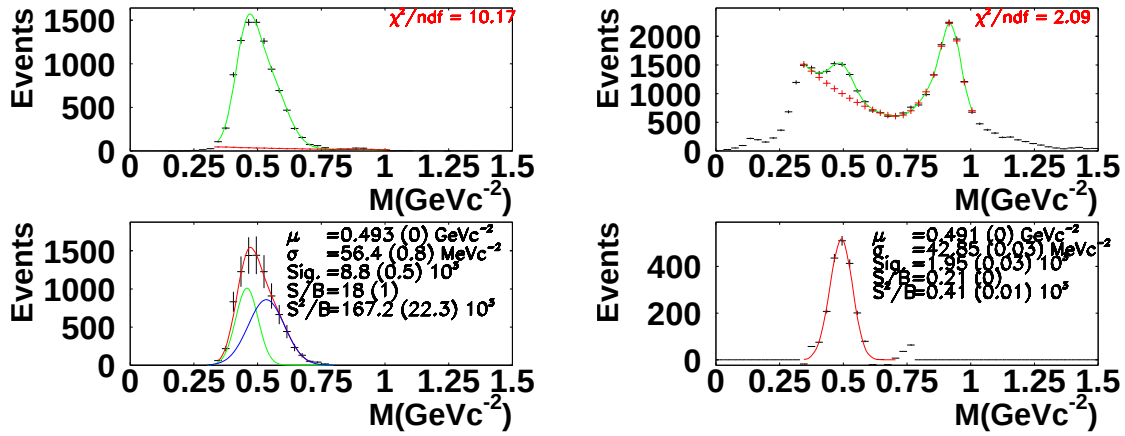


(a) (b)

Figure 3.19: Kaon mass distribution after refit and Λ selection. Left Narrow cut. Right wide cut

To obtain a better background description, the data are analysed in different bins of the kaon momentum, since the resolution of the momentum and the velocity depends on the particle momentum. Figure 3.20 shows the the kaon mass spectrum for different momentum slices. (a) is for a momentum between 0 GeV/c and 0.5 GeV/c. (b) is from 0.5 GeV/c to 0.7 GeV/c and (c) is for momenta above 0.7 GeV/c.

The distributions were fitted between a mass of 0.3 GeV/c$^2$ to 1 GeV/c$^2$. The total distri-

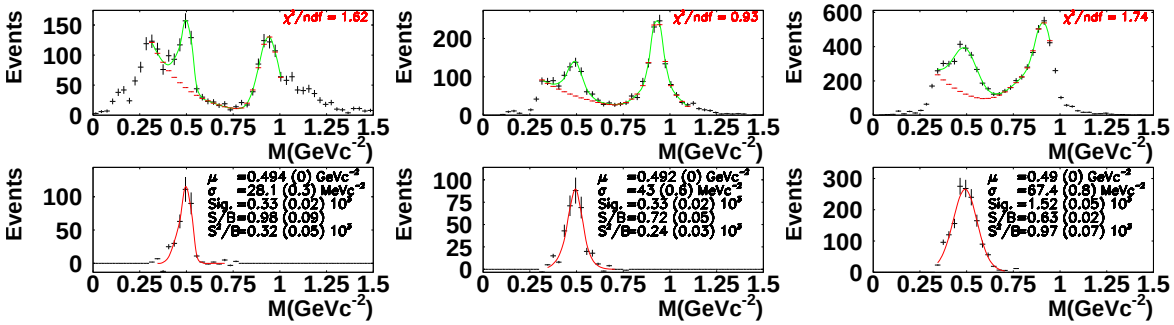


(a) (b) (c)

Figure 3.20: Kaon mass spectra for different bins of kaon momentum. (a) 0.0 - 0.5 GeV/c, (b) 0.5 - 0.6 GeV/c, (c) > 0.6 GeV/c.

bution is fitted by a sum of Gaussian functions, where the particles - the pion the kaon and the proton - are described by two Gaussian functions each. The green curve in Figure 3.20

shows the total fit function. The reduced $\chi^2$ values of the different fit functions are ranging from 0.8 to 1.9, which indicates a quite good description of the experimental distributions by the fitted function. The resulting background contribution from protons and pions is plotted by the red crosses in the same plots.
The lower plots in Figure 3.20 show the background subtracted kaon mass spectrum.
The achieved resolution, the $K^+$ signal and the signal to background values are listed in Table 3.4. The $K^+$ candidates are selected in a range of $m_K - \mu_{K,p} < 3\sigma_{K,p}$ in the corresponding

| Momentum Region | Signal ($10^3$) | S/B | $\mu_{K^+}$ (MeV/c$^2$) | $\sigma_{K^+}$ (MeV/c$^2$) |
|---|---|---|---|---|
| 0.0 - 0.5 GeV/c | 0.33 (0.02) | 0.98 (0.09) | 494.52 (0.02) | 28.1 (0.3) |
| 0.5 - 0.6 GeV/c | 0.33 (0.02) | 0.72 (0.05) | 492.01 (0.04) | 43.0 (0.6) |
| 0.6 - GeV/c | 1.52 (0.05) | 0.63 (0.02) | 499.78 (0.01) | 67.4 (0.8) |

Table 3.4: Results form Kaon spectra at different momenta regions. The listed value are the Signal of Kaons the Signal to Background ration (S/B) as well as the Kaon mass position ($\mu_{K^+}$ and the width of the signal ($\sigma_{K^+}$). The errors extracted from the fitting procedure are given in brackets.

momentum bin.

### 3.5.6 Sideband Technique

As shown in the previous paragraph after the selection of the $K^+$ a non negligible amount of background still remains. For the further steps of this analysis a better description of the background is needed.
Since this background is created by misidentification of protons and pions, we can model it by selecting an experimental sample, which consists of such kind of particles. This sample is selected in a region in which the amount of kaons can be neglected, i.e $m_K > |6\sigma_K|$.

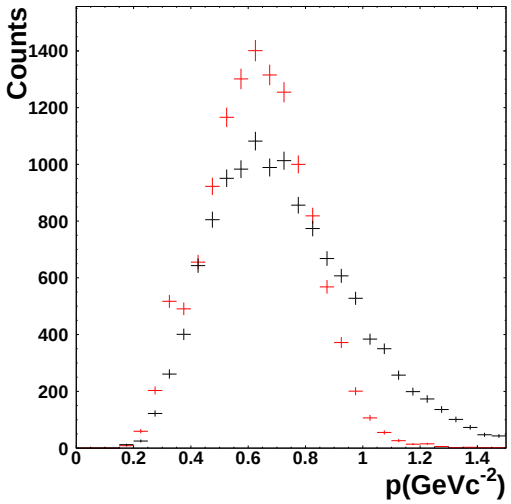


Figure 3.21: Momentum Distribution of the particles in the signal region (black crosses) and the of Momentum Comparison of Signal and Sideband.

Due to the different selected mass regions the momentum distribution is different - as shown in Figure 3.21 - for the signal region (back crosses) and the region in which the sideband sample is selected (red crosses). This effect has to be corrected by a weighting of the events in the sideband sample, such that the momentum in both regions are the same. According to Figure 3.21, sideband events with a particle momentum of 0.6 GeV/c have to be scaled by a factor lower than 1, while events with a particle momentum around 1 GeV/c are scaled by a factor bigger than 1.
By this method, we can describe the misidentified kaons in the signal region, by a sample of pure misidentified kaon in the sideband region.
After the correction of the momentum distribution the number of sideband events they is normalized to the amount of background events in the signal region. This number can be extracted from the signal and signal to background ratio, which was determined in the previous paragraph for the three different momentum slices. Thus three different background contributions are modeled, which can be summed to a total background distribution.
The correct functionality of this technique is tested by looking at the invariant mass distribution of proton-pions pairs - shown in Figure 3.22. The background distribution in this spectrum (red band) is extracted from the sideband sample. One can see that especially the distribution on the right side, which deviates from a Gaussian shape, can be described quite reasonably by the sideband background.

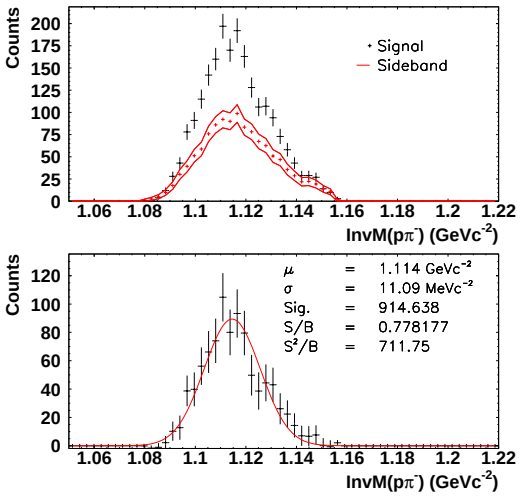


Figure 3.22: Invariant mass (p,$\pi^-$) spectrum (black crosses) with the sideband background (red band) (upper panel). The lower panel show the background subtracted signal fitted by an Gaussian function.

The lower plot in Figure 3.22 shows the background subtracted signal. It can be seen, that the signal quality has improved, with a signal width of 9.51 MeV/$c^2$ compared to the previous value of 12. MeV/$c^2$ (Figure 3.18(b))

### 3.5.7 Λ and $\Sigma^0$ Separation

After the extraction of the exclusive events and the background description method with the sideband sample, a further background contribution has to be studied.
Since the main decay channel of Σ goes into Λ and $\gamma$ (see reaction 3.9) the $\Sigma^0$ signal creates a background contribution that can not be suppressed by the $K^+$ and the Λ identification, since it differs just by an additional produced $\gamma$ particle, which cannot be measured by the FOPI spectrometer.
The only selection method which suppresses this background is the kinematical refit, since the assumption of energy and momentum conservation of the reaction p+p → p$K^+$ p $\pi^-$ is not fulfilled.
For the further analysis the amount of remaining background has to be checked.
The only channel in which the difference of the signal and the background from the Σ channel appears is the missing mass proton kaon channel, that is shown in Figure 3.23(a). The black crosses represent signal points. The red band shows the contribution of the background, which is the sum of the sideband background contribution in the three different momentum slices shown in the green, blue and yellow band.
Due to the available phase space, the missing mass values below 0.9 GeV/c$^2$ are not allowed physically. From Figure 3.23(a) it can be seen, that this region is reproduced quite well by the sideband background. The background subtracted signal is shown in Figure 3.23(b). Due

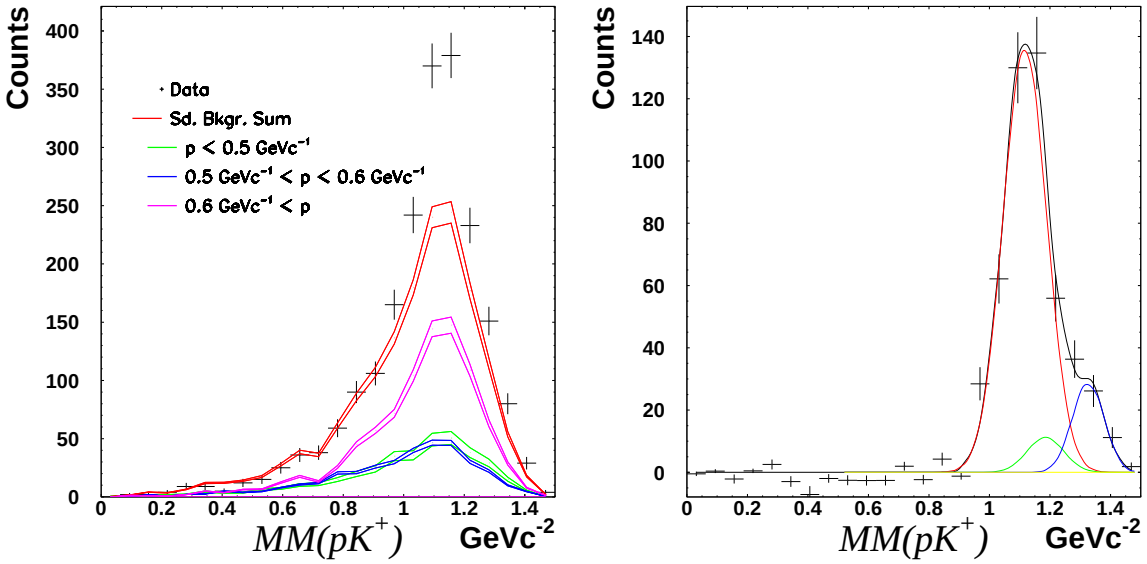


(a) (b)

Figure 3.23: Missing mass (p,$K^+$) with the contribution of the sideband background (a). The green, blue and pink lines show the distribution of the sideband background for the three different momentum slices. The red curve is the sum curve of all the three curves. In panel (b) the background subtracted spectrum is shown. The signal is fitted by an sum of three different Gaussian functions and a polynomial functions (s.text). The fit results are listed in Table 3.5

to the resolution, the Λ signal appears to be a quite broad peak, which also overlaps into the mass region of the Σ ($m_\Sigma$ = 1192 MeV/c$^2$). The contribution of the background can

be determined by fitting this spectrum by the sum of three different Gaussian functions and a polynomial function. The peak positions of the two Gaussian functions are fixed within a band of 5 MeV/c$^2$ around the nominal particle masses. The result of the fit can be seen in the same spectrum. The black curve shows the total fit function. The different coloured lines correspond to different partial functions of the fit. The negligible contribution of the polynomial function (yellow curve) shows a negligible amount of further background. The red curve corresponds to the contribution of $\Lambda$ and the green curve to the $\Sigma$. The blue curve represents a contribution, which might come from higher resonances, like $\Lambda(1405)$ or $\Sigma^*(1385)$. A more detailed identification is not possible due to resolution issues. The resulting fitting values are listed in Table 3.5.

| Particle | Mass | Fit $\mu$ | Fit $\sigma$ | Fit Amplitude |
|---|---|---|---|---|
| $\Lambda$ | 1115.8 | 1.1171 | 0.07 | 136.35 |
| $\Sigma^0$ | 1192.1 | 1.185 | 0.06 | 11.277 |
| higher Resonance contribution | | 1.32 | 0.05 | 28.8 |

Table 3.5: Fit results of background subtracted Missing Mass (p,$K^+$) spectrum.

From this method the remaining background contribution is extracted to be around 1/14.8. This shows, that the remaining background plays a minor role and will be neglected in the further analysis.

### 3.5.8 Final p$K^+\Lambda$ Sample

With the presented selection method the exclusive sample of p$K^+\Lambda$ can be extracted quite well. The method of the sideband technique allows a sufficient description of the background. In Figure 3.24 the missing mass distributions of the proton (a), the $\Lambda$ (b) and the $K^+$ are shown. The black crosses are the signal points. The turquoise band shows the total contribution of the background extracted from the sideband sample. The total amount of the

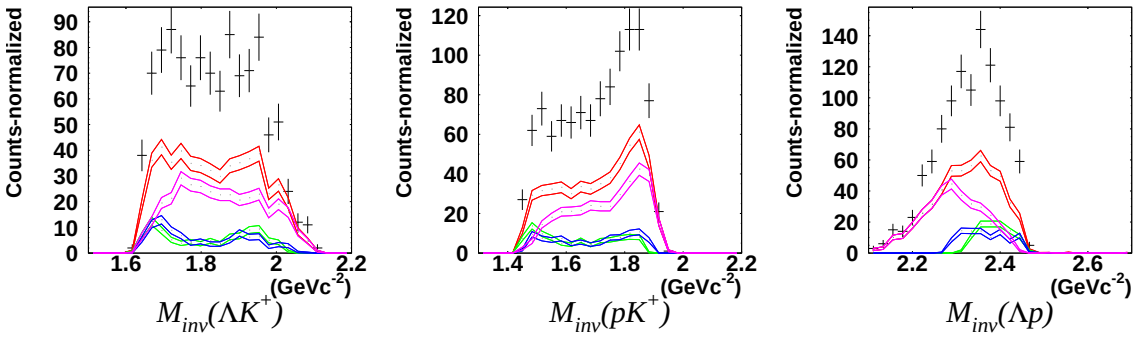


(a) (b) (c)

Figure 3.24: Missing mass distribution of the proton (a), the $\Lambda$ (b) and the Kaon (c). The black crosses show are the signal points. The colored show the distribution of the sideband background for the momentum range 0-0.5 GeV/c(green), 0.5-0.6 GeV/c(blue) and $\geq$0.6 (violet). The red band is the sum of all background distributions.

reconstructed p$K^+\Lambda$ and the background is listed in Table 3.6 for each momentum slices.

| Momentum Region | Signal Events | Background Events |
|---|---|---|
| 0.0 - 0.5 GeV/c | 177 | 146 |
| 0.5 - 0.6 GeV/c | 150 | 136 |
| 0.6 - GeV/c | 577 | 577 |
| Total | 903 | 859 |

Table 3.6: Results for signal and background for the p$K^+\Lambda$ final state in different momentum bins.

For the further analysis steps and the comparison of the data with different simulations, it is necessary to subtract the background. The resulting mass spectra are shown in Figure 3.25.

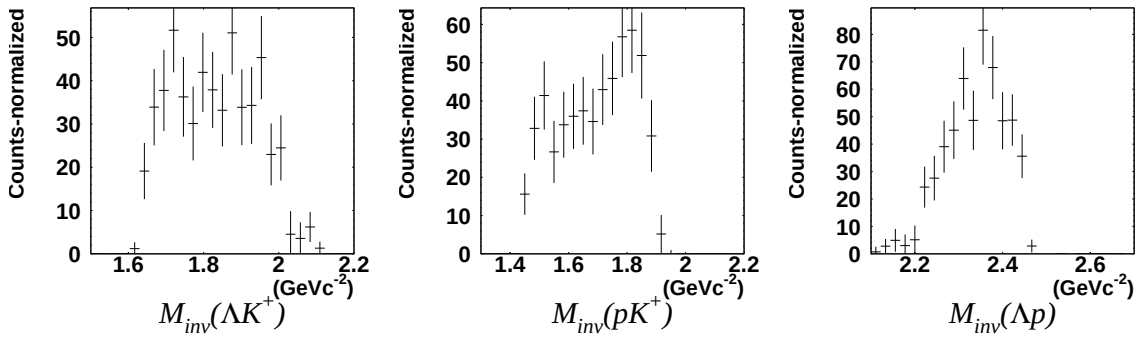


(a) (b) (c)

Figure 3.25: Missing mass distribution of the proton (a), the $\Lambda$ (b) and the Kaon (c). The black crosses show the experimental data points after the background is subtracted.

# Chapter IV

# Simulation

## 4.1 Introduction

Simulations play a very important role in hadron physics. On the one hand they serve as a cross check for the detector response. With the help of simulations different particle reactions can be modelled, which allow to extract information about the acceptance of the detector for certain physic processes. In the present work simulations were used to study the acceptance of the $\Lambda$ trigger SiΛViO for reactions, in which a $\Lambda$ particle is produced and for background reactions (see Paragraph 2.11.4). Furthermore simulations are used as cross-check for performance of the $\Lambda$ trigger, which is described in Section 5.2.
On the other hand simulations are necessary tools for the understanding of the physics processes. The particles, which are produced in reactions are emitted in the full phase-space region. Since the FOPI spectrometer does not cover the full solid angle with the same detection efficiency, the extracted signal does not describe the full reaction, which complicates the extraction of physical information from the experimental spectrum. For a sufficient comparison of the simulation with different theoretical model predictions, the modelled reaction processes have to be filtered by the acceptance and efficiency of the whole FOPI detector using the simulation framework. After the reaction process is filtered, the same analysis as for the experimental data is applied to the simulated data to select the exclusive final state.
In the following chapter the different parts of the simulation framework will be explained, beginning with the used event generators - Section 4.2 - by which different physical processes can be modeled; followed by the FOPI GEANT framework, which allows to model the behavior of the different detector systems, used in the FOPI spectrometer. This framework has to be adjusted to allow a good reproduction of the experimental data. The tuning and adjustment of the simulation package is shown in Section 4.3

## 4.2 Event Generators

The first step of the simulation is the modelling of physical processes. For the simulation in this work two different packages were used. The event generator PLUTO, which is able to simulate different user-defined exclusive reactions separately. By the Ultra relativistic Quantum Molecular Dynamics (UrQMD) transport model the full reaction of proton proton reaction is simulated based on transport theory.
Both simulations are generating an event-based list of produced particles with their physical

properties.

### Pluto - Event generator

The PLUTO event generator - developed for the HADES experiment [FCG+07,FGH+10] - is a generator phase space reaction of specific exclusive reaction channels. In our case different channels, which may contribute to the p$K^+\Lambda$ final state were simulated. The advantage of the PLUTO event generator is that input parameters like branching ratios are adjustable, which allows to simulate only user-defined channels.
The following reactions were simulated:

$p + p \rightarrow p + K^+ + \Lambda$ Dalitz Production of $p + K^+ + \Lambda$,

$p + p \rightarrow p + N^{+*}(\rightarrow K^+ + \Lambda)$ Production via an in intermediate $N^{*,+}$ resonance,

$p + p \rightarrow p + K^+ + \Sigma^0$ Background Channel,

$p + p \rightarrow K^+ + ppK^-(\rightarrow \mathbf{\Lambda} + p)$ Production of pp$K^-$ .

The used $N^*$ resonances with their properties are listed in Table 4.1 as well as the properties of the simulated pp$K^-$ [YA07]. The values for the $N^*$ resonances are not exactly known. For that reason average values for [B+12] were taken.

| Resonance | Mass (GeV/c$^2$) | Width (GeV/c$^2$) |
|---|---|---|
| $N^*$ (1650) | 1.655 | 0.165 |
| $N^*$ (1700) | 1.700 | 0.200 |
| $N^*$ (1900) | 1.900 | 0.340 |
| $N^*$ (2190) | 2.190 | 0.400 |
| pp$K^-$ | 2.322 | 0.060 |

Table 4.1: List of resonance. For the $N^*$ resonance average value for [B+12] were taken. The value for pp$K^-$ are taken from [YA07].

### Angular Distributions

The events generated by PLUTO are isotropically distributed in phase-space, e.g. no angular correlation between the particles is included. According to experimental findings [Epp14, AB+10] this model is not realistic, since the particles are not emitted isotropically, due to effects like final state interaction.
To account for such angular distributions the PLUTO simulations have to be weighted with the angular distribution. These are taken from measured data of the COSY-TOF and the HADES experiment [Epp14, AB+10]. The weighting factor for the reaction p+p→p$K^+\Lambda$ was taken from the results of the COSY-TOF experiment. The weighting for the reaction $p + p \rightarrow N^{+,*} + p \rightarrow K^+ + \Lambda + p$ for different $N^{*,+}$ resonances were taken from the HADES results. It has to be taken into account, that these results are for different energies of the protons. In spite of the fact that COSY-TOF results stated a rather weak energy dependence, it might become more dominant at our energies or the energies of the HADES experiment. Due to the lack of a suitable model for the energy dependence, we apply the same angular

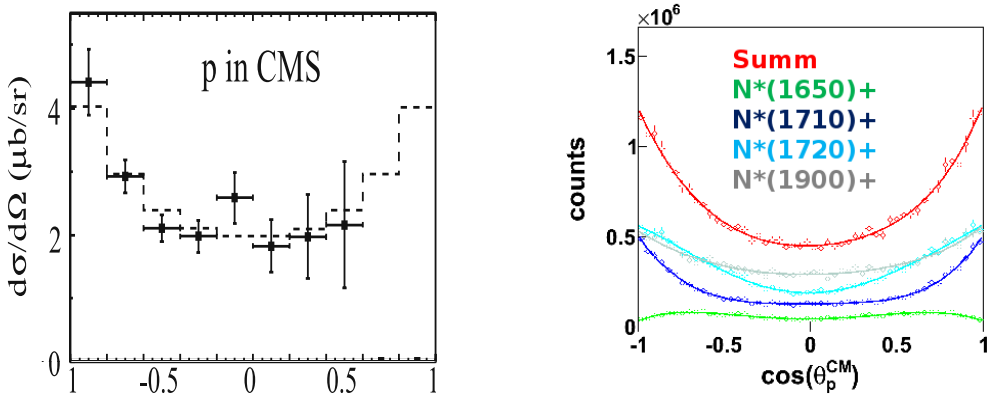


(a) (b)

Figure 4.1: Angular distribution of proton in the Center of Mass System, for the direct p$K^+\Lambda$ production [AB$^+$10] and the production via $N^*$ resonances of different mass (b) [Epp14].

| Channel | $a_0$ | $a_2$ | $a_4$ |
|---|---|---|---|
| p$K^+\Lambda$ | 953.098 | +757.042 | +126.776 |
| $N^*(1650)$ | 62000 | 8340 | -38000 |
| $N^*(1700)$ | 210000 | 223000 | 77100 |
| $N^*(1900)$ | 360000 | 165000 | 19900 |

Table 4.2: Legendre Coefficients for $\theta_{CMS,p}$ used in simulation. Value for p$K^+\Lambda$ taken from [AB$^+$10] and for $N^*$ resonances [Epp14].

dependence for our energy. Figure 4.1 shows the polar angle of protons for different reaction in the center of mass frame. The spectra are fitted by a sum of Legendre polynomials:

$$F(x) = a_0 * 1 + a_2 \left\{ \frac{1}{2} \left(3x^2 - 1\right) \right\} + a_4 \left\{ \frac{1}{8} \left(35x^4 - 30x^2 + 3\right) \right\} \qquad x = cos(\theta_{p,cms}). \quad (4.1)$$

The resulting parameters for $a_0, a_2, a_4$ are listed in Table 4.2. This parametrisation of the angular distribution is also used for the weighting of the PLUTO simulations.

### UrQMD- Event generator

The Ultra relativistic Quantum Molecular Dynamics model is a microscopic model which is mostly used to simulate (ultra)relativistic heavy ion collisions. The goal of UrQMD is the description of hadrons in nuclear matter [Gro13b]. Nevertheless, it may provide also an adequate tool to describe elementary reactions.
Transport models in general describe the full reaction of a collision of two nuclei on the base of nucleon-nucleon reactions. These are determined on small time intervals taking into account scattering cross sections, particle productions and various potentials. These are taken on

the one hand from experimental results and on the other hand - if they are not known from experiments - are deduced from certain model assumptions.
Transport calculation based on Quantum Molecular Dynamics (QMD) model [Aic91,HPA+98] are n-body calculations, which allow an event by event simulation. Each participating nucleon is described by the following wave-function:

$$\phi_i(\vec{x}_i,t) = \left(\frac{2}{L\pi}\right)^{\frac{3}{4}} \exp\left\{-(\vec{x}_i - \vec{r}_i(t))^2/L\right\} \cdot \exp\left\{i\vec{x}_i\vec{p}_i(t)\right\}, \tag{4.2}$$

with six time-dependent parameters $\vec{r}_i$ and $\vec{p}_i$ and a fixed parameter $L$ describing the extension of the wave packet in phase space. The total n-body wave function is the direct product of the single nucleon wave functions:

$$\Phi(\vec{x}_i,t) = \prod_i \phi(\vec{x}_i,\vec{r}_i,\vec{p}_i,t). \tag{4.3}$$

The aim of this approach is to describe all particle correlations. However, quantum correlations, originating from the anti symmetrization of the wave function $\Phi(\vec{x}_i,t)$, are not taken into account. The UrQMD model [WBB+96] describes ultra-relativistic heavy-ion collisions. About 50 different baryon species like nucleons, deltas, hyperons and their resonances (with masses up to 2.11 GeV/c$^2$) and 25 meson species are taken into account in the model [Mer04]. Due to this microscopic decay model used in the UrQMD transport model, the production of the final state p$K^+\Lambda$ is realized via the production of intermediate resonances which are produced in two body reactions [SGH+98, BZS+99].

## 4.3 The FOPI GEANT Framework

The output of different physical reactions is modelled by the event generator in the full phase space. Since this reaction is measured by the spectrometer in the acceptance of the sub detector with a certain efficiency and resolution, these effects have to be modelled in the simulation. This is done by the FOPI Simulation framework - based on GEANT3 [CER95]. In this environment the whole spectrometer is implemented in a way, which describes the real detector behavior in best possible way. The first step is a proper implementation of the geometry of all sub detectors, their volumes and their materials in GEANT, as well as the full target system. As a second step, the detector response has to be implemented in GEANT. In this step the resolution and the efficiency has to be implemented and adjusted to experimental data [Ben07].
For most of the detectors these steps have already been done for previous experiments. For the proton proton experiment a set of parameters have to be adjusted to optimize the description of the data. In Paragraph 4.3.1 the adjustment of the particle selection is shown. To provide a quite realistic track reconstruction in the Helitron, the track resolution had to be adjusted (4.3.2) accordingly.
Finally the different reconstruction efficiency of the Helitron and the CDC has to be corrected in the simulation, as well as the matching efficiency of CDC-RPC system (4.3.3).

### 4.3.1 Cut Tuning

Due to the different resolution in Data and Simulation the particle cuts of the proton and pions have to be adjusted in the simulation.
Starting from the cuts for the experimental data, these are modified in two steps. In the first step the effect of no perfect tracking is compensated. Due to this effect the distributions of the reconstructed particles - momentum versus velocity or energy loss versus momentum - are shifted against the nominal mass line in the momentum-velocity or the energy loss-momentum frame. Since the experimental and simulated distributions are shifted with respect to each other, correction factors have to be determined. For this procedure the simulation

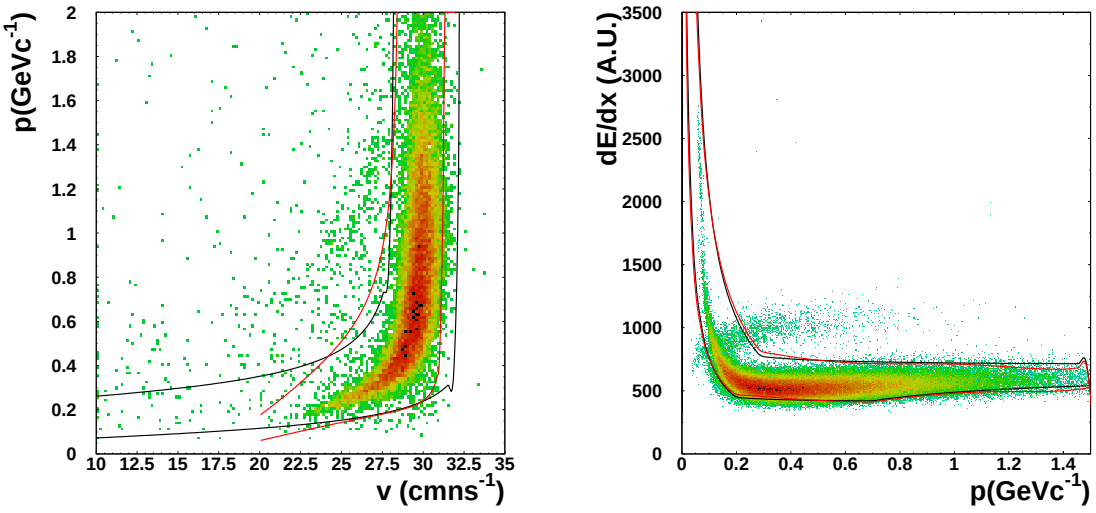


(a) (b)

Figure 4.2: Selection cuts for negative pions in the forward hemisphere (a) by the momentum versus velocity spectrum and the backward hemisphere (b) by the energy-loss versus momentum frame - The black curve shows the borders for the selection of the experimental data. The red curve mark the adjusted cut borders for the simulated data.

and experimental data are divided into different bins of particle momenta. For each particle momentum the peak position and the width of the protons and the pions is determined. From this extracted value a correction factor for the selection boarder of the simulation can be obtained, which allows the selection of the same amount of particles in data and simulation. In Figure 4.2 and Figure 4.3 the two dimensional spectra for the particle identification are shown for pions and protons, respectively. The spectra show simulation data. The black lines indicate the selection boarder for the experimental data. The red lines are the modified boarders for the selection of simulation data.

### 4.3.2 Helitron Track Resolution

For the proton-proton experiment the Helitron plays an important role in the analysis. For the reliability on the momentum reconstruction in the simulation the resolution of the hit point detection has to be adjusted. Since the Helitron was not used for momentum reconstruction in previous experiments, the simulation was not optimized for that purpose, e.g. the track

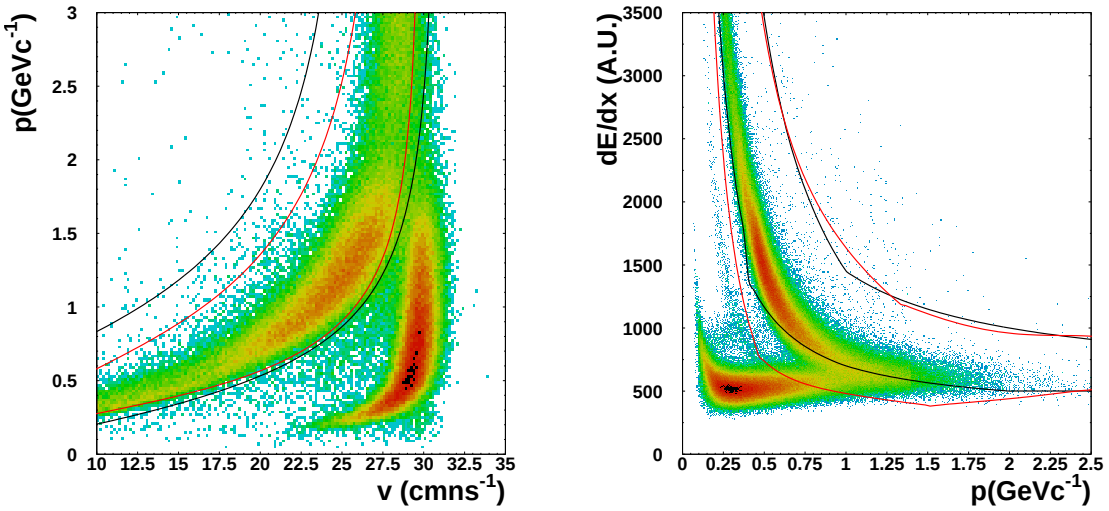


(a) (b)

Figure 4.3: Selection cuts for protons in the forward hemisphere (a) by the momentum versus velocity spectrum and the backward hemisphere (b) by the energy-loss versus momentum frame - The black curve shows the borders for the selection of the experimental data. The red curve mark the adjusted borders for the simulated data.

resolution in the simulation package was around a factor 10 better than in the experiment. The position along the sense wire in the Helitron is measured by the charge division (Equation 2.16) and the distance from the sense wire by the drift time (Equation 2.13). The resolution of the two coordinates can be changed by modifying the measured drift time $t_{\text{drift}}$ of the Helitron according to Equation 4.4 and the measured charge value $(q_i,q_o)$[1] according to Equation 4.5. The factor $r_{\text{gaussian}}$ is a random number weighted by a gaussian function with a mean position of $\mu = 0$ and a width $\sigma = 1$. This random value is scaled by an adjustable parameter $\sigma_{\text{drift time}}, \sigma_{\text{charge}}$.

$$t'_{\text{drift}}[ns] = t_{\text{drift}}[ns] + r_{\text{gaussian}} \cdot \sigma_{\text{drift time}}[ns], \tag{4.4}$$

$$q'_{i,o}[C] = q_{i,o}[C] + r_{\text{gaussian}} \cdot \sqrt{q_i[C] + q_o[C]}\sigma_{\text{charge}}. \tag{4.5}$$

The resolution of the hit points in the Helitron is determined by a fitting procedure (see Section B). After the track has been reconstructed, the track-point residuals are determined by Equation 4.6 [Ple99]

$$\sigma_a = \sqrt{\frac{\sum_{i=1}^{N}(a_{fit} - a_{measured})_i^2}{N_{Hits}}} \qquad a = (x_{DZ} \text{ or } y_{LT}), \tag{4.6}$$

with the measured position of the hit $a_{measured}$ and the position of the hit-point according to the fit results $a_{fit}$. The residuum is calculated for the distance to the wire $x_{DZ}$ and for the position along the wire $y_{LT}$. The distribution of $\sigma_{Hit}$ is shown in Figure 4.4 for the two different

[1] The sense wire of the Helitron are read out from both sides. From the two different charge measurement $q_i$,$q_o$ the hit position on the wire is determined (2.5.1)

coordinates ($x_{DZ}$ (a) / $y_{LT}$ (b)). The black curve shows the distribution of the data. The distribution for simulation (red curve) was obtained by setting the scaling factor of the random gaussian function to the the following values: $\sigma_{\text{drift time}} = 50ns$, $\sigma_{\text{charge}} = 1.2\sqrt{C}$. By these random gaussian smearing the peak position of the distributions were set to the same position.

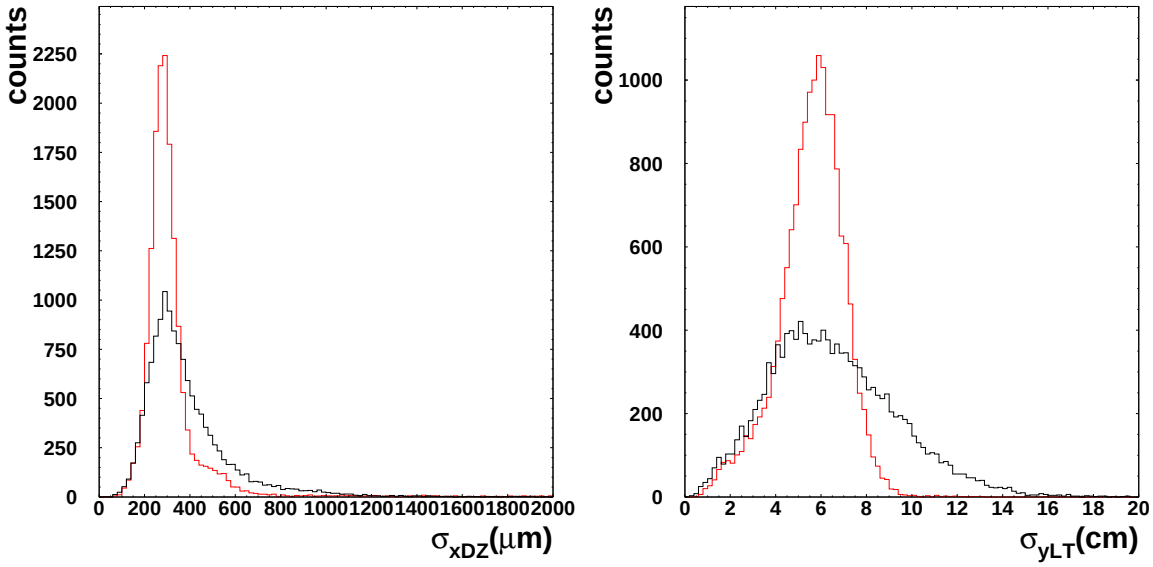


(a) (b)

Figure 4.4: Helitron track-point residua in the direction perpendicular to the sense wire (a) and along the sense wire (b) according to Equation 4.6. The black curve corresponds to experimental data and the read curve to simulation data after the tuning.

### 4.3.3 Efficiency Scaling

After the adjustment of the selection cut and the hit resolution, the most important step is the adjustment of the reconstruction efficiency of the different subsystems.
Due to numerous different effect, for example boarder effects, aging, etc. , the reconstruction efficiency of the different detectors inside FOPI is not homogeneous in the whole acceptance region and for different particle momenta. These different effects have to be included properly in the simulation.

For the comparison of the experimental and simulation data a sub sample has to be selected, for which a proper normalization can be applied. This can be done for the elastic proton proton events,explained in Section 3.3, since this sample has a negligible amount of background. Due to this reason the simulation and experimental data can be both normalized to the number of LVL1 Trigger events and the total efficiency can be determined.
In Figure 4.5 the polar angle distributions for particles detected in Helitron and SiΛViO (a), in Helitron only (b) and the CDC (c) are shown. The simulation data (red crosses) are scaled by the factor

$$N = \frac{N_{\text{LVL1 Trigger event experimental data}}}{N_{\text{LVL1 Trigger events simulation data}}}$$

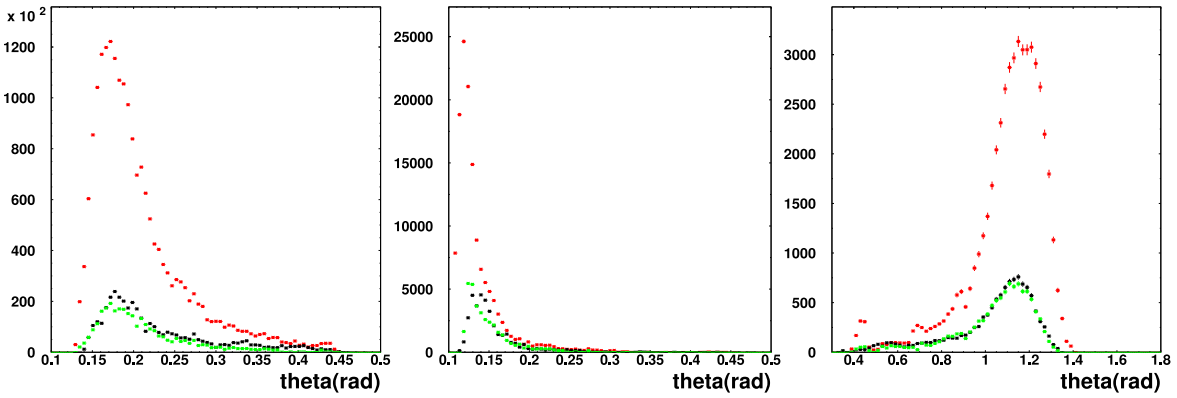


(a) (b) (c)

Figure 4.5: Polar angle Distribution for experimental data (black crosses) and simulation data (red crosses). The picture show the distribution for elastics scattered protons, which are measured by SiΛViO and Helitron (a), Helitron only (b) or the CDC (c). The green crosses show the simulation data after the efficiency correction was applied.

to the experimental data (black crosses). The spectra for all parameter ($\theta, \phi$,momentum) are shown in Appendix E.

From these pictures the difference in the reconstruction efficiency for experimental and simulation data can be extracted. Since the efficiency is higher in simulation package, this effect has to be included.

By dividing the experimental spectra by the simulated distribution, one can obtain a correction factor (CF) as a function of the kinematic variables $\theta$, $\phi$ and p: CF($\theta$),CF($\phi$),CF(p). While the distribution of CF($\phi$) is nearly constant, the correction factor has a strong dependence upon $\theta$ and the momentum. For this reason a total correction function depending on $\theta$ and p was obtained: see Equation 4.7

$$CF_{total}(\theta, p) = \sqrt{CF_{\theta}(\theta) \cdot CF_{p}(p)} \tag{4.7}$$

Due to statistical reasons, the correction factor cannot be determined double differentially in both coordinates. For that reason the total correction factor is a convolution of the correction factor in $\theta$ and p.

This efficiency correction was implemented on the track level in the simulation. After the tracks are reconstructed in the sub detector, the efficiency correction is applied. For each track the $CF_{total}$ factor is determined according to its polar angle and momentum. The track is discarded under the condition, that the efficiency factor is lower than the value $rand_{0,1}$[2]. After this selection a new sub sample of elastic scattered protons can be created for the simulation data. The resulting corrected distributions are shown in the corresponding histograms (Figure 4.6) by the green crosses.

In a second step the matching efficiency of the RPC has also to be adjusted. This is done by the same methods like in the case of the tracking efficiency. In Figure 4.6 the matching efficiency of the RPC is plotted versus the particle momentum (c) and the polar angle (a) for experimental data (black crosses) and simulation data (red crosses). The green crosses represent the matching efficiency for the efficiency corrected sub sample.

[2] $rand_{0,1}$: Random distributed value between 0 and 1 with equal probability, generated for each track.

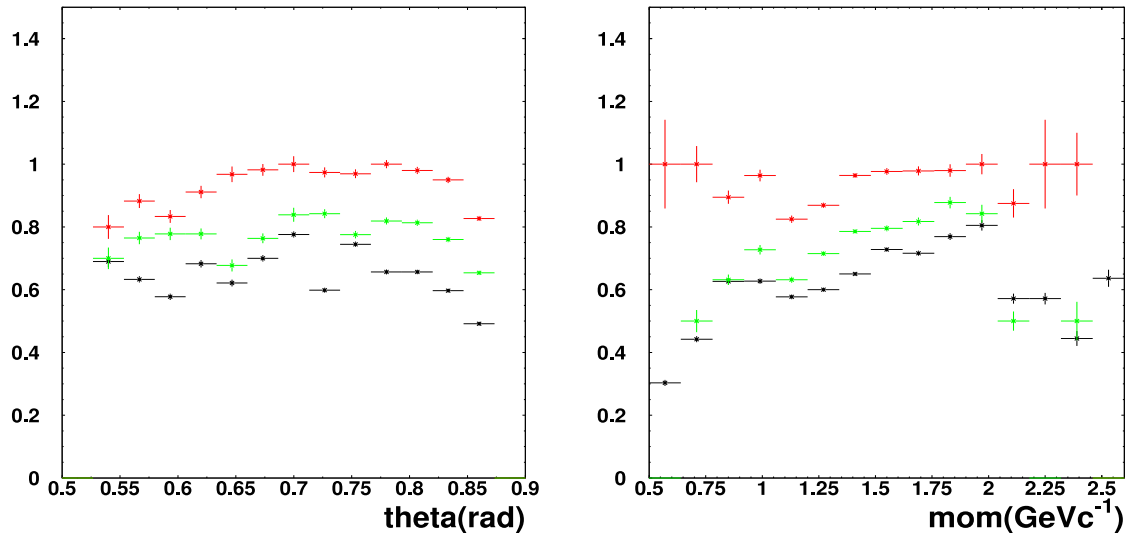


(a) (b)

Figure 4.6: Matching efficiency of the RPC with CDC versus the polar angle (a) and the particle momentum (b). The value for the experimental data are shown by the black crosses, the values for the simulation data are represented by the red crosses.The green crosses show the simulation data after the efficiency correction was applied.

From all these spectra a good overlap of the data and simulation is visible, which is sufficient for our data analysis. Also the comparison of the matching efficiency (Figure 4.6) shows an sufficient overlap of data an simulation.

### 4.3.4 Data - Simulation Comparison

The quality of the corrections can be verified by comparing the resulting invariant mass spectrum of proton and pion - explained in Section 3.4 - of experimental and simulation data. The spectra are shown in Figure 4.7. In that figure the simulation data are shown in (a) and the experimental data on (b).

The extracted results for the $\Lambda$ peak are listed in Table 4.3. The peak position and the mass resolution of the $\Lambda$ particle are comparable in simulation and experimental data. Both spectra just differ in the amount of background beneath the $\Lambda$ signal. The reason for this discrepancy originates from the fact, that in the experimental data more background events are present than in simulation. Those background events have different origins, e.g. off vertex events.

| | Peak Position [GeV/c$^2$] | Width [MeV/c$^2$] | S/B |
|---|---|---|---|
| Simulation data | 1.113 | 5.6 | 0.88 |
| Experimental data | 1.114 | 5.3 | 0.24 |

Table 4.3: Results of Fit of $\Lambda$ Spectrum.

For the comparison of the experimental and the simulated data for the exclusive reaction $pp \to pK^+\Lambda$ this difference in the background can be neglected since the the exclusive signal

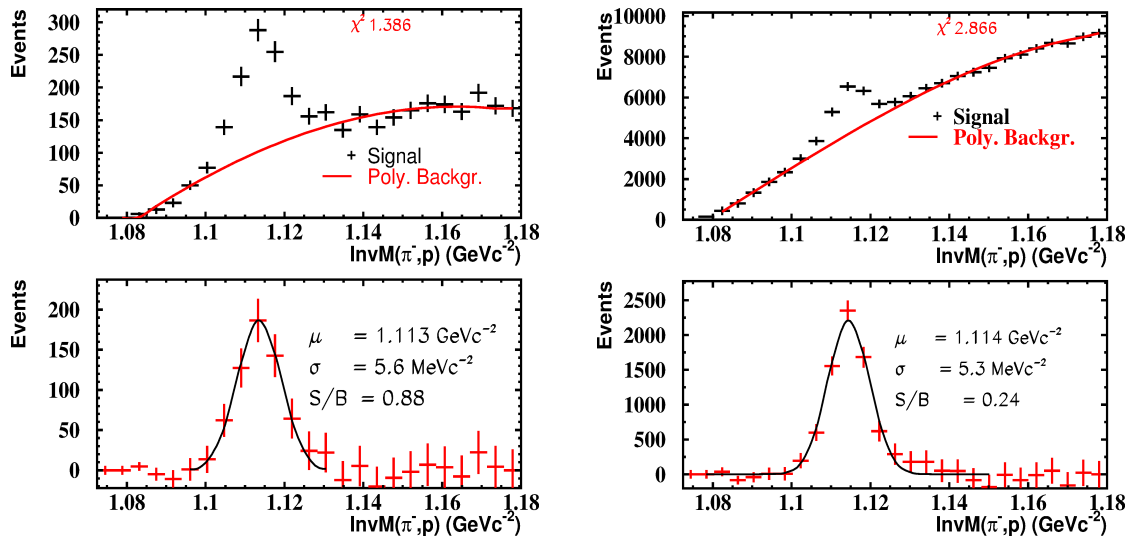


(a) (b)

Figure 4.7: Invariant mass of the $p - \pi^-$ ($\pi^-$ measured in CDC, p in Helitron) pairs from UrQMD simulation (a) and from data (b). Reconstruction is explained in Section 3.4

can be extracted, without background (see Section 3.5).

# Chapter V

# SiΛViO Performance

The trigger system SiΛViO was built for the proton-proton run at 3.1 GeV at FOPI. Beside the improvement of the tracking, which is described in Paragraph 3.1.2, the trigger was built to suppress background events. Such kind of events could originate from two different sources:

**Off target Events:** Background events induced by particles, which are not coming from the target. The origin of such events and the suppression by SiΛViO is discussed in Section 5.1

**Background p-p Events:** Background events, which originate from proton-proton reactions inside of the target volume without strangeness production. The suppression is discussed in Section 5.1

The basic idea about the trigger concept of SiΛViO is explained in Section 2.10.

## 5.1 Target Enhancement

The proton beam from the accelerator is guided inside a vacuum pipe to the FOPI spectrometer. Due to the fact, that beam particles are bended out from the original trajectory, surrounding material can be hit.
In the case that happens near to the FOPI spectrometer those particles could also fly through some sub detector and create a sufficient signal, that a readout signal is triggered.
The FOPI spectrometer was built to investigate heavy ion reactions. In such kind of reactions the amount of charge particles in a collision is quite high. For the selection of events of interest, the required multiplicity of detected particles in the trigger detectors must be sufficiently high. This trigger selection also leads to a suppression of off-vertex reactions.
In the case of proton-proton reactions the particle multiplicity per event is quite low on average. Thus, the requested multiplicity has to be lower (see Section 2.11), which reduced the capability of off-vertex suppression significantly. The ratio of off-vertex reactions was determined comparing the trigger ratio of the experiment with the target and without the target. In Table 5.1 the trigger ratio normalized to the total amount of beam particles is listed. From these data one can see, that the number of off-vertex reactions is quite high ($80.9 \pm 1.3\%$) for the first-level trigger condition.
A sufficient suppression of such reactions could be achieved by the inclusion of the $\Lambda$ -trigger

to the trigger selection. By this the amount of recorded off-vertex reactions was reduced to $10.4 \pm 1.1\%$.

| Trigger per Beam particle | LVL1 | LVL2 |
|---|---|---|
| Target | $(3.1 \pm 0.1) \cdot 10^{-3}$ | $(3.8 \pm 0.1) \cdot 10^{-4}$ |
| No target | $(2.6 \pm 0.1) \cdot 10^{-3}$ | $(3.9 \pm 0.1) \cdot 10^{-5}$ |
| Ratio | $(80.9 \pm 1.3)\%$ | $(10.4 \pm 1.1)$ % |

Table 5.1: Amount of trigger per beam particles for the LVL1 and LVL2 triggers, respectively. The last row shows the ratio of target and no-target rates.

## 5.2 Λ Enhancement

To determine the experimental enhancement of the Λ signal reached with the LVL2 settings, the reconstructed Λ signal per event for the LVL2 and the LVL1 trigger conditions was extracted and compared. For this purpose, Λ -hyperons were reconstructed in both data samples. Due to a low amount of statistics of LVL1 events a wider selection cut [1] was used to enhance the signal.

| Signal per Event ($\cdot 10^{-4}$) | LVL1 | LVL2 |
|---|---|---|
| Data | $0.17 \pm 0.09(stat)^{+0.02}_{-0.06}$ | $2.36 \pm 0.05(stat)^{+0.23}_{-0.31}$ |
| pp Simulation | $0.52 \pm 0.09(stat)^{+0.04}_{-0.01}$ | $1.68 \pm 0.36(stat)^{+0.39}_{-0.06}$ |

Table 5.2: Number of reconstructed Λ per event for the LVL1 and LVL2 event samples. The values are corrected for the "no target" events (see Table 5.1 and text for details).

Figure 5.1 shows the resulting invariant mass plot obtained for the LVL1 (left panel) and LVL2 (right panel) samples, respectively. Due to the less stringent cut conditions, the width of the signal increased slightly with respect to the results discussed in Section 3.4 from 5.3 MeV/c$^2$ to 6.0 MeV/c$^2$, while the signal to background ratio stays quite stable at a value of 0.24. The signal yield was extracted by integrating the distribution in a $3\sigma$ interval around the fitted mean value $\mu$. One can see that the Λ signal is barely visible for the LVL1 events, even if Figure 5.1 corresponds to the total collected statistics; indeed the signal to background for the reconstructed Λ goes down to 0.13. For this reason only a lower limit of the Λ -enhancement factor can be calculated. In Table 5.2 the number of reconstructed Λ candidates per event for the LVL1 and LVL2 samples are shown. The systematical errors were obtained by varying the reconstruction cuts within ±10%. One can see that the number of the reconstructed Λ in the experimental and in the simulations data is in agreement within the error. Possible differences might arise from the uncertainty of the total production cross-section in the simulations, hence one should focus more on the comparison of the ratios. From these resulting values the enhancement is finally obtained by dividing the signal per event of LVL2 and LVL1 triggers. The LVL2 to LVL1 enhancement obtained from the experimental data is $14.1 \pm 7.9(stat)^{+4.3}_{-0.6}$, where the statistical error is originating from the scarce statistics of reconstructed Λ for the LVL1 trigger. The LVL2 to LVL1 enhancement factor obtained from

[1] The selection cuts shown in Table 3.2 were used. The selection cut of dr was modified to dr $>$ 1.0 cm

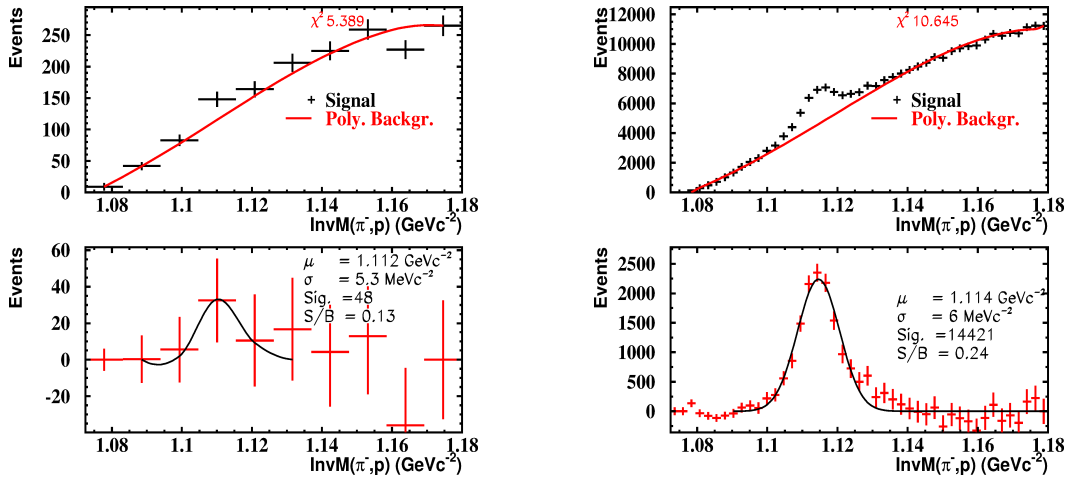


(a) (b)

Figure 5.1: Invariant mass of proton and pion for p$K^+\Lambda$ LVL1 (a) and LVL2 (b) trigger condition. The black crosses in the upper picture show the signal and the red line shows the fitted polynomial background. The lower pictures show the background subtracted signal.

UrQMD simulation is $3.40 \pm 0.59(stat)^{+0.34}_{-0.19}$ which is in good agreement with the enhancement of the pure geometrical acceptance (see Paragraph 2.11.4).
The discrepancy between the enhancement value in experimental and simulation data originates from the fact the in the experimental data the amount of off-vertex events is different in the LVL1 and LVL2 data - as shown in the previous section. This effect requires a correction of the result extracted from simulation data. After the correction the enhancement value of $\Lambda$ in simulation is $15.9 \pm 2.8(stat)^{+5.4}_{-0.5}$, which is in good agreement with the experimental data [MBF+14].
This way the performances of the LVL2 trigger have been proven and quantitatively verified.

# Chapter VI

# Physics Analysis

In the following chapter the method to achieve a quantitative description of the experimental data is presented.
The goal of this work is to extract information about the existences of kaon bound states pp$K^-$. In the in reaction p+p$\rightarrow$ $K^+$ + pp$K^-$ ($\rightarrow \Lambda$ + p) a signature should be visible in the spectrum of the invariant mass of p and $\Lambda$ - shown in Figure 6.1- where the region, in which a signal is expected is marked by the red shaded area.

Although the spectrum does not show a clear peak structure the existences of the pp$K^-$

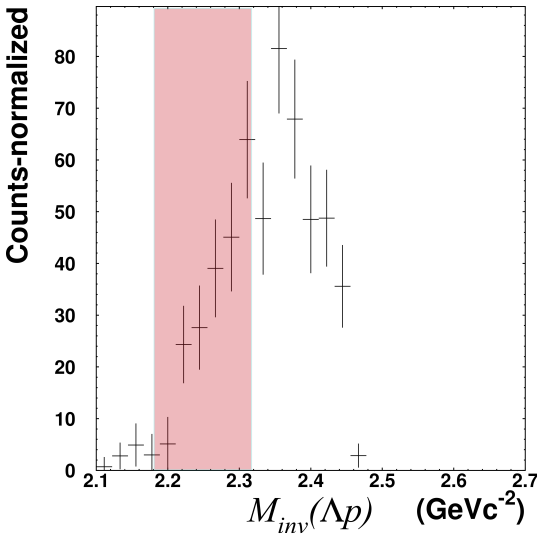


Figure 6.1: Invariant Mass of $\Lambda$ and Proton. The red shad ed area is the mass region of the expected pp$K^-$ signal.

can not be simply ruled out. From theoretical predictions it is not clear, which width one would expect for the pp$K^-$ [DHW09, SGM07, IS09, Gal11]. Since the extracted statistics of p$K^+\Lambda$ events is not very high, a pp$K^-$ with a broad width would not be clearly visible in this spectrum. From this point of view the experimental can used to determine an upper limit for the production of the pp$K^-$ bound state.
Before we can evaluate this upper limit determine the different sources contributing to the p$K^+\Lambda$ final state have to be determined. As it was shown in Section 1.5 the final state of

p$K^+\Lambda$ can be populated via different production mechanisms. In order to model the different sources as good as possible several kinematical observables are introduced (Section 6.1), which allows a complete description of the reaction kinematics.
In the following, the comparison of the experimental results with different simulations is shown. In Section 6.2 the comparison with the phase space simulation of different channels is presented, followed by the comparison with UrQMD transport model simulation (Section 6.3). A further attempt is presented in Section 6.4. In this the experimental data are described by the results of an Partial Wave Analysis. Based on this description the upper limit for the pp$K^-$ is extracted in Section 6.5.

## 6.1 Observables

In order to allow a comparison of the experimental and the simulated data, a set of observables is needed, which describes the kinematics of the reaction process. In the following section the different observables and their distributions for different production mechanism is discussed. All channels are simulated both isotropically and an - as far as known - angular distribution (see 4.2).

### 6.1.1 Invariant and Missing Mass

In the invariant and missing mass spectra intermediate resonances are visible. Since the reaction events fulfill the energy and momentum conservation, it is redundant to plot the invariant and missing mass spectra at the same time.
In Figure 6.2 (a)-(c) the invariant mass distributions for the three different particle combination are shown. These distributions originate from phase space simulations, created with the Pluto package, before the filtering through the detector acceptance and efficiency. These spectra represent the distributions for particle emitted in the full phase space.
The different colors are corresponding in all the panels to the different simulated channels. While the distribution of the phase space production of p$K^+\Lambda$ (pink line) does not show an evident structure in the three different spectra, the different $N^*$ channels have a quite significant structure. The peak position in the invariant mass $\Lambda$ -$K^+$ spectrum corresponds to the mass of the according $N^*$ resonance. The same effect can be seen for the pp$K^-$ channel (turquoise line) in the invariant mass spectrum of $\Lambda$ and p.
Beside this effect the distributions in the other two invariant mass spectra also show partially peaked structures, differently then expected for the phase space production of p$K^+\Lambda$. These structures - usually called mirror peaks - can be explained by the fact, that in these reactions two separate two body reactions take place. Since the involved particles in two body reactions are clearly correlated, all three particles are also strongly correlated.
While the invariant mass spectra are sensitive to the different production channels, they are not influenced by the angular distribution (see 4.2) as one can seen in panels (d)-(f) Figure 6.2 (d)-(f).

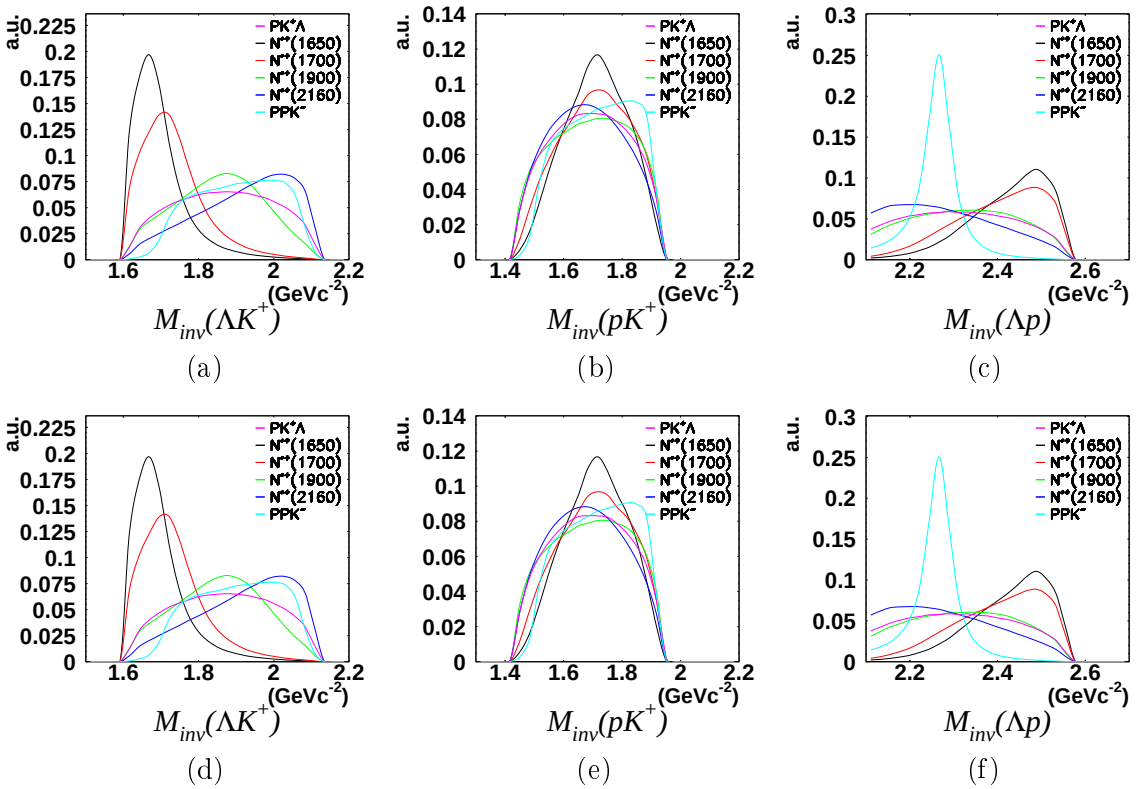


Figure 6.2: Invariant Mass Distributions: $N^*1650$ (black); $N^*1700$(red); $N^*1900$(green); $N^*2160$(violet); p$K^+\Lambda$ (pink); pp$K^-$ (turquoise). Panel (a)-(c) show the spectra for isotropic production, panel (d)-(f) show the production with an angular distribution.

### 6.1.2 Angular Distributions

As shown in the previous paragraph the invariant mass distribution are completely independent from the angular distribution. As shown in other experiments, those correlations are playing a significant role in the description of the total reaction.
For a full description of the reaction additional observables are needed, which are the center-of-mass angle, the Gottfried-Jackson angle and the Helicity angle.

#### Center of Mass Angle

The center of mass angle spectrum shows the distribution of the polar angle of one of the three particle in the center of mass reference frame of the two initial protons, which equals the center of mass system of the whole reaction. The center of mass angle is visualized schematically in Figure 6.3.In the case of an isotropic production it is independent from the different production mechanisms. This reflects in the flat distributions shown in Figure 6.4(a)-(c).
An anisotropic distribution can be explained in the picture of the one boson exchange model. In Figure 1.14 the primary proton interacts in vertex A and produces a virtual meson. Since the mass of this meson is rather low, the transferred transverse momentum is rather low.

Due to this effect, the deflection of the produced particle is small, which results in an anisotropic angular distribution. In this picture the angular distribution depends on the momentum of the exchange meson. This virtual meson interacts then further at the vertex B with the other initial proton. In case of the production of an $N^*$ (Figure 1.14 (c)) the probability for the production of resonances depends on the meson momentum. The production of the $N^*(1900)$ and $N^*(2190)$ resonances requires a meson with a higher momentum than for the case of the $N^*(1650)$. Thus a higher momentum transfer in vertex A is required, which leads to a less anisotropic angular distribution. For that reason the distributions for the low mass resonances has a stronger forward backward asymmetry than the resonances with a higher mass.

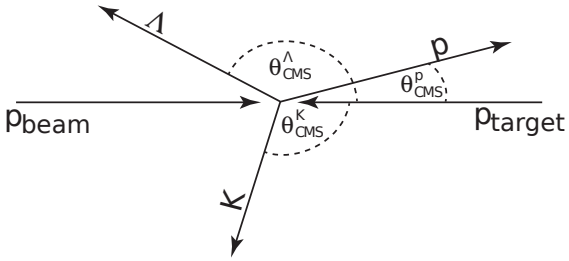


Figure 6.3: Center of Mass Angle: Angle between primary proton the final state particle in the rest frame of the initial protons.

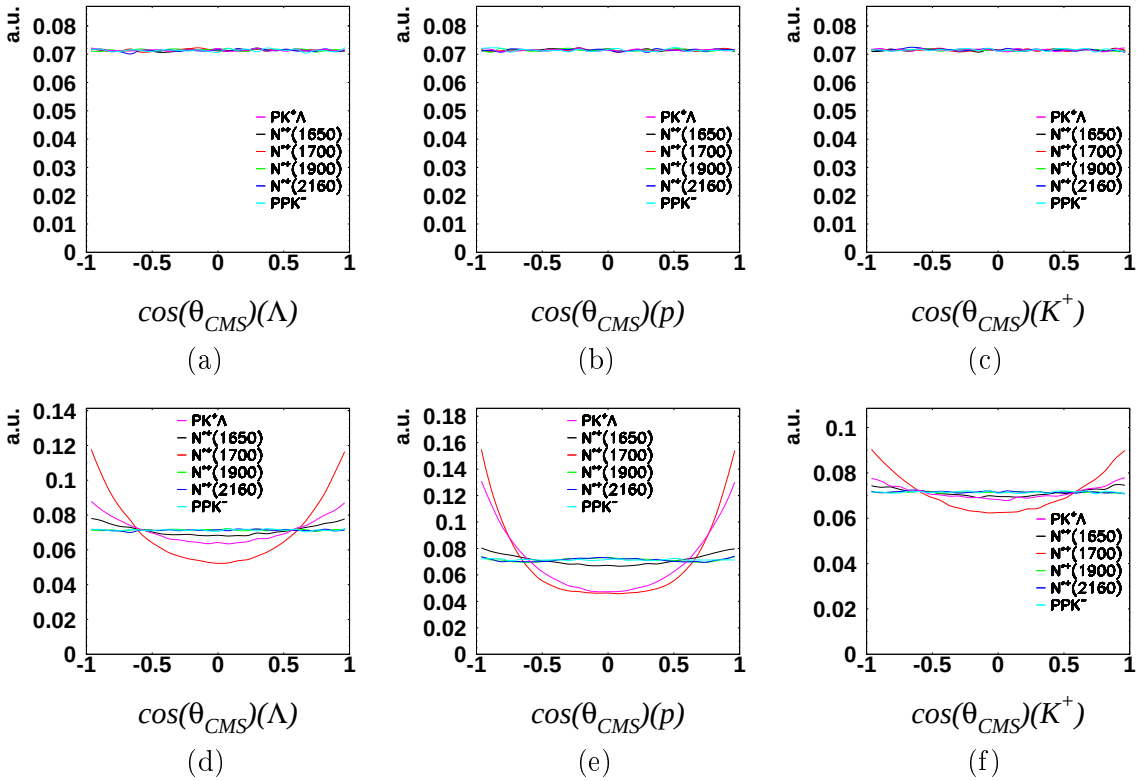


Figure 6.4: Center of Mass Angle Distributions of the $N^*(1650)$ (black), $N^*(1700)$ (red), $N^*(1900)$ (green), $N^*(2160)$ (violet), p$K^+\Lambda$ (pink), ppK (turquoise) channel. Panel (a)-(c) show the spectra for isotropic production, panel (d)-(f) show the production with an angular distribution.

### Helicity Angle

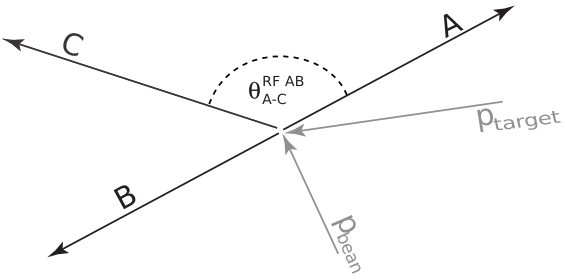


Figure 6.5: Helicity angle $\Theta^{RFAB}_{A-C}$ between particle A and B in the reference system of particles A and B.

In reactions with three particles in the final state the Helicity angle $\theta^{RFBC}_{AB}$ is defined as the angle between the particles A and B in the Helicity frame of the particles B and C. This frame is defined as the Lorentz frame in which the center of mass of the particles B and C is at rest [AB$^+$10]. A schematic view is plotted in Figure 6.5. Since the Helicity angle is defined by the three final state particles, it is in fact a special projection of the Dalitz plot. For the same reason the distributions do not show any difference between isotropic and anisotropic simulation. The spectra for the three different Helicity angles are plotted in Figure 6.6.

In this representation the direct production channel of p$K^+\Lambda$ shows a completely flat behaviour in all three distributions. On the contrary, the production channel via intermediate resonances show clear asymmetric structures. The resonances only show a flat behaviour in the distribution in the reference system of its decay particles. This is based on the assumption of an isotropic decay of those resonances.

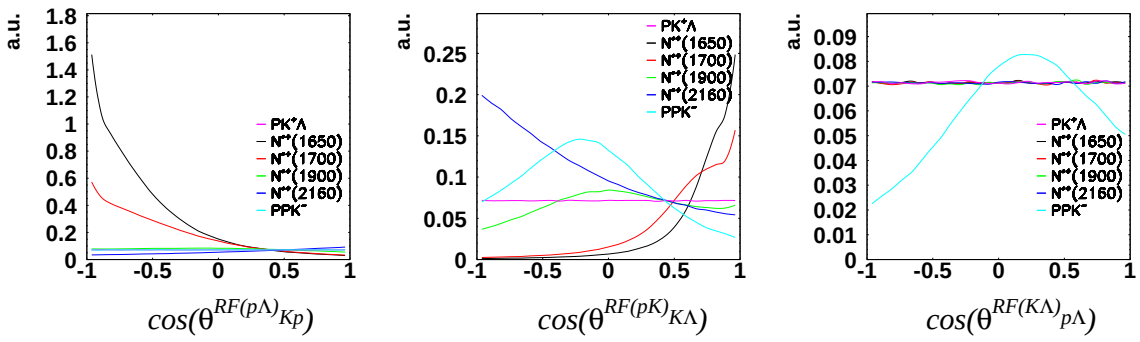


(a) (b) (c)

Figure 6.6: Helicity angle distributions of the $N^*(1650)$ (black), $N^*(1700)$(red), $N^*(1900)$(green), $N^*(2160)$(violet), p$K^+\Lambda$ (pink), ppK(turquoise) channel. The panels show the distribution of the isotropic and the simulation with applied angular distribution, which are identically.

### Gottfried-Jackson Angle

The Gottfried-Jackson angle $\theta^{RFAB}_{A,Be}$ is defined as the angle between the particle A and the incoming proton in the Jackson frame of the particles A and B, which is the same like the Helicity frame of the particles A and B. This angle connects the exit and entrance channel and carries information, which are not accessible by a Dalitz plot analysis.

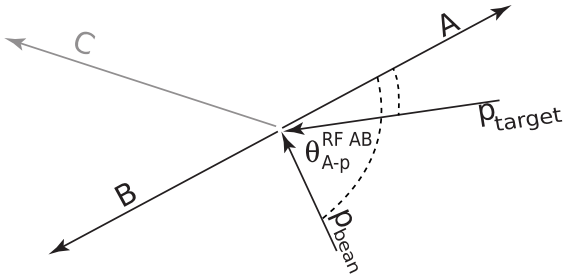


Figure 6.7: Gottfried Jackson angle $\Theta^{RFAB}_{A-p}$ between particle A and the initial proton in the Reference System of particles A and B.

The utility of the Jackson angle lays in the fact, that this angle - according to the OBE - reduces the three particle production process to a '2→2' production mechanism happening in the Vertex B in the Feynman diagrams in Figure 1.14. Thus the angular distribution can give information about the relative angular momentum involved [AB+10]. In Figure 6.8 the Gottfried-Jackson angles for phase space simulation are shown for the isotropic case (a)-(c) and anisotropic (see 4.2) case (d)-(f). One can see that an angular correlation also has influence on the Gottfried-Jackson angles. In these spectra no further angular correlations of the '2→2' sub reaction are included, since such effects are not known for the different channels.

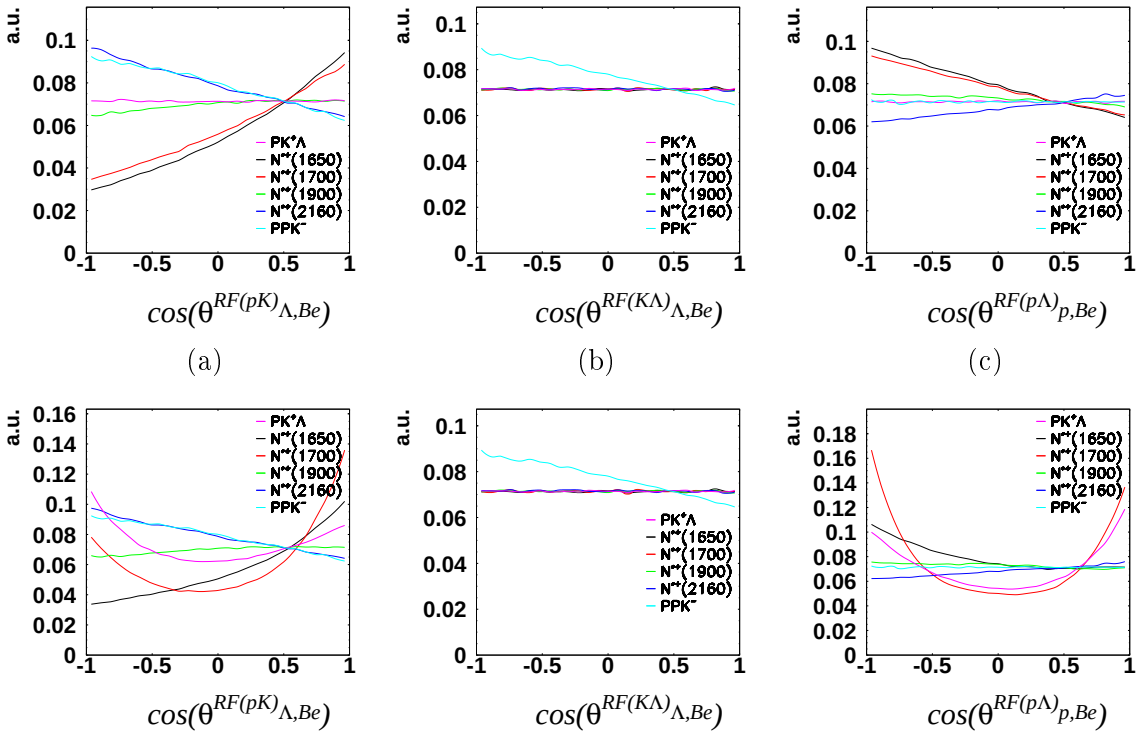


Figure 6.8: Gottfried-Jackson Distributions of the $N^*(1650)$ (black), $N^*(1700)$(red), $N^*(1900)$(green), $N^*(2160)$(violet), p$K^+\Lambda$ (pink), ppK(turquoise) channel. In the spectra (a)-(c) the results for isotropic production is plotted. The spectra (d)-(f) show the production with an angular correlation.

## 6.2 Comparison with Phase-Space Simulation

At first a comparison of the experimental data with a pure phase space simulation was done. For this comparison PLUTO simulations were used with the applied angular correlation (see 4.2). These simulations were filtered through the FOPI GEANT framework and the same analysis chain like for the experimental data was applied.

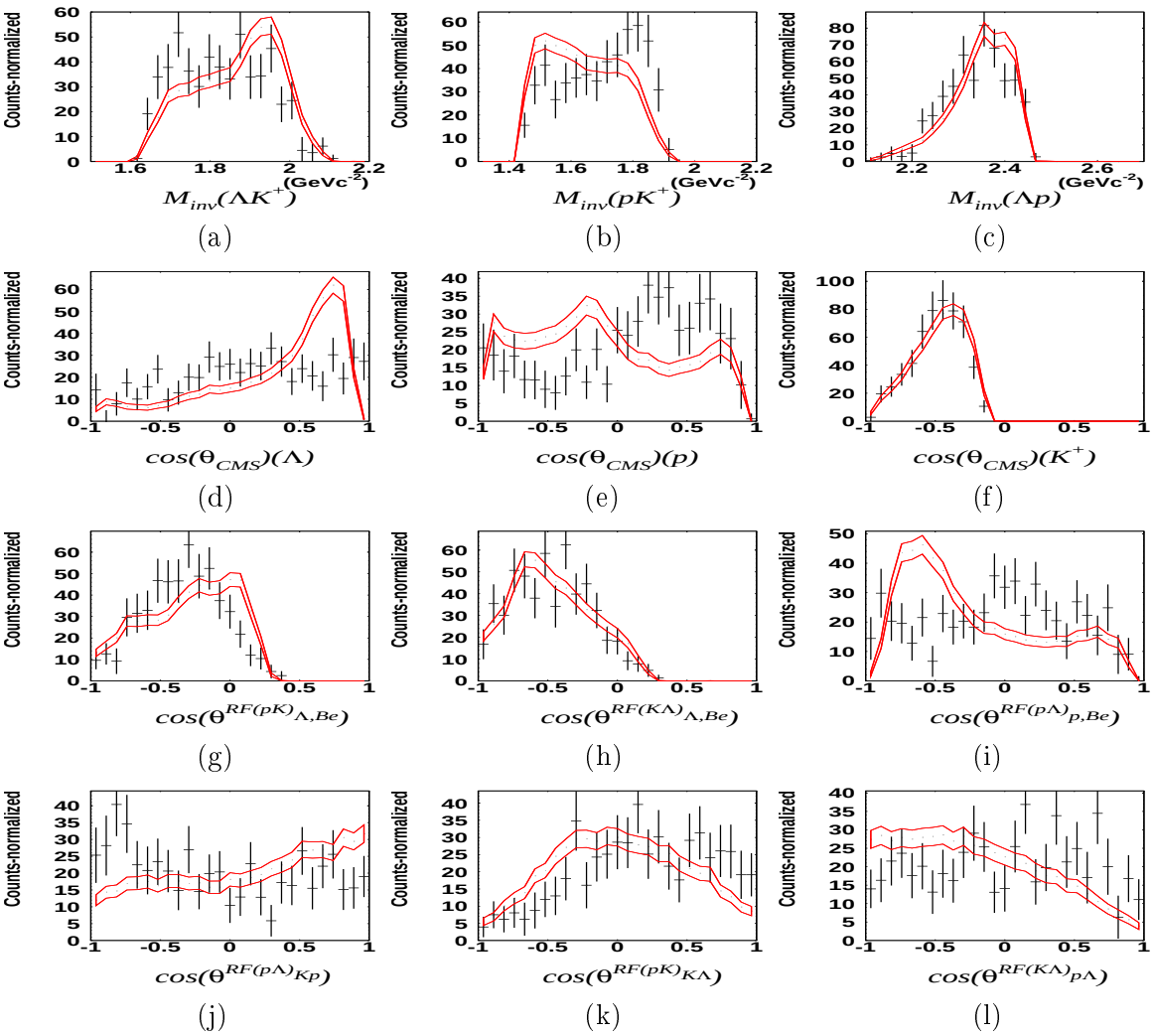


Figure 6.9: Comparison of experimental data (black crosses) with the p$K^+\Lambda$ phase space production (red band). The complete set of kinematical observables is plotted. (a)-(c) are the invariant mass distributions. (d)-(f) show the center of mass angle, (g)-(i) show the three Gottfried Jackson angle and (k)-(m) show the distribution of the Helicity angle.

In Figure 6.9 the full set of observables is plotted. The black crosses show the experimental data after the subtraction of the sideband background. The red band represents the distribution for the direct production channel of p$K^+\Lambda$ . The simulation is normalized to the integrated yield of the $M_{inv}(\Lambda K^+)$ spectrum.
By looking at the different invariant mass distribution one can see that the invariant mass

is very well explained by this model. Also from different angular distributions ((f) and (h)) this conclusion could be draw. But if one looks to the full set of observables the agreement between the experimental and simulation data is rather poor.
Looking at the discrepancy of the angular distribution of the particles, the question arises, whether the used angular distribution is correct. On the one hand an angular distributions could be created, which provides a better description of the angle spectra. One the other hand this would not provide a solution for the discrepancy of the invariant mass spectra, which are not affected by an angular distribution, which was shown in the previous section.

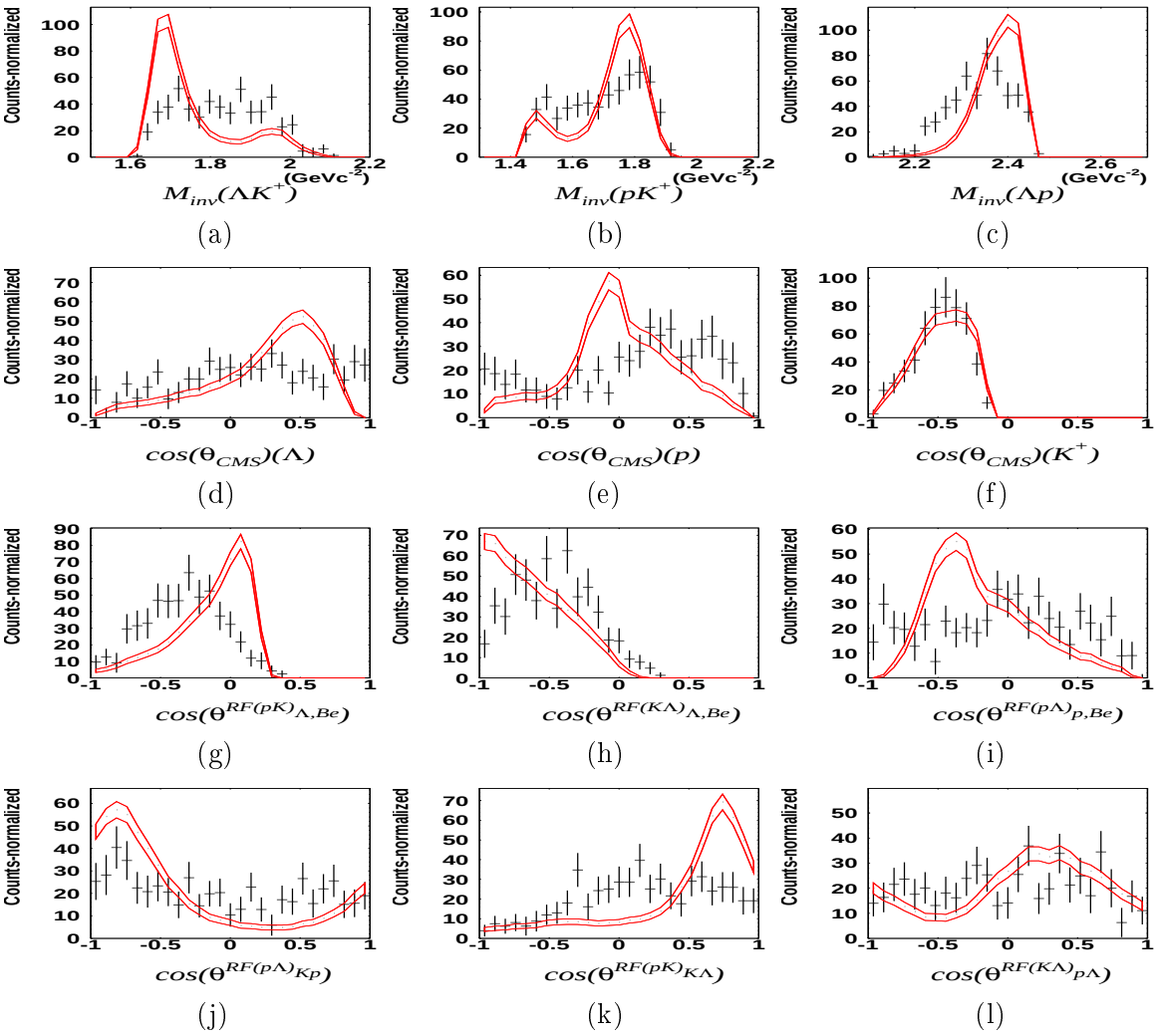


Figure 6.10: Comparison of experimental data (black dots) with $N^*(1650)$ phase space simulation (red band). The complete set of kinematical observables is plotted. (a)-(c) are the invariant mass distributions. (d)-(f) show the center of mass angle, (g)-(i) show the three Gottfried Jackson angle and (k)-(m) show the distribution of the Helicity angle.

Thus, the description of experimental data by pure phase space production of p$K^+\Lambda$ can be ruled out. This result was expected, since it was already shown by the COSY-TOF col-

laboration [AB$^+$10], that $N^*$ resonances play an important role in the production mechanism of the final state of p$K^+\Lambda$ .
For the comparison of the experimental data, $N^*$ resonances with the mass of 1650 GeV/c$^2$ , 1700 GeV/c$^2$ ,1900 GeV/c$^2$ and 2190 GeV/c$^2$ were simulated in the same way like the p$K^+\Lambda$ direct production channel (see Section 4.2).
The resulting spectra for the $N^*(1650)$ simulation are shown in Figure 6.10. The spectra for

| Channel | $chi^2/ndf$ |
|---|---|
| p$K^+\Lambda$ | 2.24 |
| $N^*(1650)$ | 5.52 |
| $N^*(1700)$ | 4.27 |
| $N^*(1900)$ | 3.00 |
| $N^*(2190)$ | 3.76 |

Table 6.1: $\chi^2$ value for the comparison of experimental and simulation data calculated with Equation 6.1. The results are listed for the comparison with the p$K^+\Lambda$ phase space simulation and the $N^*$ resonance channels of different mass.

the further simulated $N^*$ resonances are plotted Appendix F.
To quantify the agreement between different simulation models and the experimental data, a $\chi^2$ can be defined by Equation 6.1.

$$\chi^2 = \sum_{Observables} \sum_{Bins} \frac{(\text{counts}_{sim} - \text{counts}_{exp})^2}{(\sigma^2_{sim} + \sigma^2_{exp})}. \tag{6.1}$$

counts$_{sim}$ and counts$_{exp}$ are the entries of one bin of the histogram of the simulation data and experimental data, respectively. The error value of simulation and experimental data are given by $\sigma_{sim}$ and $\sigma_{exp}$. The sum runs over all bins of the nine histograms of the observables. The $\chi^2$ values for the comparison of the different $N^*$ resonances are listed in Table 6.1.

### 6.2.1 Incoherent Cocktail

From the so-far achieved results one can concluded, that experimental data can not be reproduced neither by p$K^+\Lambda$ direct production nor employing $N^*$ resonances. This result was expected, since it was already shown in [AES$^+$10], that the production of the final state p$K^+\Lambda$ is not realized via one single channel. From the poor value of the $\chi^2$ for the comparison of the different channel (Table 6.1) this results is verified.
For that reason, we have tried to find a description of the experimental data by combining the different channels.
To extract the correct contribution of the different channels a fitting procedure was applied. In this fitting procedure the distributions of each production channel is scaled by a separate factor. The distributions were added and and the sum was compared to the experimental data quantitatively by calculation of the $\chi^2$ (Equation 6.1). The fitting routine then varies the different scaling factors, in order to obtain an minimal value for the $\chi^2$ value.

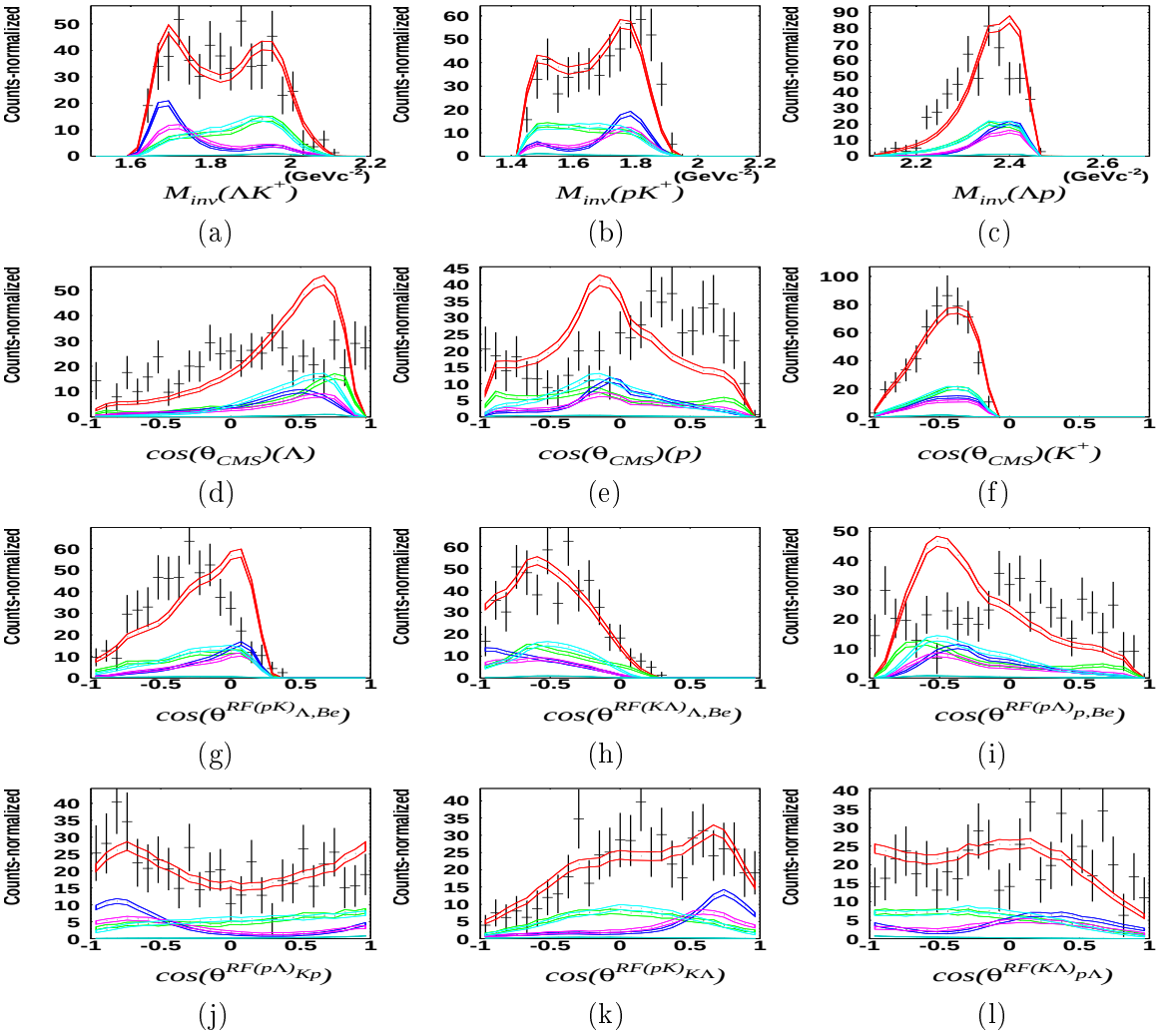


Figure 6.11: Comparison of experimental data (black crosses) with the incoherent sum of phase space simulations (red band). The contributions of $N^*(1650)$ (blue band), $N^*(1700)$ (pink band), $N^*(1900)$ (turquoise band), $N^*(2190)$ (dark green band) and $pK^+\Lambda$ (green band) are plotted separately. The complete set of kinematical observable is plotted. (a)-(c) are the invariant mass distributions. (d)-(f) show the center of mass angle, (g)-(i) show the three Gottfried Jackson angle and (k)-(m) show the distribution of the Helicity angle.

The final distribution for the sum of the scaled channels is shown in Figure 6.11. By the visual comparison the discrepancy of experimental and simulation data is already clearly visible in some kinematic variables. Also the $\chi^2$ value of the comparison of 2.68 indicates an insufficient agreement.
The reason for that can be manifold. One reason - as already mentioned - is the question about angular correlation applied to the different channels. The angular distribution for the simulations were taken from results of the COSY-TOF and the HADES experiment (see Paragraph 4.2), which have taken data at different beam energies. Since the dependency of these correlations upon the energy is not clear, it is complicated to extrapolate to our energy. Further the knowledge about the different $N^*$-resonances, like the cross section, the width

and the branching ratio to $K^+$ $\Lambda$ is quite poor, which increases the degree of freedom. The third reason for the huge discrepancy between experimental and simulation data might be, that the different production channel were added just incoherently, which does not take into account interference effects between the different states.

## 6.3 Comparison with UrQMD

As it was stated in the previous section, the experimental data cannot be explained by pure phase space simulations. Therefore in a second attempt it was tried to reproduce the experimental data by the UrQMD transport model.

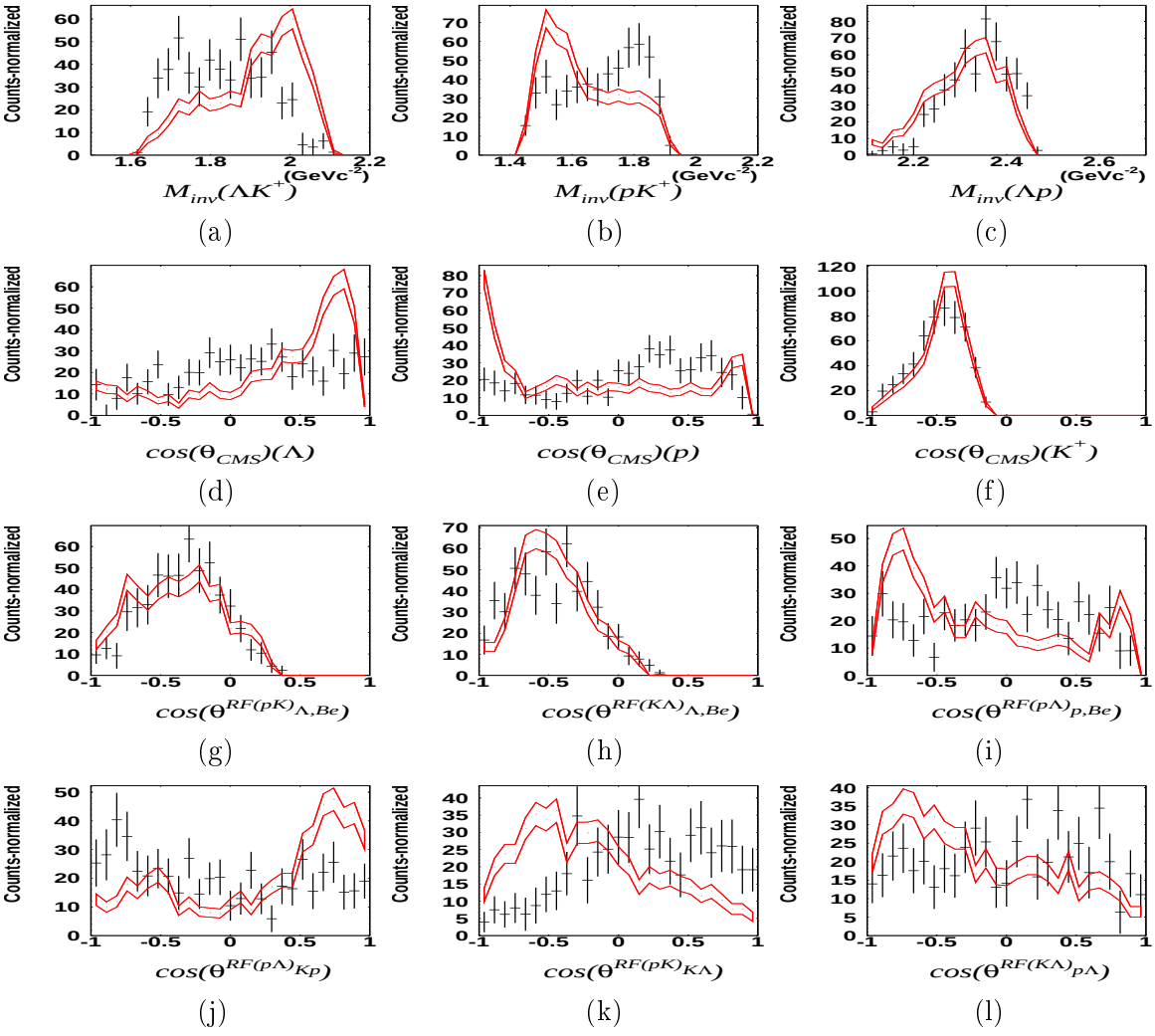


Figure 6.12: Comparison of the experimental data (black crosses) and the simulated UrQMD data (red band). The complete set of kinematical observable is plotted. (a)-(c) are the invariant mass distributions. (d)-(f) show the center of mass angles, (g)-(i) show the three Gottfried Jackson angles and (k)-(m) show the distribution of the Helicity angles.

In this model - described in Paragraph 4.2 - the trajectories of all participating particles

are simulated in the reaction process, which gives a better handle on the final state interaction between the different particles. This might lead to a better description of the angular distributions.
The results for the UrQMD transport model were filter through the detector acceptance via the FOPI GEANT framework and analyzed like the experimental data. In contrast to the PLUTO simulations, the output of the UrQMD transport model contains all possible final states, which are produced by proton proton reactions. The background channels are rejected by the analysis procedure - like for the experimental data. The remaining amount of background events in the final state sample is comparable to the one in the experimental results. The resulting distribution for the different kinematical observables are shown in Figure 6.12. The black crosses are the experimental data. The red bands are the results from the UrQMD simulated data.
By the comparison of these spectra it can be seen, that also the transport model can not reproduce all kinematical observables. The $\chi^2$ for this simulation model is 3.71. Like for the phase space simulations one can see, that only the invariant mass spectrum of p and $\Lambda$ as well as the center of mass angle distribution of the $K^+$ can be reproduced nicely. This shows, that the behaviour of the $K^+$ can explained sufficiently by the UrQMD transport model.
Looking to the further spectra, one can already identify a significant discrepancy in the invariant mass spectra of $K^+$ and $\Lambda$ . Since these two particles are the decay products of the $N^*$ , the contribution of these resonances with different masses can be roughly estimated from this spectrum. The simulation spectrum is significantly shifted to higher masses compared to the experimental data, which can be explained by a production of the p$K^+\Lambda$ state via $N^*$ resonances of higher masses then in the experimental data. In conclusion it can be stated, that the UrQMD transport model does not match with the experimental results. Actually the discrepancy is even worse then for the incoherent cocktail, which shows that the $N^*$ content in UrQMD transport model is most probably incorrect.

## 6.4 Comparison with PWA

In the previous section it was shown that the experimental data cannot be reproduced by phase space simulations or UrQMD transport calculations. From the comparison with the UrQMD simulation we can rule out, that the cocktail of production channels included in this transport model might be able to describe the data correctly. A still open question is the angular distribution between the different particles and the question about interference between different channels.
In quantum mechanics each transition from an initial wave with the quantum numbers (S,L,J) to a final state with quantum numbers ($S'$,$L'$,J) consists of a complex amplitude, which can be separated in a real amplitude and a phase.The wave functions of different transitions with the same quantum numbers can mix, which leads to interference. Those interferences can play a significant role in the description of final state spectra - as it was shown in [SF13]. In the reaction p+p$\rightarrow$ p$K^+\Lambda$ many different possible transitions could contribute. Since the amplitudes and phase parameters of these transitions are not know, they have to be fitted by a Partial Wave Analysis.

### 6.4.1 The Bonn Gatchina Partial Wave Analysis Framework

Partial Wave Analysis is a wide spread tool, used in the analysis of $\pi$N and $\gamma$N reaction data [SNA$^+$05, ABSW06, AKN$^+$11, RDH$^+$13, A$^+$12]. Those methods are able to decompose the full set of possible waves, which are contributing to a certain final state. From those, several short living baryon resonances have been identified in the mass region between 1.2 GeV/c$^2$and 2.7 GeV/c$^2$ [B$^+$12] [CI86].
Most of the available frameworks for Partial Wave Analysis are just available for the fitting of $\pi$N and $\gamma$N, since the proton-proton system is more complicated, due to the additional quark in the initial system.
One partial wave framework, which is available for the analysis of proton-proton data, is the Bonn-Gatchina Model (BG-PWA) [SNA$^+$05, CDE$^+$13].

#### Amplitude Parametrisation

In the BG-PWA the production cross section of three particles, with the four-momenta $q_{1,2,3}$, is parametrized by Equation 6.2 [AS06b]

$$d\sigma = \frac{(2\pi)^4 |A|^2}{4|\vec{k}|\sqrt{s}} \mathrm{d}\Phi_3 \left(P, q_1, q_2, q_3\right). \tag{6.2}$$

$\vec{\mathrm{k}}$ is the combined 3-momentum of the initial particles. $\sqrt{s}$ is the center of mass energy of the reaction. $d\Phi_3$ is the available phase-space for the three final particles.
The total reaction amplitude A is given by a sum over all transition waves $\alpha$ [EMN$^+$11]:

$$A = \sum_{\alpha} A^{\alpha}_{\mathrm{tr}}(s) Q^{\mathrm{in}}_{\mu_1..\mu_j}(S, L, J) A_{2b}\left(i, S_2, L_2, J_2\right) Q^{\mathrm{fin}}_{\mu_1..\mu_j}(i, S_2, L_2, J_2, S', L', J). \tag{6.3}$$

The factors $Q^{\mathrm{in}}_{\mu_1..\mu_j}(S, L, J)$ are the operators for the initial system of the reaction, described by the spin (S), orbit momentum (L) and total angular momentum (J) quantum numbers [AS06b]. The initial system of the two protons $\left(J^P = \frac{1}{2}^-\right)$ can appear in different states (see Table 6.2).

| $J^P$ | $S_{tot} = 0$ | $S_{tot} = 1$ |
|---|---|---|
| L=0 | $0^+$ | $1^+$ |
| L=1 | $1^-$ | $0^-, 1^-, 2^-$ |
| L=2 | $2^+$ | $1^+, 2^+, 3^+$ |
| L=3 | $3^-$ | $2^-, 3^-, 4^-$ |

Table 6.2: Possible combinations of the initial system of two proton. The grey shaded combination are forbidden.

Since the two initial protons are indistinguishable fermions the total wave function of both particles has to be antisymmetric, which requires the following condition

$$(-1)^{L+S+1} = -1. \tag{6.4}$$

For this reason, the grey shaded states in Table 6.2 are forbidden.
Each wave in the final state is treated as a two particle system with the quantum numbers

$S', L', J$. In the case of direct production of p$K^+\Lambda$ one is the kaon and the other one is a sub-system build from the proton and the $\Lambda$ . This subsystem is described by the quantum numbers $S_2, L_2, J_2$. The re-scattering of the $\Lambda$ and the proton is described by the factor $A_{2b}\left(i, S_2, L_2, J_2\right)$ [Sar13]:

$$A_{2b}^{\beta} = \frac{\sqrt{s_i}}{1 - \frac{1}{2} r^{\beta} q^2 a_{p\Lambda}^{\beta} + \mathrm{i} q a_{p\Lambda}^{\beta} q^{2L} / F\left(q, r^{\beta}, L\right)} \tag{6.5}$$

where q is the relative momentum between the baryons in the two particle subsystem and multi index $\beta$ denotes possible combinations of channels i and quantum numbers $S_2, L_2$ and $J_2$. $a_{p\Lambda}^{\beta}$ is the p$\Lambda$-scattering length and $r^{\beta}$ is the effective range of the $\Lambda$-p system. F(q,r,L) is the Blatt-Weisskopf factor, which is used for normalization[1] [BNSSW13].
In case of a production of $N^*$ resonance the final state is build of the $N^*$ resonance and the p with the quantum numbers $S', L', J$. In this case the factor $A_{2b}$ is replaced by a relativistic Bret-Wigner formula [EMN$^+$11, Sar13].

$$A_{2b}^{\beta} = \frac{1}{\left(M^2 - s - \mathrm{i}\Gamma M\right)}, \tag{6.6}$$

with pole mass M and the width $\Gamma$ of the corresponding resonance.
For all transition waves the amplitude $A_{\mathrm{tr}}^{\alpha}(s)$ of is given by Equation 6.7:

$$A_{\mathrm{tr}}^{\alpha}(s) = \left(a_1^{\alpha} + a_3^{\alpha}\sqrt{s}\right) exp\left(\mathrm{i}a_2^{\alpha}\right). \tag{6.7}$$

This amplitude consists of a constant amplitude $a_1^{\alpha}$, an energy dependent amplitude $a_3^{\alpha}$ and a phase $a_2^{\alpha}$.
These parameters are fitted on an event-by-event base to the experimental data.
For each fitting step the total sum of all participating waves is built. Due to the phase factor in the amplitude parametrisation, interference between different transitions of same quantum numbers ($J^P$) can occur.
This total sum is then compared to the experimental data. The total fitting quality for each step is expressed by a negative likelihood value, which is minimized by the fitting routine.

### PWA Input

**Data samples** The experimental data have to be provided in a dedicated list format to the routine (Appendix G..i.). Since the experimental data contain an amount of background, an additional list of background events has to be provided to the PWA, taken from the sideband sample (Paragraph 3.5.6). These events are assigned with a negative weighting factor, which is extracted from the signal to background values in the $K^+$ spectrum (see Paragraph 3.5.6). Additionally, a set of phase-space simulation data - filtered for acceptance and efficiency - of the channel p+p$\rightarrow$p$K^+\Lambda$ has to be provided.
Thus, in total three different event samples - experimental signal (dat.), experimental background (bkg.) and simulation data (sim) - were fed to the PWA fitting routine.
These three data samples have to be further subdivided according to the corresponding detector hemisphere combination - according to the topologies described in Paragraph 3.5.4.

[1] The Blatt-Weisskopf factor is 1 for L=0 and the explicit form for other partial waves can be found in [AS06b]

| Topology | Exp. Data | Simu. Data |
|---|---|---|
| 0-00 | 433 | 8423 |
| 0-01 | 167 | 14078 |
| 0-02 | 316 | 17800 |
| 0-10 | 124 | 2525 |
| 0-11 | 25 | 3502 |
| 0-12 | 33 | 4518 |
| 0-22 | 19 | 1256 |
| 1-00 | 54 | 2393 |

| Topology | Exp. Data | Simu. Data |
|---|---|---|
| 1-01 | 23 | 3922 |
| 1-02 | 35 | 2640 |
| 1-10 | 15 | 783 |
| 1-11 | 5 | 581 |
| 1-12 | 2 | 782 |
| 1-20 | 8 | 162 |
| 2-10 | 28 | 933 |
| 2-11 | 13 | 1090 |

Table 6.3: p$K^+\Lambda$ Statistics in different detector topologies. Only combinations with experimental statistics are listed. The simulation data are from p$K^+\Lambda$ simulation without an angular distribution.

This separate treatment in PWA is necessary, since different cut values were applied to the sub-samples. In Table 6.3 the total amount of events for the different detector topologies are listed. Since the fitting routine of the PWA is done in parallel for all sub samples, the low amount of event in some bins does not reduce the fitting capability of the PWA.
Beside these input data sets an additional data set of simulated data ($4\pi$-set) is used in the PWA fitting routine. This data set consists of isotropic phase space simulation of the free p$K^+\Lambda$ production in the full phase space. This sample allows the extrapolation of the PWA solution to the full phase space (Paragraph 6.4.1). Since this sample is included without a corresponding experimental data sample, it has no influence on the fitting result.

| Resonance | $J^P$ | Mass (GeV/c$^2$) | Width (GeV/c$^2$) |
|---|---|---|---|
| $N^*(1650)$ | $\frac{1}{2}^-$ | 1.655 | 0.150 |
| $N^*(1710)$ | $\frac{1}{2}^+$ | 1.710 | 0.100 |
| $N^*(1720)$ | $\frac{3}{2}^+$ | 1.720 | 0.250 |
| $N^*(1875)$ | $\frac{3}{2}^-$ | 1.875 | 0.220 |
| $N^*(1880)$ | $\frac{1}{2}^+$ | 1.870 | 0.235 |
| $N^*(1895)$ | $\frac{1}{2}^-$ | 2.090 | 0.090 |
| $N^*(1900)$ | $\frac{3}{2}^+$ | 1.900 | 0.250 |

Table 6.4: $N^*$ resonances included in the Partial Wave Analysis written in the spectroscopic notation with their the mass and the width, taken form [B$^+$12]. The same $N^*$ resonances like for the HADES experiment were used [Epp14].

**Mass and Parameter Definitions** The information about the set of transition waves, which should be fitted by the PWA framework, have to be provided together with the starting value for the transition amplitude parameters $a^{\alpha}_{1,2,3}$. The input format is shown in Appendix G..ii.. The initial values for the transition waves were taken from the results obtained by the HADES collaboration [Epp14].The parameters could be used as starting parameters although these data of the reaction p+p$\rightarrow$p$K^+\Lambda$ were taken at a higher beam energy of 3.5 GeV. The starting parameter set contains all $N^*$ resonances listed in Table 6.4 together

with the waves of the free p$K^+\Lambda$ production. Also the full set of initial states of the proton-proton system was used (Table 6.2). This parameter set is named full set. Since only data of one beam energies were fitted, just the parameters $a_1^\alpha$ and $\alpha_2^\alpha$ are varied. The energy dependent parameter for each wave $a_3^\alpha$ was fixed to 0.
Additionally to the transition wave parameter file, the masses and the width of the resonances has to be provided to the BG-PWA. For the analysis these values were fixed to the nominal value, listed in Table 6.4 [B$^+$12].

**PWA Output**

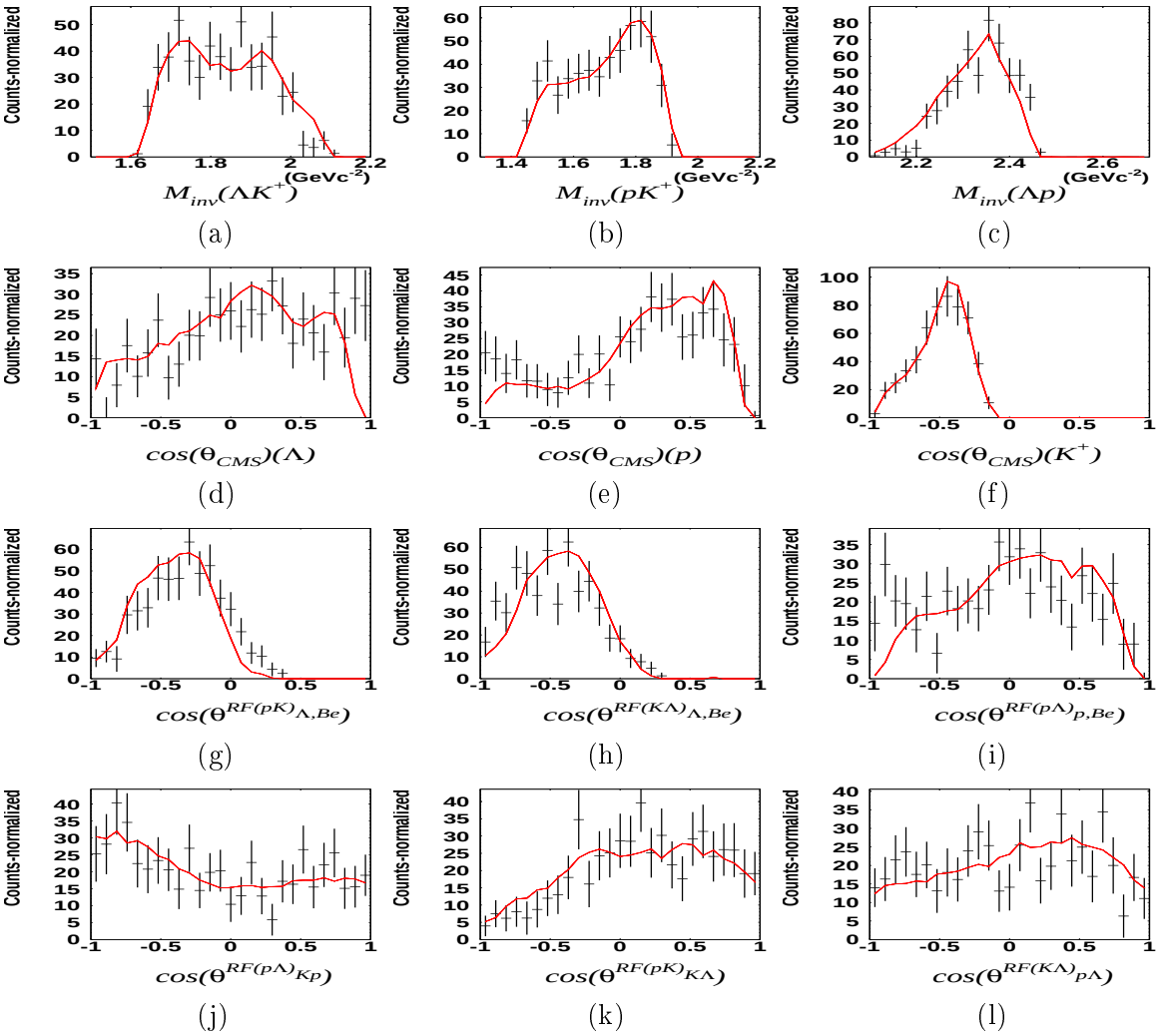


Figure 6.13: Comparison of the experimental data (black crosses) and the results of the BG-PWA (red band) using the full parameter set.

**Weighted Data Sample** The main output of the BG-PWA is a list of simulated events, which have been used for the simulation input of the PWA. Each event is assigned with a weighting factor, which gives the contribution - fitted by the BG-PWA - of this event to the total yield.

From these output events, the spectra for the observables - shown in Figure 6.13 - are filled event by event scaled by the weighting factor. From these spectra one can see the good agreement between the PWA result and the experimental data, which is reflected also in the $\chi^2$ value of 1.152.
Since this parameter set is obtained within the acceptance of the FOPI spectrometer the outcome does not show the full phase-space distribution. This information can be extracted from the $4\pi$ data set. Although the simulated events in this data set are not used for fitting, they are also assigned with a weighting factor according to the fitting result. Thus the $4\pi$ data set serves as an extrapolation of the fitting result to the full phase space. These results for the different observables are shown in Figure 6.14.

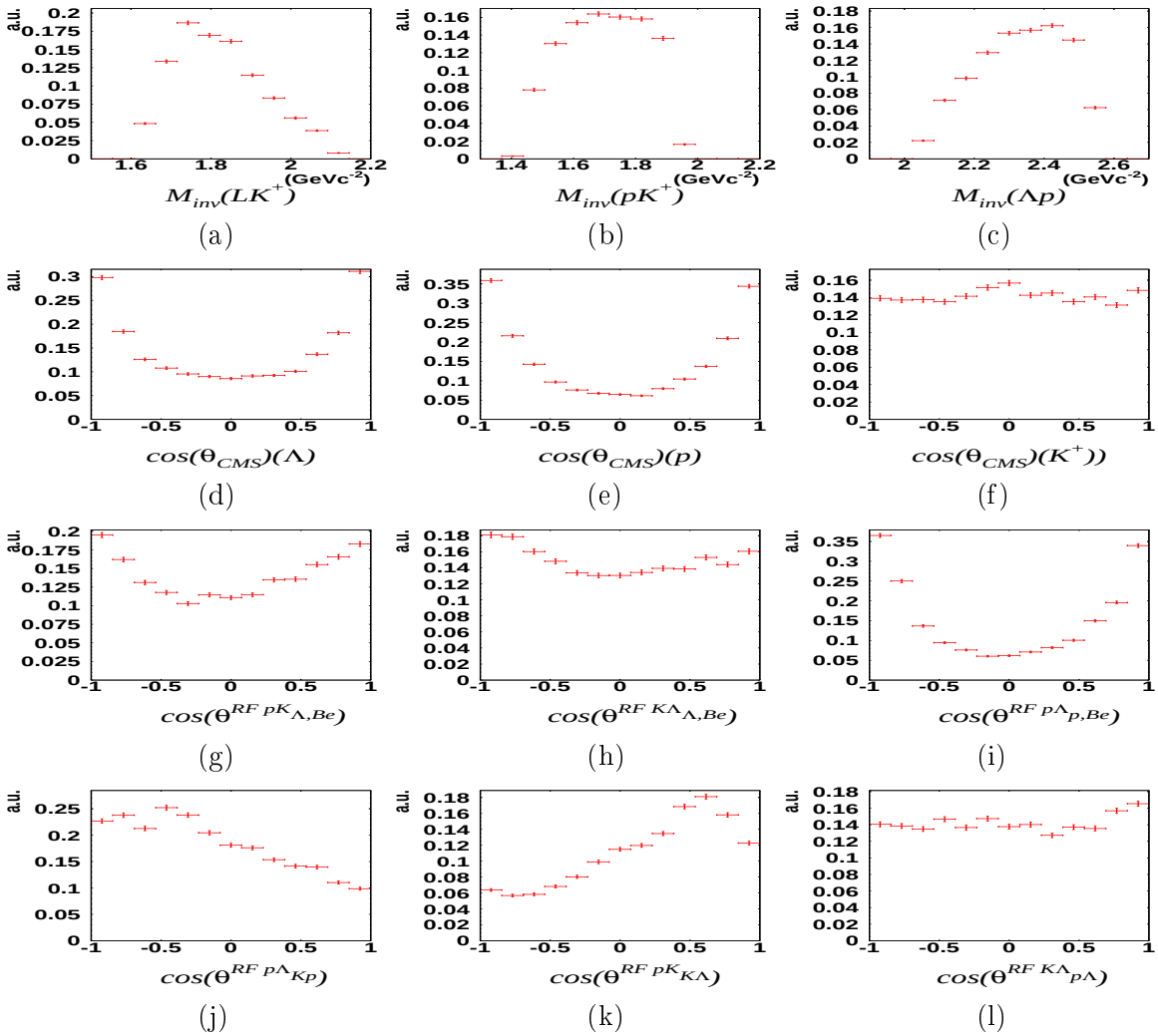


Figure 6.14: Distribution for the full phase of the reaction p+p $\rightarrow$ p$K^+\Lambda$ obtained from the PWA analysis with full parameter set. The spectra are normalized to 1.

**Output Results** Beside the weighted data also a list of all included transition waves is written out with its corresponding relative production contribution. From these value the production cross section can be calculated by a multiplication with the total production cross

section of the final state p$K^+\Lambda$ .
The production cross section for each transition wave must not be confused with the final observed cross section in the final state (final cross section). In partial wave analysis the extracted contribution corresponds to the strength of a certain wave at production stage. Since these different waves can interfere, the production cross section is not necessarily equal to the final cross section of a certain state. Furthermore, due to interference of different states the contributions in the final state cannot be assigned unambiguously to a certain wave. For that reason, in the further analysis the contributions and cross sections of different states always refer to the production state of the wave.
It has also take into account, the in the BG-PWA branching ratios for intermediate resonance are not included. Thus the extracted cross section includes the branching ratio of the resonance, which ends of in the final state p$K^+\Lambda$ .

**Output Parameter Set** The PWA provides a parameter list file in the same format like the input parameter file, which consists of the resulting fitting values for the parameter $a^{\alpha}_{1,2,3}$.

### 6.4.2 Scan of Parameter Sets

Based on the full parameters set which reproduces the experimental data quite good, a systematical scan was performed to determine the stability of the fit results. For this scan different $N^*$-resonances as well as different initial waves of the proton-proton system were disabled[2]. The nomenclature of the parameter set is shown in 6.8. The waves for $N^*(1650)$, $N^*(1710)$ and $N^*$ (1720) are included in all parameter sets.

$$\text{parameter set} = ABCDEF \tag{6.8}$$

$A =$ $N^*$ (1875) waves enabled (1) / disabled (0)
$B =$ $N^*$ (1880) waves enabled (1) / disabled (0)
$C =$ $N^*$ (1895) waves enabled (1) / disabled (0)
$D =$ $N^*$ (1900) waves enabled (1) / disabled (0)
$E =$ p$K^+\Lambda$ non resonant waves enabled (1) / disabled (0)
$F = 5$ Initial proton states: ${}^1S_0, {}^1D_2, {}^3P_0, {}^3P_1, {}^3P_2, {}^3F_3$
$= 4$ Initial proton states: ${}^1S_0, {}^1D_2, {}^3P_0, {}^3P_1, {}^3P_2$
$= 3$ Initial proton states: ${}^1S_0, {}^1D_2, {}^3P_0, {}^3P_1$
$= 2$ Initial proton states: ${}^1S_0, {}^1D_2, {}^3P_0$
$= 1$ Initial proton states: ${}^1S_0, {}^1D_2$
$= 0$ Initial proton states: ${}^1S_0$

For each parameter set the PWA routine was executed. In the first step the parameter sets, which do not produce a converging solution are discarded. In the second step for the remaining results the $\chi^2$ value from the comparison with the experimental data (Equation 6.1) was

[2] If a resonance/initial state is disabled, is it not listed in the input parameter file

determined. For further analysis steps the five parameter sets with the lowest $\chi^2$ values were used, which are listed in Table 6.5 with the corresponding value of $\chi^2$.

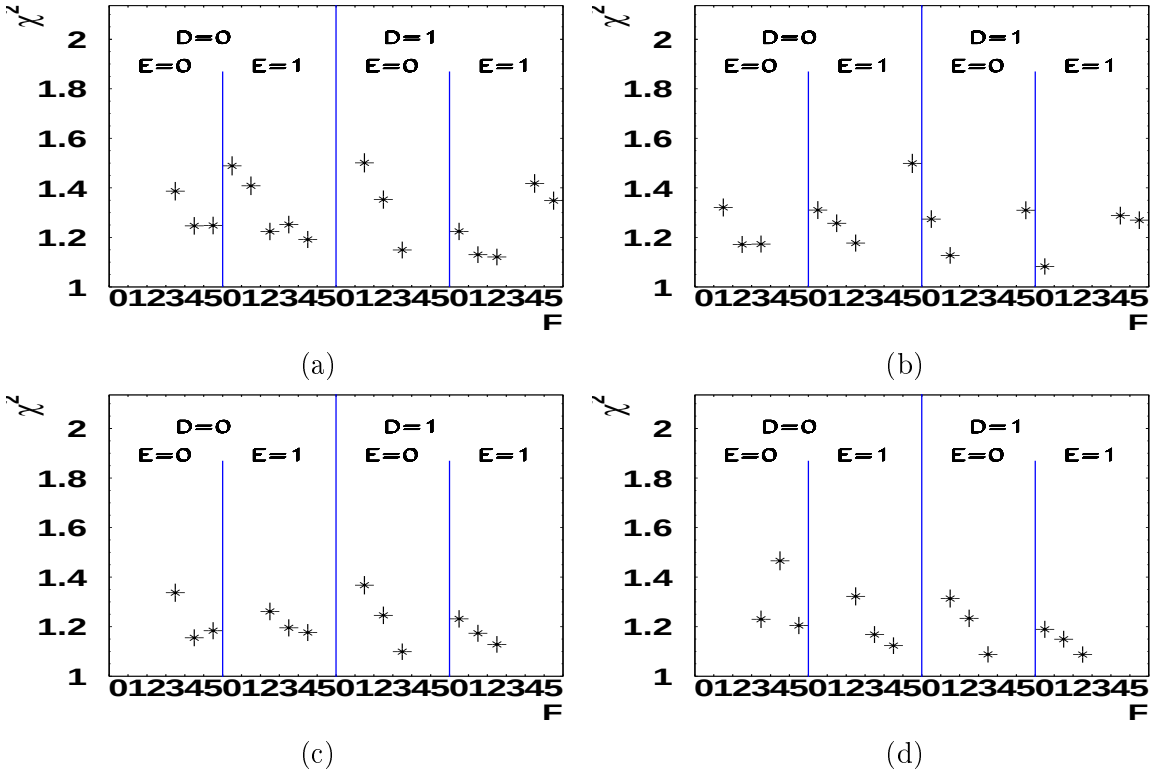


Figure 6.15: $\chi^2$ value for the PWA of different parameter sets versus the value F of the parameter set is plotted. In each spectrum four different combinations of D and E are plotted. In spectrum (a) the parameter sets=000***, in (b) the parameter sets 010***, in (c) the parameter sets 011*** and in (d) the parameter sets 110*** are shown. Results are just plotted for solutions, which did converge.

| Parameter set | $\chi^2$ | free p$K^+\Lambda$ (%) | $N^*$ (%) | | | | | | |
|---|---|---|---|---|---|---|---|---|---|
| | | | 1650 | 1710 | 1720 | 1875 | 1880 | 1895 | 1900 |
| 110103 | 1.09 | 0.0 | 11.3 | 52.4 | 11.8 | 6.3 | 10.9 | 0. | 7,3 |
| 010110 | 1.09 | 16.6 | 9.4 | 42.3 | 14.1 | 0. | 9.7 | 0. | 7.9 |
| 011103 | 1.10 | 0.0 | 11.1 | 49.5 | 7.5 | 0. | 14.1 | 9.3 | 8.5 |
| 110112 | 1.12 | 13.9 | 6.8 | 43.8 | 11.9 | 5.3 | 9.4 | 0. | 8.9 |
| 000113 | 1.15 | 21.1 | 8.6 | 41.9 | 17.6 | 0. | 0. | 0. | 10.8 |

Table 6.5: Results of the five best parameters set. Listed are the $\chi^2$ values of the PWA output compared with the experimental data and the relative contribution of the different $N^*$ resonance and the free production of p$K^+\Lambda$ - given in %.

In Figure 6.15 the $\chi^2$ value for the parameter sets with a converging solution are plotted versus the index F. Each spectrum shows the results for different combinations of D and E of the parameter set number. The different panels show different combinations of the parameters A,B,C. In this figure just those four spectra are shown, which include at least on of the five best parameter sets with the lowest $\chi^2$ values. All spectra are plotted in Appendix H.
The relative contributions (given in %) of the different $N^*$ resonances and the free p$K^+\Lambda$ production are listed in Table 6.5. The resulting parameter distributions of the five best solutions are plotted in Figure 6.16 (color code explained in the caption) together with the experimental distributions (black crosses).

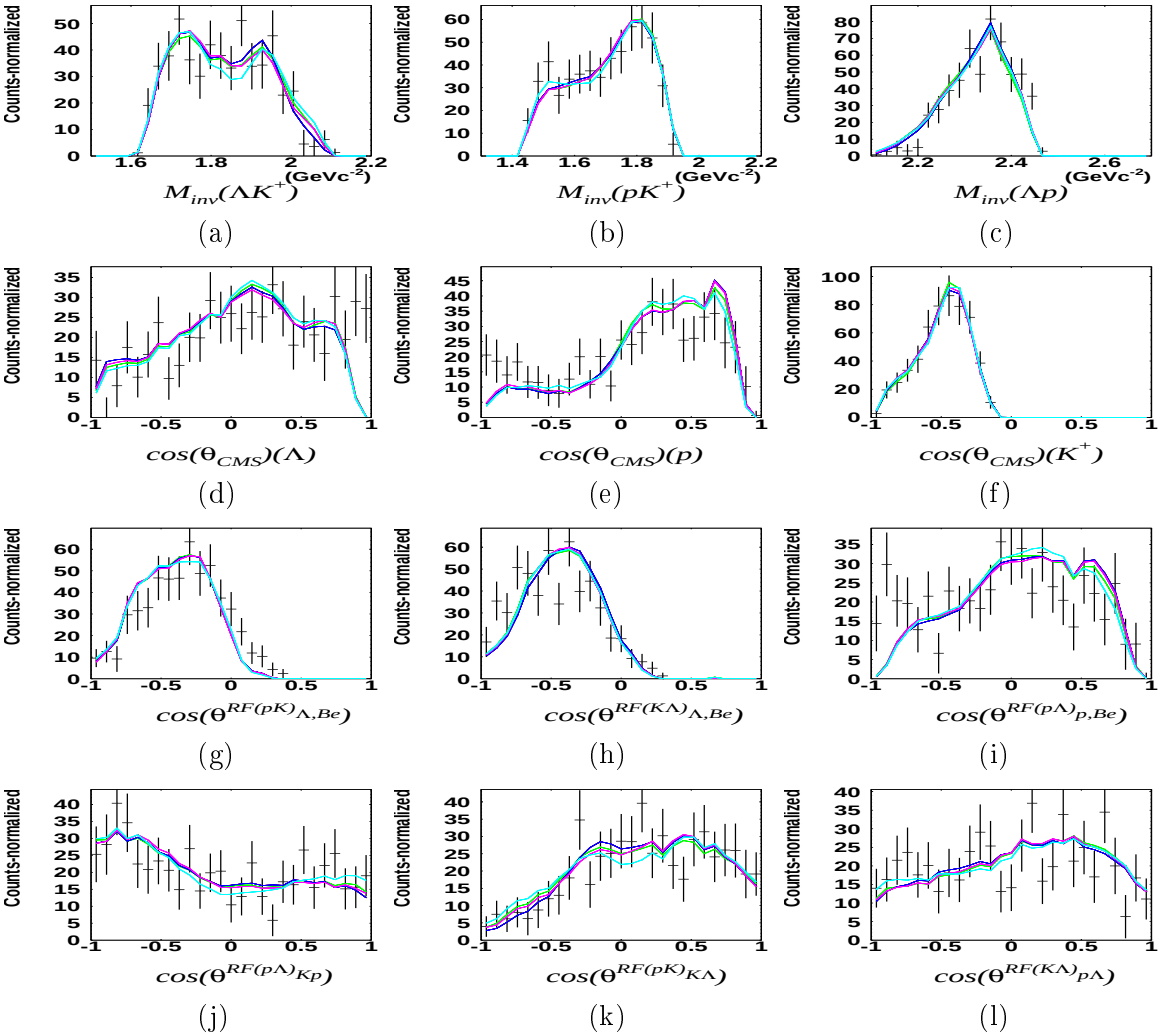


Figure 6.16: Comparison of experimental data (black crosses) with the five best results of the Partial Wave Analysis. Parameter set 000113 (turquoise), set 010110 (red), solution 011103 (pink), solution 110103 (dark blue), solution 110112 (light green)

From the spectra one can see, that the different results from the PWA fitting cannot be separated, since the distributions - as well as the $\chi^2$ value - are very similar. For example the

content of the free p$K^+\Lambda$ production varies between 0 and 22%.
On the other hand the results show also some clear trend. First, a clear dominant production via $N^*$ resonance seems to be favoured by all solutions, with a very strong component of the $N^*(1710)$ and a small contribution of $N^*(1650)$. This result is expected from the results of [AES+10], which has shown, that the contribution of $N^*(1710)$ / $N^*$ (1720) increases with increasing energies, while the contribution of $N^*(1650)$ decreases. In their energy range the $N^*(1650)$ was more dominant. At our energy the $N^*(1710)$ seems to become the dominant part.
Further the resonances $N^*(1875)$ and $N^*(1895)$ play a minor role, while a certain contribution from 6% to 13% of the $N^*(1900)$ seems to be favoured by all results.

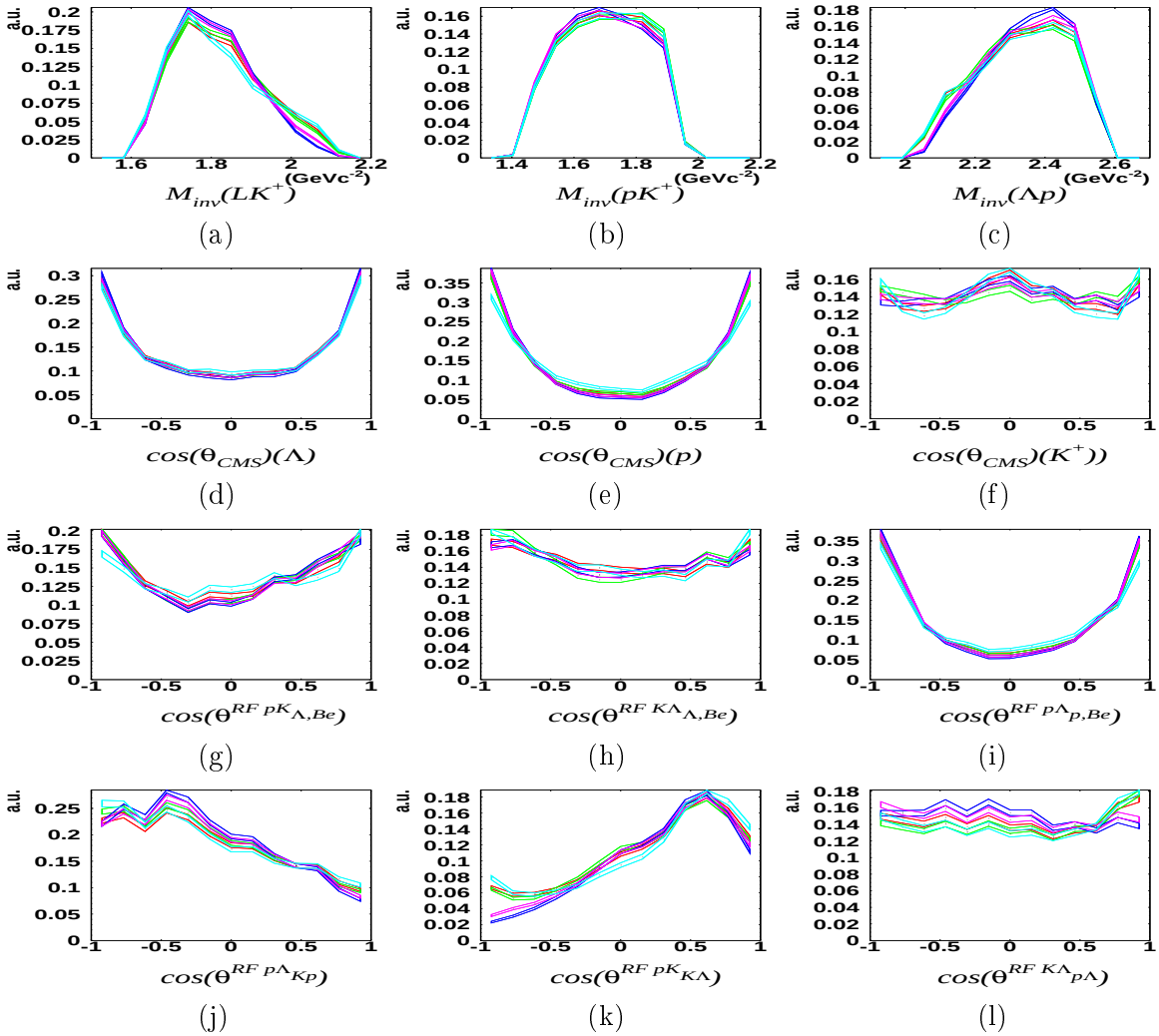


Figure 6.17: Distribution for the full phase of the reaction p+p $\rightarrow$ p$K^+\Lambda$ obtained from the five best PWA parameter sets. Parameter set 000113 (turquoise), set 010110 (red), solution 011103 (pink), solution 110103 (dark blue), solution 110112 (light green).

A more detailed separation of the different solutions is not possible due to limited statistics

in the experiment. A further improvement of the results could be obtained for the investigation of spin observables. The small difference between the different results can be seen in the full phase space spectra of the five solutions - shown in Figure 6.17. These distributions have a quite similar behaviour in most of the spectra. A more detailed separation would require more statistics.
On the other hand all of the spectra show a very anisotropic distribution in the center of mass angle of the proton and the $\Lambda$. The dominant production via $N^*$ channels is also visible in the non flat behaviour of the Helicity angle distribution in panel (j) and (k), which is expected for a resonance dominated production.
From these results we can conclude, that the experimental data can be reproduced by a coherent cocktail of different $N^*$-resonances and the free p$K^+\Lambda$ production quite sufficiently within the experimental errors. The most interesting result is, that interference effect seems to play a major role in this production mechanism, since the experimental data cannot be explained at all by an incoherent sum of different production channels.

## 6.5 Contribution of the pp$K^-$

The major goal of this work was to extract information about the production of the pp$K^-$ state in the p$K^+\Lambda$ final state. From the previous section two different conclusions on the pp$K^-$ can be drawn. On the one hand it was shown, that experimental data can be described reasonably well by the BG-PWA fitting method including only known $N^*$ resonances. This conclusion seems to exclude a strong contribution of the pp$K^-$ in the production channel of p+p$\rightarrow$p$K^+\Lambda$, which was predicted by [Y$^+$08]. On the other hand it was shown, that interference effects are playing a significant role in the underling production mechanism. This interference could lead to a less evident signature of the pp$K^-$ in the final state, while a non negligible contribution in the production state is present. Furthermore, the width and the binding energy, which is directly connected to the peak position, of the pp$K^-$ is not settled (see Section 1.4). In case of a large width, a signal of the pp$K^-$ could hardly be seen, due to the statistical errors.
With the BG-PWA framework we have a very useful tool, which allows to analyse the experimental data including the wave of the pp$K^-$ to determine the upper limit for the production of the pp$K^-$ with different values of the width and mass.

### 6.5.1 Implementation of the pp$K^-$

The pp$K^-$ is a state with a total momentum of J=0 and a negative parity [Nog63]. In the BG-PWA, this state is implemented similarly as the $N^*$ resonances with a spectral function of a relativistic Breit-Wigner distribution (see Equation 6.6). The parity of the total final system depends on the angular momentum between the pp$K^-$ and the $K^+$ ($J^P = 0^-$) and is given by $P_{\mathrm{pp}K^-\text{-}K^+} = (-1)^L$. Since both particles have J=0, the total spin of the system can only be $S_{tot} = 0$.
The final states can only be populated by a reaction of a two protons system, with the same quantum number as the final system. Thus the pp$K^-$ can be produced from the initial wave $0^+$,$1^-$ and $2^+$. Thus three different transition for the production of pp$K^-$ may occur.
In the following analysis the upper limit for the three waves will be determined separately.

### 6.5.2 Determination of an Upper limit

#### Amplitude Scan

The determination of an upper limit is achieved via a scanning procedure. As a starting point, the parameter sets of the five best solutions are used separately, with fixed parameters.
To this parameters sets, one of the three waves of the pp$K^-$ is added and the amplitude parameter $a_1^{\mathrm{pp}K^-}$ is increased stepwise.
As it was already mentioned the interferences might play a big role. A significant contribution of the pp$K^-$ could vanish due to destructive interference and the resulting spectrum would still be comparable with the experimental results. For that reason the phase space factor of the pp$K^-$ wave $a_2^{\mathrm{pp}K^-}$ (Equation 6.7) was not fixed to allow for the maximal possible destructive interference with other transition waves in the BG-PWA fitting.
It was already shown, that the predicted values for the mass and the width vary between different theoretical calculations. For that reason the scanning procedure was done for different values of the mass and the width. As background assumptions the five sets with the best results for the fitting without a pp$K^-$ wave are taken. These assumption are named according to the nomenclature given in Equation 6.8. The full list of values, for which the scanning was applied, is shown in Table 6.6.

| $M_{\mathrm{pp}K^-}$ (GeV/c$^2$) | $\Gamma_{\mathrm{pp}K^-}$ (MeV/c$^2$) | pp$K^-$ Waves | Background Assumption |
|---|---|---|---|
| 2.205 | 20 | $0^+$ | 000113 |
| 2.215 | 35 | $1^-$ | 010110 |
| 2.225 | 50 | $2^+$ | 011103 |
| 2.235 | 60 | | 110103 |
| 2.245 | 80 | | 110112 |
| 2.255 | | | |
| 2.265 | | | |
| 2.275 | | | |
| 2.285 | | | |
| 2.295 | | | |
| 2.305 | | | |

Table 6.6: List of value for which the upper limit of pp$K^-$ production was determined. As background assumptions the five sets with the best results for the fitting without a pp$K^-$ wave are taken. These assumption are named according to the nomenclature given in Equation 6.8.

An example for the change of the invariant mass spectrum of the solution of the PWA with different pp$K^-$ amplitudes is shown in Figure 6.18. The black crosses are the experimental data. The red line corresponds to the result of the BG-PWA for background solution 000113, a pp$K^-$ mass of 2.305 GeV/c$^2$ and a pp$K^-$ width of 20 MeV/c$^2$ for the production wave $0^+$. The different panels show the results for an increasing amplitude of the pp$K^-$ corresponding to a relative contribution of 0% (a), 0.63 % (b) , 3.18 % (c) and 10.89 % (d). In this example the contribution of pp$K^-$ like in panel (d) can be clearly excluded. To extract the upper limit for certain solution, the confidence level method is used.

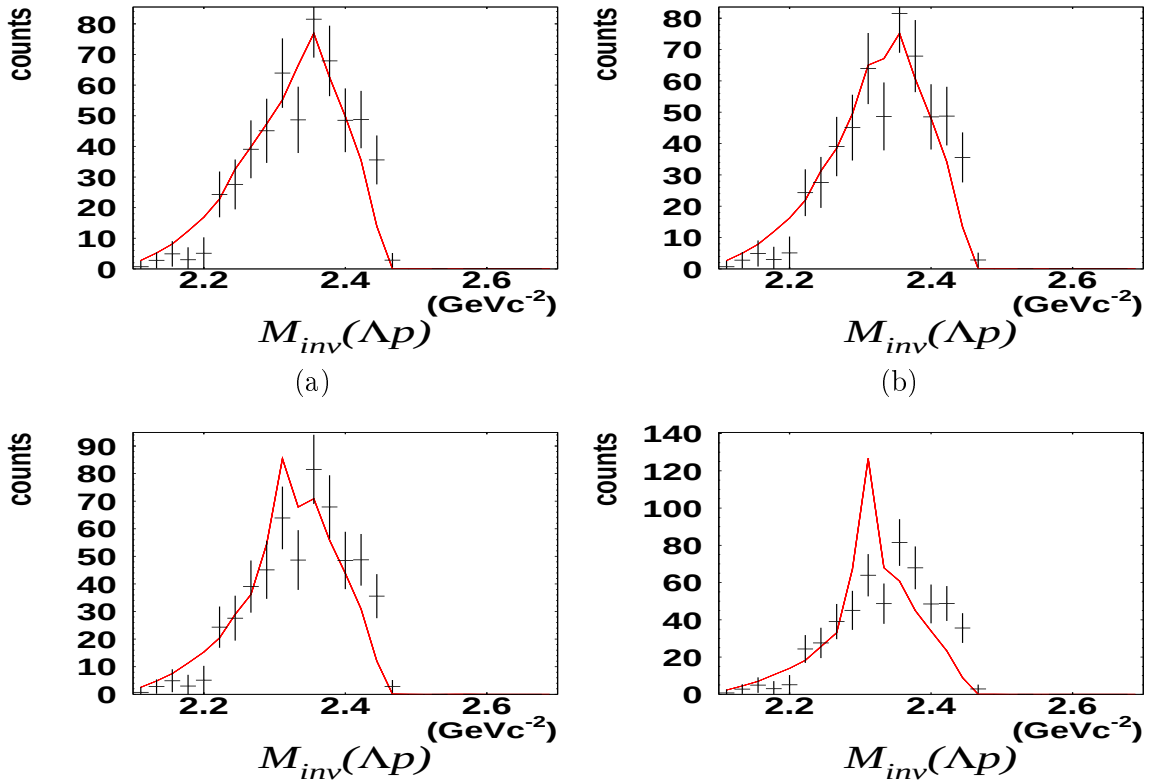


Figure 6.18: PWA Results with different relative contribution of pp$K^-$ ( 0% (a), 0.63 % (b) , 3.18 % (c) and 10.89 % (d)). The background solution 000113 is used. The pp$K^-$ is produce width a mass of 2.305 GeV/c$^2$ and a width of 20 MeV/c$^2$ in the production wave $0^+$.

### Confidence Level

In particle physics the application of the confidence level method is well suited, to express the significance of a model including a signal based on the experimental data. Especially for the extraction of a small signal in a spectrum with a dominant background contribution the confidence level is a good quantity. A confidence level, normally expressed in CL=1-$\alpha$, can be interpreted in that way, that if the same experiment would be repeated, in CL percent of these an agreement between model and data as good, or better then then observed one in this case is expected. Furthermore this method does not only allow to include particle signals, it can also be used to exclude particle yields of certain levels.
The significance of the hypothesis $\mu$ is quantified by the so called p value $p_\mu$. A hypothesis is accepted, if the condition

$$p_\mu > \alpha = 1 - CL, \tag{6.9}$$

is fulfilled and rejected otherwise.
The central point in this method is, which discrepancy variable is used for the calculation of the $p_\mu$. In literature [BCKK11] different variable are discussed.
In our analysis we decided to use the method based on the Pearson $\chi^2$ distribution, which is

calculated by the Equation 6.10:

$$\chi^2_{signal} = \sum_{bins} \frac{(x_{exp.} - x_{PWA})^2}{\sigma^2_{Exp} + \sigma^2_{PWA}} \tag{6.10}$$

with the values $x_{exp.}$ and $x_{PWA}$ and the errors $\sigma_{Exp}$ and $\sigma_{PWA}$ corresponding to the experiment data and PWA result, respectively. In contrast to the $\chi^2$ value, which is used to compare the experimental results with the different outcome of the simulation (see Equation 6.1), the $\chi^2_{signal}$ is calculated just in the signal region (2.2 GeV/c$^2$<$Inv_{\Lambda,p}$<2.4 GeV/c$^2$) of the invariant mass spectrum of $\Lambda$ and p. Since an additional signal of pp$K^-$ will appear as a peak in this mass spectrum (see Figure 6.18)[3], a $\chi^2$ value determined in this region will be more sensitive to a discrepancy between experimental data and the PWA results.
From this $\chi^2$ value the $p_\mu$ is calculated by the integration over the $\chi^2$-probability density function ($f_\nu$) from the derived value of $\chi^2_{signal}$ to $\infty$:

$$p_\mu = \int_{\chi^2_{signal}}^{\infty} f_\nu(\chi^2) d\chi^2 = \int_{\chi^2_{signal}}^{\infty} \frac{1}{2^{\frac{\nu}{2}}\Gamma\left(\frac{\nu}{2}\right)} \left(\chi^2\right)^{\frac{\nu}{2}-1} \exp\left(-\frac{1}{2}\chi^2\right) d\chi^2. \tag{6.11}$$

In the calculation the probability density function $f_\nu(\chi^2)$ of a standard $\chi^2$ distribution is used, with the degree of freedom $\nu$. This assumption is valid for a sufficient statistic in the bin (>5) [Bae14].
Since our signal hypothesis consists mainly of background the standard CL method has to be modified for our proposes. In this case the confidence level for the background has to be taken into account - according to Equation 6.12 [Jun99] [B$^+$12].

$$CL_s = \frac{CL_{S+B}}{CL_B}, \tag{6.12}$$

with the confidence level for the signal $CL_s$, the background $CL_B$ and Signal plus Background $CL_{S+B}$. The resulting modified acceptance criteria is shown in Equation 6.13:

$$p_\mu > \alpha\,(1 - p_0)\,, \tag{6.13}$$

with $p_0$ being the p value for the background only case. This method allows to take also the quality of the five background description, into account, even the differences are very small.

### Upper Limit

Using the Confidence Level method we have an adequate tool to determine the exclusion limit for the pp$K^-$. This allows the determination of an upper limit.
For each result of the BG-PWA using the different parameter set, described in Paragraph 6.5.2, the value $\frac{p_\mu}{1-p_0}$ can be calculated.

[3] In Figure 6.5 one can see, that also the distribution of the Helicity angle $\Theta^{RFK\Lambda}$ $p\Lambda$ shows a clear peak structure for the pp$K^-$ channel. Since this distribution is influenced by a possible anisotropic decay of the pp$K^-$ it is not used.

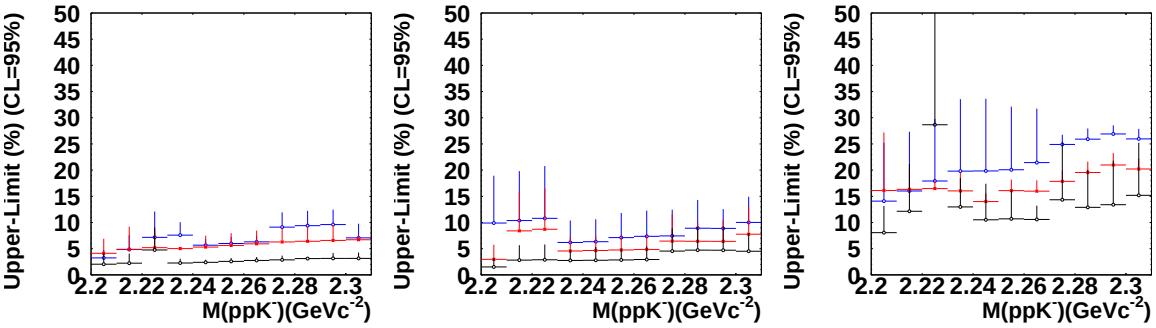


(a) (b) (c)

Figure 6.19: Upper Limit for the relative contribution of the pp$K^-$ (given in %) versus the its mass. The black crosses correspond to width of 20 MeV/c$^2$,the red crosses for 35 MeV/c$^2$ and the black crosses for 50 MeV/c$^2$. In panel (a) the upper limit is given for the $0^+$, in (b) for the $1^-$ and in (c) for the $2^+$ transition wave.

The upper limit is determined by the maximal amplitude of the pp$K^-$ for which this value is above 5% (for a confidence level of 95%).
In Figure 6.19 an example for the upper limits for the relative contribution of the pp$K^-$ at a confidence level (CL) of 95% is plotted against its mass, which is used in the BG-PWA. In this figure the upper limits for the background assumption 000113 are shown. The black crosses correspond to the width of the pp$K^-$ of 20 MeV/c$^2$, the red crosses for 35 MeV/c$^2$ and the black crosses for 50 MeV/c$^2$. The full set of spectra is shown in Appendix I.a.
The error shown in this spectrum results from the stepwise increase of the amplitude.

| [%] | Mass(GeV/c$^2$) | | | | | |
|---|---|---|---|---|---|---|
| $J^P$ | 2.205 | 2.215 | 2.225 | 2.235 | 2.245 | 2.255 |
| $0^+$ | $2.05^{+2.1}$ | $3.21^{+2.6}$ | $4.77^{+4.2}$ | $3.25^{+0.1}$ | $2.41^{+0.5}$ | $3.72^{+0.1}$ |
| $2^+$ | $10.08^{+8.6}$ | $18.88^{+18.7}$ | $28.66^{+26.2}$ | $12.98^{+5.5}$ | $10.52^{+6.8}$ | $10.7^{+5.4}$ |
| $1^-$ | $1.74^{+2.3}$ | $2.84^{+3.2}$ | $3.32^{+3.1}$ | $3.24^{+2.9}$ | $2.8^{+2.5}$ | $3.34^{+3.1}$ |

| [%] | Mass(GeV/c$^2$) | | | | |
|---|---|---|---|---|---|
| $J^P$ | 2.265 | 2.275 | 2.285 | 2.295 | 2.305 |
| $0^+$ | $2.76^{+0.6}$ | $4.19^{+0}$ | $3.12^{+0}$ | $4.57^{+0}$ | $4.81^{+1.4}$ |
| $2^+$ | $10.58^{+2.6}$ | $14.34^{+10.9}$ | $12.9^{+7.1}$ | $13.4^{+8.4}$ | $15.19^{+10}$ |
| $1^-$ | $3.43^{+3.3}$ | $4.55^{+4.3}$ | $4.73^{+4.4}$ | $4.72^{+4.4}$ | $4.88^{+4.5}$ |

Table 6.7: Upper limit value for relative contribution of pp$K^-$ - given in % - for a width $\Gamma$=20 MeV/c$^2$. The table shows the values for different initial proton-proton waves, different background approximations and pp$K^-$ masses.

For the lower value of the width the experimental data are more sensitive to the a signal. Here the upper limit is lower with values between 10% and 20%. The higher value of 28.66% for the wave $2^+$ at width 20 GeV/c$^2$ and Mass 2.225 GeV/c$^2$ originates from the step-like structure, which is visible in the invariant mass of p, $\Lambda$ in the experimental data (see Figure 6.18).

From these spectra one can see, that the upper limit in the $2^+$ production channel is much higher than for the other two production waves, which indicates, that this production wave allows more destructive interference with other channels. Since the different waves behave differently the upper limit values for each wave is shown separately in Table 6.7-Table 6.11 for the different widths.
The same results can be seen also for the broader width of 35 MeV/c$^2$ and 50 MeV/c$^2$. For the case of the width 60 MeV/c$^2$ and 80 MeV/c$^2$ the difference between the different possible production waves for the pp$K^-$ reduces. This indicates, that for these width the different suppression due to interference plays a minor role and the sensitivity of the experimental data for a signal from a pp$K^-$ reduces, which translates in rather high values for the upper limit of about 30% to 40%.

| [%] | Mass(GeV/c$^2$) | | | | | |
|---|---|---|---|---|---|---|
| $J^P$ | 2.205 | 2.215 | 2.225 | 2.235 | 2.245 | 2.255 |
| $0^+$ | $4.13^{+2.7}$ | $4.9^{+4.3}$ | $5.21^{+3.3}$ | $5.02^{+0}$ | $5.31^{+2.1}$ | $5.63^{+2.3}$ |
| $2^+$ | $16.1^{+11}$ | $16.33^{+3.9}$ | $16.48^{+1.6}$ | $16.03^{+3.4}$ | $14^{+1.5}$ | $16.09^{+2.1}$ |
| $1^-$ | $6.02^{+5.6}$ | $8.4^{+7.5}$ | $8.72^{+7.7}$ | $4.57^{+2.6}$ | $4.67^{+2.6}$ | $4.77^{+2.7}$ |

| [%] | Mass(GeV/c$^2$) | | | | |
|---|---|---|---|---|---|
| $J^P$ | 2.265 | 2.275 | 2.285 | 2.295 | 2.305 |
| $0^+$ | $5.93^{+2.5}$ | $6.29^{+2.7}$ | $6.42^{+2.8}$ | $6.76^{+1.2}$ | $7.15^{+1}$ |
| $2^+$ | $15.99^{+2}$ | $17.86^{+2}$ | $19.56^{+2}$ | $20.99^{+2.3}$ | $20.22^{+1.9}$ |
| $1^-$ | $4.86^{+2.7}$ | $6.45^{+5.1}$ | $6.43^{+3.4}$ | $6.76^{+4.7}$ | $7.77^{+5.2}$ |

Table 6.8: Upper limit value for relative contribution of pp$K^-$ - given in % - for a width $\Gamma$=35 MeV/c$^2$. The table shows the values for different initial proton-proton waves, different background approximations and pp$K^-$ masses.

| [%] | Mass(GeV/c$^2$) | | | | | |
|---|---|---|---|---|---|---|
| $J^P$ | 2.205 | 2.215 | 2.225 | 2.235 | 2.245 | 2.255 |
| $0^+$ | $3.25^{+1.5}$ | $4.84^{+2.7}$ | $7.17^{+4.9}$ | $7.59^{+2.4}$ | $5.68^{+1.1}$ | $6^{+1.2}$ |
| $2^+$ | $14.09^{+11.1}$ | $16.02^{+11.3}$ | $18.99^{+1.7}$ | $19.82^{+13.7}$ | $19.85^{+13.7}$ | $20.07^{+12}$ |
| $1^-$ | $9.9^{+9}$ | $10.38^{+9.4}$ | $12.73^{+12.1}$ | $6.19^{+4.1}$ | $6.34^{+4.2}$ | $7.12^{+4.6}$ |

| [%] | Mass(GeV/c$^2$) | | | | |
|---|---|---|---|---|---|
| $J^P$ | 2.265 | 2.275 | 2.285 | 2.295 | 2.305 |
| $0^+$ | $6.31^{+1.1}$ | $9.13^{+2.8}$ | $9.4^{+2.8}$ | $9.61^{+2.8}$ | $9.24^{+2.3}$ |
| $2^+$ | $21.44^{+10.2}$ | $24.91^{+1.8}$ | $25.92^{+2}$ | $26.9^{+1.6}$ | $25.97^{+1.9}$ |
| $1^-$ | $7.36^{+4.9}$ | $7.45^{+5}$ | $8.91^{+5.4}$ | $8.88^{+3.6}$ | $10.01^{+4.9}$ |

Table 6.9: Upper limit value for relative contribution of pp$K^-$ - given in % - for a width $\Gamma$=50 MeV/c$^2$. The table shows the values for different initial proton-proton waves, different background approximations and pp$K^-$ masses.

| [%] | Mass(GeV/c$^2$) | | | | | |
|---|---|---|---|---|---|---|
| $J^P$ | 2.205 | 2.215 | 2.225 | 2.235 | 2.245 | 2.255 |
| $0^+$ | $6.14^{+5.8}$ | $5.6^{+3.4}$ | $11.4^{+8.8}$ | $16.62^{+15.5}$ | $19.08^{+17.3}$ | $20.07^{+18.2}$ |
| $2^+$ | $15.2^{+1.1}$ | $17.9^{+1.6}$ | $19.7^{+1.6}$ | $23.66^{+0.5}$ | $23.86^{+0.7}$ | $23.86^{+0.8}$ |
| $1^-$ | $10.13^{+8.2}$ | $10.61^{+8.7}$ | $11.05^{+9.3}$ | $22.02^{+21.1}$ | $17.25^{+16.3}$ | $23.01^{+22.1}$ |

| [%] | Mass(GeV/c$^2$) | | | | |
|---|---|---|---|---|---|
| $J^P$ | 2.265 | 2.275 | 2.285 | 2.295 | 2.305 |
| $0^+$ | $26.85^{+24.3}$ | $32.96^{+32.3}$ | $33.81^{+32.9}$ | $31.23^{+28.9}$ | $31.29^{+28.6}$ |
| $2^+$ | $31.55^{+5.4}$ | $27.75^{+1.1}$ | $30.84^{+7.9}$ | $14.16^{+14.7}$ | $13.72^{+14.3}$ |
| $1^-$ | $23.34^{+21.5}$ | $18.1^{+16.1}$ | $21.47^{+19.7}$ | $36.27^{+34.5}$ | $29.63^{+27.5}$ |

Table 6.10: Upper limit value for relative contribution of pp$K^-$ - given in % - for a width $\Gamma$=60 MeV/c$^2$. The table shows the values for different initial proton-proton waves, different background approximations and pp$K^-$ masses.

| [%] | Mass(GeV/c$^2$) | | | | | |
|---|---|---|---|---|---|---|
| $J^P$ | 2.205 | 2.215 | 2.225 | 2.235 | 2.245 | 2.255 |
| $0^+$ | $12.06^{+9.1}$ | $12.86^{+9.2}$ | $13.62^{+10.3}$ | $26.56^{+23.5}$ | $34.35^{+32.8}$ | $35.75^{+33.1}$ |
| $2^+$ | $21.11^{+9.4}$ | $22.8^{+11}$ | $24.21^{+5.7}$ | $29.54^{+10.4}$ | $41.62^{+13.7}$ | $40.57^{+10}$ |
| $1^-$ | $10.73^{+9.4}$ | $9.94^{+8.5}$ | $10.32^{+9}$ | $17.5^{+15.8}$ | $17.9^{+16.2}$ | $18.22^{+16}$ |

| [%] | Mass(GeV/c$^2$) | | | | |
|---|---|---|---|---|---|
| $J^P$ | 2.265 | 2.275 | 2.285 | 2.295 | 2.305 |
| $0^+$ | $37.15^{+34.6}$ | $45.18^{+42.6}$ | $39.19^{+35.4}$ | $39.75^{+35.3}$ | $32.97^{+29.2}$ |
| $2^+$ | $40.01^{+14.6}$ | $35.4^{+1.2}$ | $40.9^{+11.5}$ | $35.92^{+1.1}$ | $36.68^{+0}$ |
| $1^-$ | $22.28^{+18.4}$ | $24.6^{+14.9}$ | $41.92^{+28.7}$ | $38.57^{+24.3}$ | $39.29^{+26.1}$ |

Table 6.11: Upper limit value for relative contribution of pp$K^-$ - given in % - for a width $\Gamma$=80 MeV/c$^2$. The table shows the values for different initial proton-proton waves, different background approximations and pp$K^-$ masses.

### Upper limit of pp$K^-$ Cross Section

Finally from the obtained upper limits for the relative contribution of the pp$K^-$ the upper limit for the cross section can be calculated. This can be done using as a reference the total p$K^+\Lambda$ cross section, which can be extracted from literature. In Figure 6.20 the measured values for the cross section (black crosses) are plotted versus the excess energy $\epsilon$ [AS$^+$06a, AES$^+$10, AB$^+$10, AESBB$^+$13, FS85].

Since no measurement for the excess energy of the present experiment of $\epsilon$=508 MeV exist, this value has to extracted by an extrapolation. This is done with the phase space function fitting to the data points [SCLR98]:

$$\sigma(\epsilon) = a\left(1 - \frac{s_0}{(\sqrt{s_0}+\epsilon)^2}\right)^b \left(\frac{s_0}{(\sqrt{s_0}+\epsilon)^2}\right)^c, \tag{6.14}$$

with the threshold energy for the reaction p+p→p$K^+\Lambda$ of $s_0$=2.314GeV and the free parameters a,b,c. The fitted function is represented by the black curve in Figure 6.20. The blue lines

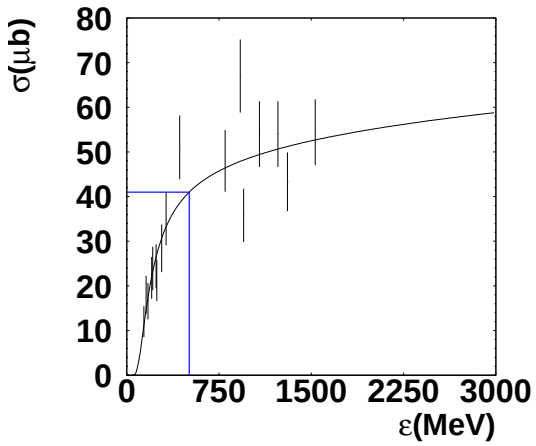


Figure 6.20: Total production cross section of the p$K^+\Lambda$ final state versus the excess energy $\epsilon$. The black lines show the phase space fit of the literature values [AS$^+$06a, AES$^+$10, AB$^+$10, AESBB$^+$13, FS85] according to Equation 6.14. The blue line indicates the extrapolated cross section for our experiment.

indicate the value for our experiment, for which are cross section of $\sigma_{\mathrm{p}K^+\Lambda} = 41.0 \pm 12.8\mu$b was extracted.
This value can be used to calculate upper limits for the cross section of the pp$K^-$, which are listed in Table 6.12. For the lower width of 20 MeV/c$^2$ and 30 MeV/c$^2$ nearly for all mass values a cross section higher than 10$\mu$b can be excluded by our analysis. Especially the low value of the upper limit for a width 20 MeV/c$^2$ could provide constraints on the production of deeply bound states, which are predicted with small widths.
For broader pp$K^-$ the upper limit exceed the value of 15$\mu$b which would be very strong contribution of the pp$K^-$. Thus the widths of 60 MeV/c$^2$ and 80 MeV/c$^2$ can not provide a strong constraint for theoretical predictions.
Nevertheless the results are able to provide some constraints for further theoretical calculations.

| $\mu$b | Mass(GeV/c$^2$) | | | |
|---|---|---|---|---|
| $\Gamma$(MeV/c$^2$) | 2.205 | 2.215 | 2.225 | 2.235 |
| 20 | $4.1\pm1.2^{+3.5}$ | $7.7\pm2.4^{+7.6}$ | $11.7\pm3.6^{+10.7}$ | $5.3\pm1.6^{+2.2}$ |
| 35 | $6.6\pm2^{+4.5}$ | $6.6\pm2^{+1.5}$ | $6.7\pm2.1^{+0.6}$ | $6.5\pm2^{+1.3}$ |
| 50 | $5.7\pm1.8^{+4.5}$ | $6.5\pm2^{+4.6}$ | $7.7\pm2.4^{+0.6}$ | $8.1\pm2.5^{+5.6}$ |
| 60 | $6.2\pm1.9^{+5}$ | $7.3\pm2.2^{+5.9}$ | $8\pm2.5^{+6.7}$ | $9.7\pm3^{+8.4}$ |
| 80 | $8.6\pm2.7^{+3.8}$ | $9.3\pm2.9^{+4.5}$ | $9.9\pm3^{+2.3}$ | $12.1\pm3.7^{+4.2}$ |

| $\mu$b | Mass(GeV/c$^2$) | | | |
|---|---|---|---|---|
| $\Gamma$(MeV/c$^2$) | 2.245 | 2.255 | 2.265 | 2.275 |
| 20 | $4.3\pm1.3^{+2.7}$ | $4.3\pm1.3^{+2.2}$ | $4.3\pm1.3^{+1}$ | $5.8\pm1.8^{+4.4}$ |
| 35 | $5.7\pm1.7^{+0.6}$ | $6.5\pm2^{+0.8}$ | $6.5\pm2^{+0.8}$ | $7.3\pm2.2^{+0.8}$ |
| 50 | $8.1\pm2.5^{+5.6}$ | $8.2\pm2.5^{+4.9}$ | $8.7\pm2.7^{+4.1}$ | $10.2\pm3.1^{+0.7}$ |
| 60 | $9.7\pm3^{+8.4}$ | $9.7\pm3^{+7.9}$ | $12.9\pm4^{+10.3}$ | $13.5\pm4.2^{+13.2}$ |
| 80 | $17\pm5.3^{+5.6}$ | $16.6\pm5.1^{+4.1}$ | $16.4\pm5.1^{+5.9}$ | $18.5\pm5.7^{+17.4}$ |

| $\mu$b | Mass(GeV/c$^2$) | | |
|---|---|---|---|
| $\Gamma$(MeV/c$^2$) | 2.285 | 2.295 | 2.305 |
| 20 | $5.2\pm1.6^{+2.9}$ | $5.4\pm1.7^{+3.4}$ | $6.2\pm1.9^{+4.1}$ |
| 35 | $8\pm2.5^{+0.8}$ | $8.6\pm2.6^{+0.9}$ | $8.2\pm2.5^{+0.7}$ |
| 50 | $10.6\pm3.3^{+0.8}$ | $11\pm3.4^{+0.6}$ | $10.6\pm3.3^{+0.7}$ |
| 60 | $13.8\pm4.3^{+13.4}$ | $15.3\pm4.7^{+1.7}$ | $16.9\pm5.2^{+16.9}$ |
| 80 | $17.1\pm5.3^{+11.7}$ | $16.2\pm5^{+14.4}$ | $16.1\pm5^{+10.7}$ |

Table 6.12: Upper limit for the production cross section of the pp$K^-$ for different value of the mass and the width. The cross section is given in $\mu$b. The first error value are origination from the extrapolation of the total cross section. The second error originates in the step procedure of the amplitude scan.

# Chapter VII

# Conclusion and Outlook

## 7.1 Summary

### 7.1.1 Λ Trigger Performance

The present work is dedicated to the data analysis of the proton proton experiment, which has taken place in the year 2009 at the FOPI spectrometer at GSI in Darmstadt. In this experiment a new detector named SiΛViO was installed for the experiment, which was used for triggering and tracking.
The hit points of this detector could be combined with the tracks in the forward hemisphere with a matching efficiency of 91.2± 0.6 %.
Due to the hit point provided by the SiΛViO detector the momentum resolution of tracks emitted to the forward hemisphere could be improved by 5 % for protons and 4 % for pions.
The ability to improve the vertex resolution for Λ particles by a factor of 10 - exploiting the SiΛViO hit information - allows to reconstruct Λ particles inclusively with a mass resolution of $5.3\,\mathrm{MeV/c^2}$. This value extracted for the experimental data sample is comparable with a full-scale simulation.
The trigger capabilities of SiΛViO were determined by the analysis of the difference in the event signature for the first level (LVL1) and second level trigger (LVL2), which includes the SiΛViO trigger information. In this work is was shown, that the SiΛViO trigger conditions allows to suppress off-vertex events by 90 %.
Furthermore the enhancement of events containing a Λ particle was determined analysing the inclusive reconstructed Λ particles. Due to the limited statistics of the LVL1 sample, a systematic error must be considered for the experimental ratio. This ratio was found to be $14.1 \pm 7.9(stat)^{+4.3}_{-0.5}$. By including the hyperon reconstruction and the contribution of the empty-target events in the simulation framework, a final value of $15.9 \pm 2.8(stat)^{+5.4}_{-0.5}$ was obtained for proton-proton simulations, which is in very good agreement with the experimental findings. These experimental findings were published in [MBF+14].

### 7.1.2 Exclusive Analysis

The main part of the analysis is dedicated to the extraction of the signal from the exclusive reaction $\mathrm{p+p} \rightarrow \mathrm{p}K^+\Lambda$ .
The interesting events were selected by different analysis steps, beginning with a pre selection of events containing four charged particles. The further selection of the exclusive events was

performed by a selection of $K^+$ candidates. These were selected from tracks, which have been measured in the Central Drift Chamber matched with a hit point in the Resistive Plate Chamber of FOPI (Matching efficiency: $62 \pm 0.5\%$). Furthermore the exclusive events were selected by a cut on $\Lambda$ candidates and the selection of a kinematical refit.
For the description of the remaining background a sideband technique was used. This method provides an excellent description of the miss identification background, which could be subtracted in the final spectra of the experimental data.
Finally a sample of 903 p$K^+\Lambda$ event could be extracted. The background from the production of p$K^+$ $\Sigma^0$ was determined to be 1/14.8.

### 7.1.3 p$K^+\Lambda$ Comparison with Models

The experimental results were compared with different simulation models. The simulation framework was adjusted to the experimental conditions exploiting elastic proton proton scattering reactions.
The comparison with the phase space simulation of the free p$K^+\Lambda$ and channel with an intermediate $N^*$ resonance leads to the result, that the data cannot be reproduced. On the one hand it was shown, that the angular distribution diverges significantly, although the phase space simulation was done with an angular distribution, which has been obtained from previous experiments. On the other hand it was shown, that the discrepancy cannot be explained just by a wrong angular distribution.
The comparison of the experimental data with UrQMD transport model leads to the conclusion that only the kinematics of the $K^+$ , like missing mass of $K^+$ and its center of mass angle, can be reproduced sufficiently. The kinematical distribution of the proton and the $\Lambda$ cannot be reproduced. Furthermore, the conclusion could be drawn, that the relative contribution of $N^*$ resonances is shifted to higher mass states than in the experimental data, which is indicated from the invariant mass spectrum of $K^+$ and $\Lambda$. This results shows, that the $N^*$ production channels are not correctly included in the transport model.
With the Bonn Gatchina Partial Wave Analysis (BG-PWA) framework a nice description of the experimental data could be achieved. With the BG-PWA tool, the contribution of different transition waves could be fitted to the experimental data. For a systematical analysis the BG-PWA fitting was applied with inclusion of different $N^*$ resonances and initial proton-proton states. On the one hand the conclusion could be drawn, that the model does not favour one single solution, which originates in the limited statistics of the experimental data and the lack of spin observable like a polarized target or beam. On the other hand it was shown, that BG-PWA can provide reasonable results, even with a low amount of statistics. The results of the BG-PWA delivers a clear trend, with an dominant production of $N^*$ resonances, which fits to the experimental finding of the COSY-TOF Collaboration. Especially the ratio of $N^*(1650)$ and $N^*(1710)$ shows a behaviour, which was indicated by those results. Another important result, which can be drawn from the results is the importance of interference between different transition waves. This effect seems to have a major influence on the experimental data, since the incoherent sum of different channels could not provide reasonable results.

### 7.1.4 Upper Limit pp$K^-$

Based on the successful description of the experimental data with known sources by the BG-PWA framework an upper limit for the pp$K^-$ channel in the reaction p+p→p$K^+\Lambda$ could be determined. For this analysis three possible transition waves of the pp$K^-$ were included in the BG-PWA. The amplitude of this state was increased stepwise, while the phase parameter was let free, to allow maximal destructive interference.
A systematical scanning procedure was performed for eleven values of the mass between 2.205 and 2.305 GeV/c$^2$ and five different values of the width (20, 35, 50, 60, 80 MeV/c$^2$). For the three lowest widths a significant difference between the results of the different transition wave of the pp$K^-$ was seen. This shows, that the analysis is sensitive for interference effects, which are different for different transition waves. For the highest two widths this could not be observed, which indicates, that due to the statistical error the experimental results are not sensitive anymore for this effect. Also a quite high value for the upper limit was deduced, which indicates the reduced sensitivity of the data. From the relative contribution obtained from the BG-PWA the upper limit of the pp$K^-$ cross sections in the reaction p+p→p$K^+\Lambda$ could be deduced. The total cross section of the reaction p+p→p$K^+\Lambda$ of $\sigma_{pK^+\Lambda} = 41.0 \pm 12.8\mu$b was extracted from a phase space fit of previous experimental results.
The resulting values for the cross section of the pp$K^-$ range between $4.1\pm1.2^{+3.5}$μb and $11.7\pm3.6^{+10.7}$μb for a width of 20 MeV/c$^2$, between $5.7\pm1.7^{+0.6}$μb and $8.6\pm2.6^{+0.9}$μb for a width of 35 MeV/c$^2$, between $5.7\pm1.8^{+4.5}$μb and $11.0\pm3.4^{+0.6}$μb for a width of 50 MeV/c$^2$, between $6.2\pm1.9^{+5.0}$μb and $16.9\pm5.2^{+16.9}$μb for a width of 60 MeV/c$^2$, between $8.6\pm2.7^{+3.8}$μb and $18.5\pm5.7^{+17.4}$μb for a width of 80 MeV/c$^2$.
Comparing these results to the outcome of the LEPS experiment (see Section 1.4), we can see, that the upper limits are significantly higher than in their results. Besides the difference in the statistical error, the difference in the upper limit might also have further reasons. On the one hand the production mechanism in the LEPS experiment and this present experiment are different. On the other hand in this analysis also interference effects have been included. Due to this a contribution of the pp$K^-$ could be washed out, which reduces the strength in the final spectrum. With this results it was shown, that even if no peak structure is visible in the final spectrum a production of the pp$K^-$ must not be ruled out.

## 7.2 Outlook

Since it was shown in this analysis that already with a small amount of statistics a conclusion about the production can be drawn from an analysis with the BG-PWA. A bigger amount of statistics could provide a more detailed analysis of the reaction p+p→p$K^+\Lambda$ . As a logical consequence an analysis initiative was established to proceed with this analysis.
A huge set of statistics, obtained by the COSY-TOF, the DISTO and the HADES collaboration, has been taken in the last years. In Table 7.1 the results from the different experiments are listed, together with the amount of obtained statistics of the reaction p+p→p$K^+\Lambda$ . Furthermore, this set of experiments does not only provide very good statistic, they also cover a broad range of center-of-mass energies $\sqrt{s}$. In Table 7.1 also the excess energy $\epsilon_{pK^+\Lambda}$ for the production of p$K^+\Lambda$ and for the production of pp$K^-$ ($\epsilon_{ppK^-}$ ) are listed. On the one hand only four experiments - including the one presented in this work - have taken data with an energy high enough to produce a pp$K^-$. On the other hand the experiment with lower energy is necessary, to improve the description of the underlying background process, like the

production of different $N^*$ resonances. Furthermore some of the data sets were taken with polarized beams or targets, which provides further constraint for the analysis.

| experiment | $\sqrt{s}$ (GeV) | $\epsilon_{pK^+\Lambda}$ | $\epsilon_{ppK^-}$ | statistics | polar. |
|---|---|---|---|---|---|
| COSY-TOF [AS$^+$06a] | 2.63 | 84.87 | -231.40 | 791 | N |
| COSY-TOF [AS$^+$06a] | 2.66 | 114.91 | -201.35 | 1037 | N |
| COSY-TOF [Rit13] | 2.67 | 121.56 | -194.71 | 160000 | ? |
| COSY-TOF [AS$^+$06a] | 2.72 | 171.05 | -145.22 | 4323 | N |
| DISTO [M$^+$10, Mag01] | 2.75 | 200.44 | -115.83 | 121000 | Y |
| COSY-TOF [M.R11] | 2.75 | 203.69 | -112.58 | 43662 | Y |
| COSY-TOF [AES$^+$10] | 2.75 | 203.69 | -112.58 | 7228 | N |
| COSY-TOF [AES$^+$10] | 2.75 | 203.69 | -112.58 | 15372 | N |
| COSY-TOF [AB$^+$10] | 2.79 | 238.95 | -77.32 | 89684 | N |
| COSY-TOF [AESBB$^+$13] | 2.79 | 245.70 | -70.57 | 30000 | N |
| COSY-TOF [AB$^+$10] | 2.83 | 284.06 | -32.21 | 3322 | N |
| COSY-TOF [AES$^+$10] | 2.83 | 284.06 | -32.21 | 5791 | N |
| COSY-TOF [AES$^+$10] | 2.87 | 318.86 | 2.60 | 6263 | N |
| DISTO [M$^+$10, Mag01] | 2.87 | 318.86 | 2.60 | 304000 | Y |
| DISTO [M$^+$10, Mag01, B$^+$99] | 2.98 | 430.48 | 114.21 | 424000 | Y |
| FOPI (this work) | 3.06 | 508.97 | 192.70 | 903 | N |
| HADES [Epp14] | 3.18 | 629.33 | 313.06 | 20000 | N |

Table 7.1: List of available statistics of the reaction p+p→p$K^+\Lambda$ obtained by the COSY-TOF, the DISTO and the HADES collaboration in context with the results from this work. In the list the center-of-mass energy $\sqrt{s}$ (given in GeV), excess energy $\epsilon_{pK^+\Lambda}$ for the p$K^+\Lambda$ production, the excess energy for the production of pp$K^-$ $\epsilon_{ppK^-}$ (both excess energies given in MeV) and the amount of statistics are shown. The data samples, for which a polarized beam respectively target was used, are marked (polar.).

The BG-PWA framework provides the opportunity to analysis several different data set in parallel. The parametrisation of the transition amplitude - presented in the Paragraph 6.4.1 - allows to include, beside the constant and the phase term, an energy dependent term. Exploiting this parameter a combined fit of different data sets can be performed, which improves the reliability of the results.
To perform this combined analysis already a partnership with the different detector collaboration was established. From these groups the experimental data will be provided as well as p$K^+\Lambda$ phase space simulations, which require no further detector specific analysis.
In the first step a separate analysis of the different data set is planned to be performed, to check the reliability of the different data samples. In a second step the different data samples will be merged to provide a combined result.

Besides our planed analysis project, further experiments are planned, which will continue in the search for the pp$K^-$.
One future experiment is the AMADEUS project at the DA$\Phi$NE accelerator at Finuda. In this project a modification of the already existing KLOE-spectrometer [AAA$^+$02] is planned. This spectrometer, consisting of an excellent geometrical acceptance for charged and neutral

particles, shall be upgraded with a helium target surrounding the beam pipe. This should allow to measure the exclusive reaction $K^-$+$^3He$→pp$K^-$+n [Zme07,Kie08].
Another experiment is planned at the J-PARC accelerator facility in Japan. In a dedicated experiment - named E15 - the same reaction as in AMADEUS shell be investigated. At the J-Parc accelerator secondary $K^-$ can be produced. In the E15 experiment a liquid $^3$He target is constructed, surrounded by a magnetic spectrometer with a nearly $4\pi$ acceptance for charge particle. For the detection of neutrons a dedicated detector wall will be used. [A$^+$13]

# Appendix A - Bibliography


[A+03] Andronic, A. et al.: Directed flow in Au + Au, Xe + CsI and Ni + Ni collisions and the nuclear equation of state. In: *Phys.Rev.* C67 (2003), S. 034907. http://dx.doi.org/10.1103/PhysRevC.67.034907. – DOI 10.1103/PhysRevC.67.034907

[A+05a] Adams, John et al.: Experimental and theoretical challenges in the search for the quark gluon plasma: The STAR Collaboration's critical assessment of the evidence from RHIC collisions. In: *Nucl.Phys.* A757 (2005), S. 102–183. http://dx.doi.org/10.1016/j.nuclphysa.2005.03.085. – DOI 10.1016/j.nuclphysa.2005.03.085

[A+05b] Agnello, M. et al.: Evidence for a kaon-bound state pp$K^-$ produced in $K^-$ absorption reactions at rest. In: *Phys.Rev.Lett.* 94 (2005), S. 212303. http://dx.doi.org/10.1103/PhysRevLett.94.212303. – DOI 10.1103/PhysRevLett.94.212303

[A+05c] Andronic, A. et al.: Excitation function of elliptic flow in Au+Au collisions and the nuclear matter equation of state. In: *Phys.Lett.* B612 (2005), S. 173–180. http://dx.doi.org/10.1016/j.physletb.2005.02.060. – DOI 10.1016/j.physletb.2005.02.060

[A+09] Agakishiev, G. et al.: $\phi$ decay: A Relevant source for $K^-$ production at SIS energies? In: *Phys.Rev.* C80 (2009), S. 025209. http://dx.doi.org/10.1103/PhysRevC.80.025209. – DOI 10.1103/PhysRevC.80.025209

[A+10] Agakishiev, G. et al.: In-Medium Effects on $K^0$ Mesons in Relativistic Heavy-Ion Collisions. In: *Phys.Rev.* C82 (2010), S. 044907. http://dx.doi.org/10.1103/PhysRevC.82.044907. – DOI 10.1103/PhysRevC.82.044907

[A+11] Agakishiev, G. et al.: Dielectron production in Ar+KCl collisions at 1.76 AGeV. In: *Phys.Rev.* C84 (2011), S. 014902. http://dx.doi.org/10.1103/PhysRevC.84.014902. – DOI 10.1103/PhysRevC.84.014902

[A+12] Adolph, C. et al.: First Measurement of Chiral Dynamics in $\pi^- \gamma \to \pi^- \pi^- \pi^+$ . In: *Phys.Rev.Lett.* 108 (2012), S. 192001. http://dx.doi.org/10.1103/PhysRevLett.108.192001. – DOI 10.1103/PhysRevLett.108.192001

[A+13] Ajimura, S. et al.: *A search for deeply-bound kaonic nuclear state at the J-PARC {E15} experiment.* http://dx.doi.org/http://dx.doi.org/10.1016/j.nuclphysa.2013.04.013. Version:2013. – {XI} International Conference on Hypernuclear and Strange Particle Physics (HYP2012)

[AAA+02] Adinolfi, M. ; Ambrosino, F. ; Antonelli, A. ; Antonelli, M. ; Anulli, F. et al.: The KLOE electromagnetic calorimeter. In: *Nucl.Instrum.Meth.* A494 (2002), S. 326–331. http://dx.doi.org/10.1016/S0168-9002(02)01488-2. – DOI 10.1016/S0168–9002(02)01488–2

[AB+10] Abdel-Bary, M. et al.: Production of Lambda and $Sigma^0$ hyperons in proton-proton collisions. In: *Eur.Phys.J.* A46 (2010), S. 27–44. http://dx.doi.org/10.1140/epja/i2010-11023-0,10.1140/epja/i2010-11062-5. – DOI 10.1140/epja/i2010–11023–0, 10.1140/epja/i2010–11062–5

[ABB+13] Agakishiev, G. ; Balanda, A. ; Belver, D. ; Belyaev, A.V. ; Berger-Chen, J.C. et al.: Baryonic resonances close to the Kbar-N threshold: the case of Lambda(1405) in pp collisions. In: *Phys. Rev. C* 87 (2013), S. 025201

[ABSW06] Arndt, R.A. ; Briscoe, W.J. ; Strakovsky, I.I. ; Workman, R.L.: Extended partial-wave analysis of $\pi$N scattering data. In: *Phys.Rev.* C74 (2006), S. 045205. http://dx.doi.org/10.1103/PhysRevC.74.045205. – DOI 10.1103/PhysRevC.74.045205

[AES+10] Abd El-Samad, S. et al.: Influence of N*-resonances on hyperon production in the channel pp→p$K^+\Lambda$ at 2.95, 3.20 and 3.30 GeV/c beam momentum. In: *Phys.Lett.* B688 (2010), S. 142–149. http://dx.doi.org/10.1016/j.physletb.2010.03.076. – DOI 10.1016/j.physletb.2010.03.076

[AESBB+13] Abd El-Samad, S. ; Borodina, E. ; Brinkmann, K. T. ; Clement, H. ; Doroshkevich, E. et al.: On the $\Sigma N$ cusp in the pp→p$K^+\Lambda$ reaction. In: *Eur.Phys.J.* A49 (2013), S. 41. http://dx.doi.org/10.1140/epja/i2013-13041-8. – DOI 10.1140/epja/i2013–13041–8

[Aic91] Aichelin, J.: 'Quantum' molecular dynamics: A Dynamical microscopic n body approach to investigate fragment formation and the nuclear equation of state in heavy ion collisions. In: *Phys.Rept.* 202 (1991), S. 233–360. http://dx.doi.org/10.1016/0370-1573(91)90094-3. – DOI 10.1016/0370–1573(91)90094–3

[AKN+11] Anisovich, A.V. ; Klempt, E. ; Nikonov, V.A. ; Sarantsev, A.V. ; Thoma, U.: P-wave excited baryons from pion- and photo-induced hyperon production. In: *Eur.Phys.J.* A47 (2011), S. 27. http://dx.doi.org/10.1140/epja/i2011-11027-2. – DOI 10.1140/epja/i2011–11027–2

[AS+06a] Abdel-Samad, S. et al.: Hyperon production in the channel pp→p$K^+\Lambda$ near the reaction threshold. In: *Phys.Lett.* B632 (2006), S. 27–34. http://dx.doi.org/10.1016/j.physletb.2005.09.086. – DOI 10.1016/j.physletb.2005.09.086

[AS06b] Anisovich, A.V. ; Sarantsev, A.V.: Partial decay widths of baryons in the spin-momentum operator expansion method. In: *Eur.Phys.J.* A30 (2006), S. 427–441. http://dx.doi.org/10.1140/epja/i2006-10102-1. – DOI 10.1140/epja/i2006–10102–1

[AY02] Akaishi, Yoshinori ; Yamazaki, Toshimitsu: Nuclear anti-K bound states in light nuclei. In: *Phys.Rev.* C65 (2002), S. 044005. http://dx.doi.org/10.1103/PhysRevC.65.044005. – DOI 10.1103/PhysRevC.65.044005

[B+97] Best, D. et al.: $K^+$ production in the reaction $^{58}$Ni + $^{58}$Ni at incident energies from 1 AGeV to 2 AGeV. In: *Nucl.Phys.* A625 (1997), S. 307–324. http://dx.doi.org/10.1016/S0375-9474(97)00409-0. – DOI 10.1016/S0375–9474(97)00409–0

[B+99] Balestra, F. et al.: Spin transfer in exclusive Lambda production from polarized-p p collisions at 3.67 GeV/c. In: *Phys.Rev.Lett.* 83 (1999), S. 1534–1537. http://dx.doi.org/10.1103/PhysRevLett.83.1534. – DOI 10.1103/PhysRevLett.83.1534

[B+12] Beringer, J. et al.: Review of Particle Physics (RPP). In: *Phys.Rev.* D86 (2012), S. 010001. http://dx.doi.org/10.1103/PhysRevD.86.010001. – DOI 10.1103/PhysRevD.86.010001

[Bae14] Baeujean, Frederick: *private communication.* 2014

[Bau00] Bauer, Johannes M.: Kinematic fit for the radiative Bhabha calibration of BaBar's electromagnetic calorimeter. (2000)

[BCKK11] Beaujean, F. ; Caldwell, A. ; Kollar, D. ; Kroninger, K.: p-values for model evaluation. In: *Phys.Rev.* D83 (2011), S. 012004. http://dx.doi.org/10.1103/PhysRevD.83.012004. – DOI 10.1103/PhysRevD.83.012004

[Ben07] Benabderrahmane, M.L.: *Measurement of the $K^0$ Inclusive Cross Section in Pion-Induced Reactions at* 1.15 GeV/c, Universität Heidelberg, Dissertation, 2007. http://www-fopi.gsi.de/pub/phd/

[Ber09] Berger, M.: *Si$\Lambda$ViO: Entwicklung eines auf Silizium basierenden Trigger und Tracking Systems*, TU München, Diplom Arbeit, 2009. https://www.e12.ph.tum.de/groups/kcluster/Publications.php

[Bet07] Bethke, Siegfried: Experimental tests of asymptotic freedom. In: *Prog.Part.Nucl.Phys.* 58 (2007), S. 351–386. http://dx.doi.org/10.1016/j.ppnp.2006.06.001. – DOI 10.1016/j.ppnp.2006.06.001

[BGH+77] Braun, O. ; Grimm, H.J. ; Hepp, V. ; Strobele, H. ; Thol, C. et al.: New Information About the Kaon-Nucleon-Hyperon Coupling Constants: G/anti-K n Sigma (1197), G / anti-K n Sigma (1385) and G anti-K n Lambda (1405). In: *Nucl.Phys.* B129 (1977), S. 1. http://dx.doi.org/10.1016/0550-3213(77)90015-3. – DOI 10.1016/0550–3213(77)90015–3

[BGL12] Barnea, N. ; Gal, A. ; Liverts, E.Z.: Realistic calculations of $\bar{K}NN$, $\bar{K}NNN$, and $\bar{K}\bar{K}NN$ quasibound states. In: *Phys.Lett.* B712 (2012), S. 132–137. http://dx.doi.org/10.1016/j.physletb.2012.04.055. – DOI 10.1016/j.physletb.2012.04.055

[BHS+09] Bühler, P ; Hartmann, O ; Schafhauser, M ; Suzuki, K ; Zmeskal, J: *Start counter and target system for the FOPI S349 experiment.* GSI Annual Report, 2009

[BNSSW13] Brinkmann, K. ; Nikonov, V.A. ; Sarantsev, A.V. ; Schulte-Wissermann, M.: *The analysis of the pp→pK$^+\Lambda$ data at beam momenta 2950,3059 and* 3200 MeV/c$^2$. 2013. – Draft from 2013

[BNW05] Borasoy, B. ; Nissler, R. ; Weise, W.: Chiral dynamics of kaon-nucleon interactions, revisited. In: *Eur.Phys.J.* A25 (2005), S. 79–96. http://dx.doi.org/10.1140/epja/i2005-10079-1. – DOI 10.1140/epja/i2005–10079–1

[BR91] Brown, G.E. ; Rho, M.: Scaling effective Lagrangians in a dense medium. In: *Phys.Rev.Lett.* 66 (1991), S. 2720–2723. http://dx.doi.org/10.1103/PhysRevLett.66.2720. – DOI 10.1103/PhysRevLett.66.2720

[BZS+99] Bleicher, M. ; Zabrodin, E. ; Spieles, C. ; Bass, S.A. ; Ernst, C. et al.: Relativistic hadron hadron collisions in the ultrarelativistic quantum molecular dynamics model. In: *J.Phys.* G25 (1999), S. 1859–1896. http://dx.doi.org/10.1088/0954-3899/25/9/308. – DOI 10.1088/0954–3899/25/9/308

[CDE+13] Ceci, S. ; Doring, M. ; Epple, E. et al.: PWA tools in Hadronic Spectroscopy. (2013)

[CER95] CERN: *CERN — Geant.* 1995. –
http://www.asdoc.web.cern.ch/wwwasdoc/geant_html3/geantall.html

[CI86] Capstick, Simon ; Isgur, Nathan: Baryons in a Relativized Quark Model with Chromodynamics. In: *Phys.Rev.* D34 (1986), S. 2809. http://dx.doi.org/10.1103/PhysRevD.34.2809. – DOI 10.1103/PhysRevD.34.2809

[CRL+08] Champion, D.J. ; Ransom, S.M. ; Lazarus, P. ; Camilo, F. ; Bassa, C. et al.: An Eccentric Binary Millisecond Pulsar in the Galactic Plane. In: *Science* 320 (2008), S. 1309–1312. http://dx.doi.org/10.1126/science.1157580. – DOI 10.1126/science.1157580

[Dah08] Dahms, Thorsten: *Dilepton spectra in p+p and Au+Au at RHIC*, Stony Brook University, Diss., 2008

[Dan01] Danielewicz, Pawel: Nuclear equation of state. In: *arXiv* nucl-th/0112006 (2001), S. 24–42

[Daw94] Dawson, S.: Introduction to the physics of Higgs bosons. In: *arXiv* hep-ph/9411325 (1994)

[d'E09] d'Enterria, David ; 1-23A, Landolt-Boernstein V. (Hrsg.): *Jet quenching*. Bd. nucl-ex/0902.2011. Springer Verlag, 2009

[DHW08] Dote, Akinobu ; Hyodo, Tetsuo ; Weise, Wolfram: pp$K^-$ system with chiral SU(3) effective interaction. In: *Nucl.Phys.* A804 (2008), S. 197–206. http://dx.doi.org/10.1016/j.nuclphysa.2008.02.001. – DOI 10.1016/j.nuclphysa.2008.02.001

[DHW09] Dote, Akinobu ; Hyodo, Tetsuo ; Weise, Wolfram: Variational calculation of the pp$K^-$ system based on chiral SU(3) dynamics. In: *Phys.Rev.* C79 (2009), S. 014003. http://dx.doi.org/10.1103/PhysRevC.79.014003. – DOI 10.1103/PhysRevC.79.014003

[DL95] Dong, Shao-Jing ; Liu, Keh-Fei: pi N sigma term and quark spin content of the nucleon. In: *Nucl.Phys.Proc.Suppl.* 42 (1995), S. 322–324. http://dx.doi.org/10.1016/0920-5632(95)00239-6. – DOI 10.1016/0920–5632(95)00239–6

[DLL02] Danielewicz, Pawel ; Lacey, Roy ; Lynch, William G.: Determination of the equation of state of dense matter. In: *Science* 298 (2002), S. 1592–1596. http://dx.doi.org/10.1126/science.1078070. – DOI 10.1126/science.1078070

[DPR+10] Demorest, Paul ; Pennucci, Tim ; Ransom, Scott ; Roberts, Mallory ; Hessels, Jason: Shapiro Delay Measurement of A Two Solar Mass Neutron Star. In: *Nature* 467 (2010), S. 1081–1083. http://dx.doi.org/10.1038/nature09466. – DOI 10.1038/nature09466

[DW07] Dote, Akinobu ; Weise, Wolfram: Study of light kaonic nuclei with a Chiral SU(3): Based anti-K N interaction. In: *Prog.Theor.Phys.Suppl.* 168 (2007), S. 593–597. http://dx.doi.org/10.1143/PTPS.168.593. – DOI 10.1143/PTPS.168.593

[EFK+65] Engler, A. ; Fisk, H.E. ; Kraemer, R.w. ; Meltzer, C.M. ; Westgard, J.B.: Spin of the $Y_0^*(1405)$. In: *Phys.Rev.Lett.* 15 (1965), S. 224. http://dx.doi.org/10.1103/PhysRevLett.15.224. – DOI 10.1103/PhysRevLett.15.224

[EMN+11] Ermakov, K.N. ; Medvedev, V.I. ; Nikonov, V.A. ; Rogachevsky, O.V. ; Sarantsev, A.V. et al.: The study of the proton-proton collisions at the beam momentum 1628 MeV/c. In: *Eur.Phys.J.* A47

(2011), S. 159. http://dx.doi.org/10.1140/epja/i2011-11159-3. – DOI 10.1140/epja/i2011–11159–3

[Epp14] Epple, Eliane: *Measurable consequences of an attractive $\bar{K}N$ interaction.*, TU M$\ddot{\text{u}}$nchen, Dissertation, 2014. https://www.e12.ph.tum.de/groups/kcluster/Publications.php

[Esk95] Eskola, K.J.: Formation and evolution of quark - gluon plasma at RHIC and LHC. In: *Nucl.Phys.* A590 (1995), S. 383C–398C. http://dx.doi.org/10.1016/0375-9474(95)00249-Z. – DOI 10.1016/0375–9474(95)00249–Z

[FCG+07] Frohlich, I. ; Cazon, Lorenzo ; Galatyuk, T. ; Hejny, V. ; Holzmann, R. et al.: Pluto: A Monte Carlo Simulation Tool for Hadronic Physics. In: *PoS* ACAT2007 (2007), S. 076

[FGH+10] Frohlich, I. ; Galatyuk, T. ; Holzmann, R. ; Markert, J. ; Ramstein, B. et al.: Design of the Pluto Event Generator. In: *J.Phys.Conf.Ser.* 219 (2010), S. 032039. http://dx.doi.org/10.1088/1742-6596/219/3/032039. – DOI 10.1088/1742–6596/219/3/032039

[FH11] Fukushima, Kenji ; Hatsuda, Tetsuo: The phase diagram of dense QCD. In: *Rept.Prog.Phys.* 74 (2011), S. 014001. http://dx.doi.org/10.1088/0034-4885/74/1/014001. – DOI 10.1088/0034–4885/74/1/014001

[FHR73] Foeth, H. ; Hammarstroem, R. ; Rubbia, C.: On the localization of the position of the particle along the wire of a multiwire proportional chamber. In: *Nucl.Instrum.Meth.* 109 (1973), S. 521–524. http://dx.doi.org/10.1016/0029-554X(73)90566-1. – DOI 10.1016/0029–554X(73)90566–1

[FKOU95] Fukugita, M. ; Kuramashi, Y. ; Okawa, M. ; Ukawa, A.: Lattice QCD solution to the U(1) problem. In: *Phys.Rev.* D51 (1995), S. 3952–3954. http://dx.doi.org/10.1103/PhysRevD.51.3952. – DOI 10.1103/PhysRevD.51.3952

[FS67] Ferrari, E. ; Serio, S.: Three-Body Associated Production in Proton-Proton Collisions and the One-Boson-Exchange Model. In: *Phys.Rev.* 167 (1967), S. 1298–1308

[FS85] Fuchs, K. ; Soffel, H.C.: Geophysics. In: *Landolt-Börnstein, New Series* Bd. V/2. Heidelberg : Springer-Verlag, 1985, S. 417(a) and 468(b)

[Fuc06] Fuchs, Christian: Kaon production in heavy ion reactions at intermediate energies. In: *Prog.Part.Nucl.Phys.* 56 (2006), S. 1–103. http://dx.doi.org/10.1016/j.ppnp.2005.07.004. – DOI 10.1016/j.ppnp.2005.07.004

[Gal11] Gal, Avraham: Anti-K nuclear interactions and dynamics. In: *Int.J.Mod.Phys.* A26 (2011), S. 438–443. http://dx.doi.org/10.1142/S0217751X11051792. – DOI 10.1142/S0217751X11051792

[GGG+02] Geissel, H. ; Gilg, H. ; Gillitzer, A. ; Hayano, R.S. ; Hirenzaki, S. et al.: Deeply bound 1s and 2p pionic states in Pb-205 and determination of the S wave part of the pion nucleus interaction. In: *Phys.Rev.Lett.* 88 (2002), S. 122301. http://dx.doi.org/10.1103/PhysRevLett.88.122301. – DOI 10.1103/PhysRevLett.88.122301

[GGK+00] Gilg, H. ; Gillitzer, A. ; Knulle, M. ; Munch, M. ; Schott, W. et al.: Deeply bound pi- states in Pb-207 formed in the Pb-208(d, He-3) reaction Part I: Experimental method and results. In: *Phys.Rev.* C62 (2000), S. 025201. http://dx.doi.org/10.1103/PhysRevC.62.025201. – DOI 10.1103/PhysRevC.62.025201

[Goe95] Goebel, G.: *Untersuchung der Bose-Einstein Korrelationen geladener Pionen in relativistischen Schwerionenkollisionen der Systeme Au + Au und Ni + Ni im Energiebereich von 1 AGeV bis 2 AGeV (Investigation of the Bose-Einstein correlations of charged pions in relativistic heavy-ion collisions of the systems Au + Au and Ni + Ni in the energy range from 1 AGeV to 2 AGeV)*, Ruprecht-Karls-Universität Heidelberg, Dissertation, 1995

[Gro13a] Group, The U.: *UNILAC Overview.* Website, Dezember 2013. – https://www.gsi.de/work/fairgsi/linac_operations/linac/unilac.htm

[Gro13b] Group, The U.: *The UrQMD Model.* http://urqmd.org/. Version: Juli 2013

[Har03] Hartmann, O.: *Experimentelle Untersuchung der asymmetrischen Schwerionen Ca+Au und Au+Ca bei 1,5 GeV/u Projektilenergie*, TU Darmstadt, Dissertation, 2003. http://www-fopi.gsi.de/pub/phd/hartmann_phd_03.pdf

[Her96] Herrmann, N.: Particle production and flow at SIS energies. In: *Nucl.Phys.* A610 (1996), S. 49C–62C. http://dx.doi.org/10.1016/S0375-9474(96)00342-9. – DOI 10.1016/S0375–9474(96)00342–9

[Her12] Hermann, Norbert: *private communication.* 2012

[HOL+12] Hartnack, Christoph ; Oeschler, Helmut ; Leifels, Yvonne ; Bratkovskaya, Elena L. ; Aichelin, Jörg: Strangeness Production close to Threshold in Proton-Nucleus and Heavy-Ion Collisions. In: *Phys.Rept.* 510 (2012), S. 119–200. http://dx.doi.org/10.1016/j.physrep.2011.08.004. – DOI 10.1016/j.physrep.2011.08.004

[HPA+98] Hartnack, C. ; Puri, Rajeev K. ; Aichelin, J. ; Konopka, J. ; Bass, S.A. et al.: Modeling the many body dynamics of heavy ion collisions: Present status and future perspective. In: *Eur.Phys.J.* A1 (1998), S. 151–169. http://dx.doi.org/10.1007/s100500050045. – DOI 10.1007/s100500050045

[HW08] Hyodo, Tetsuo ; Weise, Wolfram: Effective anti-K N interaction based on chiral SU(3) dynamics. In: *Phys.Rev.* C77 (2008), S. 035204. http://dx.doi.org/10.1103/PhysRevC.77.035204. – DOI 10.1103/PhysRevC.77.035204

[IKMW05] Ivanov, A.N. ; Kienle, P. ; Marton, J. ; Widmann, E.: Phenomenological model of the kaonic nuclear cluster K- pp in the ground state. (2005)

[IOH+00] Itahashi, K. ; Oyama, K. ; Hayano, R.S. ; Gilg, H. ; Gillitzer, A. et al.: Deeply bound pi- states in Pb-207 formed in the Pb-208(d, He-3) reaction Part II: Deduced binding energies and widths and the pion-nucleus interaction. In: *Phys.Rev.* C62 (2000), S. 025202. http://dx.doi.org/10.1103/PhysRevC.62.025202. – DOI 10.1103/PhysRevC.62.025202

[IS07] Ikeda, Y. ; Sato, T.: Strange dibaryon resonance in the anti-K NN - $\pi\Sigma$ N system. In: *Phys.Rev.* C76 (2007), S. 035203. http://dx.doi.org/10.1103/PhysRevC.76.035203. – DOI 10.1103/PhysRevC.76.035203

[IS09] Ikeda, Yoichi ; Sato, Toru: On the resonance energy of the anti-K NN - pi YN system. In: *Phys.Rev.* C79 (2009), S. 035201. http://dx.doi.org/10.1103/PhysRevC.79.035201. – DOI 10.1103/PhysRevC.79.035201

[JFM+99] Jones, L.L. ; French, M.J. ; Morrissey, Q. ; Neviani, A. ; Raymond, M. et al.: The APV25 deep submicron readout chip for CMS detectors. In: *Conf.Proc.* C9909201 (1999), S. 162–166

[JHB+05] Jacoby, Bryan A. ; Hotan, A. ; Bailes, M. ; Ord, S. ; Kulkarni, S.R.: The Mass of a millisecond pulsar. In: *Astrophys.J.* 629 (2005), S. L113–L116. http://dx.doi.org/10.1086/449311. – DOI 10.1086/449311

[JM12] Jacak, Barbara V. ; Müller, Berndt: The exploration of hot nuclear matter. In: *Science* 337 (2012), S. 310–314. http://dx.doi.org/10.1126/science.1215901. – DOI 10.1126/science.1215901

[Jun99] Junk, Thomas: Confidence level computation for combining searches with small statistics. In: *Nucl.Instrum.Meth.* A434 (1999), S. 435–443. http://dx.doi.org/10.1016/S0168-9002(99)00498-2. – DOI 10.1016/S0168–9002(99)00498–2

[Kai13] Kaiser, Bianca: *Optimization oif the kikinematic refit for the pp-anlysis in FOPI.* 2013. – Internal Report 2013

[KCD+11] Kis, M. ; Ciobanu, M. ; Deppner, I. ; Hildenbrand, K.D. ; Herrmann, N. et al.: A multi-strip multi-gap RPC barrel for time-of-flight measurements. In: *Nucl.Instrum.Meth.* A646 (2011), S. 27–34. http://dx.doi.org/10.1016/j.nima.2011.02.076. – DOI 10.1016/j.nima.2011.02.076

[KG13] KG, Mesystec GmbH & C.: *Mesytec - Detector Readout Systems*. Website, 2013. – www.mesytec.com

[Kie08] Kienle, Paul: Towards exclusive antikaonic nuclear cluster search with AMADEUS. In: *Nucl.Phys.* A804 (2008), S. 286–295. http://dx.doi.org/10.1016/j.nuclphysa.2008.01.008. – DOI 10.1016/j.nuclphysa.2008.01.008

[KL96] Ko, C.M. ; Li, Guo-Qiang: Medium effects in high-energy heavy ion collisions. In: *J.Phys.* G22 (1996), S. 1673–1725. http://dx.doi.org/10.1088/0954-3899/22/12/002. – DOI 10.1088/0954–3899/22/12/002

[KN86] Kaplan, D.B. ; Nelson, A.E.: Strange Goings on in Dense Nucleonic Matter. In: *Phys.Lett.* B175 (1986), S. 57–63. http://dx.doi.org/10.1016/0370-2693(86)90331-X. – DOI 10.1016/0370–2693(86)90331–X

[Koc95] Koch, Volker: Introduction to chiral symmetry. In: *arXiv* nucl-th/9512029 (1995)

[KSW95] Kaiser, Norbert ; Siegel, P.B. ; Weise, W.: Chiral dynamics and the low-energy kaon - nucleon interaction. In: *Nucl.Phys.* A594 (1995), S. 325–345. http://dx.doi.org/10.1016/0375-9474(95)00362-5. – DOI 10.1016/0375–9474(95)00362–5

[L+99] Laue, F. et al.: Medium effects in kaon and anti-kaon production in nuclear collisions at subthreshold beam energies. In: *Phys.Rev.Lett.* 82 (1999), S. 1640–1643. http://dx.doi.org/10.1103/PhysRevLett.82.1640. – DOI 10.1103/PhysRevLett.82.1640

[Lea05] Leaver, James D.: *Testing and development of the CMS silicon tracker front end readout electronics*, Imperial Coll. , London, Diss., 2005

[Lei11] Leifels, Yvonne: *private communication.* 2011

[LJMR94] Lee, Chang-Hwan ; Jung, Hong ; Min, Dong-Pil ; Rho, Mannque: Kaon - nucleon scattering from chiral Lagrangians. In: *Phys.Lett.* B326 (1994), S. 14–20. http://dx.doi.org/10.1016/0370-2693(94)91185-1. – DOI 10.1016/0370–2693(94)91185–1

[LP01] Lattimer, J.M. ; Prakash, M.: Neutron star structure and the equation of state. In: *Astrophys.J.* 550 (2001), S. 426. http://dx.doi.org/10.1086/319702. – DOI 10.1086/319702

[Lut04] Lutz, Matthias F.: Chiral symmetry and strangeness at SIS energies. In: *Prog.Part.Nucl.Phys.* 53 (2004), S. 125–136. http://dx.doi.org/10.1016/j.ppnp.2004.02.008. – DOI 10.1016/j.ppnp.2004.02.008

[M+10] Maggiora, M. et al.: DISTO data on K- pp. In: *Nucl.Phys.* A835 (2010), S. 43–50. http://dx.doi.org/10.1016/j.nuclphysa.2010.01.173. – DOI 10.1016/j.nuclphysa.2010.01.173

[Mag01] Maggiora, M.: New results from DISTO for spin observables in exclusive hyperon production. In: *Nucl.Phys.* A691 (2001), S. 329–335. http://dx.doi.org/10.1016/S0375-9474(01)01053-3. – DOI 10.1016/S0375–9474(01)01053–3

[MBF+14] Münzer, Robert ; Berger, Martin ; Fabbietti, Laura et al.: SiΛViO : A trigger for Λ -hyperons. In: *Nuclear Instruments and Methods in Physics Research Section A: Accelerators, Spectrometers, Detectors and Associated Equipment* 745 (2014), Nr. 0, 38 - 49. http://dx.doi.org/http://dx.doi.org/10.1016/j.nima.2014.01.050. – DOI http://dx.doi.org/10.1016/j.nima.2014.01.050. – ISSN 0168–9002

[Mer04] Merschmeyer, M.: *Production and Flow of Neutral Strange Particles in Ni+Ni Collisions at 1.93 AGeV*, Universität Heidelberg, Dissertation, 2004. http://www-fopi.gsi.de/pub/phd/Mmerschmeyer.ps.gz

[Moh96] Mohren, S.: *Ein FOPI-Experiment: $^{40}Ar$ auf $^{40}Ca$ bei einer Strahlenergie von 400 MeV/Nukleon (A FOPI experiment: $^{40}Ar$ on $^{40}Ca$ at 400 MeV/nucleon)*, Ruprecht-Karls-Universität Heidelberg, Dissertation, 1996

[MORT06] Magas, V.K. ; Oset, E. ; Ramos, A. ; Toki, H.: A Critical view on the deeply bound pp$K^-$ system. In: *Phys.Rev.* C74 (2006), S. 025206. http://dx.doi.org/10.1103/PhysRevC.74.025206. – DOI 10.1103/PhysRevC.74.025206

[M.R11] M.Roeder: *Final state interactions and polarization observables in the reaction pp–>p$K^+\Lambda$ close to threshold*, Ruhr Universität Bochum, Dissertation, 2011

[MS10] Moriya, Kei ; Schumacher, Reinhard: Properties of the Λ(1405) Measured at CLAS. In: *Nucl.Phys.* A835 (2010), S. 325–328. http://dx.doi.org/10.1016/j.nuclphysa.2010.01.210. – DOI 10.1016/j.nuclphysa.2010.01.210

[Mue08] Muenzer, R.: *SiΛViO : Entwicklung eines auf Silizium basierenden Trigger und Tracking Systems*, TU München, Diplom Arbeit, 2008. https://www.e12.ph.tum.de/groups/kcluster/Publications.php

[Mue13] Muenzer, R.: Search for kaonic bound states. In: *PoS* Bormio2013 (2013), S. 025

[NK87] Nelson, Ann E. ; Kaplan, David B.: Strange Condensate Realignment in Relativistic Heavy Ion Collisions. In: *Phys.Lett.* B192 (1987), S. 193. http://dx.doi.org/10.1016/0370-2693(87)91166-X. – DOI 10.1016/0370–2693(87)91166–X

[Nog63] Nogami, Y.: Possible existence of $\bar{K}$NN bound states. In: *Phys.Lett.* 7 (1963), Nr. 4, S. 288–289. http://dx.doi.org/10.1016/0031-9163(63)90336-6. – DOI 10.1016/0031–9163(63)90336–6

[Nor98] Norenberg, W.: Restoration of chiral symmetry in nucleus-nucleus collisions around 10-GeV/u. In: *Acta Phys.Polon.* B29 (1998), S. 3259–3268

[NOTR99] Nacher, J.C. ; Oset, E. ; Toki, H. ; Ramos, A.: Photoproduction of the $\Lambda(1405)$ on the proton and nuclei. In: *Phys.Lett.* B455 (1999), S. 55–61. http://dx.doi.org/10.1016/S0370-2693(99)00380-9. – DOI 10.1016/S0370–2693(99)00380–9

[OM01] Oller, J.A. ; Meissner, Ulf G.: Chiral dynamics in the presence of bound states: Kaon nucleon interactions revisited. In: *Phys.Lett.* B500 (2001), S. 263–272. http://dx.doi.org/10.1016/S0370-2693(01)00078-8. – DOI 10.1016/S0370–2693(01)00078–8

[OR98] Oset, E. ; Ramos, A.: Nonperturbative chiral approach to s wave anti-K N interactions. In: *Nucl.Phys.* A635 (1998), S. 99–120. http://dx.doi.org/10.1016/S0375-9474(98)00170-5. – DOI 10.1016/S0375–9474(98)00170–5

[Pin95] Pinkenburg, Christpher H.: *Flusseffekte geladener Pionne im System Au+Au bei $E_p$ = 1 AGeV*, University of Heidelberg, Dissertation, 1995

[Ple99] Plettner, CH.: *Strangenessproduktion bei kleinen transversalen Impulsen und mittleren Rapiditaeten in der Reaktion $^{96}Ru+^{96}Ru$ @ 1.69 AGev*, TU Dresden, Dissertation, 1999

[Ple12] Pleiner, D.: *Hunting the $ppK^-$: A kinematic refit for the exclusive analysis of the reaction $pp \to pK^+\Lambda$*, Technische Universität München, Diplomarbeit, 2012

[RBW05] Roth, Th. ; Buballa, M. ; Wambach, J.: Medium modifications of antikaons in dense matter. In: *arXiv* nucl-th/0504056 (2005)

[RCF+00] Raymond, M. ; Cervelli, G. ; French, M. ; Fulcher, J. ; Hall, G. et al.: The CMS tracker APV25 0.25-mu-m CMOS readout chip. In: *Conf.Proc.* C00091111 (2000), S. 130–134

[RDH+13] Rönchen, D. ; Doring, M. ; Huang, F. ; Haberzettl, H. ; Haidenbauer, J. et al.: Coupled-channel dynamics in the reactions $\pi N \to \pi N$, $\eta N$, $K\Lambda$ , $K\Sigma^0$ . In: *Eur.Phys.J.* A49 (2013), S. 44. http://dx.doi.org/10.1140/epja/i2013-13044-5. – DOI 10.1140/epja/i2013–13044–5

[Rit95] Ritman, J.: The FOPI detector at SIS/GSI. In: *Nucl.Phys.Proc.Suppl.* 44 (1995), S. 708–715. http://dx.doi.org/10.1016/0920-5632(95)00606-0. – DOI 10.1016/0920–5632(95)00606–0

[Rit13] Ritmann, J.: *private Communication.* 2013

[RO00] Ramos, A. ; Oset, E.: The Properties of $\bar{K}$ in the nuclear medium. In: *Nucl.Phys.* A671 (2000), S. 481–502. http://dx.doi.org/10.1016/S0375-9474(99)00846-5. – DOI 10.1016/S0375–9474(99)00846–5

[RW00] Rapp, R. ; Wambach, J.: Chiral symmetry restoration and dileptons in relativistic heavy ion collisions. In: *Adv.Nucl.Phys.* 25 (2000), S. 1. http://dx.doi.org/10.1007/0-306-47101-9. – DOI 10.1007/0–306–47101–9

[Ryu09] Ryu, M.S.: *Production of the proton and light fragments in Ru+Ru collisions at SIS18 energies and the Multigap Resistive Plate Chamber*, Korea Univeristy, Dissertation, 2009

[S+05] Schael, S. et al.: Branching ratios and spectral functions of tau decays: Final ALEPH measurements and physics implications. In: *Phys.Rept.* 421 (2005), S. 191–284. http://dx.doi.org/10.1016/j.physrep.2005.06.007. – DOI 10.1016/j.physrep.2005.06.007

[S+06] Scheinast, W. et al.: First observation of in-medium effects on phase space distributions of antikaons measured in proton-nucleus collisions. In: *Phys.Rev.Lett.* 96 (2006), S. 072301. http://dx.doi.org/10.1103/PhysRevLett.96.072301. – DOI 10.1103/PhysRevLett.96.072301

[Sar13] Sarantsev, Adrey: *private Communication.* 2013

[SB08] Schaffner-Bielich, Jürgen: Hypernuclear Physics for Neutron Stars. In: *Nucl.Phys.* A804 (2008), S. 309–321. http://dx.doi.org/10.1016/j.nuclphysa.2008.01.005. – DOI 10.1016/j.nuclphysa.2008.01.005

[SCLR98] Sibirtsev, A. ; Cassing, W. ; Lykasov, G.I. ; Rzyanin, M.V.: Reanalysis of anti-proton production in proton nucleus and nucleus-nucleus reactions at subthreshold energies. In: *Nucl.Phys.* A632 (1998), S. 131–152. http://dx.doi.org/10.1016/S0375-9474(97)00809-9. – DOI 10.1016/S0375–9474(97)00809–9

[Sco13] Scomparin, Enrico: ALICE results on quarkonia. In: *Nucl.Phys.A904-905* 2013 (2013), S. 202c–209c. http://dx.doi.org/10.1016/j.nuclphysa.2013.01.067. – DOI 10.1016/j.nuclphysa.2013.01.067

[SF13] Siebenson, Johannes ; Fabbietti, Laura: Investigation of the Lambda(1405) line shape observed in pp collisions. In: *Physical Review C* 11 (2013), S. 88(5)

[SGH+98] Spieles, C. ; Gerland, L. ; Hammon, N. ; Bleicher, M. ; Bass, S.A. et al.: A Microscopic calculation of secondary Drell-Yan production in heavy ion collisions. In: *Eur.Phys.J.* C5 (1998), S. 349–355. http://dx.doi.org/10.1007/s100520050279. – DOI 10.1007/s100520050279

[SGM07] Shevchenko, N.V. ; Gal, A. ; Mares, J.: Faddeev calculation of a K- p p quasi-bound state. In: *Phys.Rev.Lett.* 98 (2007), S. 082301. http://dx.doi.org/10.1103/PhysRevLett.98.082301. – DOI 10.1103/PhysRevLett.98.082301

[SGMR07] Shevchenko, N.V. ; Gal, A. ; Mares, J. ; Revai, J.: anti-K NN quasi-bound state and the anti-K N interaction: Coupled-channel Faddeev calculations of the anti-K NN - pi Sigma N system. In: *Phys.Rev.* C76 (2007), S. 044004. http://dx.doi.org/10.1103/PhysRevC.76.044004. – DOI 10.1103/PhysRevC.76.044004

[Sie10] Siebenson, J.: *Exclusive analysis of the Λ(1405) resonance in the charged Σπ decay channels*, Technische Universität München, Diplomarbeit, 2010

[Sie13] Siebenson, Johannes: *Strange baryonic resonances below the KN threshold - Results from p+p reactions at the HADES experiment*, Technische Universität München, Diss., 2013

[SNA+05] Sarantsev, A.V. ; Nikonov, V.A. ; Anisovich, A.V. ; Klempt, E. ; Thoma, U.: Decays of baryon resonances into $\Lambda\, K^+$ , $\Sigma^0\, K^+$ and $\Sigma^+ K^0$. In: *Eur.Phys.J.* A25 (2005), S. 441–453. http://dx.doi.org/10.1140/epja/i2005-10121-4. – DOI 10.1140/epja/i2005–10121–4

[SPM01] Shyam, R. ; Penner, G. ; Mosel, U.: Role of N*(1650) in the near threshold pp→p$K^+\Lambda$ and pp→p$\Sigma^0 K^+$ reactions. In: *Phys.Rev.* C63 (2001), S. 022202. http://dx.doi.org/10.1103/PhysRevC.63.022202. – DOI 10.1103/PhysRevC.63.022202

[STC+12] Sagert, Irina ; Tolos, Laura ; Chatterjee, Debarati ; Schaffner-Bielich, Jürgen ; Sturm, Christian: Soft nuclear equation-of-state from heavy-ion data and implications for compact stars. In: *Phys.Rev.* C86 (2012), S. 045802. http://dx.doi.org/10.1103/PhysRevC.86.045802. – DOI 10.1103/PhysRevC.86.045802

[Stu01] Sturm, Christian: *$K^+$-Produktion in Schwerionenreaktionen als Sonde für die Inkompressibilität von Kernmaterie*, Technische Universität Darmstadt, Diss., 2001

[T+14] Tokiyasu, A.O. et al.: Search for $K^- pp$ bound state via $\gamma d \to K^+ \pi^- X$ reaction at $E_\gamma = 1.5 - 2.4$ GeV. In: *Phys.Lett.* B728 (2014), S. 616–621. http://dx.doi.org/10.1016/j.physletb.2013.12.039. – DOI 10.1016/j.physletb.2013.12.039

[TEFK73] Thomas, D.W. ; Engler, A. ; Fisk, H.E. ; Kraemer, R.W.: Strange particle production from $\pi^-$ p interactions at 1.69 GeV/c. In: *Nucl.Phys.* B56 (1973), S. 15–45. http://dx.doi.org/10.1016/0550-3213(73)90217-4. – DOI 10.1016/0550–3213(73)90217–4

[WBB+96] Winckelmann, L.A. ; Bass, S.A. ; Bleicher, M. ; Brandstetter, M. ; Dumitru, A. et al.: Microscopic calculations of stopping and

flow from 160-A/MeV to 160-A/GeV. In: *Nucl.Phys.* A610 (1996), S. 116C–123C. http://dx.doi.org/10.1016/S0375-9474(96)00347-8. – DOI 10.1016/S0375–9474(96)00347–8

[WCSB12] Weissenborn, S. ; Chatterjee, D. ; Schaffner-Bielich, J.: Hyperons and massive neutron stars: the role of hyperon potentials. In: *Nucl.Phys.* A881 (2012), S. 62–77. http://dx.doi.org/10.1016/j.nuclphysa.2012.02.012. – DOI 10.1016/j.nuclphysa.2012.02.012

[WG09] Wycech, S. ; Green, A.M.: Variational calculations for K- few-nucleon systems. In: *Phys.Rev.* C79 (2009), S. 014001. http://dx.doi.org/10.1103/PhysRevC.79.014001. – DOI 10.1103/PhysRevC.79.014001

[Win78] Wind, H.: An Improvement to Iterative Tracking for Momentum Determination. In: *Nucl.Instrum.Meth.* 153 (1978), S. 195–197. http://dx.doi.org/10.1016/0029-554X(78)90637-7. – DOI 10.1016/0029–554X(78)90637–7

[Wyc86] Wycech, S.: On Possibilities of Narrow Nuclear States of $K^-$. In: *Nucl.Phys.* A450 (1986), S. 399C–402C. http://dx.doi.org/10.1016/0375-9474(86)90574-9. – DOI 10.1016/0375–9474(86)90574–9

[Y+08] Yamazaki, T. et al.: First exclusive measurements of the K- pp state populated in the pp→p$K^+\Lambda$ reaction at 2.85 GeV. In: *Hyperfine Interactions* 193 (2008), S. 181–187. http://dx.doi.org/10.1007/s10751-009-9997-5. – DOI 10.1007/s10751–009–9997–5

[YA02] Yamazaki, T. ; Akaishi, Y.: (K-,pi-) production of nuclear anti-K bound states in proton-rich systems via Lambda* doorways. In: *Phys.Lett.* B535 (2002), S. 70–76. http://dx.doi.org/10.1016/S0370-2693(02)01738-0. – DOI 10.1016/S0370–2693(02)01738–0

[YA07] Yamazaki, Toshimitsu ; Akaishi, Yoshinori: The Basic anti-K nuclear cluster pp$K^-$ and its enhanced formation in the p+p→$K^+$ + X reaction. In: *Phys.Rev.* C76 (2007), S. 045201. http://dx.doi.org/10.1103/PhysRevC.76.045201. – DOI 10.1103/PhysRevC.76.045201

[YHI+96] Yamazaki, T. ; Hayano, R.S. ; Itahashi, K. ; Oyama, K. ; Gillitzer, A. et al.: Discovery of deeply bound pi- states in the Pb-208 (d, He-3) reaction. In: *Z.Phys.* A355 (1996), S. 219–221. http://dx.doi.org/10.1007/s002180050101. – DOI 10.1007/s002180050101

[Zme07] Zmeskal, J.: Search for kaonic nuclei at DAFNE2: The AMADEUS project. In: *Int.J.Mod.Phys.* A22 (2007), S. 374–379. http://dx.doi.org/10.1142/S0217751X07035550. – DOI 10.1142/S0217751X07035550

# Appendix B

# Momentum calculation in the Helitron

In the following section the momentum reconstruction of tracks, which are measured with the Helitron drift chamber is explained.
Due to the presence of a magnetic field, particles with the charge q and the velocity $\vec{v}$ are bended due to the Lorentz force $\vec{F}_L$:

$$\vec{F}_L = q\vec{v} \times \vec{B}. \tag{B.1}$$

For the special case $\vec{B}$= (0,0,$B_z$) the particle follows Equation B.2; $v_t$ is the transverse component of the particle velocity, $m$ is the particle mass and the $r$ is the radius of the circle.

$$\frac{mv_t^2}{r} = qv_tB_Z. \tag{B.2}$$

In the case of homogeneous magnetic field the particle momentum can be calculated from this formula. In the case of the Helitron the magnetic field is starting to be inhomogeneous, what is visualised in Figure B.1. In this graph the longitudinal and the radial component of the magnetic field is shown versus the z position along the beam axis is shown. The nominal target position of the FOPI Spectrometer is located a z=0. The different colour lines correspond to different radial distances from the beam axis. In the region of the Helitron (marked in the pictures) the field is becoming inhomogeneous.
Due to this, a tracking routine based on the method developed in [Win78] was implemented for the Helitron. This routine determines the particle momentum by normalised cubic B Splines. This procedure allows the reconstruction - in contrast to Runge-Kutta-Integration - without the assumption of a track model. For this method the particle track has to be parametrised by $\vec{X} = (x(z), y(z), z)^T$. Additional the first and second derivative $\frac{d\vec{X}}{dz}, \frac{d^2\vec{X}}{dz^2}$ has to be known [Moh96].
From the equation of motion inside the magnetic field the following equation can be derived

$$p\frac{d^2x(z)}{dz^2} = \sqrt{1 + \frac{dx(z)}{dz}^2 + \frac{dy(z)^2}{dz}} \cdot \left( B_z\frac{dy(z)}{dz} + B_x\frac{dx(z)}{dz}\frac{dy(z)}{dz} - B_y(1 + \frac{dx(z)}{dz}^2 \right) \tag{B.3}$$

$$p\frac{d^2y(z)}{dz^2} = \sqrt{1 + \frac{dx(z)}{dz}^2 + \frac{dx(z)^2}{dz}} \cdot \left( -B_z\frac{dx(z)}{dz} - B_x\frac{dx(z)}{dz}\frac{dy(z)}{dz} + B_x(1 + \frac{dy(z)}{dz}^2 \right) \tag{B.4}$$

The right sides of these equations are parametrised by splines and are integrated two times. By the comparison with the left side, the values for the particle momentum can be determined.

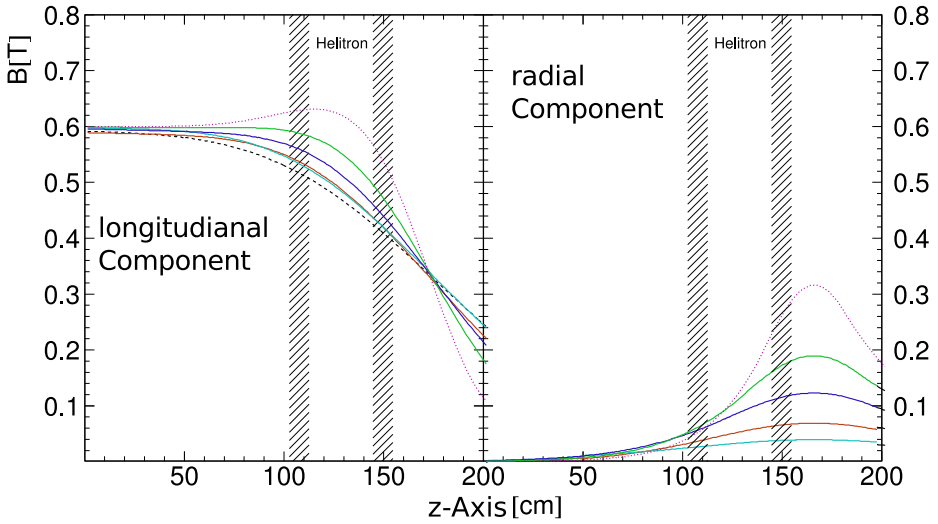


Figure B.1: Longitudinal and radial component of the magnetic field inside FOPI along the z-Axis (beam axis) (given in cm).The center of the magnet is locate as z=0. The different colour correspond to different radial positions (r=0cm(black dashed), 20cm(turquoise), 40cm(orange), 60cm(violet), 80cm(green), 100cm(pink)). The Helitron is locate between z=100 and z=150 (marked region) [Ple99].

Additionally from the procedure a new parametrisation of $x(z), y(z)$ is obtained, which fits the actual track in more accurate way. With the new parametrisation the procedure is repeated. The limit of this iterative procedure equals the actual particle momentum. The momentum resolution of this procedure - ignoring detector resolution effects - is in region of 0.5% [Moh96, Ple99].
This procedure allows also the extrapolation of the particle track in both direction of the Helitron, which allow the matching with other detectors like the PLAWA and SiΛViO (see Paragraph 3.1.1).
The crucial part of this procedure is the determination of the initial track parametrisation. This is done by a fit of the hit points by a cubic function in the x versus z and y versus z plane. Additional to Helitron hit point the target point has to be used for this fit, to ensure the procedure to converge. Because of this requirement, this tracking procedure has limited capability for secondary vertex reconstruction.

# Appendix C

# Kinematical Refit

The kinematical refit is a mathematical procedure, which allows to combine physical laws, like conservation rules, with the measured track information of particles. In this method the track observable of the reconstructed particle, which are the momentum and the flight direction of the particles are forced to fulfil certain kinematical constraints of the exclusive reaction which is investigated [Ple12]. Due to finite resolution of detector the measured four momenta of the particles and their track parameters are afflicted by a statistical error. Such errors always lead to a broadening of the measured mass of particles which are reconstructed, such as final measured particles like protons, kaons and pions or intermediate particle like Λ-hyperon.
Since such particles have to be selected by mass or track cuts, hence such a broadening leads to a increase of particles, that are wrongly selected by such cuts, which increase the amount of background.

## C.a General Principles

The mathematical background of the kinematical refit is based on the minimization of the Lagrange equation show in Equation C.1 with respect to $\vec{\alpha}$ and $\vec{\lambda}$:

$$L(\vec{\alpha}, \vec{\lambda}) = (\vec{\alpha} - \vec{\alpha}_0)^T V_{\vec{\alpha}_0}^{-1} (\vec{\alpha} - \vec{\alpha}_0) + 2\vec{\lambda}^T \vec{H}((\vec{\alpha}). \tag{C.1}$$

$V_{\vec{\alpha}_0}^{-1}$ is the inverse of the measurement covariance matrix, $\vec{\alpha}$ contains the 6n refitted and $\vec{\alpha}_0$ the 6n unconstrained parameters of the n tracks [Ple12]. The covariance matrix contain the uncertainties of the measured unconstrained parameter $\alpha_0$.

$$V_{\vec{\alpha}_0}^{-1} = \begin{pmatrix} \frac{1}{\sigma^2_{\alpha_1}} & a_2 & \dots & 0 \\ 0 & \frac{1}{\sigma^2_{\alpha_2}} & \dots & 0 \\ \vdots & \vdots & \ddots & \vdots \\ 0 & 0 & \dots & \frac{1}{\sigma^2_{\alpha_2}} \end{pmatrix} \qquad \vec{\alpha} = \begin{pmatrix} \vec{\alpha}_1 \\ \vec{\alpha}_2 \\ \vdots \\ \vec{\alpha}_n \end{pmatrix} \qquad \vec{\alpha}_i = \begin{pmatrix} p_{x,i} \\ p_{y,i} \\ p_{z,i} \\ x_i \\ y_i \\ z_i \end{pmatrix} \tag{C.2}$$

The constraints for the kinematic refit are parametrized in the vector $\vec{H}(\vec{\alpha})$ with the vector of the Lagrange multiplier $\vec{\lambda}$.
By the minimization of the Equation C.1 a new set of parameters $\alpha$ is created. The sector term forces the new set of parameters to fulfill the constraint of $\vec{H}(\vec{\alpha})$. The first term in Equation C.1 ensure, that the new set stays as close as possible to the unconstrained parameters

set $\alpha_0$. Coincidentally, the parameters are shifted only within the measurement uncertainties $\sigma^2_{\alpha_i}$, which are contained in the covariance matrix $V_{\vec{\alpha_0}}$. For the correct functionality of the kinematic refit, it is advantageous, that the errors are gaussian distributed [Ple12].

## C.b Quality Criteria

For a sufficient functionality of the kinematical refit the correct input of the uncertainties to the covariance matrix $V_{\vec{\alpha_0}}$ is crucial. In the case of certain tracking procedures, these parameters can be extracted from the tracking method quite precisely. In the case of the FOPI tracking these values have to be determined. For the validation of this error, it is necessary to have a set of criteria which are a measure for the quality of the fit and that indicates the presence of misidentified events and whether the error input is correct.

### C.b.i. Pull Distributions

The pull distribution are a good handle for the quality of each uncertainties of each parameters separately. These values are defined by Equation C.3, with the original track parameter $\alpha_{0,i}$, the refitted track parameter $\alpha_i$, the measurement uncertainties of the original track parameter $\sigma_{\alpha_{0,i}}$ and $\sigma_{\alpha_i}$ the measurement uncertainties of the refitted track parameter $\sigma_{\alpha_i}$.

$$P(\alpha_i) = \frac{\alpha_{0,i} - \alpha_i}{\sqrt{\sigma^2_{\alpha_{0,i}} - \sigma^2_{\alpha_i}}}. \tag{C.3}$$

The value - calculated for each parameter separately - is a measure, how far the refitted parameter $\alpha$ differs from the unconstrained parameter $\alpha_0$. The denominator normalises the difference to the reduced error difference. If the covariance matrix $V_{\alpha_0}$ is estimated correctly, the pull distributions for the single parameters are gaussian distributed around 0 with a standard deviation of $\sigma = 1$. The effect of wrongly estimated uncertainties or systematic errors can directly be read out of the shape of the pull distributions. Hence, they are a very important and highly sensitive quality criterion for the kinematic refit. Indeed, if the covariance matrix is only roughly known in advance, the pull distributions can be used to tune the errors to the correct values afterwards (see Paragraph D) [Ple12].

### C.b.ii. $\chi^2$ and pvalue

$$\chi^2 = (\vec{\alpha} - \vec{\alpha}_0)^T V^{-1}_{\vec{\alpha}_0} (\vec{\alpha} - \vec{\alpha}_0) = \sum_l^{6n} \frac{(\alpha_l - \alpha_{0,l})^2)}{\sigma^2_{\alpha_l}} \tag{C.4}$$

The $\chi^2$ value of the refit - calculated by Equation C.4 - is a global quality criteria of the refit. According to its definition in the case of a perfect working kinematical refit, the $\chi^2$ values should be distributed according the probability density function (Equation C.6), with the mean value of $\nu$. The value $\nu$ equals the degree of freedom of the kinematical refit. Figure C.1 show the probability density function for the $\chi^2$ distribution for different degrees of freedom (ndf).

$$f_\nu\left(\chi^2\right) = \frac{1}{2^{\frac{\nu}{2}}\Gamma\left(\frac{\nu}{2}\right)} \left(\chi^2\right)^{\frac{\nu}{2}-1} \exp\left(-\frac{1}{2}\chi^2\right) \tag{C.5}$$

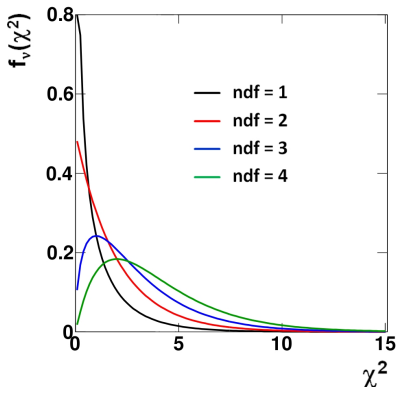


Figure C.1: Probability density of the $\chi^2$ distributions for different values of the ndf. The functions are shifted towards higher $\chi^2$ values for an increasing ndf, since the fit has to move the parameters $\vec{\alpha_0}$ within a larger distance if more constraints are applied. In the limit of $\nu \to infinity$, the $\chi^2$ distribution approaches a normal distribution. This follows from the central limit theorem [Sie10].

A more convenient representation of the fit quality is given by the pvalue. For a $\chi^2$ value value resulting for a refit $\chi^2_{fit}$ the pvalue is calculated by Equation C.6

$$pvalue = \int_{\chi^2_{fit}}^{\infty} f_\nu(\chi^2) d\chi^2. \tag{C.6}$$

Instead of looking at the $\chi^2$ distribution, it is more descriptive to map the $\chi^2$ to a flat distribution [Bau00]. If the error input is correct, the p-value is indeed evenly distributed between 0 and 1. Since high $\chi^2$ values correspond to low p-values, misidentified events are located at low p-values. Cutting on the p-value therefore enables the reduction of the background [Ple12].

# Appendix D

# Determination of Error Values for Exclusive Analysis

The error value for the kinematical refit have to be optimized in a dedicated procedure.
By executing a kinematical refit the track parameters, i.e. the momentum and the direction, are altered. The size of this change is characterized by the so called pull distribution (C.b.i.), which should have - in the ideal case - a gaussian shape, with an peak position of 0 and standard deviation of 1. For the exclusive analysis there are 15 statistical error values that need to be optimized - 3 parameter for four particles in the CDC and 3 particle in the Helitron. They should influence the width of the gaussian fit.
To correct for systematical errors - which are visible in a shifted mean position of the distribution - a systematical shift correction of the parameter $\alpha_0$ can be applied to the parameters according to Equation D.1.

$$\alpha_0 = \alpha_0 \cdot \epsilon_{shiftcorrection} \tag{D.1}$$

Thus additional 15 parameters have to be tuned.
At first all the errors and the shifts for the inverted momentum, the polar angles $\theta$ and the azimuthal angle $\phi$ are set at a specific value according to sophisticated assumptions based on the detector's resolution. Thereafter they are adjusted manually, in order to improve the gaussian fit. This is described in D.a
To obtain a more complete results, a scan of a huge set of different parameter combination - a so called iteration approach - was done. This procedure - described in Appendix D.b - should create an optimal set.

## D.a Manual Adaption of Error Parameters

In a first attempt, the variables are changed manually. After each new set of errors and shifts the track parameters are refitted. If the variables were linearly related to the gaussian fit, as one might assume, a good match could be found easily. After several different variable combinations an slightly sufficient set of parameters could be determined. The values for the statistical errors are shown in Table D.1 and for the systematical shifts correction factor $\epsilon_{shiftcorrection}$ in Table D.2.
The pull distribution obtained by the manual adaption of the errors are shown in Figure D.1-D.7. The fit value are listed in Table D.3 Especially, the plots of the particles from HELITRON

| | 1/p | $\theta$ | $\phi$ |
|---|---|---|---|
| proton | 0.099 | 0.014 | 0.052 |
| kaon | 0.78 | 0.035 | 0.042 |
| pion | 0.049 | 0.007 | 0.011 |

| | 1/p | $\theta$ | $\phi$ |
|---|---|---|---|
| proton | 0.0.105 | 0.032 | 0.013 |
| pion | 0.045 | 0.01 | 0.012 |

Table D.1: Extracted values for the statistical errors in CDC (left) and Helitron (right) by the manual adaption.

| | 1/p | $\theta$ | $\phi$ |
|---|---|---|---|
| prim. proton | 0.92 | 1.00 | 1.00 |
| sec. proton | 1.02 | 1.00 | 1.00 |
| kaon | 10.6 | 1.00 | 1.00 |
| pion | 0.95 | 1.09 | 1.00 |

| | 1/p | $\theta$ | $\phi$ |
|---|---|---|---|
| prim. proton | 0.97 | 1.05 | 1.00 |
| sec. proton | 1.00 | 0.95 | 1.00 |
| pion | 1.00 | 0.85 | 1.00 |

Table D.2: Extracted value for the systematical shift correction factor $\epsilon_{shiftcorrection}$ in CDC (left) and Helitron (right) by manual adaption

seem to fit well to the optimal shape. On the other side the pull distributions of the secondary proton in CDC differ strongly due to the low amount of signals. In general one can imply, that the data distributions are already gaussian shaped with an acceptable mean value but a too high width $\sigma$. [Kai13]

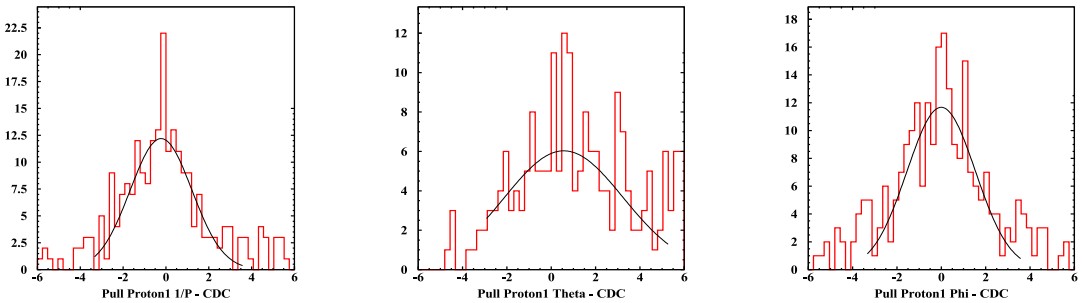


(a) (b) (c)

Figure D.1: Pull Distribution of Primary Proton in CDC with manual adaption. Inverted momentum (a), polar angle $\theta$ (b) and azimuthal angle $\phi$ (c).

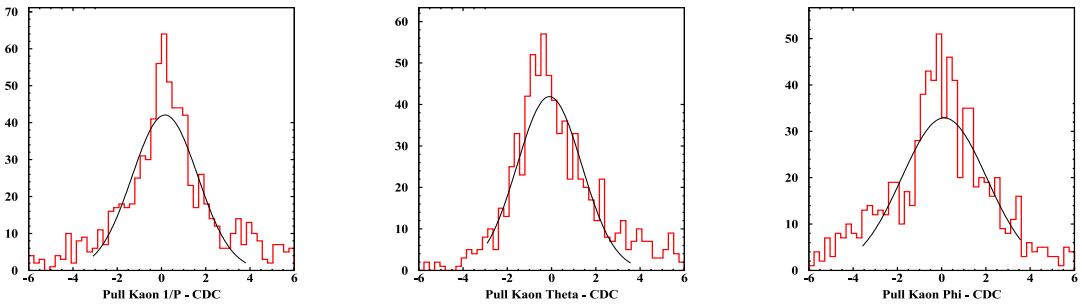


(a) (b) (c)

Figure D.2: Pull Distribution of Kaon in CDC with manual adaption. Inverted momentum (a), polar angle $\theta$ (b) and azimuthal angle $\phi$ (c).

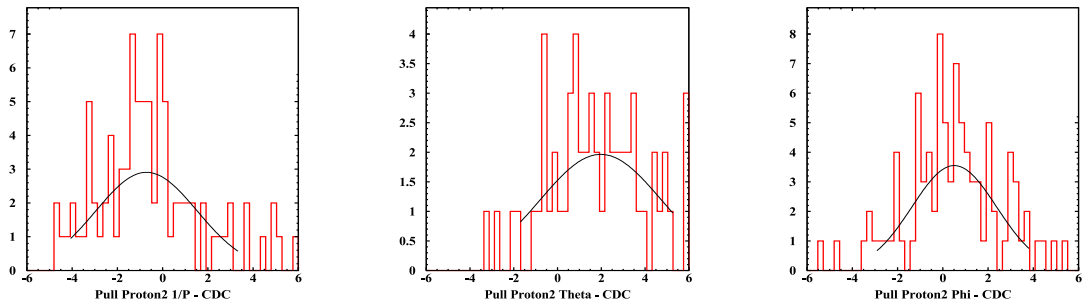


(a) (b) (c)

Figure D.3: Pull Distribution of Secondary Proton in CDC with manual adaption. Inverted momentum (a), polar angle $\theta$ (b) and azimuthal angle $\phi$ (c).

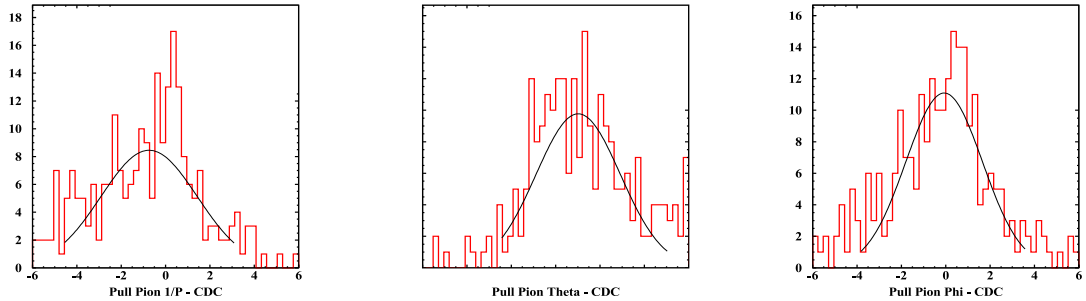


(a) (b) (c)

Figure D.4: Pull Distribution of Pion in CDC with manual adaption. Inverted momentum (a), polar angle $\theta$ (b) and azimuthal angle $\phi$ (c).

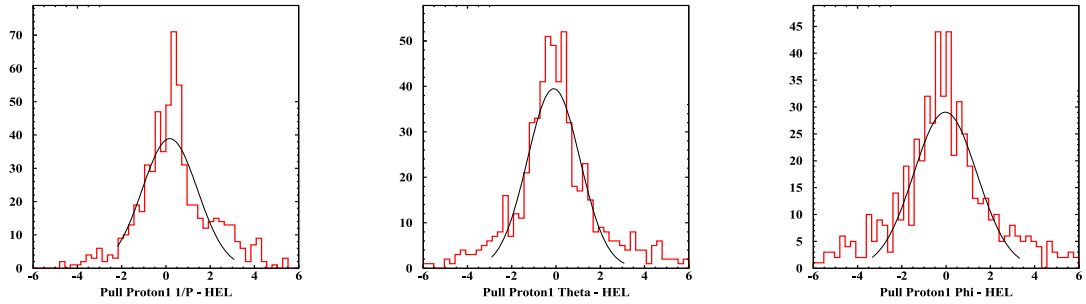


(a) (b) (c)

Figure D.5: Pull Distribution of Primary Proton in Helitron with manual adaption. Inverted momentum (a), polar angle $\theta$ (b) and azimuthal angle $\phi$ (c).

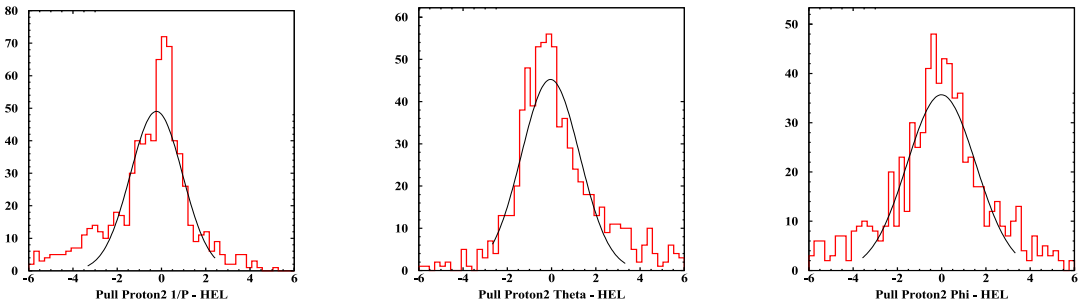


(a) (b) (c)

Figure D.6: Pull Distribution of Secondary Proton in Helitron with manual adaption. Inverted momentum (a), polar angle $\theta$ (b) and azimuthal angle $\phi$ (c).

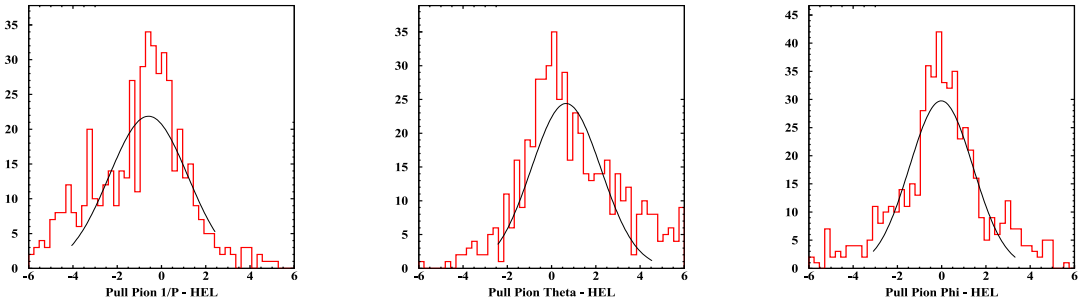


(a) (b) (c)

Figure D.7: Pull Distribution of Pion in Helitron with manual adaption. Inverted momentum (a), polar angle $\theta$ (b) and azimuthal angle $\phi$ (c).

## D.b Iterative Approach of Error Parameter Adaption

From the attempt of an manual adaption of the fit errors, it was found out, that the pull distribution and the error parameters are correlated also for different parameter and particle combinations.
Thus an more sophisticated method must be used. A possible procedure, that leads to a satisfying result, is the Iteration of possible combination of the error and shift parameters. Since it is not possible, to iterated over all possible combination the shift parameters and statistical (D.b.i.) error parameters are iterated separately (D.b.ii.).

### D.b.i. Iteration over Shift Values

In the first iteration step the shifts in the CDC and one in the HELITRON, as shown in Table D.4, are varied.

| Chamber | Particle | Parameter | $\chi^2/ndf$ | Mean | Sigma |
|---|---|---|---|---|---|
| CDC | Primary Proton | p | 1.03 | -0.225 | 1.442 |
| CDC | Primary Proton | $\theta$ | 0.89 | 0.569 | 2.679 |
| CDC | Primary Proton | $\phi$ | 0.98 | -0.002 | 1.543 |
| CDC | Kaon | p | 2.00 | 0.161 | 1.484 |
| CDC | Kaon | $\theta$ | 2.11 | -0.092 | 1.460 |
| CDC | Kaon | $\phi$ | 2.61 | 0.117 | 1.924 |
| CDC | Secondary Proton | p | 0.78 | -0.710 | 2.241 |
| CDC | Secondary Proton | $\theta$ | 0.35 | 1.977 | 2.778 |
| CDC | Secondary Proton | $\phi$ | 0.89 | 0.509 | 1.871 |
| CDC | Pion | p | 1.20 | -0.740 | 2.172 |
| CDC | Pion | $\theta$ | 1.05 | 1.019 | 1.902 |
| CDC | Pion | $\phi$ | 0.79 | -0.069 | 1.727 |
| HEL | Primary Proton | p | 3.26 | 0.179 | 1.251 |
| HEL | Primary Proton | $\theta$ | 2.02 | -0.100 | 1.188 |
| HEL | Primary Proton | $\phi$ | 2.03 | -0.030 | 1.429 |
| HEL | Secondary Proton | p | 3.34 | -0.224 | 1.177 |
| HEL | Secondary Proton | $\theta$ | 2.23 | -0.044 | 1.316 |
| HEL | Secondary Proton | $\phi$ | 1.83 | -0.007 | 1.554 |
| HEL | Pion | p | 2.22 | -0.584 | 1.780 |
| HEL | Pion | $\theta$ | 2.68 | 0.659 | 1.569 |
| HEL | Pion | $\phi$ | 2.05 | -0.016 | 1.434 |

Table D.3: Pull Value results with manual adaption [Kai13].

| | first iter | | second iter | | third iter | |
|---|---|---|---|---|---|---|
| shift type | value range | iter step | value range | iter step | value range | iter step |
| prim pr mom | [0.8;1.05] | $\Delta$ 0.05 | [0.95;1.05] | $\Delta$ 0.02 | [0.98;1.02] | $\Delta$ 0.01 |
| prim pr $\theta$ | [0.8;1.05] | $\Delta$ 0.05 | [0.9;0.97] | $\Delta$ 0.01 | [0.915;0.925] | $\Delta$ 0.005 |
| sec pr mom | [0.9; 1.15] | $\Delta$ 0.05 | [1.15; 1.25] | $\Delta$ 0.02 | [1.0; 1.2] | $\Delta$ 0.05 |
| sec pr $\theta$ | [0.8; 1.05] | $\Delta$ 0.05 | [0.8; 1.05] | $\Delta$ 0.05 | [0.8; 1.05] | $\Delta$ 0.05 |
| Kaon mom | [0.9; 1.05] | $\Delta$ 0.05 | [1.0; 1.1] | $\Delta$ 0.02 | [1.02; 1.06] | $\Delta$ 0.01 |
| Kaon $\theta$ | [0.9; 1.15] | $\Delta$0.07 | [0.95; 1.05] | $\Delta$0.02 | [0.98; 1.02] | $\Delta$0.01 |
| prim pr $\theta$ Hel | [0.95; 1.05] | $\Delta$ 0.02 | [0.98; 1.13] | $\Delta$ 0.03 | [0.98; 1.13] | $\Delta$ 0.03 |

Table D.4: Range and step width for different iteration (iter). Listed are the value for $\theta$ and momentum values for Protons and the Kaon in CDC and for the primary proton in Helitron (prim=primary; pr=proton; mom=momentum; sec=secondary; Hel=in HELITRON)

After conducting the kinematical refit with every combination, each mean value of the pull distribution is plotted against the iterated shift values excluding at once the insignificant histograms. The resulting correlation of the mean position of the pull distribution of different parameters versus the iterate shift of the kaon momentum are shown in the histograms in Figure D.8

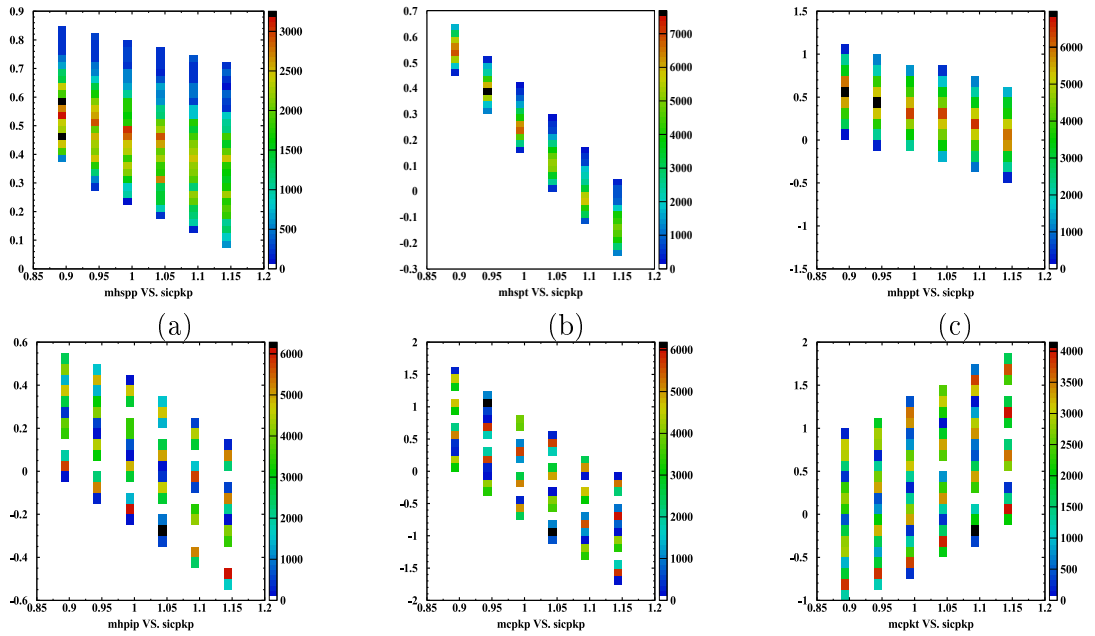


Figure D.8: Mean position of the Pull Distribution of different parameters versus the iterated shift value of the momentum of the Kaon in the CDC (sicpkp):
a)the mean of the momentum of the secondary proton in HELITRON (mhspp) b)the mean of $\theta$ of the secondary proton in HELITRON (mhspt) c)the mean of $\theta$ of the primary proton in HELITRON (mhppt) d)the mean of the momentum of the pion in HELITRON (mhpip) e)the mean of the momentum of the kaon (mcpkp) f)the mean of $\theta$ of the kaon (mcpkt) [Kai13].

As one can see, an increase in the shift value of the momentum of the kaon arouses an increase only for the mean of the $\theta$ angle of the kaon (panel (f)). The remaining histograms all show a decrease, which is the strongest for the mean of the $\theta$ angle of the secondary proton in HELITRON and the weakest for the momentum of the secondary proton. Most of these values meet the zero-point around the shift value 1. Afterwards one must extract the area in the histograms, where most of the plots of the kinematical refit have the smallest distance from the favored value, i.e. the width $\sigma$ or the mean. This method is repeated with a more specified parameters iteration range until a satisfying result is obtained.

### D.b.ii. Iteration over Statistical Errors

After the shift parameters are fixed, the statistical error parameters are fixed with the same method like the systematical shift parameters. The initial iterations steps are listed in Table D.5

| *in CDC* | | |
|---|---|---|
| *error type* | *value range* | *iteration step* |
| *proton momentum* | $[0.1; 0.3]$ | $\Delta 0.04$ |
| *kaon momentum* | $[0.05; 0.25]$ | $\Delta 0.04$ |
| *pion momentum* | $[0.05; 0.25]$ | $\Delta 0.04$ |
| *$\theta$ of proton* | $[0.1; 0.3]$ | $\Delta 0.04$ |
| *in HELITRON* | | |
| *proton momentum* | $[0.07; 0.27]$ | $\Delta 0.04$ |
| *pion momentum* | $[0.04; 0.24]$ | $\Delta 0.04$ |
| *$\theta$ of proton* | $[0.07; 0.27]$ | $\Delta 0.04$ |

Table D.5: Iteration values of the systematical shift parameter $\epsilon_{shiftcorrection}$ in CDC and HELITRON

Also for this error parameters the iteration are repeated with a more specified range until a satisfying result is obtained.

## D.c Final Outcome

After the iteration an optimal set for the systematical and statistical error parameters is extracted, which is shown in Table D.6 and Table D.7.

| | momentum | theta | phi |
|---|---|---|---|
| prim. proton | 0.099 | 0.014 | 0.052 |
| sec. proton | 0.099 | 0.014 | 0.052 |
| kaon | 0.079 | 0.035 | 0.042 |
| pion | 0.099 | 0.014 | 0.052 |

| | momentum | theta | phi |
|---|---|---|---|
| prim. proton | 0.105 | 0.032 | 0.012 |
| sec. proton | 0.045 | 0.010 | 0.011 |
| pion | 0.099 | 0.014 | 0.052 |

Table D.6: Extracted value for the statistical errors in CDC (left) and Helitron (right) after scan adaption

| | momentum | theta | phi |
|---|---|---|---|
| prim. proton | 0.90 | 1.00 | 1.00 |
| sec. proton | 1.08 | 1.00 | 1.00 |
| kaon | 1.01 | 1.00 | 1.00 |
| pion | 0.96 | 1.00 | 1.00 |

| | momentum | theta | phi |
|---|---|---|---|
| prim. proton | 0.97 | 1.05 | 1.00 |
| sec. proton | 1.00 | 0.95 | 1.00 |
| pion | 1.00 | 0.85 | 1.00 |

Table D.7: Extracted value for the systematical shift correction $\epsilon_{shiftcorrection}$ in CDC (left) and Helitron (right) after scan adaption

Applying this final set to the kinematical refit, the pull distributions show an improved shape - shown in Figure D.9-D.15 and Table D.8.

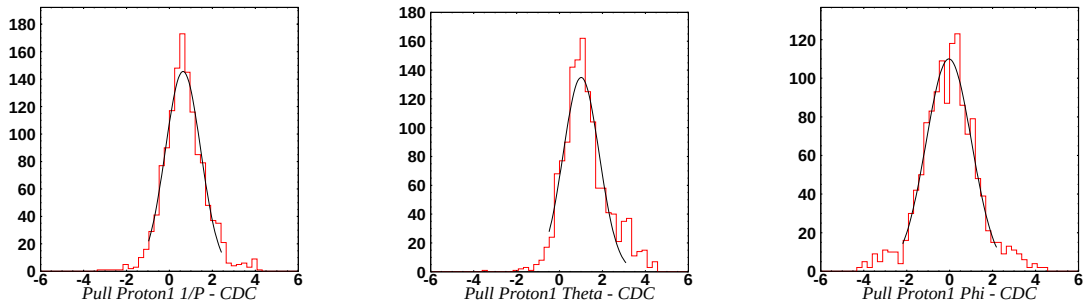


(a) (b) (c)

Figure D.9: Pull Distribution of Primary Proton in CDC with final adaption. Inverted momentum (a), polar angle $\theta$ (b) and azimuthal angle $\phi$ (c).

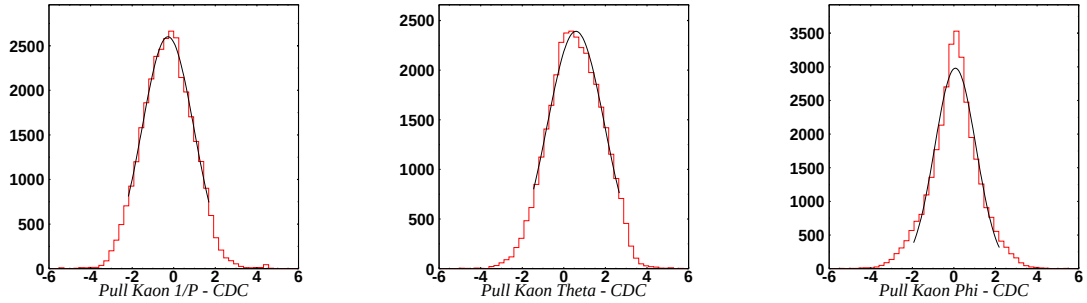


(a) (b) (c)

Figure D.10: Pull Distribution of Kaon in CDC with final adaption. Inverted momentum (a), polar angle $\theta$ (b) and azimuthal angle $\phi$ (c).

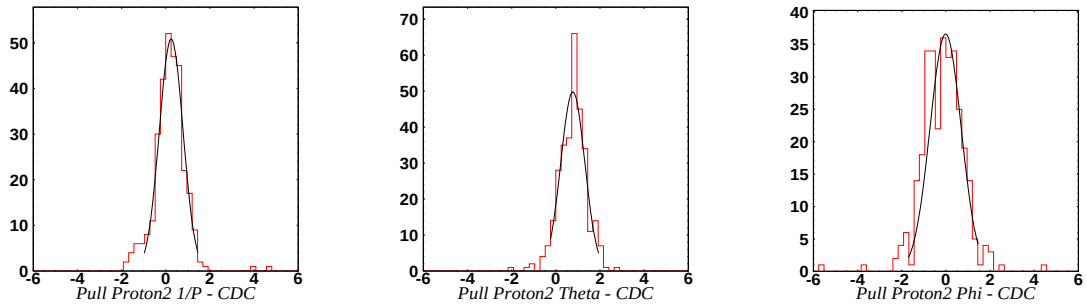


(a) (b) (c)

Figure D.11: Pull Distribution of Secondary Proton in CDC with final adaption. Inverted momentum (a), polar angle $\theta$ (b) and azimuthal angle $\phi$ (c).

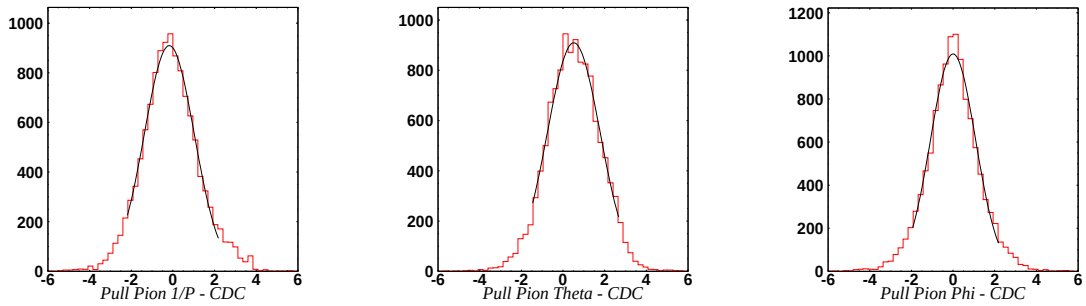


(a) (b) (c)

Figure D.12: Pull Distribution of Pion in CDC with final adaption. Inverted momentum (a), polar angle $\theta$ (b) and azimuthal angle $\phi$ (c).

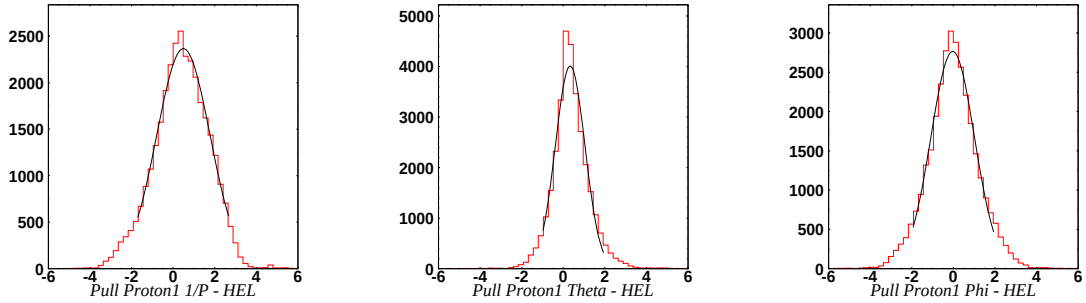


(a) (b) (c)

Figure D.13: Pull Distribution of Primary Proton in Helitron with final adaption. Inverted momentum (a), polar angle $\theta$ (b) and azimuthal angle $\phi$ (c).

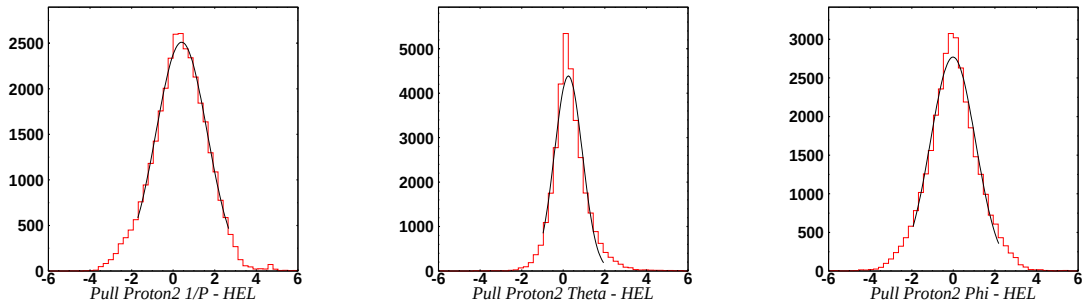


(a) (b) (c)

Figure D.14: Pull Distribution of Secondary Proton in Helitron with final adaption. Inverted momentum (a), polar angle $\theta$ (b) and azimuthal angle $\phi$ (c).

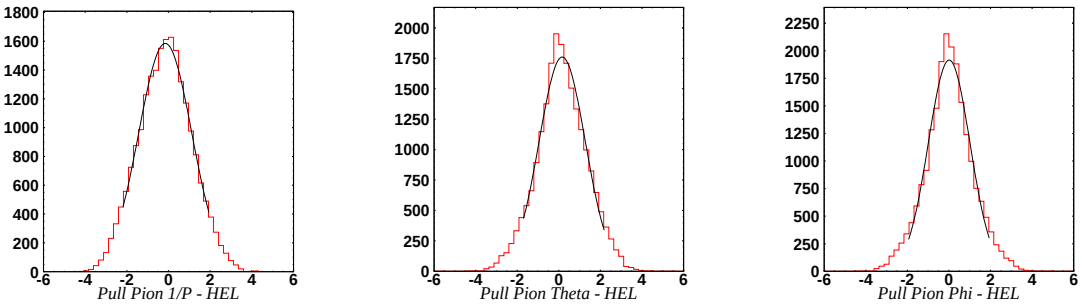


(a) (b) (c)

Figure D.15: Pull Distribution of Pion in Helitron with final adaption. Inverted momentum (a), polar angle $\theta$ (b) and azimuthal angle $\phi$ (c).

| Chamber | Particle | Parameter | $\chi^2/ndf$ | Mean | Sigma |
|---|---|---|---|---|---|
| CDC | Primary Proton | p | 1.75 | 0.634 | 0.824 |
| CDC | Primary Proton | $\theta$ | 5.05 | 1.007 | 0.839 |
| CDC | Primary Proton | $\phi$ | 1.04 | -0.036 | 1.062 |
| CDC | Kaon | p | 2.00 | -0.227 | 1.247 |
| CDC | Kaon | $\theta$ | 3.44 | 0.583 | 1.377 |
| CDC | Kaon | $\phi$ | 28.7 | 0.070 | 0.994 |
| CDC | Secondary Proton | p | 0.66 | 0.254 | 0.537 |
| CDC | Secondary Proton | $\theta$ | 2.41 | 0.768 | 0.543 |
| CDC | Secondary Proton | $\phi$ | 2.69 | -0.014 | 0.704 |
| CDC | Pion | p | 1.22 | -0.175 | 1.202 |
| CDC | Pion | $\theta$ | 2.23 | 0.517 | 1.268 |
| CDC | Pion | $\phi$ | 3.82 | -0.030 | 1.081 |
| HEL | Primary Proton | p | 4.08 | 0.490 | 1.283 |
| HEL | Primary Proton | $\theta$ | 48.3 | 0.517 | 0.712 |
| HEL | Primary Proton | $\phi$ | 8.45 | -0.002 | 1.046 |
| HEL | Secondary Proton | p | 2.16 | 0.407 | 1.231 |
| HEL | Secondary Proton | $\theta$ | 77.9 | 0.248 | 0.672 |
| HEL | Secondary Proton | $\phi$ | 13.6 | -0.017 | 1.084 |
| HEL | Pion | p | 1.61 | -0.156 | 1.276 |
| HEL | Pion | $\theta$ | 7.78 | 0.163 | 1.111 |
| HEL | Pion | $\phi$ | 11.4 | -0.011 | 1.003 |

Table D.8: Pull Value Results (manual Adaption).
Pull Value results with manual adaption [Kai13].

## D.d Pvalue Distribution for Exclusive Analysis

The pvalue of the refit is used to suppress the amount of background in the experimental data. Since the three particle are detected in the different detector regions (the Kaon is measured only by the CDC and RPC), the pvalue distribution is plotted for the different particle-detector combinations separately. The cut on the pvalue distribution is also applied

separately.

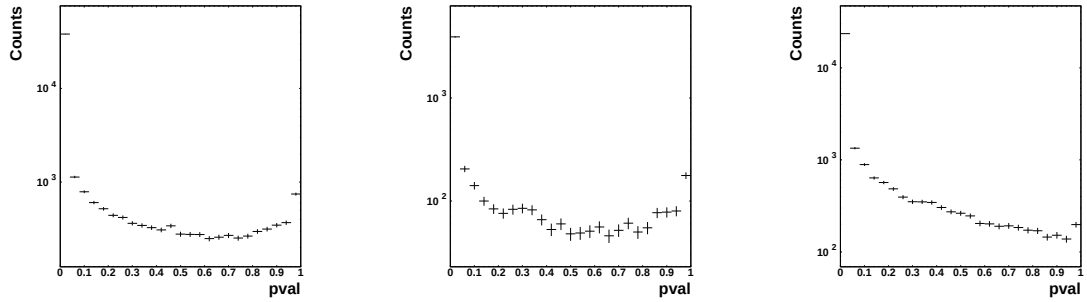


(a) (b) (c)

Figure D.16: Confidence level distribution for following combination: secondary proton detected in SiΛViO and Helitron and $\pi^-$ detected in SiΛViO and Helitron. The primary proton is reconstructed in SiΛViO and Helitron (a), in Helitron only (b) and CDC (c).

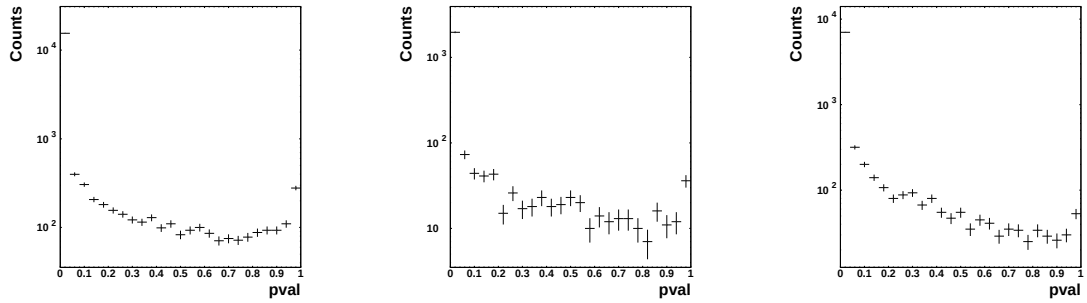


(a) (b) (c)

Figure D.17: Confidence level distribution for following combination: secondary proton detected in SiΛViO and Helitron and $\pi^-$ detected in Helitron only. The primary proton is reconstructed in SiΛViO and Helitron (a), in Helitron only (b) and CDC (c).

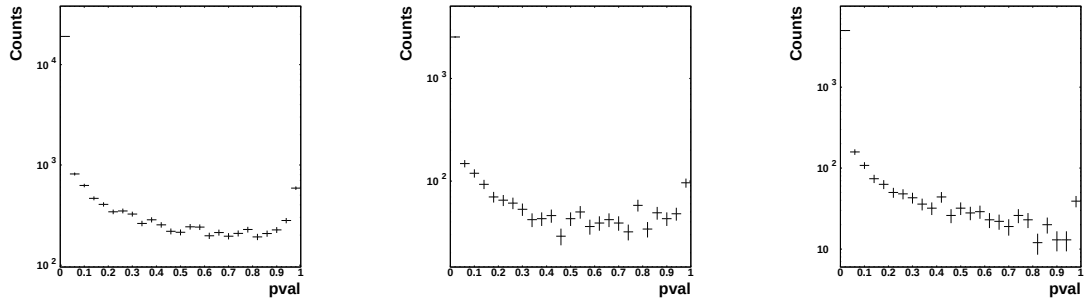


(a) (b) (c)

Figure D.18: Confidence level distribution for following combination: secondary proton detected in SiΛViO and Helitron and $\pi^-$ detected in CDC. The primary proton is reconstructed in SiΛViO and Helitron (a), in Helitron only (b) and CDC (c).

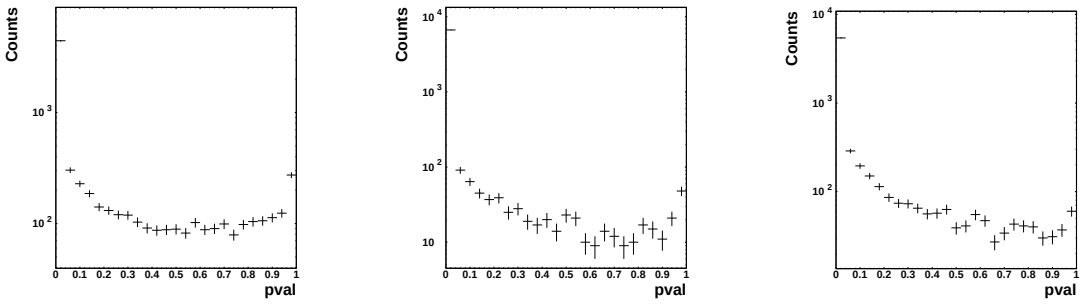


(a) (b) (c)

Figure D.19: Confidence level distribution for following combination: secondary proton detected in Helitron only and $\pi^-$ detected in SiΛViO and Helitron. The primary proton is reconstructed in SiΛViO and Helitron (a), in Helitron only (b) and CDC (c).

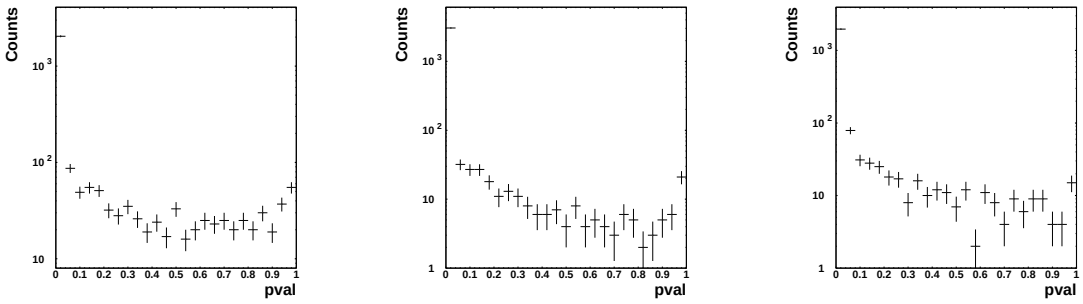


(a) (b) (c)

Figure D.20: Confidence level distribution for following combination: secondary proton detected in Helitron only and $\pi^-$ detected in Helitron only. The primary proton is reconstructed in SiΛViO and Helitron (a), in Helitron only (b) and CDC (c).

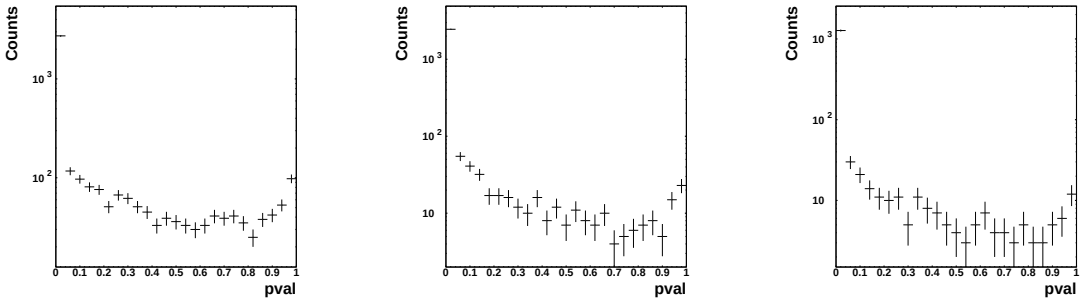


(a) (b) (c)

Figure D.21: Confidence level distribution for following combination: secondary proton detected in Helitron only and $\pi^-$ detected in CDC. The primary proton is reconstructed in SiΛViO and Helitron (a), in Helitron only (b) and CDC (c).

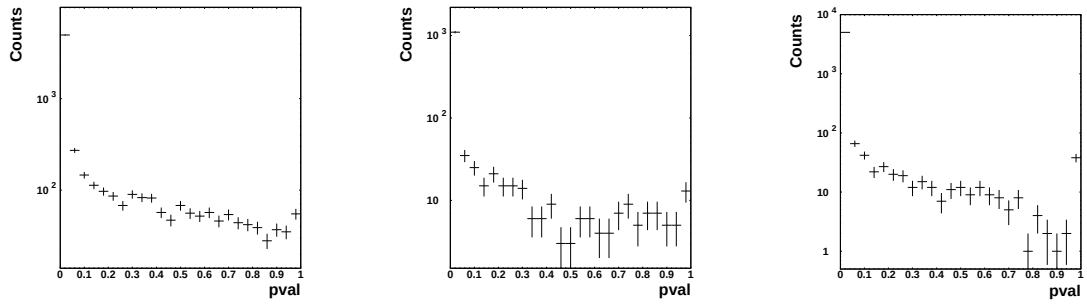


(a) (b) (c)

Figure D.22: Confidence level distribution for following combination: secondary proton detected in CDC and $\pi^-$ detected in SiΛViO and Helitron. The primary proton is reconstructed in SiΛViO and Helitron (a), in Helitron only (b) and CDC (c).

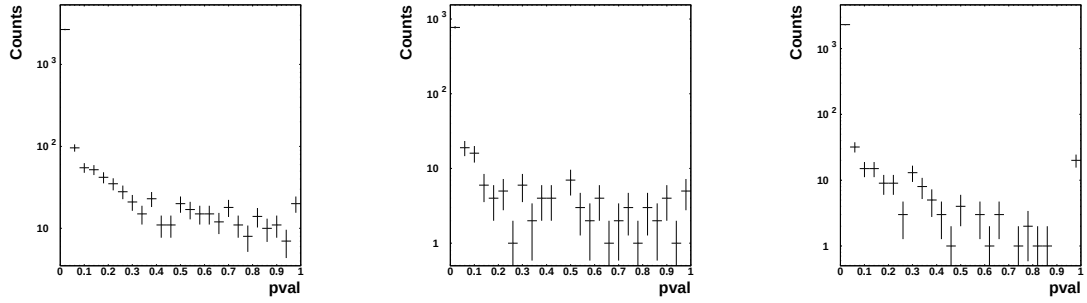


(a) (b) (c)

Figure D.23: Confidence level distribution for following combination: secondary proton detected in CDC and $\pi^-$ detected in Helitron only. The primary proton is reconstructed in SiΛViO and Helitron (a), in Helitron only (b) and CDC (c).

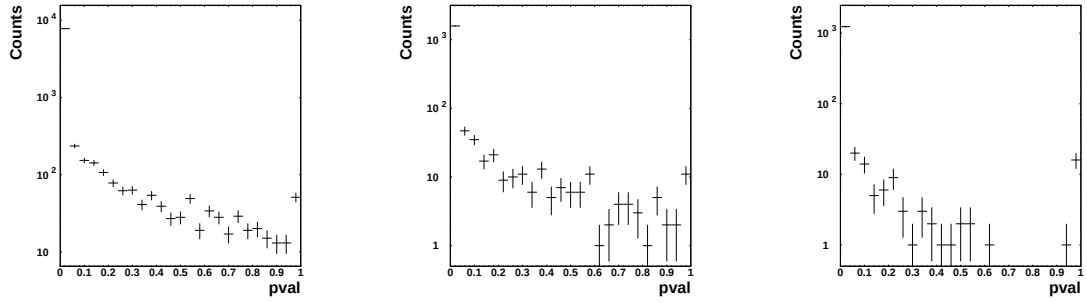


(a) (b) (c)

Figure D.24: Confidence level distribution for following combination: secondary proton detected in CDC and $\pi^-$ detected in CDC. The primary proton is reconstructed in SiΛViO and Helitron (a), in Helitron only (b) and CDC (c).

# Appendix E

# Efficiency Comparison Data-Simulation

In the following the particle spectra of elastic scattered protons for the full set of parameters (p,$\theta$,$\phi$) for the different detector hemisphere, which are used for efficiency correction if the simulation, are shown.

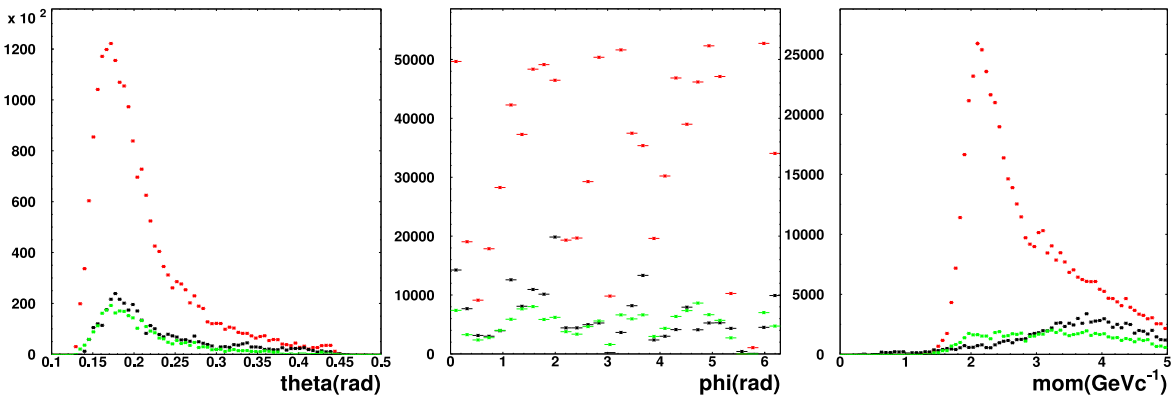


(a) (b) (c)

Figure E.1: Parameters distributions for tracks measured in the Helitron and SiΛViO . Experimental data(black), Simulation data before scaling (red dots) and after efficiency scaling (green dots).

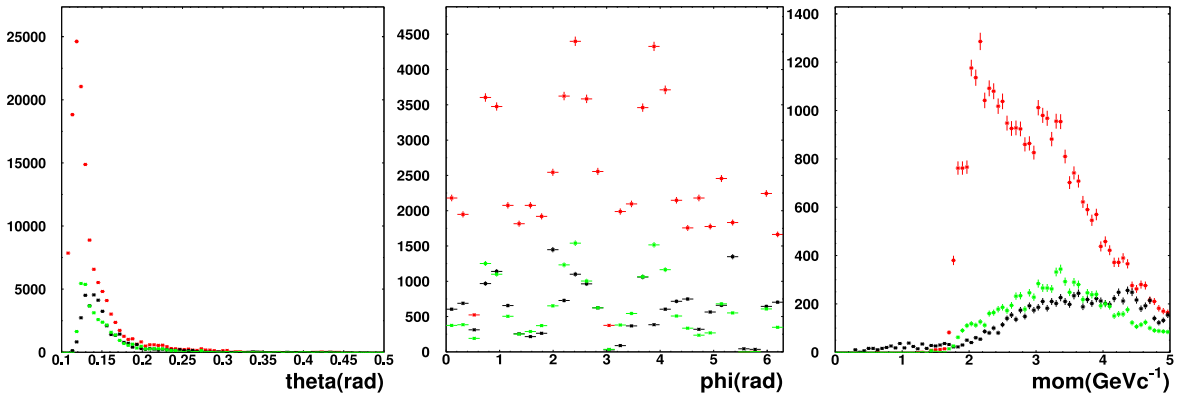


(a) (b) (c)

Figure E.2: Parameters distributions for tracks measured in the Helitron. Experimental data(black), Simulation data before scaling (red dots) and after efficiency scaling (green dots).

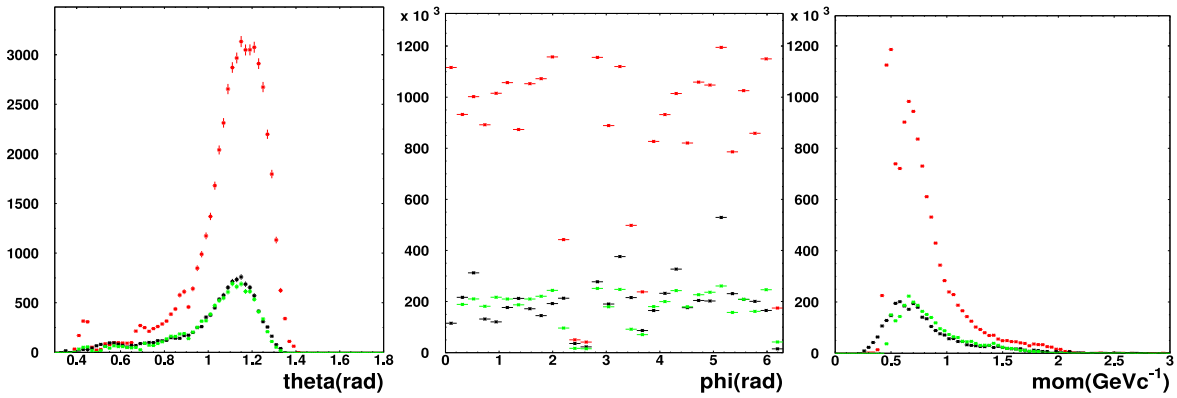


(a) (b) (c)

Figure E.3: Parameters distributions for tracks measured in the CDC. Experimental data(black), Simulation data before scaling (red dots) and after efficiency scaling (green dots).

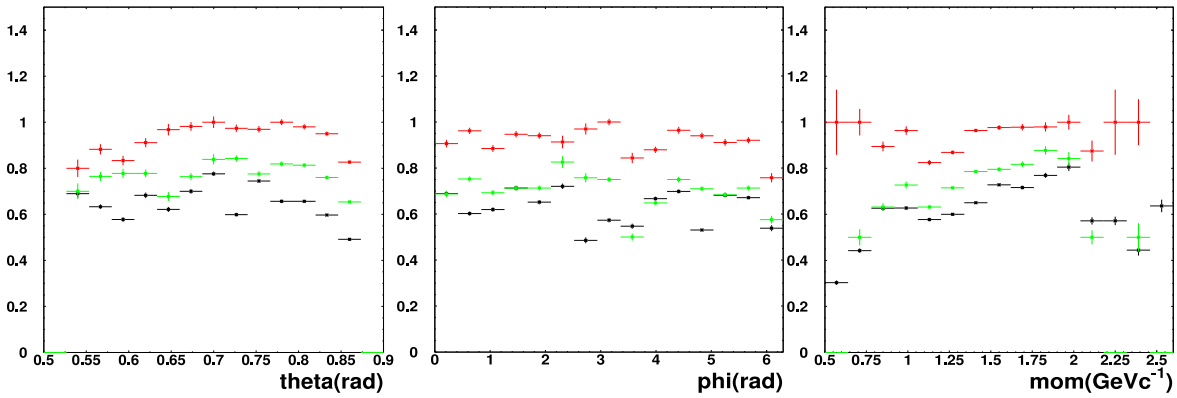


(a) (b) (c)

Figure E.4: CDC-RPC matching efficiency given in %. Experimental data(black), Simulation data before scaling (red dots) and after efficiency scaling (green dots).

# Appendix F

# Comparison Spectra of $N^*$ Resonances

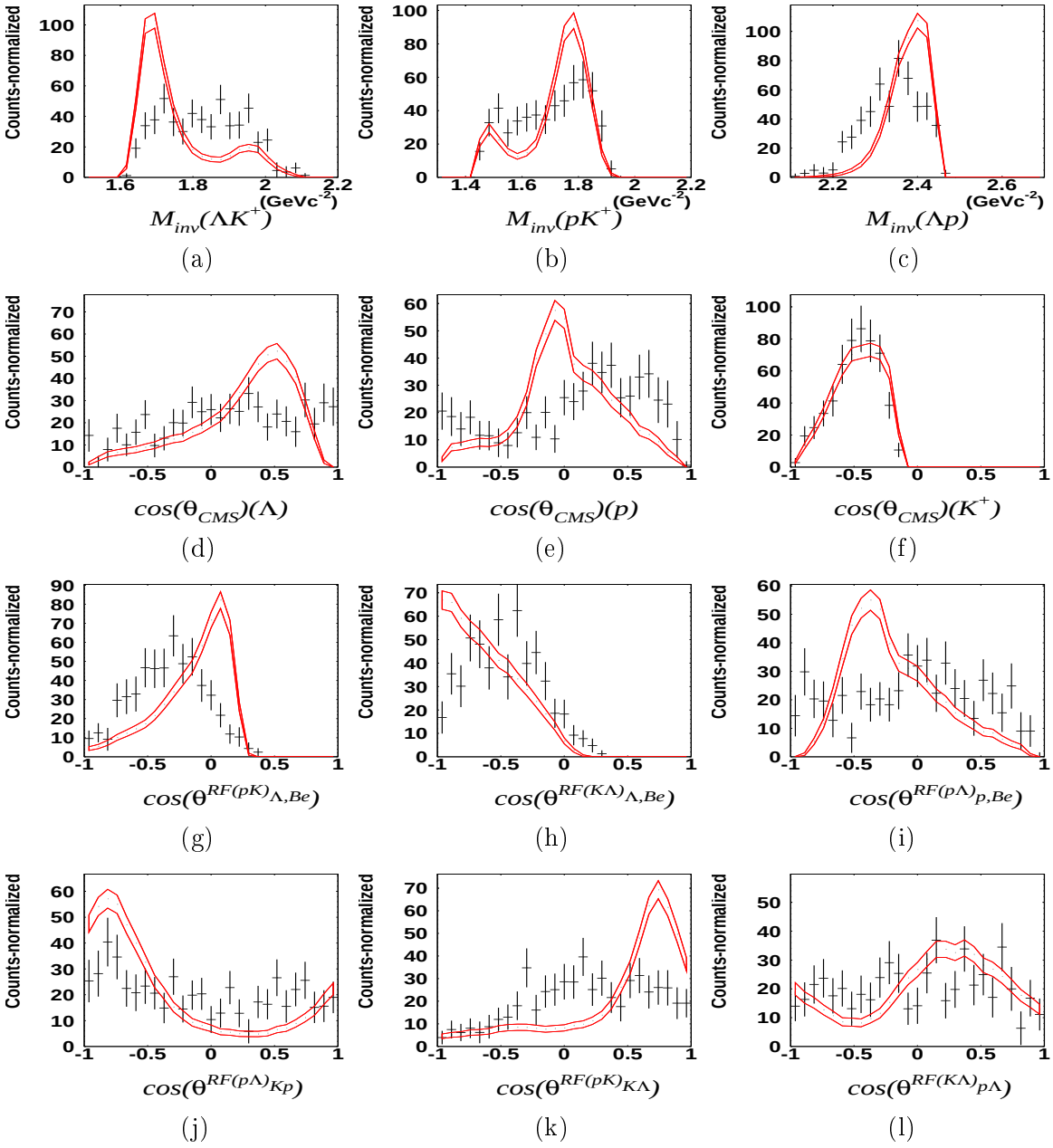


Figure F.1: Comparison of experimental data (black dots) with $N^*(1650)$ phase space simulation (red band). The complete set of kinematical observables is plotted. (a)-(c) are the invariant mass distributions. (d)-(f) show the center of mass angle, (g)-(i) show the three Gottfried Jackson angle and (k)-(m) show the distribution of the Helicity angle.

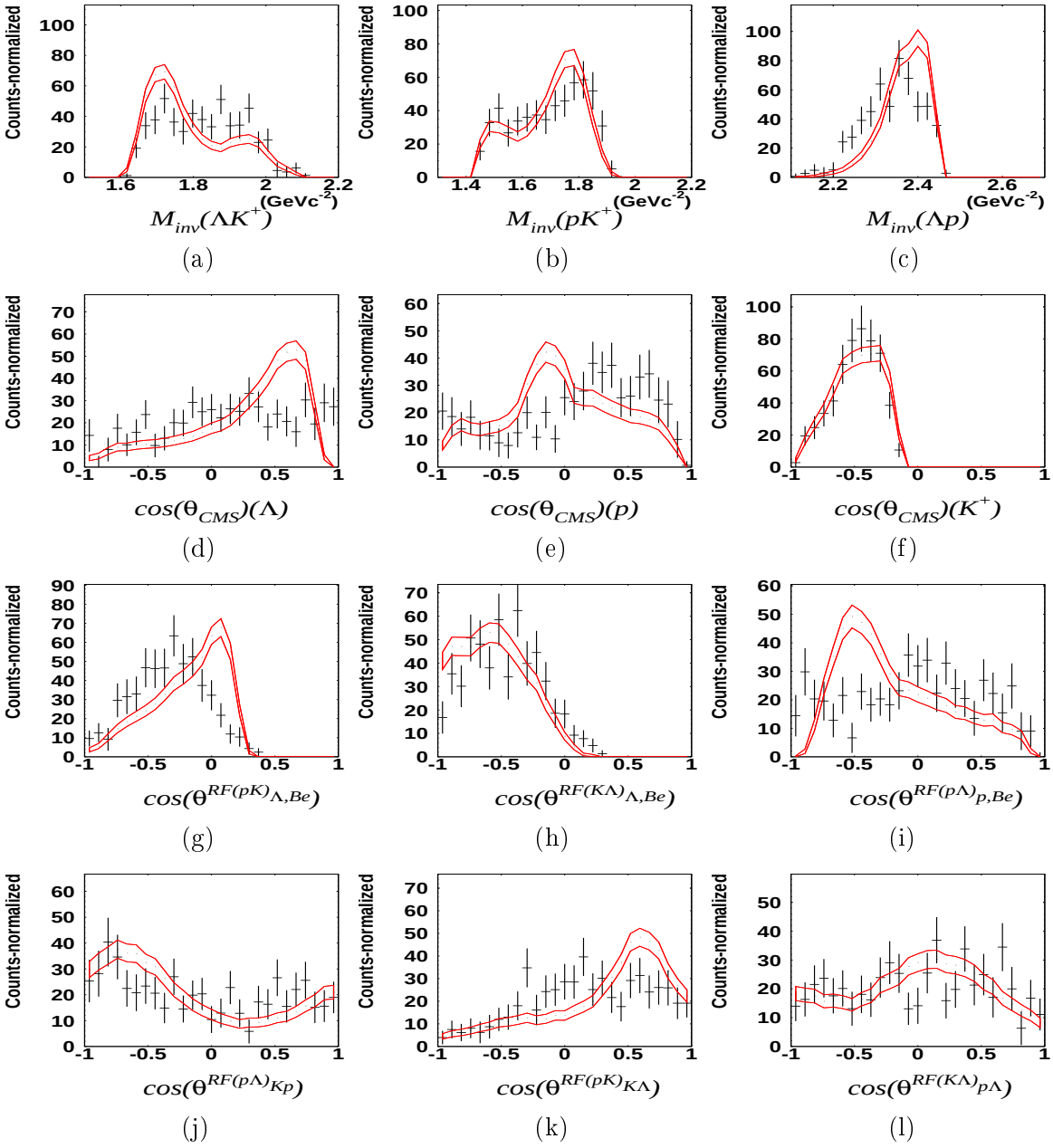


Figure F.2: Comparison of experimental data (black dots) with $N^*(1700)$ phase space simulation (red band). The complete set of kinematical observables is plotted. (a)-(c) are the invariant mass distributions. (d)-(f) show the center of mass angle, (g)-(i) show the three Gottfried Jackson angle and (k)-(m) show the distribution of the Helicity angle.

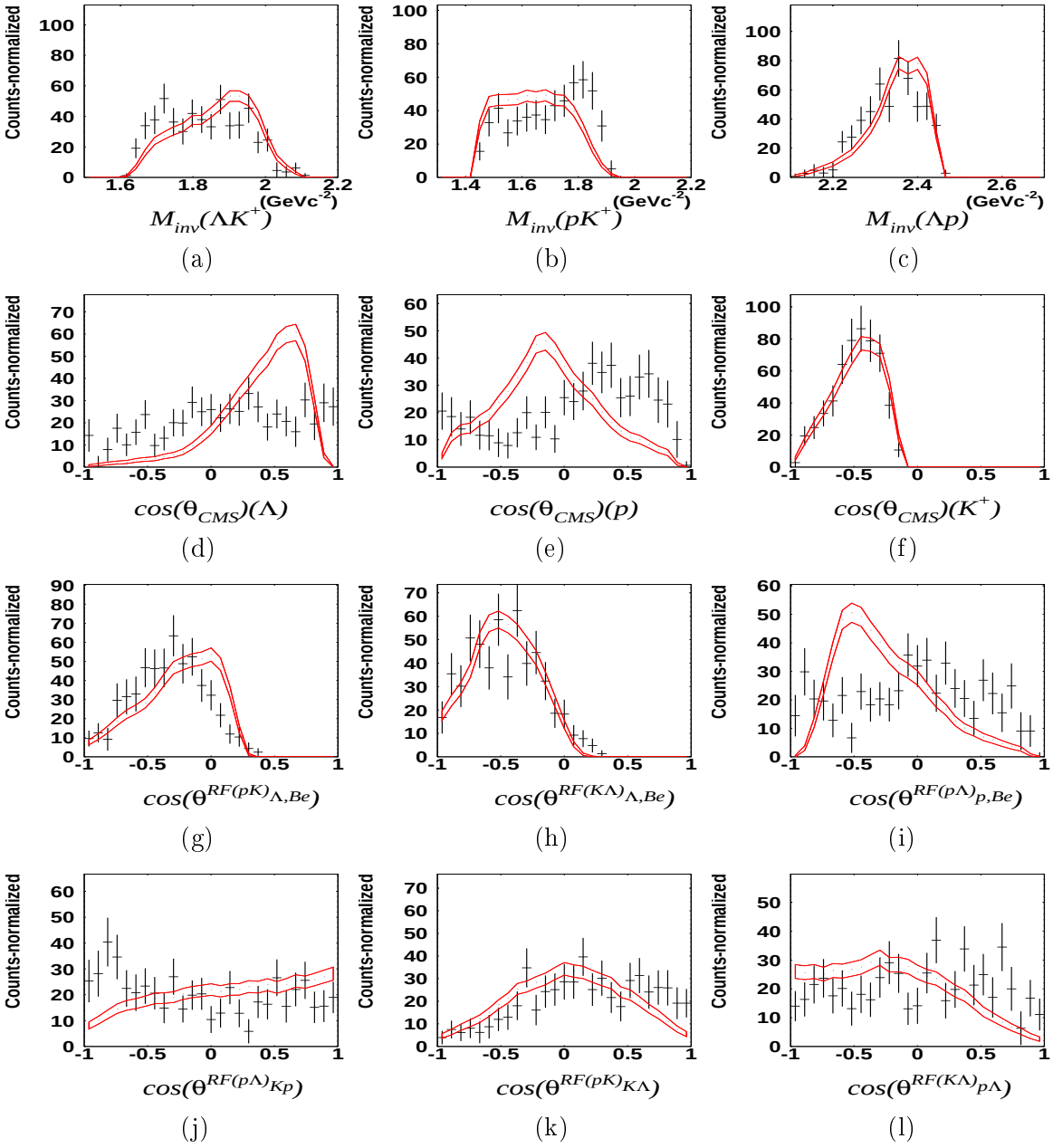


Figure F.3: Comparison of experimental data (black dots) with $N^*(1900)$ phase space simulation (red band). The complete set of kinematical observables is plotted. (a)-(c) are the invariant mass distributions. (d)-(f) show the center of mass angle, (g)-(i) show the three Gottfried Jackson angle and (k)-(m) show the distribution of the Helicity angle.

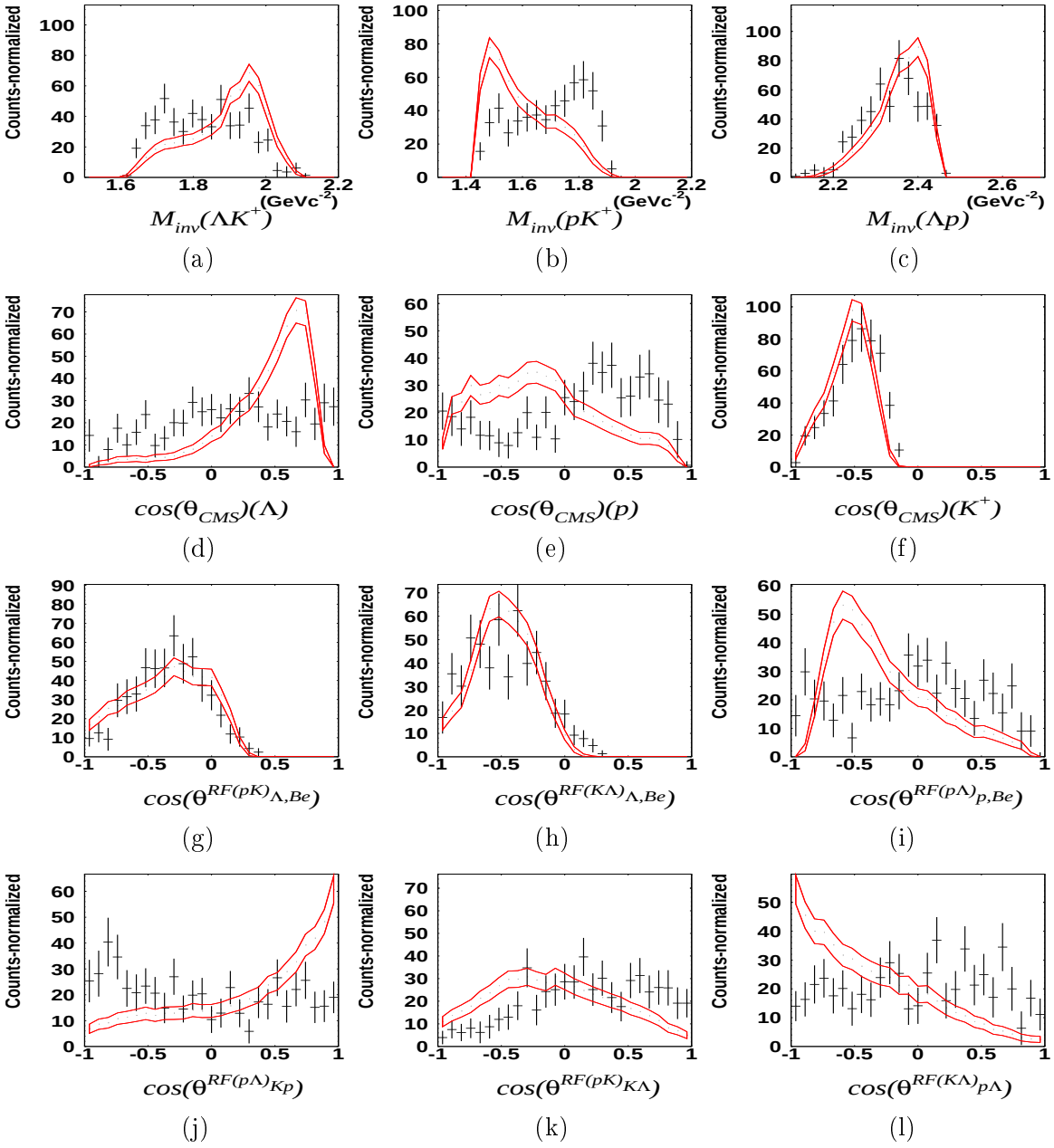


Figure F.4: Comparison of experimental data (black dots) with $N^*(2190)$ phase space simulation (red band). The complete set of kinematical observables is plotted. (a)-(c) are the invariant mass distributions. (d)-(f) show the center of mass angle, (g)-(i) show the three Gottfried Jackson angle and (k)-(m) show the distribution of the Helicity angle.

# Appendix G

# The BG-PWA Framework

### G..i. Input Data Format

The experimental, the background and the simulation data have to provided to the BG-PWA as text in a dedicated list format.
Each event has to be provided in the following way:

| | | | |
|---|---|---|---|
| Event Number | Spare | Weighting Factor | Spare |
| $p_x(K^+)$ | $p_y(K^+)$ | $p_z(K^+)$ | $E(K^+)$ |
| $p_x(p)$ | $p_y(p)$ | $p_z(p)$ | $E(p)$ |
| $p_x(\lambda)$ | $p_y(\lambda)$ | $p_z(\lambda)$ | $E(\lambda)$ |

The weighting factor is just used for the background sample of the experimental value. The spare value are not used in the proton-proton partial wave analysis.

### G..ii. Parameter File Format

In the wave transition parameter file the full set of transitions waves are arranged in groups, of the corresponding quantum numbers of the initial proton-proton state, which is written in the following way:

Isospin $N_{multiplets}$ L J $N_{fin.stat}$

After each initial state notation the parameter of the final state are listed in the following format:

| | | | | | |
|---|---|---|---|---|---|
| I | $a_1^\alpha$(init.) | $a_1^\alpha$(step.) | $a_1^\alpha$(min.) | $a_1^\alpha$(max.) | Final State Notation |
| I | $a_2^\alpha$(init.) | $a_2^\alpha$(step.) | $a_2^\alpha$(min.) | $a_2^\alpha$(max.) | |
| I | $a_3^\alpha$(init.) | $a_3^\alpha$(step.) | $a_3^\alpha$(min.) | $a_3^\alpha$(max.) | |

I is the parameter, which is incremented in each line. For the parameter the starting value (init.), the step width for the fit (step.), the minimal value (min.) and the maximal value (max.) have to provided. The Final State Notation consists of the state configuration, the state multiplet and the angular momentum (e.g 'S11(1650)-p' 3 'P')

# Appendix H

# PWA Solution Scan

## H.a Parameters Scan

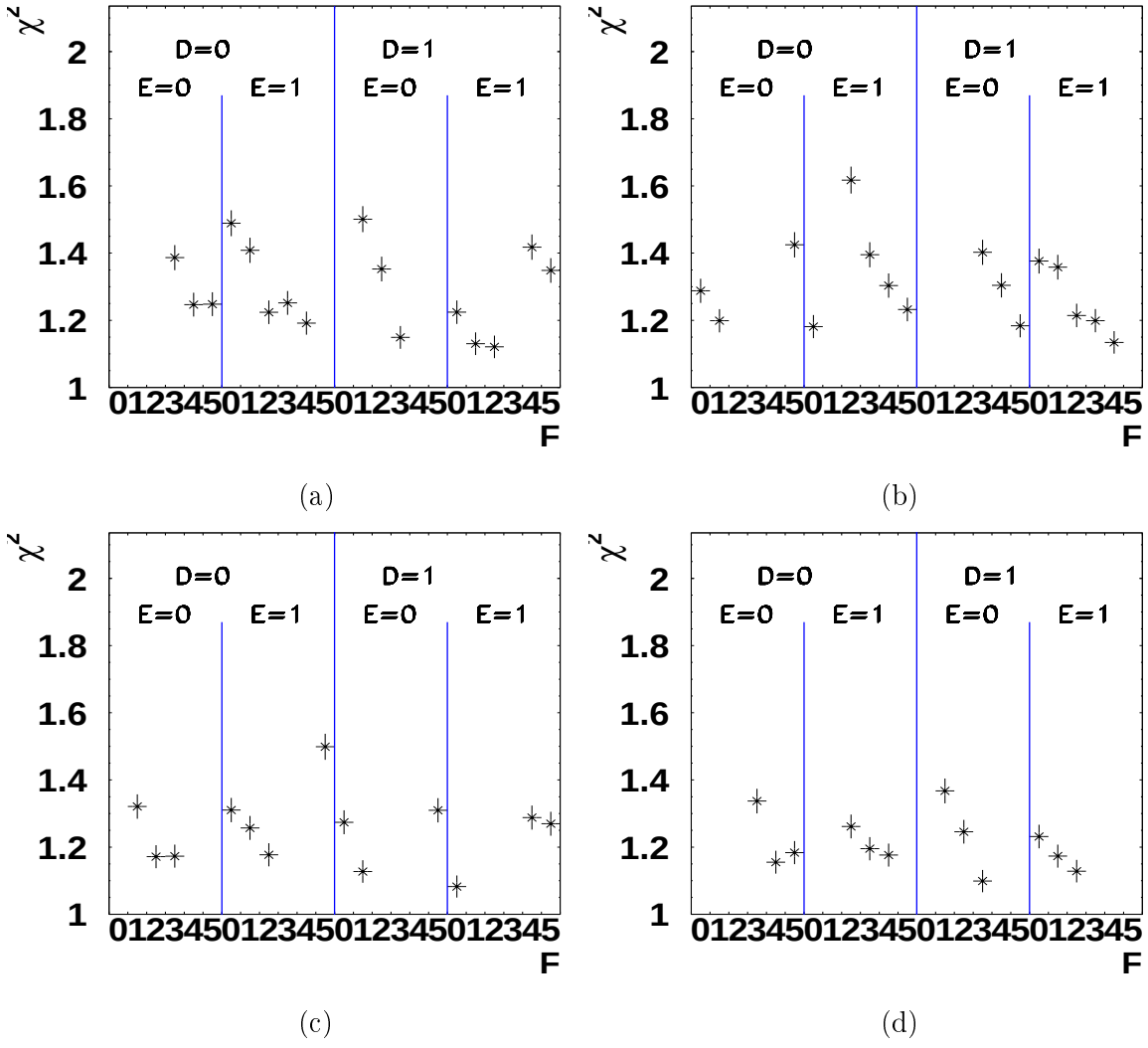


(a) (b)

(c) (d)

Figure H.1: $\chi^2$ value for the PWA of different parameter sets versus the value F of the parameter set is plot. In spectrum (a) the parameter sets=000***, in (b) the parameter sets 001***, in (c) the parameter sets 010*** and in (d) the parameter sets 011*** are shown. Results are just plotted for solution, which did converges.

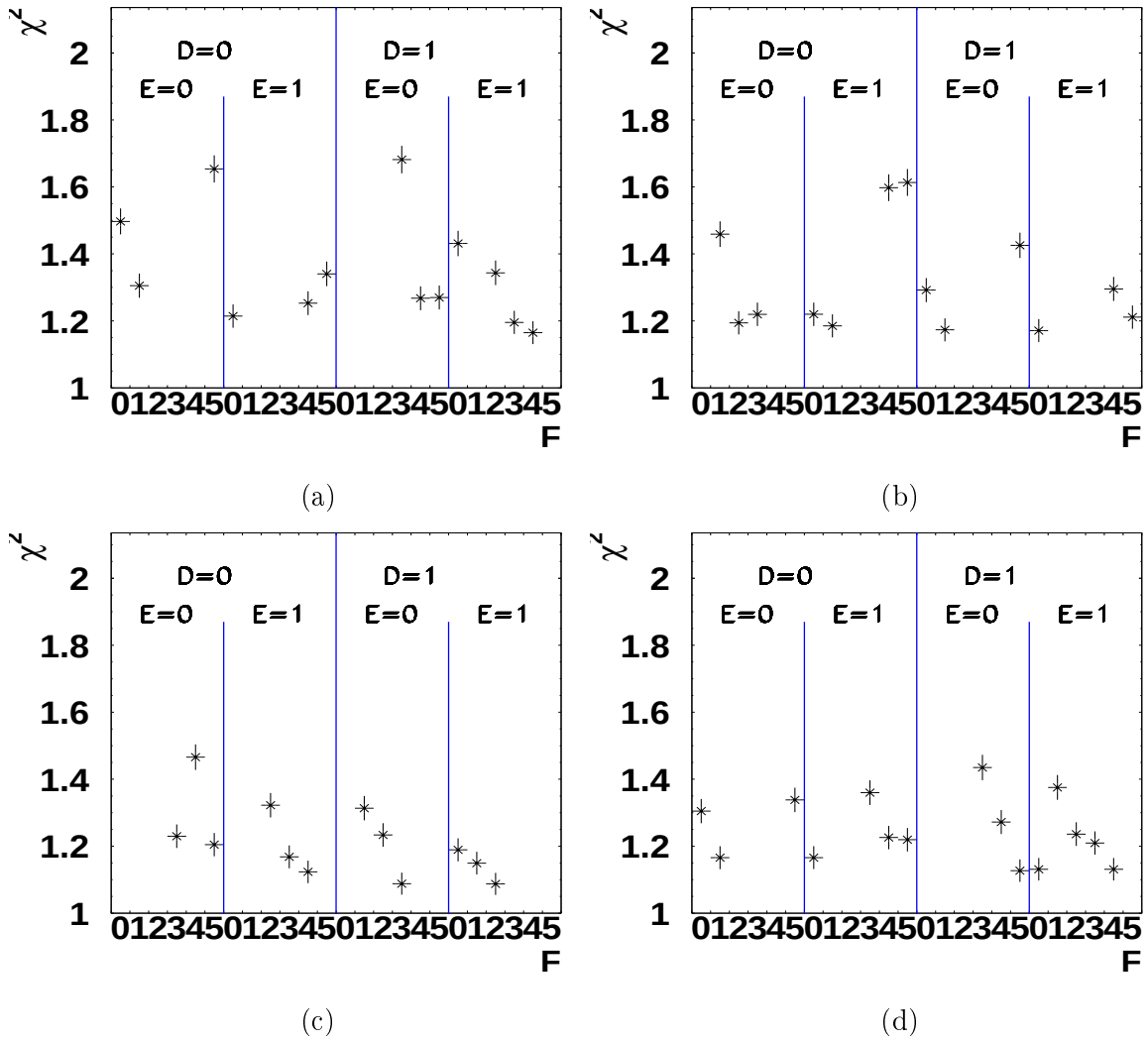


(a) (b)

(c) (d)

Figure H.2: $\chi^2$ value for the PWA of different parameter sets versus the value F of the parameter set is plot. In spectrum (a) the parameter sets=100***, in (b) the parameter sets 101***, in (c) the parameter sets 110*** and in (d) the parameter sets 111*** are shown. Results are just plotted for solution, which did converges.

## H.b Legendre Parameters

In the following tables the parameters of a Legendre fits - according to Equation H.1 - of the angular spectra in the full phase space are listed, obtained from the five best parameters set of the BG-PWA.

$$F(x) = a_1 * x + a_2 \left\{ \frac{1}{2} \left(3x^2 - 1\right) \right\} + a_3 \left( \frac{1}{2} \left(5x^3 - 3x\right) \right) + a_4 \left\{ \frac{1}{8} \left(35x^4 - 30x^2 + 3\right) \right\} \quad \text{(H.1)}$$

| | $a_1$ | $a_2$ | $a_3$ | $a_4$ |
|---|---|---|---|---|
| $\theta_{CMS}(\lambda)$ | 0.01±0.01 | 1.03±0.01 | 0.03±0.02 | 0.4±0.02 |
| $\theta_{CMS}(p)$ | -0.03±0.01 | 1.49±0.01 | -0.04±0.01 | 0.42±0.02 |
| $\theta_{CMS}(K^+)$ | 0.01±0.01 | -0.03±0.01 | 0.02±0.01 | 0.28±0.02 |
| $\theta^{RFpK}_{\lambda,Be}$ | 0.04±0.01 | 0.47±0.01 | -0.11±0.01 | 0.1±0.02 |
| $\theta^{RFK\lambda}_{\lambda,Be}$ | -0.05±0.01 | 0.17±0.01 | 0.05±0.01 | 0.01±0.02 |
| $\theta^{RFp\lambda}_{p,Be}$ | -0.07±0.01 | 1.43±0.01 | -0.08±0.01 | 0.41±0.02 |
| $\theta^{RFp\lambda}_{K,p}$ | -0.43±0.01 | -0.13±0.01 | 0.07±0.01 | -0.03±0.02 |
| $\theta^{RFpK}_{\lambda,K}$ | 0.59±0.01 | -0.05±0.01 | -0.4±0.01 | -0.15±0.02 |
| $\theta^{RFK\lambda}_{\lambda,p}$ | 0.02±0.01 | 0.13±0.01 | 0.11±0.01 | 0.06±0.02 |

Table H.1: Legendre Parameters for Parameter Set 0100110

| | $a_1$ | $a_2$ | $a_3$ | $a_4$ |
|---|---|---|---|---|
| $\theta_{CMS}(\lambda)$ | 0.02±0.01 | 1.05±0.01 | 0.03±0.01 | 0.42±0.02 |
| $\theta_{CMS}(p)$ | -0.03±0.01 | 1.48±0.01 | -0.04±0.01 | 0.47±0.02 |
| $\theta_{CMS}(K^+)$ | 0.01±0.01 | 0.06±0.01 | 0.02±0.01 | 0.1±0.02 |
| $\theta^{RFpK}_{\lambda,Be}$ | 0.05±0.01 | 0.51±0.01 | -0.19±0.01 | 0.05±0.02 |
| $\theta^{RFK\lambda}_{\lambda,Be}$ | -0.06±0.01 | 0.26±0.01 | -0.03±0.01 | -0.07±0.02 |
| $\theta^{RFp\lambda}_{p,Be}$ | -0.08±0.01 | 1.43±0.01 | -0.11±0.01 | 0.4±0.02 |
| $\theta^{RFp\lambda}_{K,p}$ | -0.47±0.01 | -0.11±0.01 | 0.07±0.01 | -0.02±0.02 |
| $\theta^{RFpK}_{\lambda,K}$ | 0.59±0.01 | -0.1±0.01 | -0.4±0.01 | -0.07±0.02 |
| $\theta^{RFK\lambda}_{\lambda,p}$ | 0.08±0.01 | 0.15±0.01 | 0.11±0.01 | 0.07±0.02 |

Table H.2: Legendre Parameters for Parameter Set 110112

| | $a_1$ | $a_2$ | $a_3$ | $a_4$ |
|---|---|---|---|---|
| $\theta_{CMS}(\lambda)$ | 0.01±0.01 | 1.14±0.01 | 0.03±0.01 | 0.46±0.02 |
| $\theta_{CMS}(p)$ | -0.03±0.01 | 1.65±0.01 | -0.04±0.01 | 0.45±0.02 |
| $\theta_{CMS}(K^+)$ | 0.01±0.01 | -0.09±0.01 | 0.02±0.01 | 0.13±0.02 |
| $\theta^{RFpK}_{\lambda,Be}$ | 0.07±0.01 | 0.49±0.01 | -0.2±0.01 | 0±0.02 |
| $\theta^{RFK\lambda}_{\lambda,Be}$ | -0.05±0.01 | 0.16±0.01 | 0±0.01 | -0.07±0.02 |
| $\theta^{RFp\lambda}_{p,Be}$ | -0.08±0.01 | 1.57±0.01 | -0.12±0.01 | 0.41±0.02 |
| $\theta^{RFp\lambda}_{K,p}$ | -0.5±0.01 | -0.25±0.01 | 0.15±0.01 | -0.07±0.01 |
| $\theta^{RFpK}_{\lambda,K}$ | 0.79±0.01 | -0.3±0.01 | -0.46±0.01 | -0.2±0.01 |
| $\theta^{RFK\lambda}_{\lambda,p}$ | -0.08±0.01 | -0.04±0.01 | 0.07±0.01 | 0.04±0.02 |

Table H.3: Legendre Parameters for Parameter Set 110103

| | $a_1$ | $a_2$ | $a_3$ | $a_4$ |
|---|---|---|---|---|
| $\theta_{CMS}(\lambda)$ | 0.01±0.01 | 1.05±0.01 | 0.03±0.01 | 0.41±0.02 |
| $\theta_{CMS}(p)$ | -0.03±0.01 | 1.59±0.01 | -0.04±0.01 | 0.45±0.02 |
| $\theta_{CMS}(K^+)$ | 0.01±0.01 | -0.02±0.01 | 0.02±0.01 | 0.13±0.02 |
| $\theta^{RFpK}_{\lambda,Be}$ | 0.07±0.01 | 0.51±0.01 | -0.15±0.01 | 0.04±0.02 |
| $\theta^{RFK\lambda}_{\lambda,Be}$ | -0.04±0.01 | 0.17±0.01 | 0.01±0.01 | -0.06±0.02 |
| $\theta^{RFp\lambda}_{p,Be}$ | -0.08±0.01 | 1.5±0.01 | -0.09±0.01 | 0.38±0.02 |
| $\theta^{RFp\lambda}_{K,p}$ | -0.47±0.01 | -0.22±0.01 | 0.12±0.01 | -0.06±0.01 |
| $\theta^{RFpK}_{\lambda,K}$ | 0.74±0.01 | -0.22±0.01 | -0.4±0.01 | -0.2±0.01 |
| $\theta^{RFK\lambda}_{\lambda,p}$ | -0.06±0.01 | 0.04±0.01 | 0.03±0.01 | 0.03±0.02 |

Table H.4: Legendre Parameters for Parameter Set 011103

| | $a_1$ | $a_2$ | $a_3$ | $a_4$ |
|---|---|---|---|---|
| $\theta_{CMS}(\lambda)$ | 0.02±0.01 | 0.97±0.02 | 0.04±0.02 | 0.42±0.02 |
| $\theta_{CMS}(p)$ | -0.02±0.01 | 1.18±0.02 | -0.04±0.02 | 0.23±0.02 |
| $\theta_{CMS}(K^+)$ | 0±0.01 | 0±0.01 | 0.02±0.02 | 0.42±0.02 |
| $\theta^{RFpK}_{\lambda,Be}$ | 0.08±0.01 | 0.34±0.01 | -0.03±0.02 | 0.16±0.02 |
| $\theta^{RFK\lambda}_{\lambda,Be}$ | -0.06±0.01 | 0.26±0.01 | 0.06±0.02 | 0.07±0.02 |
| $\theta^{RFp\lambda}_{p,Be}$ | -0.08±0.01 | 1.21±0.02 | -0.16±0.02 | 0.31±0.02 |
| $\theta^{RFp\lambda}_{K,p}$ | -0.46±0.01 | -0.01±0.01 | 0.04±0.02 | -0.04±0.02 |
| $\theta^{RFpK}_{\lambda,K}$ | 0.62±0.01 | 0.11±0.01 | -0.41±0.02 | -0.18±0.02 |
| $\theta^{RFK\lambda}_{\lambda,p}$ | 0.07±0.01 | 0.2±0.01 | 0.11±0.02 | 0.06±0.02 |

Table H.5: Legendre Parameters for Parameter Set 000113

| | $a_1$ | $a_2$ | $a_3$ | $a_4$ |
|---|---|---|---|---|
| $\theta_{CMS}(\lambda)$ | 0.01±0.01 | 1.11±0.01 | 0.03±0.01 | 0.46±0.02 |
| $\theta_{CMS}(p)$ | -0.02±0.01 | 1.46±0.01 | -0.03±0.01 | 0.41±0.01 |
| $\theta_{CMS}(K^+)$ | 0±0.01 | -0.03±0.01 | 0.02±0.01 | 0.11±0.01 |
| $\theta^{RFpK}_{\lambda,Be}$ | 0.03±0.01 | 0.43±0.01 | -0.14±0.01 | 0.03±0.01 |
| $\theta^{RFK\lambda}_{\lambda,Be}$ | -0.08±0.01 | 0.21±0.01 | -0.03±0.01 | -0.04±0.01 |
| $\theta^{RFp\lambda}_{p,Be}$ | -0.08±0.01 | 1.47±0.01 | -0.13±0.01 | 0.4±0.01 |
| $\theta^{RFp\lambda}_{K,p}$ | -0.433±0.009 | -0.12±0.01 | 0.1±0.01 | -0.04±0.01 |
| $\theta^{RFpK}_{\lambda,K}$ | 0.57±0.009 | -0.12±0.01 | -0.39±0.01 | -0.13±0.01 |
| $\theta^{RFK\lambda}_{\lambda,p}$ | 0.04±0.01 | 0.08±0.01 | 0.1±0.01 | 0.06±0.01 |

Table H.6: Legendre Parameters for Parameter Set 111115

# Appendix I

# pp$K^-$ Upper Limit scan

## I.a Upper Limit Spectra

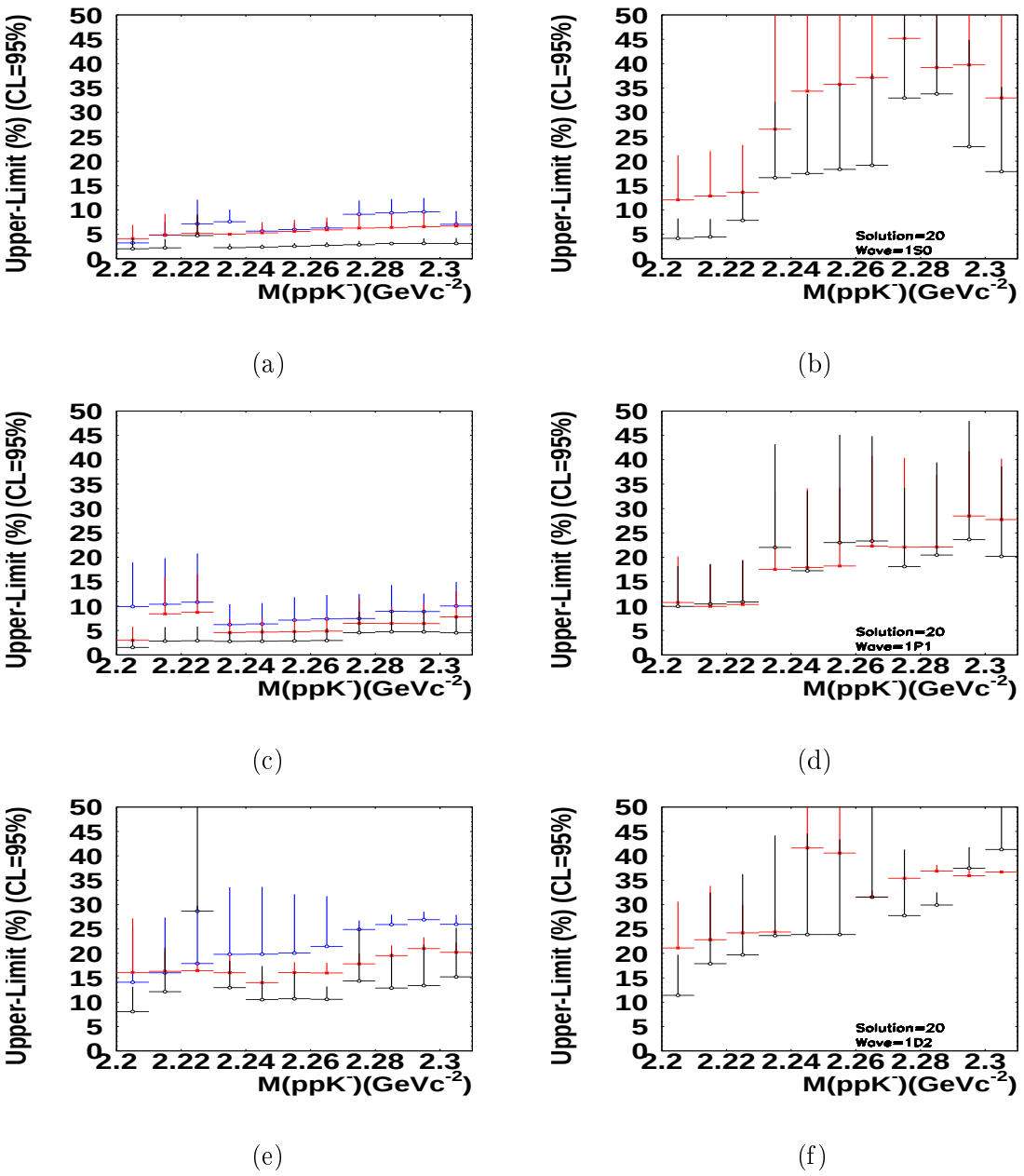


Figure I.1: Upper Limit of the relative contribution of the pp$K^-$ production (given in %) for a exclusion confidence Level of 95% versus the peak mass of the pp$K^-$ used in the PWA fit.The production of the pp$K^-$ is from the initial proton state $0^+$ (a,b), $1^-$ (c,d) or $(2^+)$. In spectra (a),(c) and (e) the $\Gamma$ of pp$K^-$ on PWA is set to 20 MeV/c$^2$(blue crosses), 35 MeV/c$^2$(red crosses) and 50 MeV/c$^2$(black crosses). In spectra (b),(d) and (f) the $\Gamma$ of pp$K^-$ on PWA is set 80 MeV/c$^2$(red crosses) and 60 MeV/c$^2$(black crosses). For the background assumption solution number 000113 was used.

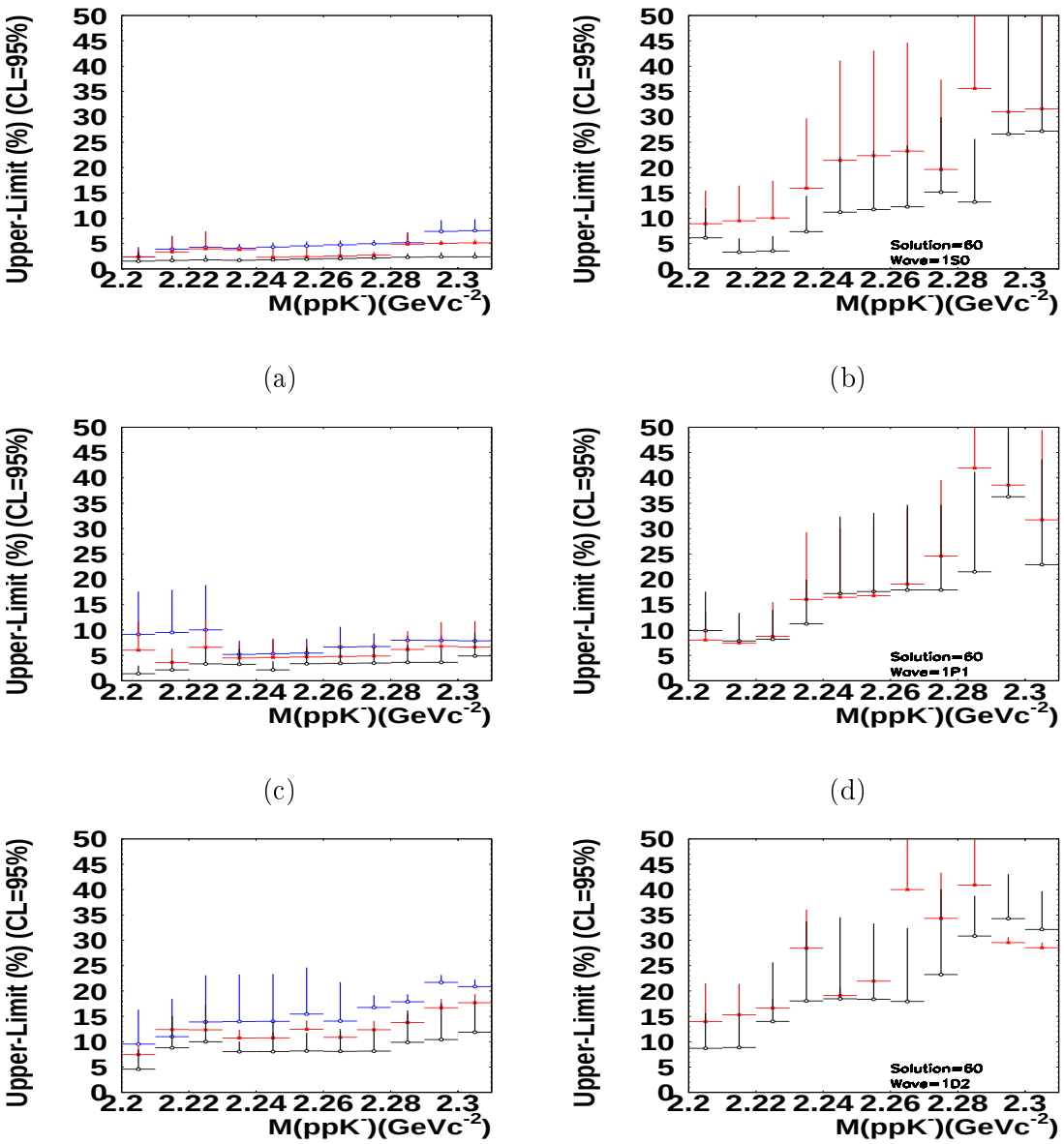


Figure I.2: Upper Limit of the relative contribution of the pp$K^-$ production (given in %) for a exclusion confidence Level of 95% versus the peak mass of the pp$K^-$ used in the PWA fit.The production of the pp$K^-$ is from the initial proton state $0^+$ (a,b), $1^-$ (c,d) or $(2^+)$. In spectra (a),(c) and (e) the $\Gamma$ of pp$K^-$ on PWA is set to 20 MeV/c$^2$(blue crosses), 35 MeV/c$^2$(red crosses) and 50 MeV/c$^2$(black crosses). In spectra (b),(d) and (f) the $\Gamma$ of pp$K^-$ on PWA is set , 80 MeV/c$^2$(red crosses) and 60 MeV/c$^2$(black crosses). For the background assumption solution number 010110 was used.

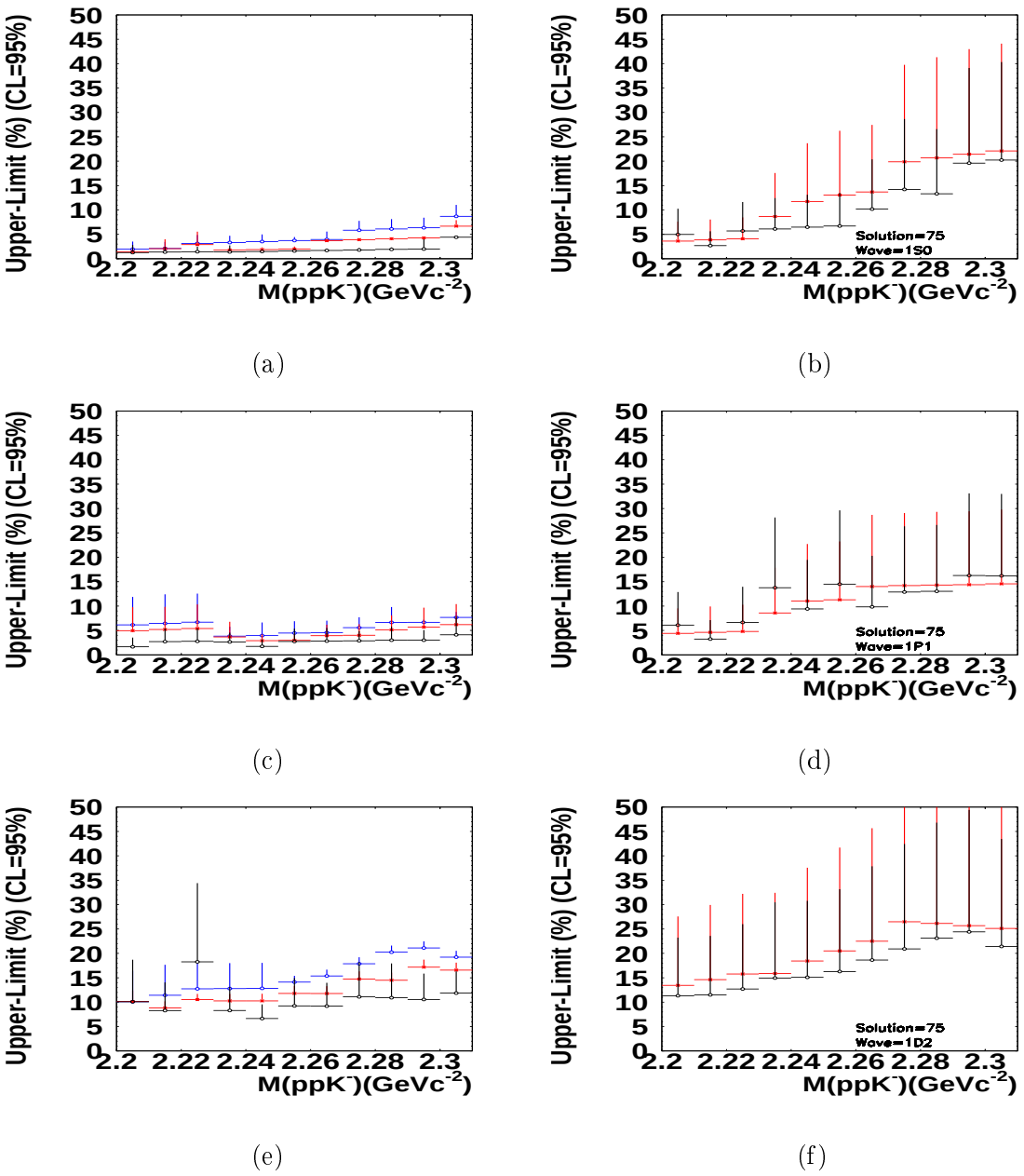


(a) (b) (c) (d) (e) (f)

Figure I.3: Upper Limit of the relative contribution of the pp$K^-$ production (given in %) for a exclusion confidence Level of 95% versus the peak mass of the pp$K^-$ used in the PWA fit.The production of the pp$K^-$ is from the initial proton state $0^+$ (a,b), $1^-$ (c,d) or $(2^+)$. In spectra (a),(c) and (e) the $\Gamma$ of pp$K^-$ on PWA is set to 20 MeV/c$^2$(blue crosses), 35 MeV/c$^2$(red crosses) and 50 MeV/c$^2$(black crosses). In spectra (b),(d) and (f) the $\Gamma$ of pp$K^-$ on PWA is set , 80 MeV/c$^2$(red crosses) and 60 MeV/c$^2$(black crosses). For the background assumption solution number 011103 was used.

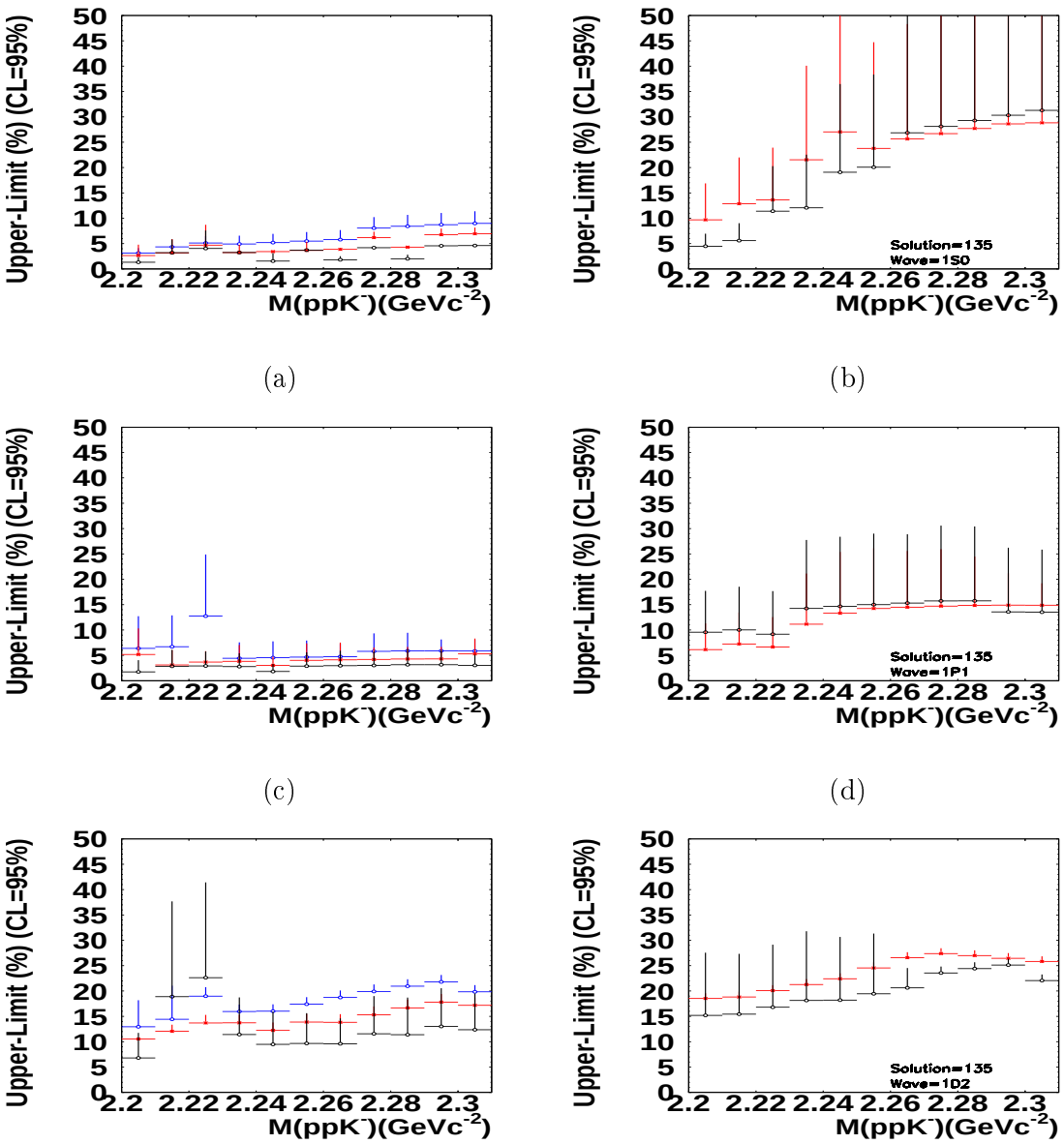


Figure I.4: Upper Limit of the relative contribution of the pp$K^-$ production (given in %) for a exclusion confidence Level of 95% versus the peak mass of the pp$K^-$ used in the PWA fit.The production of the pp$K^-$ is from the initial proton state $0^+$ (a,b), $1^-$ (c,d) or $(2^+)$. In spectra (a),(c) and (e) the $\Gamma$ of pp$K^-$ on PWA is set to 20 MeV/c$^2$(blue crosses), 35 MeV/c$^2$(red crosses) and 50 MeV/c$^2$(black crosses). In spectra (b),(d) and (f) the $\Gamma$ of pp$K^-$ on PWA is set , 80 MeV/c$^2$(red crosses) and 60 MeV/c$^2$(black crosses). For the background assumption solution number 110103 was used.

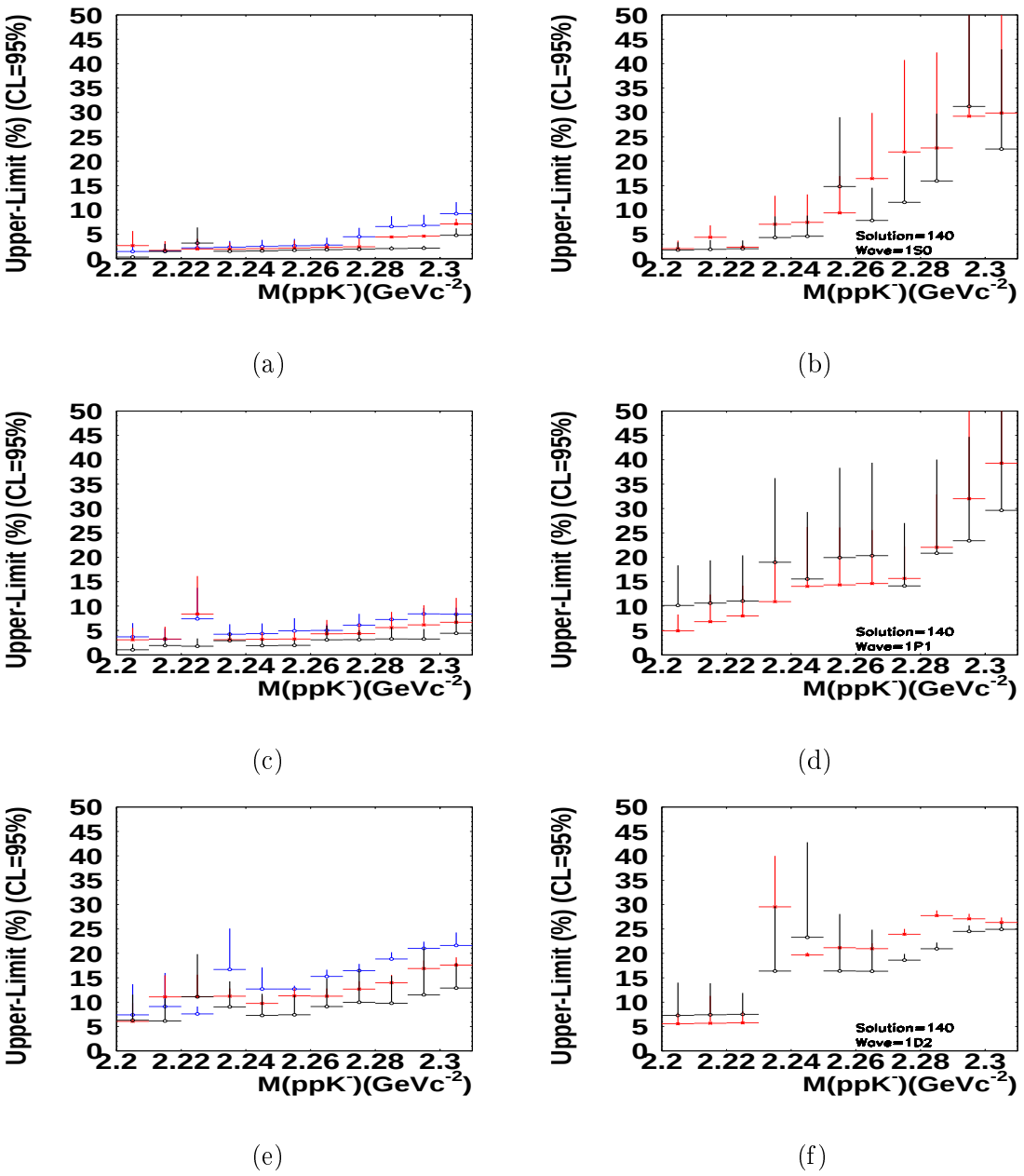


(a) (b) (c) (d) (e) (f)

Figure I.5: Upper Limit of the relative contribution of the pp$K^-$ production (given in %) for a exclusion confidence Level of 95% versus the peak mass of the pp$K^-$ used in the PWA fit.The production of the pp$K^-$ is from the initial proton state $0^+$ (a,b), $1^-$ (c,d) or ($2^+$). In spectra (a),(c) and (e) the $\Gamma$ of pp$K^-$ on PWA is set to 20 MeV/c$^2$(blue crosses), 35 MeV/c$^2$(red crosses) and 50 MeV/c$^2$(black crosses). In spectra (b),(d) and (f) the $\Gamma$ of pp$K^-$ on PWA is set , 80 MeV/c$^2$(red crosses) and 60 MeV/c$^2$(black crosses). For the background assumption solution number 110112 was used.

## I.b Upper Limit Values

| Mass (GeV/c$^2$) | 2.205 | 2.215 | 2.225 | 2.235 | 2.245 | 2.255 |
|---|---|---|---|---|---|---|
| 000113 | $2.05^{+2.1}$ | $2.24^{+1.8}$ | $4.77^{+4.2}$ | $2.28^{+0.7}$ | $2.41^{+0.5}$ | $2.58^{+0.6}$ |
| 010110 | $1.54^{+1.7}$ | $1.69^{+0.9}$ | $1.78^{+0.9}$ | $1.72^{+0.4}$ | $1.82^{+0.4}$ | $1.95^{+0.4}$ |
| 011103 | $1.26^{+1.5}$ | $1.38^{+1}$ | $1.45^{+1}$ | $1.41^{+1.3}$ | $1.49^{+0.4}$ | $1.6^{+0.4}$ |
| 110103 | $1.33^{+1}$ | $3.21^{+2.6}$ | $4.04^{+3.5}$ | $3.25^{+0.1}$ | $1.56^{+1.5}$ | $3.72^{+0.1}$ |
| 110112 | $0.35^{+0}$ | $1.51^{+1.5}$ | $3.22^{+3.1}$ | $1.54^{+0.5}$ | $1.63^{+0.4}$ | $1.75^{+0.4}$ |
| Max | $2.05^{+2.1}$ | $3.21^{+2.6}$ | $4.77^{+4.2}$ | $3.25^{+0.1}$ | $2.41^{+0.5}$ | $3.72^{+0.1}$ |

| Mass (GeV/c$^2$) | 2.265 | 2.275 | 2.285 | 2.295 | 2.305 |
|---|---|---|---|---|---|
| 000113 | $2.76^{+0.6}$ | $2.88^{+0.8}$ | $3.12^{+0}$ | $3.15^{+1}$ | $3.16^{+1.1}$ |
| 010110 | $2.07^{+0.5}$ | $2.17^{+0.6}$ | $2.32^{+0.7}$ | $2.4^{+0.8}$ | $2.41^{+0.9}$ |
| 011103 | $1.7^{+0.4}$ | $1.8^{+0.3}$ | $1.93^{+0.3}$ | $2^{+2}$ | $4.42^{+0}$ |
| 110103 | $1.81^{+0.7}$ | $4.19^{+0}$ | $2.02^{+0.8}$ | $4.57^{+0}$ | $4.61^{+0}$ |
| 110112 | $1.87^{+0.4}$ | $1.97^{+0.4}$ | $2.1^{+0.4}$ | $2.18^{+0.4}$ | $4.81^{+1.4}$ |
| Max | $2.76^{+0.6}$ | $4.19^{+0}$ | $3.12^{+0}$ | $4.57^{+0}$ | $4.81^{+1.4}$ |

Table I.1: Upper limit value for relative Contribution of pp$K^-$ of the Width $\Gamma$=20 MeV/c$^2$. The table shows the values for different initial proton-proton wave $0^+$, different background approximations and pp$K^-$ masses.

| Mass (GeV/c$^2$) | 2.205 | 2.215 | 2.225 | 2.235 | 2.245 | 2.255 |
|---|---|---|---|---|---|---|
| 000113 | $8.06^{+5}$ | $12.15^{+9}$ | $28.66^{+26.2}$ | $12.98^{+5.5}$ | $10.52^{+6.8}$ | $10.7^{+5.4}$ |
| 010110 | $4.59^{+3.8}$ | $8.8^{+6.2}$ | $10^{+7.1}$ | $8.04^{+1.9}$ | $8.05^{+6}$ | $8.18^{+3.5}$ |
| 011103 | $10.08^{+8.6}$ | $8.28^{+5.7}$ | $18.26^{+16.1}$ | $8.3^{+4.8}$ | $6.65^{+2.8}$ | $9.23^{+5.7}$ |
| 110103 | $6.8^{+4.9}$ | $18.88^{+18.7}$ | $22.62^{+18.7}$ | $11.41^{+7.3}$ | $9.48^{+6.4}$ | $9.66^{+5.9}$ |
| 110112 | $6.3^{+5.2}$ | $6.15^{+4.5}$ | $11.1^{+8.7}$ | $9.04^{+5.2}$ | $7.28^{+4.4}$ | $7.41^{+4}$ |
| Max | $10.08^{+8.6}$ | $18.88^{+18.7}$ | $28.66^{+26.2}$ | $12.98^{+5.5}$ | $10.52^{+6.8}$ | $10.7^{+5.4}$ |

| Mass (GeV/c$^2$) | 2.265 | 2.275 | 2.285 | 2.295 | 2.305 |
|---|---|---|---|---|---|
| 000113 | $10.58^{+2.6}$ | $14.34^{+10.9}$ | $12.9^{+7.1}$ | $13.4^{+8.4}$ | $15.19^{+10}$ |
| 010110 | $8.1^{+4}$ | $8.14^{+4.4}$ | $9.89^{+6.2}$ | $10.43^{+7.1}$ | $11.87^{+6.2}$ |
| 011103 | $9.19^{+4.7}$ | $11.09^{+7.1}$ | $10.91^{+7}$ | $10.55^{+5.3}$ | $11.85^{+4.4}$ |
| 110103 | $9.59^{+5}$ | $11.56^{+7.4}$ | $11.38^{+7.3}$ | $13.01^{+7.5}$ | $12.36^{+7.1}$ |
| 110112 | $9.11^{+5.7}$ | $9.98^{+6.8}$ | $9.79^{+5.5}$ | $11.52^{+9.6}$ | $12.89^{+5.1}$ |
| Max | $10.58^{+2.6}$ | $14.34^{+10.9}$ | $12.9^{+7.1}$ | $13.4^{+8.4}$ | $15.19^{+10}$ |

Table I.2: Upper limit value for relative Contribution of pp$K^-$ of the Width $\Gamma$=20 MeV/c$^2$. The table shows the values for initial proton-proton wave $2^+$, different background approximations and pp$K^-$ masses.

| Mass (GeV/c$^2$) | 2.205 | 2.215 | 2.225 | 2.235 | 2.245 | 2.255 |
|---|---|---|---|---|---|---|
| 000113 | $1.52^{+1.7}$ | $2.82^{+2.8}$ | $2.89^{+2.9}$ | $2.76^{+2}$ | $2.8^{+2.5}$ | $2.86^{+2.1}$ |
| 010110 | $1.38^{+1.6}$ | $2.13^{+1.8}$ | $3.32^{+3.1}$ | $3.24^{+2.9}$ | $2.12^{+1.6}$ | $3.34^{+3.1}$ |
| 011103 | $1.66^{+1.8}$ | $2.72^{+2.7}$ | $2.78^{+2.6}$ | $2.65^{+1.9}$ | $1.74^{+1.4}$ | $2.75^{+2.6}$ |
| 110103 | $1.74^{+2.3}$ | $2.84^{+3.2}$ | $2.9^{+2.8}$ | $2.77^{+2.6}$ | $1.82^{+1.4}$ | $2.88^{+2.7}$ |
| 110112 | $1.03^{+1.1}$ | $1.91^{+1.7}$ | $1.77^{+1.5}$ | $2.91^{+1.7}$ | $1.9^{+1.3}$ | $1.95^{+1.1}$ |
| Max | $1.74^{+2.3}$ | $2.84^{+3.2}$ | $3.32^{+3.1}$ | $3.24^{+2.9}$ | $2.8^{+2.5}$ | $3.34^{+3.1}$ |

| Mass (GeV/c$^2$) | 2.265 | 2.275 | 2.285 | 2.295 | 2.305 |
|---|---|---|---|---|---|
| 000113 | $2.94^{+2.5}$ | $4.55^{+4.3}$ | $4.73^{+4.4}$ | $4.72^{+4.4}$ | $4.52^{+3.4}$ |
| 010110 | $3.43^{+3.3}$ | $3.47^{+3.2}$ | $3.62^{+3.3}$ | $3.62^{+2.8}$ | $4.88^{+4.5}$ |
| 011103 | $2.83^{+2.6}$ | $2.88^{+2}$ | $3.01^{+2.8}$ | $3.01^{+2}$ | $4.11^{+3.7}$ |
| 110103 | $2.96^{+2.9}$ | $3.01^{+2.8}$ | $3.15^{+3}$ | $3.15^{+2.9}$ | $3.02^{+2}$ |
| 110112 | $3.08^{+2.8}$ | $3.12^{+1.9}$ | $3.26^{+2.3}$ | $3.25^{+2}$ | $4.42^{+4}$ |
| Max | $3.43^{+3.3}$ | $4.55^{+4.3}$ | $4.73^{+4.4}$ | $4.72^{+4.4}$ | $4.88^{+4.5}$ |

Table I.3: Upper limit value for relative Contribution of pp$K^-$ of the Width $\Gamma$=20 MeV/c$^2$. The table shows the values for initial proton-proton wave $1^-$, different background approximations and pp$K^-$ masses.

| Mass (GeV/c$^2$) | 2.205 | 2.215 | 2.225 | 2.235 | 2.245 | 2.255 |
|---|---|---|---|---|---|---|
| 000113 | $4.13^{+2.7}$ | $4.9^{+4.3}$ | $5.21^{+3.3}$ | $5.02^{+0}$ | $5.31^{+2.1}$ | $5.63^{+2.3}$ |
| 010110 | $2.37^{+1.5}$ | $3.37^{+3}$ | $3.96^{+3.4}$ | $3.81^{+0}$ | $2.3^{+1.7}$ | $2.44^{+1.8}$ |
| 011103 | $1.45^{+0.7}$ | $2.08^{+1.9}$ | $2.91^{+2.6}$ | $1.77^{+0.4}$ | $1.88^{+0.4}$ | $2^{+0.5}$ |
| 110103 | $2.65^{+2.1}$ | $3.17^{+2.7}$ | $4.7^{+4}$ | $3.24^{+1.5}$ | $3.43^{+0}$ | $3.65^{+1.6}$ |
| 110112 | $2.69^{+3}$ | $1.72^{+1.9}$ | $2.02^{+2}$ | $1.95^{+1.3}$ | $2.06^{+0}$ | $2.19^{+1.5}$ |
| Max | $4.13^{+2.7}$ | $4.9^{+4.3}$ | $5.21^{+3.3}$ | $5.02^{+0}$ | $5.31^{+2.1}$ | $5.63^{+2.3}$ |

| Mass (GeV/c$^2$) | 2.265 | 2.275 | 2.285 | 2.295 | 2.305 |
|---|---|---|---|---|---|
| 000113 | $5.93^{+2.5}$ | $6.29^{+2.7}$ | $6.42^{+2.8}$ | $6.59^{+2.9}$ | $6.71^{+0.8}$ |
| 010110 | $2.58^{+1.8}$ | $2.71^{+0.7}$ | $4.89^{+2.2}$ | $5.05^{+0.5}$ | $5.16^{+0.6}$ |
| 011103 | $3.71^{+0}$ | $3.91^{+0}$ | $4.12^{+0}$ | $4.28^{+0}$ | $6.68^{+1.2}$ |
| 110103 | $3.87^{+0.1}$ | $6.2^{+1.1}$ | $4.3^{+0.1}$ | $6.76^{+1.2}$ | $6.94^{+1.2}$ |
| 110112 | $2.33^{+0.6}$ | $2.46^{+1.6}$ | $4.47^{+0.1}$ | $4.63^{+0.1}$ | $7.15^{+1}$ |
| Max | $5.93^{+2.5}$ | $6.29^{+2.7}$ | $6.42^{+2.8}$ | $6.76^{+1.2}$ | $7.15^{+1}$ |

Table I.4: Upper limit value for relative Contribution of pp$K^-$ of the Width $\Gamma$=35 MeV/c$^2$. The table shows the values for initial proton-proton wave $0^+$, different background approximations and pp$K^-$ masses.

| Mass (GeV/c$^2$) | 2.205 | 2.215 | 2.225 | 2.235 | 2.245 | 2.255 |
|---|---|---|---|---|---|---|
| 000113 | $16.1^{+11}$ | $16.33^{+3.9}$ | $16.48^{+1.6}$ | $16.03^{+3.4}$ | $14^{+1.5}$ | $16.09^{+2.1}$ |
| 010110 | $7.45^{+1.7}$ | $12.4^{+2.7}$ | $12.34^{+0.3}$ | $10.73^{+1.6}$ | $10.76^{+1}$ | $12.45^{+1.7}$ |
| 011103 | $10.14^{+2.2}$ | $8.82^{+1.3}$ | $10.54^{+1.1}$ | $10.26^{+1.4}$ | $10.27^{+1.4}$ | $11.79^{+1.5}$ |
| 110103 | $10.54^{+0.1}$ | $12.05^{+1.3}$ | $13.69^{+1.6}$ | $13.73^{+1.6}$ | $12.23^{+1.5}$ | $13.87^{+1.6}$ |
| 110112 | $6.07^{+3.7}$ | $11.07^{+4.4}$ | $11.14^{+4.4}$ | $11.23^{+1.5}$ | $9.74^{+1.5}$ | $11.29^{+1.5}$ |
| Max | $16.1^{+11}$ | $16.33^{+3.9}$ | $16.48^{+1.6}$ | $16.03^{+3.4}$ | $14^{+1.5}$ | $16.09^{+2.1}$ |

| Mass (GeV/c$^2$) | 2.265 | 2.275 | 2.285 | 2.295 | 2.305 |
|---|---|---|---|---|---|
| 000113 | $15.99^{+2}$ | $17.86^{+2}$ | $19.56^{+2}$ | $20.99^{+2.3}$ | $20.22^{+1.9}$ |
| 010110 | $10.86^{+1.6}$ | $12.36^{+1.7}$ | $13.78^{+1.7}$ | $16.7^{+1.7}$ | $17.68^{+1.6}$ |
| 011103 | $11.77^{+1.5}$ | $14.73^{+1.5}$ | $14.49^{+1.5}$ | $17.17^{+1.5}$ | $16.58^{+1.5}$ |
| 110103 | $13.83^{+1.6}$ | $15.31^{+1.6}$ | $16.67^{+1.6}$ | $17.81^{+1.6}$ | $17.18^{+1.5}$ |
| 110112 | $11.23^{+1.5}$ | $12.68^{+1.6}$ | $13.99^{+1.6}$ | $16.9^{+1.6}$ | $17.62^{+1.5}$ |
| Max | $15.99^{+2}$ | $17.86^{+2}$ | $19.56^{+2}$ | $20.99^{+2.3}$ | $20.22^{+1.9}$ |

Table I.5: Upper limit value for relative Contribution of pp$K^-$ of the Width $\Gamma$=35 MeV/c$^2$. The table shows the values for initial proton-proton wave $2^+$, different background approximations and pp$K^-$ masses.

| Mass (GeV/c$^2$) | 2.205 | 2.215 | 2.225 | 2.235 | 2.245 | 2.255 |
|---|---|---|---|---|---|---|
| 000113 | $2.98^{+2.7}$ | $8.4^{+7.5}$ | $8.72^{+7.7}$ | $4.57^{+2.6}$ | $4.67^{+2.6}$ | $4.77^{+2.7}$ |
| 010110 | $6.02^{+5.6}$ | $3.6^{+2.7}$ | $6.59^{+5.6}$ | $4.48^{+2.4}$ | $4.58^{+3.7}$ | $4.68^{+2.5}$ |
| 011103 | $4.96^{+4.8}$ | $5.21^{+4.6}$ | $5.4^{+4.9}$ | $3.67^{+3.1}$ | $2.9^{+1.2}$ | $2.97^{+1.3}$ |
| 110103 | $5.17^{+5.1}$ | $3.11^{+2.8}$ | $3.68^{+2.1}$ | $3.82^{+3.2}$ | $3.03^{+1.6}$ | $4.01^{+3.3}$ |
| 110112 | $3.09^{+2.4}$ | $3.25^{+2.5}$ | $8.37^{+7.7}$ | $3.11^{+1.3}$ | $3.19^{+1.3}$ | $3.25^{+1.3}$ |
| Max | $6.02^{+5.6}$ | $8.4^{+7.5}$ | $8.72^{+7.7}$ | $4.57^{+2.6}$ | $4.67^{+2.6}$ | $4.77^{+2.7}$ |

| Mass (GeV/c$^2$) | 2.265 | 2.275 | 2.285 | 2.295 | 2.305 |
|---|---|---|---|---|---|
| 000113 | $4.86^{+2.7}$ | $6.45^{+5.1}$ | $6.43^{+3.4}$ | $6.41^{+4.1}$ | $7.77^{+5.2}$ |
| 010110 | $4.78^{+2.6}$ | $4.86^{+2.6}$ | $6.17^{+3.5}$ | $6.76^{+4.7}$ | $6.62^{+5.1}$ |
| 011103 | $3.94^{+2.2}$ | $4.02^{+2.2}$ | $5.14^{+2.9}$ | $5.68^{+3.9}$ | $6.19^{+4.2}$ |
| 110103 | $4.11^{+3.4}$ | $4.19^{+2.3}$ | $4.28^{+2.3}$ | $4.29^{+2.3}$ | $5.28^{+3}$ |
| 110112 | $4.3^{+2.8}$ | $4.38^{+2}$ | $5.59^{+3.2}$ | $6.15^{+4}$ | $6.68^{+4.9}$ |
| Max | $4.86^{+2.7}$ | $6.45^{+5.1}$ | $6.43^{+3.4}$ | $6.76^{+4.7}$ | $7.77^{+5.2}$ |

Table I.6: Upper limit value for relative Contribution of pp$K^-$ of the Width $\Gamma$=35 MeV/c$^2$. The table shows the values for initial proton-proton wave $1^-$, different background approximations and pp$K^-$ masses.

| Mass (GeV/c$^2$) | 2.205 | 2.215 | 2.225 | 2.235 | 2.245 | 2.255 |
|---|---|---|---|---|---|---|
| 000113 | $3.25^{+1.5}$ | $4.84^{+2.7}$ | $7.17^{+4.9}$ | $7.59^{+2.4}$ | $5.68^{+1.1}$ | $6^{+1.2}$ |
| 010110 | $2.41^{+1.9}$ | $3.92^{+2.6}$ | $4.26^{+2.7}$ | $4.09^{+0.8}$ | $4.32^{+0.8}$ | $4.55^{+0.8}$ |
| 011103 | $1.96^{+1.5}$ | $2.11^{+1.3}$ | $3.13^{+1.7}$ | $3.33^{+1.3}$ | $3.53^{+1.4}$ | $3.74^{+0.7}$ |
| 110103 | $3.16^{+0.9}$ | $4.36^{+0.4}$ | $5.12^{+1.3}$ | $4.92^{+1.6}$ | $5.2^{+1.7}$ | $5.49^{+1.8}$ |
| 110112 | $1.5^{+1.5}$ | $1.59^{+1.5}$ | $2.24^{+1.5}$ | $2.38^{+1.2}$ | $2.52^{+1.3}$ | $2.67^{+1.4}$ |
| Max | $3.25^{+1.5}$ | $4.84^{+2.7}$ | $7.17^{+4.9}$ | $7.59^{+2.4}$ | $5.68^{+1.1}$ | $6^{+1.2}$ |

| Mass (GeV/c$^2$) | 2.265 | 2.275 | 2.285 | 2.295 | 2.305 |
|---|---|---|---|---|---|
| 000113 | $6.31^{+1.1}$ | $9.13^{+2.8}$ | $9.4^{+2.8}$ | $9.61^{+2.8}$ | $7.07^{+2.7}$ |
| 010110 | $4.77^{+0.8}$ | $4.98^{+0.7}$ | $5.17^{+2}$ | $7.42^{+2.2}$ | $7.56^{+2.2}$ |
| 011103 | $3.95^{+1.6}$ | $5.85^{+1.9}$ | $6.12^{+2}$ | $6.36^{+2}$ | $8.7^{+2.3}$ |
| 110103 | $5.79^{+1.8}$ | $8.06^{+2.1}$ | $8.42^{+2.2}$ | $8.73^{+2.3}$ | $9^{+2.3}$ |
| 110112 | $2.81^{+1.4}$ | $4.52^{+1.8}$ | $6.61^{+2.1}$ | $6.84^{+2.1}$ | $9.24^{+2.3}$ |
| Max | $6.31^{+1.1}$ | $9.13^{+2.8}$ | $9.4^{+2.8}$ | $9.61^{+2.8}$ | $9.24^{+2.3}$ |

Table I.7: Upper limit value for relative Contribution of pp$K^-$ of the Width $\Gamma$=50 MeV/c$^2$. The table shows the values for initial proton-proton wave $0^+$, different background approximations and pp$K^-$ masses.

| Mass (GeV/c$^2$) | 2.205 | 2.215 | 2.225 | 2.235 | 2.245 | 2.255 |
|---|---|---|---|---|---|---|
| 000113 | $14.09^{+11.1}$ | $16.02^{+11.3}$ | $17.93^{+11.8}$ | $19.82^{+13.7}$ | $19.85^{+13.7}$ | $20.07^{+12}$ |
| 010110 | $9.53^{+6.8}$ | $11^{+7.4}$ | $13.89^{+9.2}$ | $13.97^{+9.2}$ | $14.02^{+9.3}$ | $15.45^{+9.1}$ |
| 011103 | $10.1^{+6.3}$ | $11.42^{+6.2}$ | $12.74^{+5.1}$ | $12.79^{+5.2}$ | $12.83^{+5.2}$ | $14.12^{+1.2}$ |
| 110103 | $12.94^{+5.2}$ | $14.42^{+6.6}$ | $18.99^{+1.7}$ | $15.96^{+1.3}$ | $16.02^{+1.3}$ | $17.41^{+1.3}$ |
| 110112 | $7.4^{+6.2}$ | $9.1^{+6.8}$ | $7.6^{+1.5}$ | $16.71^{+8.3}$ | $12.71^{+4.4}$ | $12.7^{+0.6}$ |
| Max | $14.09^{+11.1}$ | $16.02^{+11.3}$ | $18.99^{+1.7}$ | $19.82^{+13.7}$ | $19.85^{+13.7}$ | $20.07^{+12}$ |

| Mass (GeV/c$^2$) | 2.265 | 2.275 | 2.285 | 2.295 | 2.305 |
|---|---|---|---|---|---|
| 000113 | $21.44^{+10.2}$ | $24.91^{+1.8}$ | $25.92^{+2}$ | $26.9^{+1.6}$ | $25.97^{+1.9}$ |
| 010110 | $14.07^{+7.6}$ | $16.76^{+2.3}$ | $17.88^{+1.4}$ | $21.7^{+1.4}$ | $20.87^{+1.3}$ |
| 011103 | $15.37^{+1.3}$ | $17.87^{+1.3}$ | $20.25^{+1.3}$ | $21.12^{+1.3}$ | $19.23^{+1.3}$ |
| 110103 | $18.72^{+1.3}$ | $19.91^{+1.3}$ | $20.95^{+1.3}$ | $21.8^{+1.3}$ | $19.85^{+1.3}$ |
| 110112 | $15.28^{+1.3}$ | $16.46^{+1.3}$ | $18.86^{+1.3}$ | $21.03^{+1.3}$ | $21.64^{+2.6}$ |
| Max | $21.44^{+10.2}$ | $24.91^{+1.8}$ | $25.92^{+2}$ | $26.9^{+1.6}$ | $25.97^{+1.9}$ |

Table I.8: Upper limit value for relative Contribution of pp$K^-$ of the Width $\Gamma$=50 MeV/c$^2$. The table shows the values for initial proton-proton wave $2^+$, different background approximations and pp$K^-$ masses.

| Mass (GeV/c$^2$) | 2.205 | 2.215 | 2.225 | 2.235 | 2.245 | 2.255 |
|---|---|---|---|---|---|---|
| 000113 | $9.9^{+9}$ | $10.38^{+9.4}$ | $10.8^{+9.9}$ | $6.19^{+4.1}$ | $6.34^{+4.2}$ | $7.12^{+4.6}$ |
| 010110 | $9.14^{+8.4}$ | $9.51^{+8.3}$ | $10.02^{+8.8}$ | $5.18^{+2.6}$ | $5.32^{+2.7}$ | $5.44^{+2.8}$ |
| 011103 | $6.14^{+5.7}$ | $6.44^{+5.9}$ | $6.7^{+5.8}$ | $3.84^{+1.9}$ | $3.95^{+2.6}$ | $4.47^{+2.4}$ |
| 110103 | $6.38^{+6.3}$ | $6.7^{+6.1}$ | $12.73^{+12.1}$ | $4.42^{+3.1}$ | $4.54^{+3.2}$ | $4.65^{+3.2}$ |
| 110112 | $3.69^{+2.8}$ | $3.2^{+2.2}$ | $7.38^{+6.3}$ | $4.23^{+2}$ | $4.35^{+2}$ | $4.91^{+2.6}$ |
| Max | $9.9^{+9}$ | $10.38^{+9.4}$ | $12.73^{+12.1}$ | $6.19^{+4.1}$ | $6.34^{+4.2}$ | $7.12^{+4.6}$ |

| Mass (GeV/c$^2$) | 2.265 | 2.275 | 2.285 | 2.295 | 2.305 |
|---|---|---|---|---|---|
| 000113 | $7.36^{+4.9}$ | $7.45^{+5}$ | $8.91^{+5.4}$ | $8.88^{+3.6}$ | $10.01^{+4.9}$ |
| 010110 | $6.64^{+3.9}$ | $6.73^{+2.5}$ | $7.96^{+0.9}$ | $7.94^{+0.9}$ | $7.85^{+1.1}$ |
| 011103 | $4.56^{+2.4}$ | $5.57^{+2.1}$ | $6.65^{+3.1}$ | $6.66^{+0.5}$ | $7.68^{+1.1}$ |
| 110103 | $4.75^{+2.5}$ | $5.79^{+3.5}$ | $5.87^{+3.5}$ | $5.88^{+2.2}$ | $5.85^{+2.2}$ |
| 110112 | $5^{+1.2}$ | $6.09^{+2.3}$ | $7.25^{+0.6}$ | $8.4^{+1.2}$ | $8.32^{+1.3}$ |
| Max | $7.36^{+4.9}$ | $7.45^{+5}$ | $8.91^{+5.4}$ | $8.88^{+3.6}$ | $10.01^{+4.9}$ |

Table I.9: Upper limit value for relative Contribution of pp$K^-$ of the Width $\Gamma$=50 MeV/c$^2$. The table shows the values for initial proton-proton wave $1^-$, different background approximations and pp$K^-$ masses.

| Mass (GeV/c$^2$) | 2.205 | 2.215 | 2.225 | 2.235 | 2.245 | 2.255 |
|---|---|---|---|---|---|---|
| 000113 | $4.19^{+4}$ | $4.49^{+3.6}$ | $7.87^{+6.1}$ | $16.62^{+15.5}$ | $17.48^{+16.3}$ | $18.34^{+17.5}$ |
| 010110 | $6.14^{+5.8}$ | $3.33^{+2.6}$ | $3.54^{+2.9}$ | $7.36^{+7}$ | $11.2^{+10.8}$ | $11.74^{+11.6}$ |
| 011103 | $4.99^{+5.2}$ | $2.7^{+2.9}$ | $5.71^{+5.9}$ | $6.12^{+6.3}$ | $6.48^{+6.6}$ | $6.72^{+6.7}$ |
| 110103 | $4.48^{+2.4}$ | $5.6^{+3.4}$ | $11.4^{+8.8}$ | $12.06^{+10.4}$ | $19.08^{+17.3}$ | $20.07^{+18.2}$ |
| 110112 | $1.8^{+1.5}$ | $1.93^{+1.9}$ | $2.06^{+1.6}$ | $4.36^{+4.3}$ | $4.62^{+4.2}$ | $14.82^{+14.2}$ |
| Max | $6.14^{+5.8}$ | $5.6^{+3.4}$ | $11.4^{+8.8}$ | $16.62^{+15.5}$ | $19.08^{+17.3}$ | $20.07^{+18.2}$ |

| Mass (GeV/c$^2$) | 2.265 | 2.275 | 2.285 | 2.295 | 2.305 |
|---|---|---|---|---|---|
| 000113 | $19.16^{+18.7}$ | $32.96^{+32.3}$ | $33.81^{+32.9}$ | $22.98^{+21.9}$ | $17.88^{+17.3}$ |
| 010110 | $12.26^{+12.1}$ | $15.16^{+14.7}$ | $13.2^{+12.4}$ | $26.61^{+25.7}$ | $27.18^{+26.3}$ |
| 011103 | $10.18^{+10.1}$ | $14.22^{+14.4}$ | $13.32^{+13.2}$ | $19.6^{+19.5}$ | $20.24^{+20}$ |
| 110103 | $26.85^{+24.3}$ | $28.11^{+25.7}$ | $29.28^{+25.9}$ | $30.33^{+26.9}$ | $31.29^{+28.6}$ |
| 110112 | $7.86^{+6.6}$ | $11.58^{+9.4}$ | $15.96^{+13.7}$ | $31.23^{+28.9}$ | $22.5^{+20.4}$ |
| Max | $26.85^{+24.3}$ | $32.96^{+32.3}$ | $33.81^{+32.9}$ | $31.23^{+28.9}$ | $31.29^{+28.6}$ |

Table I.10: Upper limit value for relative Contribution of pp$K^-$ of the Width $\Gamma$=60 MeV/c$^2$. The table shows the values for initial proton-proton wave $0^+$, different background approximations and pp$K^-$ masses.

| Mass (GeV/c$^2$) | 2.205 | 2.215 | 2.225 | 2.235 | 2.245 | 2.255 |
|---|---|---|---|---|---|---|
| 000113 | $11.4^{+8.3}$ | $17.9^{+14.5}$ | $19.7^{+16.5}$ | $23.66^{+20.5}$ | $23.86^{+20.7}$ | $23.86^{+19.5}$ |
| 010110 | $8.7^{+6.9}$ | $8.86^{+6.9}$ | $14^{+11.6}$ | $18.04^{+15.6}$ | $18.46^{+16}$ | $18.36^{+14.9}$ |
| 011103 | $11.32^{+11.9}$ | $11.5^{+12}$ | $12.71^{+13.2}$ | $14.94^{+15.5}$ | $15.1^{+15.6}$ | $16.29^{+16.8}$ |
| 110103 | $15.2^{+12.3}$ | $15.44^{+11.8}$ | $16.8^{+12.3}$ | $18.14^{+13.6}$ | $18.2^{+12.4}$ | $19.46^{+11.8}$ |
| 110112 | $7.29^{+6.7}$ | $7.42^{+6.4}$ | $7.51^{+4.3}$ | $16.38^{+13.2}$ | $23.3^{+19.4}$ | $16.4^{+11.6}$ |
| Max | $15.2^{+12.3}$ | $17.9^{+14.5}$ | $19.7^{+16.5}$ | $23.66^{+20.5}$ | $23.86^{+20.7}$ | $23.86^{+19.5}$ |

| Mass (GeV/c$^2$) | 2.265 | 2.275 | 2.285 | 2.295 | 2.305 |
|---|---|---|---|---|---|
| 000113 | $31.55^{+25.2}$ | $27.75^{+13.5}$ | $29.91^{+2.6}$ | $37.46^{+4.3}$ | $41.31^{+41.3}$ |
| 010110 | $17.94^{+14.4}$ | $23.24^{+16.8}$ | $30.84^{+7.9}$ | $34.28^{+8.7}$ | $32.14^{+7.5}$ |
| 011103 | $18.64^{+19.2}$ | $20.92^{+21.5}$ | $23.11^{+23.7}$ | $24.41^{+25}$ | $21.42^{+22}$ |
| 110103 | $20.63^{+3.8}$ | $23.56^{+1.2}$ | $24.42^{+1.2}$ | $25.11^{+1.2}$ | $22.06^{+1.2}$ |
| 110112 | $16.35^{+8.5}$ | $18.63^{+1.2}$ | $20.95^{+1.2}$ | $24.51^{+1.2}$ | $24.93^{+1.2}$ |
| Max | $31.55^{+25.2}$ | $27.75^{+13.5}$ | $30.84^{+7.9}$ | $37.46^{+4.3}$ | $41.31^{+41.3}$ |

Table I.11: Upper limit value for relative Contribution of pp$K^-$ of the Width $\Gamma$=60 MeV/c$^2$. The table shows the values for initial proton-proton wave $2^+$, different background approximations and pp$K^-$ masses.

| Mass (GeV/c$^2$) | 2.205 | 2.215 | 2.225 | 2.235 | 2.245 | 2.255 |
|---|---|---|---|---|---|---|
| 000113 | $9.94^{+8.2}$ | $10.42^{+8.1}$ | $10.84^{+8.5}$ | $22.02^{+21.1}$ | $17.25^{+16.3}$ | $23.01^{+22.1}$ |
| 010110 | $9.87^{+7.6}$ | $7.84^{+5.5}$ | $8.18^{+5.7}$ | $11.2^{+8.7}$ | $17.2^{+15.1}$ | $17.59^{+15.5}$ |
| 011103 | $6.1^{+6.7}$ | $3.23^{+3.8}$ | $6.65^{+7.3}$ | $13.76^{+14.4}$ | $9.42^{+10}$ | $14.5^{+15.1}$ |
| 110103 | $9.57^{+8.1}$ | $10.02^{+8.5}$ | $9.18^{+8.4}$ | $14.25^{+13.4}$ | $14.66^{+13.7}$ | $14.99^{+14}$ |
| 110112 | $10.13^{+8.2}$ | $10.61^{+8.7}$ | $11.05^{+9.3}$ | $18.99^{+17.2}$ | $15.55^{+13.7}$ | $19.94^{+18.4}$ |
| Max | $10.13^{+8.2}$ | $10.61^{+8.7}$ | $11.05^{+9.3}$ | $22.02^{+21.1}$ | $17.25^{+16.3}$ | $23.01^{+22.1}$ |

| Mass (GeV/c$^2$) | 2.265 | 2.275 | 2.285 | 2.295 | 2.305 |
|---|---|---|---|---|---|
| 000113 | $23.34^{+21.5}$ | $18.1^{+16.1}$ | $20.46^{+18.9}$ | $23.64^{+24.2}$ | $20.18^{+18.4}$ |
| 010110 | $17.89^{+16.8}$ | $17.89^{+16.8}$ | $21.47^{+19.7}$ | $36.27^{+34.5}$ | $22.89^{+20.7}$ |
| 011103 | $9.84^{+10.4}$ | $12.88^{+13.4}$ | $13.02^{+13.6}$ | $16.26^{+16.8}$ | $16.2^{+16.7}$ |
| 110103 | $15.31^{+13.5}$ | $15.73^{+14.8}$ | $15.74^{+14.6}$ | $13.56^{+12.6}$ | $13.52^{+12.3}$ |
| 110112 | $20.34^{+19}$ | $14.14^{+12.8}$ | $20.84^{+19.1}$ | $23.4^{+21.2}$ | $29.63^{+27.5}$ |
| Max | $23.34^{+21.5}$ | $18.1^{+16.1}$ | $21.47^{+19.7}$ | $36.27^{+34.5}$ | $29.63^{+27.5}$ |

Table I.12: Upper limit value for relative Contribution of pp$K^-$ of the Width $\Gamma$=60 MeV/c$^2$. The table shows the values for initial proton-proton wave $1^-$, different background approximations and pp$K^-$ masses.

| Mass (GeV/c$^2$) | 2.205 | 2.215 | 2.225 | 2.235 | 2.245 | 2.255 |
|---|---|---|---|---|---|---|
| 000113 | $12.06^{+9.1}$ | $12.86^{+9.2}$ | $13.6^{+9.7}$ | $26.56^{+23.5}$ | $34.35^{+32.8}$ | $35.75^{+33.1}$ |
| 010110 | $8.92^{+6.5}$ | $9.5^{+6.9}$ | $10.06^{+7.3}$ | $15.93^{+13.7}$ | $21.42^{+19.6}$ | $22.35^{+20.7}$ |
| 011103 | $3.62^{+3.9}$ | $3.86^{+4.1}$ | $4.1^{+4.3}$ | $8.66^{+8.9}$ | $11.74^{+11.9}$ | $13.06^{+13.1}$ |
| 110103 | $9.7^{+7.1}$ | $12.86^{+9.1}$ | $13.62^{+10.3}$ | $21.54^{+18.5}$ | $27.04^{+24.2}$ | $23.79^{+20.9}$ |
| 110112 | $2.08^{+1.6}$ | $4.4^{+2.4}$ | $2.36^{+0.4}$ | $7.08^{+5.8}$ | $7.46^{+5.7}$ | $9.4^{+7.5}$ |
| Max | $12.06^{+9.1}$ | $12.86^{+9.2}$ | $13.62^{+10.3}$ | $26.56^{+23.5}$ | $34.35^{+32.8}$ | $35.75^{+33.1}$ |

| Mass (GeV/c$^2$) | 2.265 | 2.275 | 2.285 | 2.295 | 2.305 |
|---|---|---|---|---|---|
| 000113 | $37.15^{+34.6}$ | $45.18^{+42.6}$ | $39.19^{+35.4}$ | $39.75^{+35.3}$ | $32.97^{+29.2}$ |
| 010110 | $23.25^{+21.3}$ | $19.64^{+17.7}$ | $35.59^{+32.6}$ | $30.99^{+28}$ | $31.59^{+28.3}$ |
| 011103 | $13.7^{+13.7}$ | $19.88^{+19.8}$ | $20.68^{+20.6}$ | $21.42^{+21.5}$ | $22.1^{+22}$ |
| 110103 | $25.64^{+22.6}$ | $26.7^{+23.8}$ | $27.7^{+24.5}$ | $28.62^{+25.3}$ | $28.83^{+25.4}$ |
| 110112 | $16.45^{+13.4}$ | $21.9^{+18.8}$ | $22.71^{+19.5}$ | $29.22^{+25.4}$ | $29.88^{+26.6}$ |
| Max | $37.15^{+34.6}$ | $45.18^{+42.6}$ | $39.19^{+35.4}$ | $39.75^{+35.3}$ | $32.97^{+29.2}$ |

Table I.13: Upper limit value for relative Contribution of pp$K^-$ of the Width $\Gamma$=80 MeV/c$^2$. The table shows the values for initial proton-proton wave $0^+$, different background approximations and pp$K^-$ masses.

| Mass (GeV/c$^2$) | 2.205 | 2.215 | 2.225 | 2.235 | 2.245 | 2.255 |
|---|---|---|---|---|---|---|
| 000113 | $21.11^{+9.4}$ | $22.8^{+11}$ | $24.21^{+5.7}$ | $24.39^{+2.4}$ | $41.62^{+13.7}$ | $40.57^{+10}$ |
| 010110 | $13.96^{+7.5}$ | $15.31^{+6}$ | $16.63^{+1.8}$ | $28.44^{+7.6}$ | $19.15^{+1.7}$ | $21.95^{+1.1}$ |
| 011103 | $13.45^{+14.1}$ | $14.63^{+15.3}$ | $15.77^{+16.4}$ | $15.88^{+16.5}$ | $18.45^{+19.1}$ | $20.51^{+21.1}$ |
| 110103 | $18.53^{+1}$ | $18.82^{+1}$ | $20.08^{+1}$ | $21.28^{+1}$ | $22.42^{+1}$ | $24.55^{+1}$ |
| 110112 | $5.58^{+2.2}$ | $5.68^{+5.6}$ | $5.75^{+2.4}$ | $29.54^{+10.4}$ | $19.67^{+0.5}$ | $21.16^{+0}$ |
| Max | $21.11^{+9.4}$ | $22.8^{+11}$ | $24.21^{+5.7}$ | $29.54^{+10.4}$ | $41.62^{+13.7}$ | $40.57^{+10}$ |

| Mass (GeV/c$^2$) | 2.265 | 2.275 | 2.285 | 2.295 | 2.305 |
|---|---|---|---|---|---|
| 000113 | $31.58^{+1.3}$ | $35.4^{+1.2}$ | $36.86^{+1.2}$ | $35.92^{+1.1}$ | $36.68^{+0}$ |
| 010110 | $40.01^{+14.6}$ | $34.32^{+9}$ | $40.9^{+11.5}$ | $29.54^{+1}$ | $28.54^{+1}$ |
| 011103 | $22.5^{+23.1}$ | $26.48^{+27.1}$ | $26.14^{+26.8}$ | $25.69^{+26.3}$ | $25.12^{+25.8}$ |
| 110103 | $26.58^{+1}$ | $27.38^{+1}$ | $26.98^{+1}$ | $26.45^{+1}$ | $25.83^{+1}$ |
| 110112 | $20.96^{+1}$ | $23.93^{+1}$ | $27.75^{+1}$ | $27.08^{+1}$ | $26.33^{+1}$ |
| Max | $40.01^{+14.6}$ | $35.4^{+1.2}$ | $40.9^{+11.5}$ | $35.92^{+1.1}$ | $36.68^{+0}$ |

Table I.14: Upper limit value for relative Contribution of pp$K^-$ of the Width $\Gamma$=80 MeV/c$^2$. The table shows the values for initial proton-proton wave $2^+$, different background approximations and pp$K^-$ masses.

| Mass (GeV/c$^2$) | 2.205 | 2.215 | 2.225 | 2.235 | 2.245 | 2.255 |
|---|---|---|---|---|---|---|
| 000113 | $10.73^{+9.4}$ | $9.94^{+8.5}$ | $10.32^{+9}$ | $17.5^{+15.8}$ | $17.9^{+16.2}$ | $18.22^{+16}$ |
| 010110 | $8.02^{+5.5}$ | $7.45^{+5.5}$ | $8.73^{+6.7}$ | $16.04^{+13.2}$ | $16.44^{+13.6}$ | $16.76^{+13.8}$ |
| 011103 | $4.41^{+5.1}$ | $4.61^{+5.3}$ | $4.79^{+5.4}$ | $8.58^{+9.2}$ | $11.02^{+11.7}$ | $11.28^{+11.9}$ |
| 110103 | $6.13^{+5.1}$ | $7.24^{+6.2}$ | $6.65^{+5.8}$ | $11.14^{+9.9}$ | $13.3^{+12}$ | $14.24^{+11.8}$ |
| 110112 | $4.92^{+3.3}$ | $6.79^{+5.5}$ | $7.96^{+6.2}$ | $10.92^{+9.1}$ | $14.03^{+12.1}$ | $14.35^{+11.7}$ |
| Max | $10.73^{+9.4}$ | $9.94^{+8.5}$ | $10.32^{+9}$ | $17.5^{+15.8}$ | $17.9^{+16.2}$ | $18.22^{+16}$ |

| Mass (GeV/c$^2$) | 2.265 | 2.275 | 2.285 | 2.295 | 2.305 |
|---|---|---|---|---|---|
| 000113 | $22.28^{+18.4}$ | $22.06^{+18.3}$ | $22.1^{+14.7}$ | $28.47^{+13.3}$ | $27.73^{+12.4}$ |
| 010110 | $19.07^{+15}$ | $24.6^{+14.9}$ | $41.92^{+28.7}$ | $38.57^{+24.3}$ | $31.73^{+17.7}$ |
| 011103 | $14^{+14.6}$ | $14.2^{+14.8}$ | $14.32^{+14.9}$ | $14.38^{+15}$ | $14.56^{+15.2}$ |
| 110103 | $14.5^{+11}$ | $14.7^{+11.2}$ | $14.84^{+9.6}$ | $14.9^{+6.3}$ | $14.88^{+4.3}$ |
| 110112 | $14.63^{+10.9}$ | $15.66^{+6.5}$ | $22.04^{+10.8}$ | $32^{+19.6}$ | $39.29^{+26.1}$ |
| Max | $22.28^{+18.4}$ | $24.6^{+14.9}$ | $41.92^{+28.7}$ | $38.57^{+24.3}$ | $39.29^{+26.1}$ |

Table I.15: Upper limit value for relative Contribution of pp$K^-$ of the Width $\Gamma$=80 MeV/c$^2$. The table shows the values for initial proton-proton wave $1^-$, different background approximations and pp$K^-$ masses.

# Danksagung

Das Proton-Proton Projekt begann für mich im jahr 2007 als Laura Fabbietti mich einlud zu einem ersten Test des SiΛViO Detektor an die GSI mitzufahren.
Daraus entwickelte sich ein erfolgreiches Projekt, das ich in Ihrer Gruppe durchführen konnte. Dabei habe ich von Ihr viel über alle Aspekte der Experimental Physik gelernt, von der Arbeit mit Detektoren bis zur physikalischen Interpretation von Ergebnissen. Ihren teils sehr genauen Fragen brachten mich stets zu einer sehr genauen und überlegten Arbeit. Die vielen Konferenzbesuche, die mir durch Laura ermöglicht wurden, haben zu einer starken Verbesserung meiner Präsentationfähigkeiten beigetragen. Dafür möchte ich mich herzlich bei ihr bedanken.
Des weitern möchte ich der gesamten KClus Gruppe danken, in der ich nicht nur gute Kollegen sondern sehr gute Freunde fürs Leben gefunden habe.
Im besonderen gilt meine dank Martin Berger, mit dem ich seit meinem Beginn in der Gruppe eng zusammengeabreitet habe. In vielen Stunden auf Schichten in der FOPI Messhüte oder auch bei der täglichen Arbeit führten wir oft sehr ergibige physikalische Gespräche, während unsere Dispute über gesellschaftspolitische Themen nicht immer den gleichen Nenner fanden. Martin und seiner Frau Jia-Chii Berger-Chen, die auch schon einige Jahre in unserer Gruppe arbeit, möchte ich für die vielen Korrekturen von Postern und Vorträgen danken, die sich sehr positiv auf meine Layoutentwicklung ausgewirkt haben.
Dank gilt auch Eliane Epple, die ganz besonders zum Verständniss und Umgang mit dem BG-PWA Framework und der Upper-Limit Bestimmung beigetragen hat. Ebenso möchte ich Kirill Lapidus und Johannes Siebenson für die meist sehr guten Fragen in Gruppenbesprechungen danken, die mir viele Impulse für meine Analsyse gegeben haben.
Für die vielen physikalischen und nicht physikalischen Diskussion möchte ich Oliver Arnold und Rafal Lalik danken, insbesondere für die vielen angeregten Gespräche über die Spiele des FC Bayern und Borussia Dortmund.
Eine absolute Bereicherung sowohl in der Arbeit aber auch privat war, als Piotr Gasik zu unserer Gruppe nach München kam. Die eingeführte *Hugging* Zeremonie möchte ich nicht mehr missen.
Auch meinem ehemaligen Kollegen und Studeten Olaf Hartmann, Dominik Soliman, Jakob Wirzbowski, Matthias Danner, Stephen Hessenberger und Bianca Kaiser möchte ich für Mitarbeit bei der Analyse danken. Insbesondere war mir Dominik Soliman eine großartige Hilfe, bei der Entwicklung des kinematischen Refits für die Analyse der Daten.
Ein großer Dank gilt auch der gesamten FOPI Kollaboration, durch die eine Realisierung des Experiments ermöglicht wurde. Im besondern gilt der Dank Yvonne Leifels und Norbert Hermann, die sich nicht nur während des Experiments die Nächte um die Ohren geschlagen haben, sondern mir auch bei der späteren Analyse immer mit Rat und Tat zur Seite standen.
Ebenfalls möchte ich dem gesamten Lehrstuhl E12 danken, insbesondere Roman Gernhäuser,

Jürgen Friese und Ludwig Maier.
Meiner ganzen Familie, insbesonde meinem Bruder Stephan, meiner Mutter Marion und meinem Vater Wolfgang, möchte ich danken für die viele Unterstützung die sie mir entgegen gebracht haben und mich motiviert haben.
Zum Schluss möchte ich meiner Frau Sarah-Maria danken. Als ich sie kennenlernte war ich kurz vor dem Abschluss meiner Hauptdiplomprüfungen. Seit damals war sie stets an meiner Seite und der beste Rückhalte den man sich nur wünschen kann. Mit ihrer lebensfrohen positiven Art konnte sie mich immer wieder aufbauen, auch wenn in meine Analyse einen scheinbar zur Verzweiflung bringenden Punkt erreicht hatte.